The University Of Sheffield.

Production and development of titanium alloys derived directly from synthetic rutile using electrochemical deoxidation.

Lyndsey Benson

A thesis submitted in partial fulfilment of the requirements for the degree of Doctor of Philosophy

The University of Sheffield
Faculty of Engineering
Department of Materials Science

August 2017

Abstract

Titanium's unique blend of properties, a high strength to weight ratio, outstanding biocompatibility and excellent corrosion resistance have granted the metal a premium status. However, the high cost of both extraction and fabrication of the material have severely limited the use of titanium to industries of a less cost-conscious nature, such as the aerospace and military markets. The FFC Metalysis process is a novel electrolytic extraction technique, capable of producing metals from their corresponding oxides. Use of this powder producing technique, in combination with low cost power metallurgy fabrication routes, could lead to a step change within the titanium industry.

Further, the FFC Metalysis process is capable of extracting titanium directly from ore like materials, such as synthetic rutile (SR), further reducing the cost of titanium production. As synthetic rutile is a derivate from titanium's alternative ore, ilmenite, it contains the presence of remnant elements, principally iron. This thesis assesses for the first time the physical, chemical and mechanical properties produced of the novel titanium alloy produced directly from synthetic rutile. Synthetic rutile feedstock has also been characterised, along with the determination of its reduction throughout the electrochemical deoxidation process using partial reductions. A particular emphasis was placed on the pathway of iron throughout reduction.

Following reduction, the baseline synthetic rutile derived titanium alloy revealed a β rich α+β titanium alloy with a similar compressive yield strength and strain to failure value of that of the widespread Ti-6Al-4V alloy. Further, the effect of residual carbon within the titanium alloys produced via the FFC process has been evaluated in powder form and following consolidation via the field assisted sintering technique. Once the characterisation and understanding of the baseline synthetic rutile derived titanium alloy had been achieved, alloy development allowed the properties of the baseline alloy to be tailored towards specific applications, (specifically springs) exemplifying the vast versatility that can be achieved by altering the baseline synthetic rutile feedstock.

Alteration of the feedstock was achieved via the incorporation of metal oxides prior to reduction. Various pseudo binary (SR-Al, SR-Mo) and pseudo ternary (SR-Al-Mo) alloys have been produced to assess the effects of additional alloying elements on the baseline SR derived titanium alloy. Building upon this work, a range of compositions were designed to produce titanium alloys suitable for spring applications. Due to the high potency of Fe as a beta stabiliser and its fast diffusion within titanium, Fe concentrations were increased within the spring alloy design to increase the beta stabilisation of the resulting alloy, whilst allowing a reduction in the

initial expensive beta stabilising Mo additions. Main limitations of the study were slight differences in interstitial values from run to run at an R&D scale and the presence of porosity (2-3%) within the resulting alloys.

Finally, the data generated during the production of various SR based titanium alloys has been used to produce a predictive model to aid future alloy development projects.

Acknowledgements

Firstly, I am grateful to both of my supervisors for their help, support and advice throughout the entirety of this work. Dr Martin Jackson, whose vision of a low-cost titanium future inspired me to undertake this project and gave me the opportunity to become a part of it and Dr Ian Mellor, whom has been a source of constant encouragement throughout this process.

I have been fortunate enough to have had a project that encompassed a wide range of areas, allowing me to learn many skills and techniques. I am grateful and indebted to those who took time from their own work to teach me.

In teaching me the wonders of the FFC process: Lucy Grainger, Dr Greg Doughty, Dr Nader Khan & Dr Mel Conti.

In teaching me how to use the FAST machine, conducting some of the compression testing, artwork used in this thesis and general FAST guru advice, I am grateful to Dr Nick Weston.

I am also grateful to Dr Nik-Reeves McLaren, for his assistance with any XRD related quires.

Part of this work was used towards an external project, in which Dr Luke Benson Marshall designed the small-scale testing FAST moulds and completed some compression testing. Luke's help, support and useful discussions have been of great benefit to this work.

I am also thankful to all those who have helped, played a part, or aided my experiments: Kyle Arnold, Neil Hind, Terri Ellis, Ruth Graham, Joe Campion, Ben Howe, and Sarah Boot.

I am particularly thankful to the analytical team leader Dan Kitson, who has kindly given his time to explain and teach me many analytical techniques during my studies.

A large gratitude is also to be paid to both John Bultitude-Paull and Nick Bernard from Iluka resources, who have provided expertise and excellent advice throughout my PhD on the SR feedstock. John has kindly spent much time explaining to me many aspects of SR production as well as the complex phases associated with the feedstock. Without the aid of John, full characterisation of the XRD of SR would not have been achieved. John and Nick also allowed me to visit the production site of SR in Capel, Australia, which both enriched my development as a researcher and allowed me to put my work into perspective. Thanks also go to Les & Dean at the MTF facility for their help during my visit!

I have been fortunate enough to have had the support of the Sheffield Titanium Alloy Research group, whom are a great bunch, as well as the staff at Metalysis, who have always made me feel welcome.

Acknowledgement is also due to Nick Penfold, for his relentless and unyielding optimism and hours of listening to presentations.

To my family, Anton, Julie, Michael and Paul, thank you for the years of encouragement.

Finally, for all the sacrifices he had made, in making sure I had the opportunities he did not, this thesis is dedicated to my father.

1.0 Introduction 1

2.0 Background & Literature Review 9

2.1 Rutile & Ilmenite 11

2.1.1 Becher Process 12

2.2 Titanium 13

2.2.1 Alpha Titanium 15

2.2.2 Alpha + Beta Titanium 16

2.3 Beta Titanium 17

2.3.1 Beta Titanium Introduction 17

2.3.2 Beta Titanium Chemistry 18

2.3.3 Beta Titanium Alloys and Applications 19

2.3.4 High Strength Metastable Beta Titanium Alloys 22

2.3.5 High Strength Metastable Beta Titanium Alloy Development 22

2.4 Conventional Titanium Production Routes 24

2.4.1 The Kroll Process 24

2.4.2 Vacuum Arc Remelting and Cold Hearth Melting 25

2.4.3 Powder Producing Methods 26

2.5 Alternative Extraction Routes 28

2.5.1 The ADMA Process 28

2.5.2 The Armstrong Process – Cristal 29

2.5.3 MER Corporation Process 30

2.5.4 TiRO™ Process 32

2.5.5 Summary of Low Cost Extractive Titanium Processes 32

2.6 The Fray Farthing Chen (FFC) Process 34

2.6.1 FFC Mechanism Studies 35

2.6.2 FFC Reductions of Rutile 38

2.6.2 FFC Conclusions 39

2.7 Powder Metallurgy 40

2.7.1 Powder Metallurgy Introduction 40

2.7.2 Powder Metallurgy Methods 41

2.7.2.1 Field Assisted Sintering Technique/ Spark Plasma Sintering 41

2.7.2.2 Continuous Rotary Extrusion / Conform Process 43

2.8 Alloy Development 45

2.8.1 Alloy Development Introduction 45

2.8.2 Alloy Design for Powder Metallurgy 46

2.8.3 Alloy Elements & Effects – Aluminium 47

2.8.4 Alloying Elements & Effects – Molybdenum 50

2.8.5 Alloying Elements & Effects – Iron 52

3.0 Experimental Methods 67

3.1 FFC Reductions at R&D Scale 69

3.2 Calcination of Synthetic Rutile 70

3.2.1 Calcination of Doped Samples 70

3.3 Morphology Studies 72

3.4 Characterisation Techniques 72

3.4.1 X-ray Diffraction Analysis 72

3.4.2 Powder Characterisation Techniques 73

3.4.3 Chemical Analysis 73

3.4.3.1 XRF Spectroscopy 73

3.5 Consolidation via the Field Assisted Sintering Technique 73

3.6 Porosity Measurements 75

3.7 Physical Property Testing 75

3.7.1 Beta Transus Testing 75

3.7.2 Hardness Testing 76

3.7.3 Nanoindentation 76

3.8 Compression Testing 76

3.9 Modelling Software 76

4.0 Characterisation of Synthetic Rutile Derived Titanium Alloys 77

4.1 Synthetic Rutile Feedstock Characterisation 80

4.1.1 Synthetic Rutile X-ray Diffraction 80

4.1.2 Elemental Analysis 82

4.1.3 Microstructural Analysis 83

4.1.4 Physical Properties Characterisation 85

4.2 Partial Reductions of Synthetic Rutile 86

4.2.1 General Observations of Partially Reduced Synthetic Rutile 87

4.2.2 XRD & SEM of Partially Reduced Synthetic Rutile 87

4.2.3 Overview of Partial Reductions of Synthetic Rutile 95

4.3 Synthetic Rutile Derived Titanium Alloy 98

4.4 Consolidation of Synthetic Rutile Derived Titanium Alloy Powder 100

4.5 Determination of the Beta Transus via Experimental and Modelling Methods 103

4.6 Mechanical and Physical Data of Synthetic Rutile Derived Titanium Alloy 105

4.7 Large Scale Mechanical Properties of the Synthetic Rutile Derived Titanium Alloy 107

4.8 TiC Formation in SR Derived Titanium Alloys 108

4.8.1 TiC Formation in Consolidated Synthetic Derived Alloys with Low C (<0.3 wt%) 112

4.8.2 TiC Formation Summary 116

4.9 Formation of Metal Matrix Composites - TiC Formation in Consolidated Synthetic Rutile Derived Alloys with High Carbon Content (>0.5 wt%) 117

4.10 TiC Avoidance 120

5.0 Alloy Development of Synthetic Rutile Derived Titanium Alloys 125

5.1 Small-Scale Testing Approach 129

5.1.1 Small-Scale Mould Design 130

5.1.2 Validation of the Small-Scale Testing Approach Using Commercial Alloys 133

5.1.3 Comparison of Commercial Alloys and SR Derived Titanium Alloy 139

5.2 Pseudo Binary SR Alloys (SR-Al and SR-Mo) Introduction and Limitations 140

5.3 Aluminium alloy powder Introduction 142

5.3.1 Pseudo Binary SR-Al Feedstock Production 142

5.4 Pseudo Binary SR-Al Titanium Derived Alloys Powder Analysis Following Reduction 148

5.4.1 SR-Al Consolidation and Mechanical Testing 152

5.4.2 Mechanical Properties and Microstructure of Pseudo Binary SR-Al Alloys 154

5.4.3 Al:Fe Relationship in Pseudo Binary SR-Al Titanium Alloys 157

5.5 Mo alloy powder production introduction 159

5.5.1 Mo Powder Production 160

5.5.2 Consolidation of SR-Mo Powders 163

5.5.3 Kirkendall Effect in SR-Mo Alloys 166

5.6 Mechanical Testing of SR-Mo Alloys 168

5.7 Low Cost Alloy Design – Replacement of Mo with Fe 171

5.8 Pseudo Tertiary Alloys (SR-Al-Mo) 174

5.8.1 Small-scale testing of pseudo tertiary SR alloys (SR-Al-Mo) 177

5.8.2 Effect of Mo on Al:Fe – Strain to Failure Relationship 180

5.9 Alloy Development of Synthetic Rutile Derived Alloys Conclusions 181

6.0 Spring Alloy Design from a Synthetic Rutile Baseline 189

6.1 Introduction 191

6.2 Spring Alloys Background 193

6.3 Synthetic Rutile Derived Spring Alloy Candidates 195

6.3.1 Consolidation and Mechanical Testing of Spring Candidate Alloys 196

6.3.2 Spring Alloy Candidate Comparison 199

6.3.3 Spring Alloy Candidate Overview 200

6.3.4 Spring Alloy Candidate Conclusion 202

6.4 Large Scale Production of Spring Alloy Compositions 202

6.5 Multiple Regression 208

6.5.1 Multiple Regression Model 209

6.5.2 Improvements and Examples of the Multiple Regression Model 213

6.6 Chapter 6 Conclusions 215

7.0 Conclusion & Impact statement 219

7.1 Conclusion 221

7.1.2 Final remarks 225

7.2 Impact Statement 226

8.0 Future Work 229

8.1 Further Experiments on the Reduction Process 231

8.2 Further Alloy Development 232

8.3 Downstream Processing 236

8.4 Upscaling 236

8.5 Future Work Conclusions 237

Appendices 239

Chapter 1:

Introduction

1.0 Introduction

Ubiquitous use of titanium and its alloys is largely inhibited by the large costs associated with its production. Harbouring many attractive properties, such as a high strength to weight ratio, excellent corrosion resistance and outstanding biocompatibility, the use of titanium and its alloys is mostly restricted to the aerospace, medical and military markets. However, with recent advances in low cost extraction technology as well as powder metallurgy (PM), titanium may soon become an attractive commodity to the more cost conscious industries, including the automotive and construction sectors.

A key factor that inhibits the production of low cost titanium is its extraction. Currently, titanium is commercially produced via the notoriously expensive and laborious Kroll process. However, much research has gone into investigating new novel techniques aimed at reducing the cost of extraction. One such method is a solid-state extraction method known as the FFC process named after its inventors, Fray, Farthing and Chen [1]. The FFC process is capable of reducing metal ores and oxides to their metallic state via an electrochemical deoxidation process [1]. As the reaction occurs in the solid state, titanium alloys which were previously problematic to produce homogenously due to differences in melting point or density, can now be made in a much simpler and efficient manner. However, the main advantage of the FFC process is the cost effectiveness of the low-cost powder producing extraction route, particularly when coupled with near net shape powder metallurgy techniques.

PM techniques can produce dense titanium components near the final component shape, vastly reducing the wastage and high machining costs associated with titanium production. However, at present, powder metallurgy relies upon titanium produced via the Kroll process, which has been outlined as costly, laborious and time intensive [2]. Additionally, further processing must occur after the Kroll process to obtain a powder. Hydride-dehydride (HDH) processing, gas atomisation (GA) and the plasma rotating electron processes (PREP) are commonly employed to achieve this. These processes contribute significant cost factors, limiting the cost effectiveness of PM techniques and rendering PM as an expensive titanium production route.

In contrast, new titanium extraction processes, such as the FFC process [1], are capable of directly producing a powder product, removing the requirement for powder production operations and hence, drastically reducing costs. PM itself is not an expensive process, compared with traditional titanium processing, in which the cost of fabrication alone can be up to 47% of the total cost of the component [3]. Hence, a PM route coupled with the FFC

process could enable a much more economically viable approach to the production of titanium components.

Within the evolution of low cost titanium production, alloy development has a crucial role to play. A low-cost titanium alloy allowing a high sintered density with good mechanical properties, could provide the key to linking low cost extraction processes with low cost powder metallurgy methods. A further expense reduction is made possible by the revelation that titanium can be extracted directly from its ore – rutile. Natural rutile (TiO_2) is often found in Australia, Mexico and India [4] and goes through some minor separation techniques to produce a feedstock of around 95% purity [5]. Rutile can also be produced artificially via the removal of iron from titanium's alternative ore – ilmenite ($FeTiO_3$). Rutile produced in this manner is known as synthetic rutile (SR). Because of its ilmenite origins, synthetic rutile contains a different impurity profile compared to that of natural rutile, with a particularly noticeable increase in iron concentration. However, many of the remnant elements are often added to commercial titanium alloys as alloying elements.

New low cost Ti alloys could have application in a wide variety of markets, particularly the automotive sector replacing valve train, suspension and exhaust systems [6]. Typically, over the past five decades it has been difficult to introduce new alloys to the market due to the high costs of qualification [7]. However, by directly producing titanium alloys from a SR feedstock, followed by near net shape PM techniques, the significant reduction in cost makes the introduction of new alloys viable, particularly for non-critical components.

Of the titanium alloys, metastable beta titanium alloys are particularly underutilised. By virtue of the precipitation of the alpha phase within the beta matrix, metastable beta titanium alloys are particularly susceptible to heat treatments. Due to this susceptibility, a wide range of microstructures can be achieved, making this class of alloys markedly adaptable. Although primarily noted for their high strengths, metastable beta titanium alloys are also capable of being processed at lower temperatures and possessing low Young's modulus values. Due to their unique blend of properties, metastable beta titanium alloys have the potential to be utilized in a wide range of industries for a variety of applications such as biomedical implants, geothermal equipment and numerous aeronautical components [7].

Hence this collection of work aims to produce a low cost beta alloy derived directly from synthetic rutile. To achieve this aim, the work was split into three sections.

Initially, synthetic rutile was fully characterised at every stage of reduction. This involves the full characterisation of the synthetic rutile feedstock and resulting titanium alloy powder as well as undertaking partial reductions to determine the reduction pathway of the SR feedstock. Consolidation of the resulting titanium alloy powder was achieved using the field assisted sintering technique (FAST), shown in Fig. 1.1 and the resulting microstructure analysed to reveal a beta rich α+β morphology. Finally, mechanical testing of the baseline titanium alloy produced was conducted to determine its baseline properties.

A major outcome from this work was the discovery of the favourable properties of the synthetic rutile derived baseline alloy, exhibiting similar flow behaviour, compressive yield strength, ultimate compressive strength and strain to failure values to that of workhorse α+β alloy, Ti-6Al-4V.

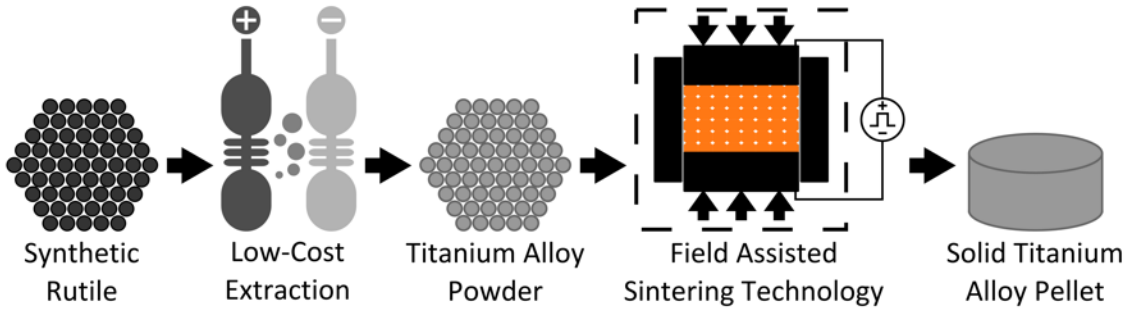

Fig. 1.1: Schematic diagram of the production of a solid titanium alloy pellet from a loose synthetic rutile feedstock powder consisting of extraction via the FFC Metalysis process and subsequent consolidation using field assisted sintering technique.

Once the reduction mechanism had been understood and the baseline properties of the resulting alloy established the next stage of alloy development began. A novel small-scale testing technique was developed and employed to determine the mechanical properties of alloy developed from the baseline SR titanium alloy.

Alloying elements Al and Mo were initially chosen to observe the effects of α and β stabilisers upon reduction and the mechanical properties of the baseline synthetic rutile derived alloy. Both Al and Mo were added to synthetic rutile separately and a range of Al/Mo enhanced pseudo binary synthetic rutile derived alloys produced. Such alloys underwent consolidation via the field assisted sintering technique (FAST) and compression testing via the small-scale testing approach followed by microstructure analysis. Data from the mechanical testing were used to produce a multiple regression model using modelling software, Minitab [8], which should aid future alloy design.

Finally, using initial work, a speculative spring alloy candidate was designed and analysed. Iluka resources, who have invested £20 million into the Metalysis process, produced feedstock around the spring compositions developed within this thesis. The feedstock produced has been characterised and will be reduced on a large scale at Metalysis in future work.

From this work, two new and encouraging alloys have been derived directly from synthetic rutile (Baseline SR and an alloy intended for spring applications). Moreover, the underlying principles of creating alloys with set properties from a SR baseline feedstock have begun to be determined. However, absolute resolution of the optimum alloys requires significantly more investigation. Once variability of the alloys produced at an R&D scale (chemical, porosity) can be reduced, a higher resolution is achievable, which can be used in conjunction with the work detailed within the thesis for proficient alloy development. This work was not intended to produce a final alloy composition, but instead will act as a starting point for future alloy development projects.

As a synopsis to this work; Chapter 2 gives a background and literature review whereas Chapter 3 lists the details of the experimental techniques used throughout this work. Results generated throughout this work have been split into three separate chapters. Chapter 4 covers the initial characterisation of the SR feedstock and resulting SR derived titanium alloy, alongside an in-depth study undertaken to understanding the reduction pathway utilised partial reductions. Chapter 5 focuses on initial alloy development, delving into the production and assessment of pseudo binary SR-Al and SR-Mo titanium alloys. A small-scale testing approach was developed during this work which is also detailed. Tertiary alloys of composition SR-Al-Mo were also assessed within this chapter. From this initial alloy development, the use of iron as a replacement for expensive isomorphous beta stabiliser Mo, also became apparent which led to Chapter 6 – the production of a spring alloy, developed using data generated during chapter 5. Chapter 6 also details the production of a multiple regression model, which may be used to aid future alloy development projects. An impact statement of the work reported within this thesis is also provided in Chapter 7, alongside a list of potential projects for future investigations in Chapter 8.

References

[1] G. Z. Chen, D. J. Fray and T. W. Farthing, "Direct electrochemical reduction of titanium dioxide to titanium in molten calcium chloride," *Nature,* vol. 407, pp. 361-364, 2000.

[2] *EHK Technologies. Prepared for US Department of Energy and Oak Ridge National Laborator, Summary of emerging titanium cost reduction technologies,* Subcontract 4000023694, 2003.

[3] D. J. Fray, "Novel methods for the production of titanium," *International materials review,* vol. 53, no. 1, pp. 79-86, 2008.

[4] G. Meinhold, "Rutile and its applications in earth sciences," *Earth science reviews,* vol. 102, pp. 1-28, 2010.

[5] W. Zhang, Z. Zhu and C. Y. Cheng, "A literature review of titanium metallurgical processes," *Hydrometallurgy,* vol. 108, pp. 177-188, 2011.

[6] M. Jackson, "Automotive Applications for Titanium," in *Encyclopedia of Automotive Engineering*, 2014, pp. 1-15.

[7] J. D. Cotton, R. D. Briggs, R. R. Boyer, S. Tamirisakandala, P. Russo, N. Shchetnikov and J. C. Fanning, "State of the art in beta titanium alloys for airframe applications," *JOM,* vol. 67, no. 6, pp. 1281-1303, 2015.

[8] Minitab, "Minitab V17," All such material remains the exclusive property and copyright of Minitab Inc. All rights reserved.

Chapter 2:

Background & Literature Review

2.0 Background & Literature Review

2.1 Rutile & Ilmenite

Most commonly, titanium is found as ilmenite, $FeTiO_3$ ($FeO.TiO_2$), titanomagnetite, $Fe_{3-x}Ti_xO_4$ where ($0 \leq x \leq 1$) [1] or rutile, TiO_2. TiO_2 is known to exist as at least six polymorphs of TiO_2, rutile, anatase, brookite, TiO_2 (B), TiO_2 (II) and TiO_2 (H), with rutile being both the most stable and most common TiO_2 polymorph [2]. Located predominantly in Australia, Mexico, Sierra Leonne and India, naturally sourced rutile crystallises into a tetragonal space group and exists as a slightly distorted octahedral structure with each titanium atom surrounded by six oxygen atoms [2] [3]. Typically, natural rutile is purified via electrostatic and magnetic separation to produce products of around 95% TiO_2 [4].

Although rutile contains a higher proportion of titanium, an alternative ore, ilmenite is much more abundant. Furthermore, the price of ilmenite with relation to titanium content, is cheaper than that of rutile. Rutile prices can also be unstable, depending on factors such as demand for zircon, which is mined simultaneously [5].

Ilmenite usually contains between 40-65% titanium depending on its location and geological history; weathering is known to leach iron, resulting in titanium enrichment. This beach sand derived ore is commonly converted to the higher titanium containing compound, rutile [4]. Rutile created in this manner is known as synthetic rutile (SR). A wide range of processes are known to convert ilmenite into synthetic rutile such as the Becher, Murso, Laporte and Austpac ERMS processes [4] [6] [7] [8]. Each process involves the thermal oxidation and reduction of the iron via a roasting procedure, followed by the removal of reduced iron via chemical and physical separation techniques [4]. More detailed descriptions of these processes along with advantages and disadvantages of each can be found in Ref [4]. However, at present, the Becher process is the only commercially operating procedure to produce SR. Hence, the SR used throughout this project was produced by Iluka via the Becher process and a more detailed review will be given of this process.

2.1.1 Becher Process

Developed in 1961 [9], patented in 1963 [8] and commercialised in 1969 [9], the Becher process removes the high iron content of ilmenite (57-60% TiO_2) to produce a higher purity TiO_2 product (up to 95% TiO_2) [10]. Originally, the process involved the oxidation of 'primary' ilmenites (53 to 55% TiO_2), resulting in the conversion of Fe^{II} to Fe^{III} to produce ferric pseudobrookite (Fe_2TiO_5) [11]. This process changed when it was realised that weathered ilmenites (57 to 63% TiO_2) can be reduced without the pre-oxidation step, which is the process used at two remaining Becher plants in Australia [9].

Instead of pre-oxidation, the process begins with the reduction of iron present within the ilmenite to produce metallic iron, Fe^0. This reduction step takes place over 12 hours at ~1100°C using coal as both a heat source and a source of reductant (carbon monoxide) [9]. The product at this stage, commonly referred to as reduced ilmenite, has been aptly described by Farrow et. al as a TiO_2 matrix, honeycombed with metallic iron [12]. Embedded iron within the matrix is then removed via an accelerated rusting procedure, known as aeration [9]. An ammonium chloride catalyst is used to aid the aeration process, which results in the precipitation of fine iron oxides outside of the reduced ilmenite grains in the slurry [9] [12]. Finally, to complete the process route, these iron oxides are separated from the SR using wet separation, typically hydrocyclones [9].

A porous product is observed following the removal of iron oxides with the particle size remaining intact throughout the procedure. A schematic diagram illustrating the separate stages of Iluka's synthetic rutile production route on an ilmenite particle is shown in Figure 2.1.1 [13].

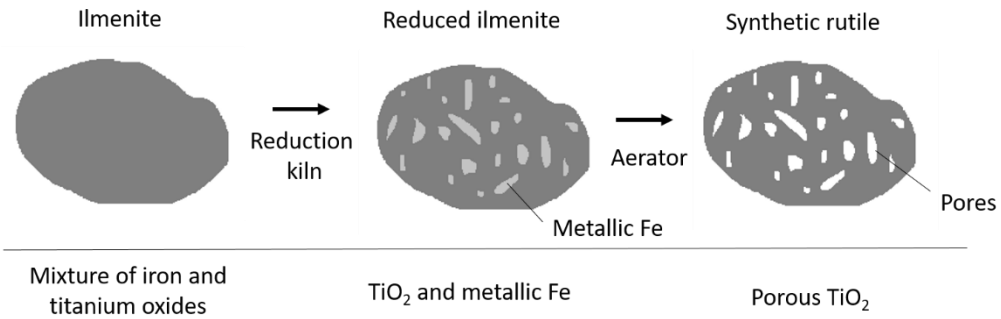

Fig. 2.1.1: Schematic diagram following the evolution of the ilmenite to synthetic rutile throughout the Becher process, redrawn from [13].

2.2 Titanium

Titanium exists in two distinct crystallographic forms. At temperatures below 883°C, pure titanium exhibits its hexagonal close packed phase, (HCP) known as the alpha phase [14]. Above 883°C, an allotropic transformation occurs as the crystal structure changes to body centred cubic (BCC), known as the beta phase. Beta transus is the term used to identify the temperature at which this crystallographic transformation takes place. Above the beta transus temperature, titanium exists solely within the beta phase [15].

Addition of alloying elements can stabilise the alpha and beta phases and thus, change the temperature at which the beta transus occurs. Elements that reinforce the HCP structure are known as alpha stabilisers (Al, O, N, C), whereas elements that favour the BCC structure, by lowering the beta transus temperature, are known as beta stabilisers [16]. Beta stabilizers which do not form intermetallic compounds with titanium are known as isomorphous (Mo, V, Nb, Ta). Those that do, are eutectoid beta stabilisers (Fe, Mn, Cr, Co, Ni, Cu and Si). Figure 2.2.1 depicts the effect of various alloying elements on the phase diagrams of titanium alloys [17]. Formation of too many intermetallic compounds can create problems with the mechanical properties produced, as they are known to cause embrittlement.

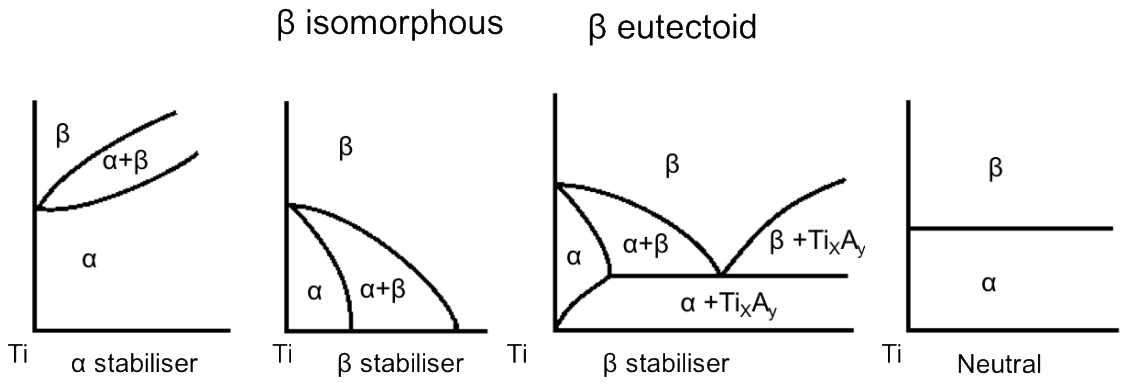

Fig. 2.2.1: Effect of various alloying elements upon the phase diagrams of titanium alloys redrawn from [17].

In addition to alpha and beta stabilizers, elements which have little to no effect on the beta transus temperature, such as Hf, Zr and Sn are described as neutral elements. Hf and Zr, like Ti, are group IV transition metals in the periodic table and possess similar properties to Ti, including an isomorphous crystal structure [17]. Hence, these elements are also allotropic, displaying both the alpha and beta phases; granting them complete solubility throughout the alpha and beta phases of titanium. Assigning these elements complete neutrality is not entirely true, as they are known to stabilise either phase depending on the presence of alpha/beta stabilisers, thus leading to their alternative name; host stabilisers [18]. Although technically belonging to the beta eutectoids, presence of Sn has no consequence upon the beta transus temperature. However, Sn is capable of stabilising the alpha HCP structure when present with aluminium by replacing Al in the Ti_3Al phase (α_2) [17].

Depending on the concentration of alpha and beta stabilisers present, different classes of titanium alloys are formed. Unalloyed titanium is classified as an alpha alloy. Additions of alpha stabilisers help to preserve the alpha phase HCP crystal structure and are hence known as alpha alloys. With increasing concentration of beta stabilisers, retention of the beta phase at room temperature becomes possible, resulting in α+β and beta alloys. These three main classes can be subdivided further to create the near alpha and near beta classes.

Near alpha alloys allow only small amounts of beta stabilisers, whereas α+β alloys contain enough beta stabiliser to allow more noticeable amounts of beta phase to be retained at room temperature. Finally, metastable beta alloys contain a significant concentration of beta stabilisers, granting a large proportion of beta phase to be retained at room temperature [19].

2.2.1 Alpha Titanium Alloys

As discussed previously, alpha titanium alloys can firstly be split into two distinct categories of fully α-alloys, containing almost no beta stabilisers, and near α alloys, which can accommodate up to 2 wt% beta stabilisers [20]. Fully α alloys consist of a single phase HCP crystal structure and as such, are not heat treatable [14]. These alloys generally have low strength, good ductility and fair creep resistance, by virtue of their high thermal stability [20]. In practice, only the unalloyed, commercially pure (CP) grades, as well as Ti-Cu and Ti-5Al-2.5Sn have found much real world application [20].

Currently, four commercially pure titanium grades are available. The main difference between these grades are oxygen and iron content, resulting in varying levels of both strength (240 MPa to 740 MPa) and ductility [15]. Strength is principally dictated by the concentration of oxygen in solid solution [14], by modifying the oxygen content, varying degrees of strength can be attained. However, high levels of oxygen are also linked with lower ductility levels.

Although renowned for their reputation as the weakest class of titanium alloys, CP alloys are also some of the most corrosion resistant [16]. Hence, this alloy class is commonly chosen for applications in which high strength is not crucial and corrosion resistance is a key property requirement.

Allowing small concentrations of beta stabilisers to widen the α+β phase field, near alpha alloys exploit the attractive creep properties associated with alpha alloys combined with the higher strengths associated with α+β alloys, making them ideal for high temperature applications [15]. Due to lack of a beta phase, heat treatments have little effect on alpha alloys, in fact, age hardening can have a detrimental effect upon creep resistance. As such, near alpha alloys are often utilised in an annealed condition [16].

Specific examples include Ti-8Al-1Mo-1V, known for its excellent weldability, a property often found in near alpha alloys due to their minimal response to heat treatments [16]. This alloy is also known for its low density and high Young's modulus [21]. However, this alloy is known to have a decreased ductility after being exposed to high temperatures for prolonged periods of time, due to the formation of the brittle α_2 phase [20].

Hence, an alternative near alpha alloy was developed [20], Ti-6242S, (Ti-6Al-2Sn-4Zr-2Mo-0.08Si) which is capable of attaining high levels of toughness and strength in combination with excellent creep resistance up to temperatures of 565°C [22]. Due to a combination of these

properties Ti-6242S is utilised in components for gas turbines where high strength, toughness and creep resistance at elevated temperatures is vital [22].

2.2.2 Alpha + Beta Titanium Alloys

α+β alloys are by far the most utilised class of titanium alloy, mostly due to the enormous success of Ti-6Al-4V alloy, known as the 'workhorse' of titanium alloys. Compared to α alloys, a large range of microstructures can be generated through thermomechanical processing and chemistry alterations of α+β alloys [14]. This increased range of microstructures available, produces a wide array of properties which can be tailored for specific applications [14]. Of these microstructures, there are three main distinct categories: lamellar, equiaxed and duplex [17]. A large proportion of α+β alloys are used for aerospace applications. Depending on the specific application, α+β alloys are usually chosen for their high yield strength, fatigue strength, working temperature ability and corrosion resistance in comparison to competing materials, such as high strength aluminium alloys and steels [17].

Ti-6Al-4V was originally developed in the 1950's and is widely used for gas turbine engines components and airframe applications. In the automotive industry, the alloy has found some application in high performance racing cars as connecting rods and rocker arms [23]. However, although Ti-6Al-4V has been extremely successful, it is not without its limitations. Ti-6Al-4V has a maximum temperature application of around 300°C. Hence the usage of Ti-6Al-4V is limited to the cooler parts of aero engines such as the fan [17].

Further, although initially employed widely within the biomedical industry for a variety of joint replacements, concerns of cytotoxicity of Al and V has led to the introduction of alternative alloys – often beta alloys are chosen for their low Young's modulus.

2.3 Beta Titanium Alloys

As a key aim of this work was to produce a low cost metastable beta titanium alloy, derived from synthetic rutile intended for automotive application, a more in-depth review of beta titanium alloys is provided here.

2.3.1 Introduction to Beta Titanium Alloys

Affording a wide range of attractive combinations of desirable properties such as ductility, strength and fatigue resistance, beta titanium alloys are a particularly resourceful class of titanium alloy. Popularity of this class of alloys has slowly been increasing, finding application in the aerospace, medical and automotive sectors [17]. This class of alloys is particularly versatile, by virtue of the extent of their susceptibility to heat treatment, which allows the production of complex microstructures, leading to unique blends of properties. In addition to novel property combinations, the beta alloys offer other advantages, such as high strength due to precipitation of the alpha phase. Increased formability is also offered, afforded by the lower temperature of the beta transus, which allows low energy deformation in the more ductile beta phase to take place at lower temperatures [17].

Despite these attractive properties, beta titanium alloys are not without their disadvantages. Beta stabilising alloying elements generally belong to the heavier transition metals, hence, large differences in density compared to titanium are present, inducing segregation throughout production, which can be problematic, especially within the melting stages [24] [25]. This particular disadvantage can be avoided using a combination the new extractive FFC process and solid-state processing. As this production route occurs entirely in the solid state, the requirement for melting procedures is removed. Other disadvantages are not as easily avoided. The heavier stabilising elements can cause beta alloys to have relatively higher densities compared to α+β alloys which is a slight disadvantage, most notably for weight saving applications. More complicated processing routes alongside narrow processing windows can also be difficult to work with. However, for many applications, the benefits offered by the beta titanium alloys strongly outweigh their shortcomings [26].

While beta titanium alloys can offer many benefits and unique property combinations, their application is still largely eclipsed by alpha and α+β alloys. Although their utilization has begun to steadily increase, a particular hindrance to the widespread use of these alloys has been cost. Generally, beta titanium alloys are more expensive to produce than their alpha, or α/+β counterparts [15]. This disadvantage arises from the cost of expensive isomorphous alloying

additions such as Mo and V as well as the many melting procedures required to prevent segregation. These expensive isomorphous alloying additions are often chosen over eutectoid alloying additions as they do not form intermetallic compounds, which are known to cause embrittlement. Hence, expensive alloying additions combined with high production expenditures has resulted in the severe restriction of this class of alloys. However, with advances in technology, cheaper production routes and a deeper understanding of the processing methods, this class of alloys may be made accessible to both performance driven and cost conscious industries.

2.3.2 Chemistry of Beta Titanium Alloys

Beta titanium alloys are commonly described as alloys containing enough beta stabilising elements to avoid the martensitic transformation upon quenching [17] [26]. Critical minimum concentration of beta stabiliser required to avoid this transformation is shown as β_c in Figure 2.3.1 below. Alloys possessing a concentration of beta stabiliser equal or higher than β_c, but below β_s are known as metastable beta alloys, possessing both alpha and beta phases. Beyond β_s, the alloy is comprised solely of the beta phase and are known as stable beta alloys.

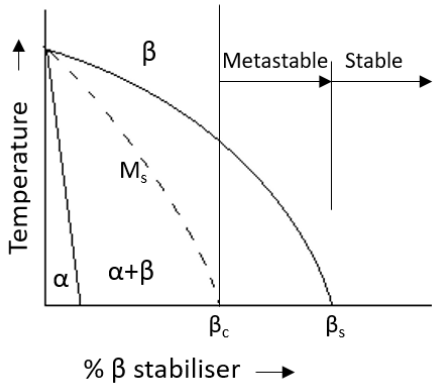

Fig. 2.3.1: Equilibrium binary phase diagram of titanium with increasing beta stabiliser concentration, redrawn from Ref [26].

Stability of beta alloys is aptly described by the molybdenum equivalency which is given by Equation 2.3.1. Note, aluminium is a negative value as it is an alpha stabiliser and as such, will actively stabilise the alpha phase instead.

Equation 2.3.1:

Mo eq. = 1.0(Mo) + 0.67(V) + 0.44 (W) + 0.28 (Nb) + 0.22(Ta) + 2.9(Fe) + 1.6(Cr) +1.7(Mn) -1.0 (Al)

This equation allows the assessment of the effectiveness of beta stabilising elements within titanium alloys [26]. Potency of each element at stabilising the beta phase, is reflected by the constant presented before it within the equation. This potency is calculated by employing the arbitrarily chosen molybdenum as a reference point and dividing the β_c of the chosen element by the β_c of Mo (10) as shown by Equation 2.3.2 below.

Equation 2.3.2:

$$Constant = \frac{\beta_c\, Mo}{\beta_c\, Element}$$

From Equation 2.3.2 it can be observed that generally, eutectoid forming beta stabilisers are much more effective than isomorphous beta stabilisers and as such, have a much greater effect at depressing the beta transus [26].

Generally, alloys with a Mo equivalent of ~10 and above are classed as “beta alloys”. For reference, Table 2.1 lists Ti-6Al-4V alongside some commercial metastable beta titanium alloys and their corresponding Mo equivalence.

Table 2.1: Mo equivalency of commercial titanium alloys.

Common alloy name	Alloy Composition (wt %)	Mo eq.
Ti-64	Ti-6Al-4V	-3.3
Timetal LCB	Ti-1.5Al-4.5Fe-6.8Mo	18.4
Ti-15-333	Ti-15V-3Cr-3Al-3Sn	11.9
Ti-10-2-3	Ti-10V-2Fe-3Al	9.5
Timetal-5553	Ti-5Mo-5V-5Al-3Cr	9.9
Beta III	Ti-11.5Mo-6Zr-4.5Sn	11.5
Beta C	Ti-3Cr-8Mo-6Cr-4Mo-4.5Sn	16

2.3.3 Beta Titanium Alloys and Applications

High strength metastable beta titanium alloys contain a larger percentage of the alpha phase than ‘heavily stabilised’ beta alloys, which possess a much lower alpha phase concentration [17]. The large volume fraction of alpha phase found in the high strength metastable beta alloys can be precipitated out, allowing solid solution strengthening to take place, giving rise to their high strengths. Heavily stabilised beta alloys can therefore not obtain the same levels of strength as their high strength metastable beta analogues [17].

High strength forging alloy, Ti-10-2-3 (Ti-10V-2Fe-3Al) is an excellent example of a high strength metastable beta alloy and of the combination of properties that metastable beta alloys can exhibit. High strength coupled with toughness and good fatigue properties justify the use of this alloy, especially within the aerospace sector [19]. Boeing 777 aircraft landing gear truck beams are almost entirely constructed from Ti-10-2-3 [27]. Although the cost of using titanium is initially much higher than that of steel, titanium offers resistance to stress corrosion, a problem that results in replacement of high strength steel materials at least once throughout the lifetime of the aircraft [15]. Ti-10-2-3 has also found application upon helicopters, providing the material of choice for the Westland Super Lynx helicopter rotor head, as well as the inboard beam for the V-22 Osprey [28] [17].

Initially created to rival Ti-10-2-3, the metastable beta alloy Ti-5553 (Ti-5Al-5V-5Mo-3Cr-0.5Fe) is also a forging alloy of interest to the aerospace sector [19]. Ti-5553 shares many attractive properties with Ti-10-2-3 such as high strength, high fracture toughness and good ductility. Ti-5553 however, possesses some additional advantages over its counterpart, such as higher hardenability, improved fatigue performance as well as increased producibility [19]. A simplified production process is afforded by the larger processing window available for Ti-5553 as well as the ability to be air cooled, compared to Ti-10-2-3 which must be water quenched, limiting its thickness [29]. Thus, Ti-5553 is used in many aerospace applications such as landing gear forgings in the 787 Dreamliner.

Ti-15-3 (Ti-15V-3Cr-3Al-3Sn) is a metastable beta alloy that has taken advantage of its beta rich chemistry to also find success within aerospace markets. By virtue of its beta heavy content, Ti-15-3 is able to undergo cold deformation operations, a trait that not only decreases the cost of the alloy, but also allows repairs to be made in the field [30]. Other properties such as its high strength when aged and tolerance to differing process variables have also facilitated its popularity [30]. Commonly produced as strip, this alloy has found application as clock springs as well as in critical components of both aircraft and space vehicles [19].

A further alloy designed with aerospace in mind was β-21S (Ti-15Mo-2.7Nb-3Al-0.2Si). Originally designed by Timet, this alloy exhibits excellent thermal stability with properties such as oxidation resistance and creep resistance similar to that of Ti-6-4 [31]. These properties make β-21S an ideal candidate for high temperature applications [27]. Accompanying these attractive properties lies its main functionality; resistance to hot hydraulic fluid [27]. At temperatures above 130°C, hydraulic fluid breaks down forming organophosphoric acid, which etches titanium causing severe hydrogen embrittlement [19] [27]. β-21S has therefore found application on

aircraft in areas where temperatures exceed 130°C, such as the nacelle structure and the airframe near the engine exhaust [17] [19].

Springs are yet another aerospace component for which beta titanium alloys are widely applied. The low modulus of elasticity displayed by beta alloys, combined with their high yield strength and low density make them an optimum choice for spring material, especially in weight sensitive applications [17]. Possession of these properties also allows large savings in volume to be made, requiring only half the coils compared to a steel spring. Traditionally, alloys such as Beta-C have been used as spring materials, however the introduction of new low cost alloys, such as Timetal low cost beta (LCB) has provided a cheaper alternative, especially for the automotive industry.

In fact, Timetal LCB (Ti-6.8Mo-4.5Fe-1.5Al) was specifically designed with automotive spring applications in mind. Exhibiting a low elastic modulus, moderate strength and a reduced cost, Timetal LCB represents a valid candidate for mass produced automotive spring components [32]. Utilizing the initially inexpensive steel making additive, ferro-molybdenum, TIMET managed to significantly reduce the cost of producing a beta alloy via low cost alloying additions [33]. Finding application within a variety of automotive vehicles such as the Volkswagen Lupo FSI, Ferrari Challenge Stradale and the Ford Focus FCV, this alloy has successfully broadened the range of applications applicable to titanium [32]. However, although initially successful, the increasing cost of ferro-molybdenum in the early part of the 21st century has since halted the uptake of Timetal LCB into commercial applications.

Biomedical applications are a source of non-aerospace titanium alloy utilisation, as titanium has long been known to possess excellent biocompatibility properties. Traditionally, α+β alloys have dominated this market, especially Ti-6Al-4V. However with concerns of the cytotoxicity of both aluminium and vanadium, there has been increased interest in alternative titanium alloys using less cytotoxic alloying elements such as Ta or Mo [34]. Compared with α+β alloys, beta alloys have a lower elastic modulus, increased fatigue strength, higher corrosion resistance and an improved tissue response [34]. High elasticity is an attractive trait within biomedical alloys as the Young's modulus of bone is relatively low at around 30 GPa. Hence, using materials with modulus values closer to that of bone reduces the stress shielding effect [35]. Hence, in recent years, significant research has gone into the development of beta alloys for biomedical use [34] [36].

Due to their strength and corrosion resistance, beta titanium alloys have also been applied to structural components for offshore chemical plants. Further, beta titanium alloys have found

application within the leisure industry. Due to its combination of good corrosion resistance and strength, Ti-15Mo-5Zr-3Al has been utilised in the production of a range of sports equipment such as diver knives, golf club shafts and various fishing accessories [37].

2.3.4 High Strength Metastable Beta Titanium Alloys

High strength metastable beta alloys, such as previously mentioned Ti-10-2-3 and Ti-5553, are distinctive by their large proportion of fine alpha phase precipitates, the volume fraction and morphology of which, dictate the strength of the alloy [38]. Precipitation of these alpha particles within the beta matrix, via solution treatments and ageing, restrict the movement of dislocations, granting these alloys their high strengths. Despite the high strength levels, ductility can be retained, provided the beta grain size is limited [39]. Hence, these alloys can possess an enticing combination of mechanical properties.

Although high strength metastable beta Ti alloys can offer enhanced properties over conventional Ti-6Al-4V, the high cost of qualification coupled with expensive isomorphous alloying elements or multiple remelts limit their more widespread distribution [40].

2.3.5 High Strength Metastable Beta Titanium Alloy Development

Using the same base elements as Ti-10-2-3 (Ti-V-Fe-Al), two near beta alloys were developed and submitted for patents in 1993 [41]. Further, a considerable amount of research went into understanding the Ti-V-Fe-Al system, in order to produce superior high strength alloys [42] [41] [43]. Strength levels of up to 1708 MPa were achieved, coupled with reasonable tensile ductility of 4.4% elongation, and good fracture toughness [41]. However, these alloys never made it to commercial production.

Superior property combinations were also achieved in the recently produced Ti-8V-1.5Mo-2Fe-3Al alloy. Based on Ti-10-2-3, this alloy was also designed to produce high strengths, with a reduction in cost [44]. Despite this alloy reporting to have similar properties with an improved strength-ductility balance, the changes may not be enough to supersede popular Ti-10-2-3 or Ti-5553.

Similarly, an alloy compositionally akin to another high strength beta alloy, Ti-5553 has also recently been produced – Ti-6Cr–5Mo–5V–4Al [45].When solution treated and aged in the α+β phase field, this alloy has shown to produce a good combination of high strength (1400-1600 MPa) and ductility (22-52% reduction in area). Fine β grain size and precipitation of mixed α precipitates were attributed to the attractive combination of properties [46].

Although recently there has been a noticeable interest in lower cost high strength titanium alloys, development of alternatives to Ti-10-2-3, it may be difficult for these alloys to penetrate the current market place, especially with the high cost of qualification [40].

Hence, introduction of new beta titanium alloys would likely only be achieved through that of a disruptive technology. Such a technology would need to be disruptive enough to significantly lower the cost of titanium component production to justify the significant expenditure of qualification.

Creation of high strength metastable beta alloys derived directly from low cost synthetic rutile powder using the FFC process could allow substantial cost savings, especially when joint with low cost powder consolidation techniques. This solid-state production route may reduce the cost of Ti alloys enough to justify the high cost of qualification. Further, development of the baseline SR titanium alloy could allow the manipulation of its properties to be tailored towards specific applications. In particular, spring applications within the automotive industry have been identified as a potential application for such rutile derived titanium alloys. A more in-depth review of spring applications is given in section 6.2. Additionally, as the technology has the potential to be game-changing, there is also the possibility of the creation and stimulation of new markets with novel applications, using low cost titanium alloys derived from a synthetic rutile baseline.

2.4 Conventional Titanium Production Routes

Although many advances have been made within titanium metallurgy since its commercialisation, the basic method of production has largely remained intact. Typically, titanium's ore, rutile (TiO_2) or a slag produced from titanium's other ore ilmenite ($FeTiO_3$), are chlorinated before being reduced via the Kroll process to produce a porous titanium sponge. This sponge is then mechanically crushed before going for melting to produce an 8 to 10 tonne ingot. After significant open die forging and heat treatments to breakdown the course grain structure, a variety of techniques can then be used to produce the desired component shape, such as closed die forging, rolling or extrusion. If powder is required, further processing of the ingot is required via processes such as gas atomisation, the plasma rotating electrode process or hydride dehydride processing.

2.4.1 The Kroll Process

Throughout the last seven decades, the major production route of titanium metal has been achieved primarily using the metallothermic Kroll process [47]. Despite its laborious and discontinuous nature, no other process routes have yet managed to displace it on a commercial scale. Although many attempts have been made, titanium extraction has been particularly difficult to attain in a cost-efficient manner due to the metals high affinity for oxygen, resulting in a particularly large negative free enthalpy of formation of the oxide [48] [49].

Toxic titanium tetrachloride ($TiCl_4$) is used as the feedstock for the Kroll process, which is produced via a carbochlorination reaction [48]. At 1300K, Cl_2 is fed into a fluidized bed chlorinator where it reacts with the fluidized TiO_2 and C (coke) as shown in Equations 2.4.1 and 2.4.2 [48] [17].

$TiO_2 + 2Cl_2 + C \rightarrow TiCl_4 + CO_2$ **(Equation 2.4.1)**

$TiO_2 + 2Cl_2 + 2C \rightarrow TiCl_4 + 2CO$ **(Equation 2.4.2)**

The gaseous $TiCl_4$ product is then tapped off and fed directly into a fractional distillation column for purification. CO and CO_2 are removed throughout the distillation process as well as any remaining impurities [17].

Once pure, the titanium tetrachloride can now be used in the Kroll process, where it is reduced by liquid magnesium via Equations 2.4.3 and 2.4.4

$TiCl_4 + Mg \rightarrow TiCl_2 + MgCl_2$ **(Equation 2.4.3)**

$TiCl_2 + Mg \rightarrow Ti + MgCl_2$ **(Equation 2.4.4)**

$TiCl_4$ is fed into the Kroll reactor which has been previously loaded with magnesium ingots and heated to ~1223K for around 3 days [50]. As this reaction is highly exothermic, the $TiCl_4$ addition must be carefully controlled. Attentive heat regulation prevents excessive densification of the solid titanium product, avoiding trapping volatile compounds within the pores. Heat extraction from the retort is rate determining, which is one of the reasons for the long reduction times [48].

Following reduction, the $MgCl_2$ by-product and excess Mg is evaporated over a 3 day period [50]. Following extraction, the $MgCl_2$ is recondensed and recycled by regaining the constituent Mg and Cl_2 components via electrolysis [17]. Once the distillation process is complete, the retort is cooled to reveal a porous titanium sponge which then goes for cutting and crushing [17]. Figure 2.4.1 gives a good overview of the whole process.

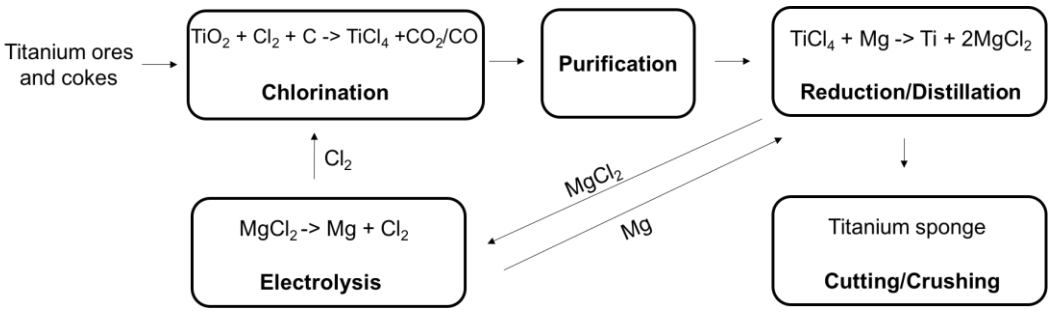

Fig. 2.4.1: Schematic diagram of the production of $TiCl_4$ and the Kroll process, redrawn from Ref [50].

2.4.2 Vacuum Arc Remelting and Cold Hearth Melting

Once the titanium sponge has been produced and crushed, it is then melted into an ingot. Extreme care is taken throughout the melting procedure, as it is at this point where most defects are introduced into the material, which can be problematic to remove [17]. Hence, melting procedures are expensive and can contribute up to 15% of the cost of a titanium component [51]. Alloys which are prone to segregation, such as Ti-10-2-3, add further costs as these must be prepared in smaller ingots, with lower melting rates [17]. Some alloys are entirely uneconomical to produce using current melting procedures, as large differences in melting points and/or densities, would require a significant number of remelts to ensure a homogenous product is produced.

Vacuum arc remelting (VAR) involves blending the titanium sponge with alloying elements before crushing the homogeneous mixture into a block shaped die using a hydraulic press [17]. Many of the blocks are then electron beam welded together in an inert atmosphere to create a first melt electrode, which is held in the VAR furnace by a titanium stub of the same alloy composition [17]. After melting, the ingot is inverted and melted again to ensure a homogenous product.

Cold hearth remelting (CHM) is a newer melting technique which offers advantages such as increased efficiency, increased use of titanium scraps, reduction of dense inclusions from electrodes or WC tooling as well as the ability to produce non-axisymmetric shapes over VAR [17]. In this technique, the molten titanium is contained within a water-cooled hearth. By balancing the heat input from the furnace with the rate of heat extraction via the water cooling, a thin layer of solid titanium is maintained on the hearth. Hence, the molten titanium only comes into contact with the solidified titanium lining the hearth [17].

Following the melting procedure, the solid ingot is then further processed into the desired component shape.

2.4.3 Powder Producing Methods

If powder is required, further processing techniques are also required. Widely used powder producing processes include gas atomisation (GA), the plasma rotating electrode process (PREP) and hydride dehydride processing (HDH). Both GA and PREP give spherical powders, whereas HDH processing yields powders with a morphology more akin to that of sponge fines; angular and irregular [16].

GA consists of a ring of high pressure gas jets into which a stream of molten titanium is sprayed via a nozzle [16]. The high-pressure results in the atomisation of the titanium metal. In comparison, centrifugal force is utilised within the PREP process. At speeds of around 18, 000 rpm, a titanium bar is spun within a chamber filled with an inert gas [17]. The molten titanium is flung outwards, which forms spherical droplets due to surface tension before solidifying mid-flight [17]. Typically, powder produced via PREP has a larger diameter than that of gas atomisation, however the PREP process is known to produce less satellites, which are formed when drops of metal impinge on other particles [17].

Both GA and PREP are relatively expensive powder producing methods [17]. If a spherical morphology is not required, titanium may be produced via the cheaper HDH process. This process involves heating titanium within a hydrogen atmosphere. Uptake of hydrogen into the

titanium deeply embrittles the material, resulting in the production of the extremely friable TiH_2, which is then easily pulverised into a powdered state [16]. Following powder production, the hydrogen is then removed by heating the material within a vacuum, resulting in the production of a titanium powder [16].

2.5 Alternative Extraction Routes

Considering the highly profitable nature of producing a low-cost titanium powder, there has been great interest, resulting in many ongoing research and industrial efforts invested in reducing the cost of titanium extraction. It is well known that Wilhelm Kroll himself predicted that his own metallothermic production route of titanium would be overtaken by an electrolytic route within 15 years [50]. Although the timeframe of his prediction was incorrect, there have since been many attempts at electrolytic extraction, such as the FFC process (discussed in detail in section 2.6), the calciothermic OS (Ono-Suzuki) process [52], and the oxy-carbide technique, investigated by the MER (Materials and Electrochemical Research) corporation [53] and Carnegie Mellon University [54] amongst others [55].

Non-electrolytic routes are also under investigation, including processes such as the TiH_2 yielding ADMA process [56], CSIRO's TiRO process and Cristal's Armstrong process. The basis of both the TiRO and Armstrong processes is of converting the classic Kroll/Hunter reactions (respectively) into continuous processes [50]. The TiRO process utilises a fluidised bed reactor, which allows a large reduction in the rate of reaction and operating costs [50], whereas the Armstrong process utilises a molten sodium stream into which gaseous $TiCl_4$ is sprayed to produce titanium and sodium chloride [50]. A good overview of the alternative titanium extraction processes is given by Fray [50] as well as Mellor and Doughty [55]. However, a more in-depth explanation of TiRO, Armstrong, MER and ADMA process will also be given here.

2.5.1 The ADMA Process

Following the Kroll process, the ADMA process replaces cooling of the titanium sponge using an inert gas with hydrogen gas. The result is the production of TiH_2, an extremely brittle material that is much more friable and easier to break down than classic titanium sponge, reducing mechanical crushing costs [57]. ADMA produced TiH_2 powder has been consolidated using a press and sinter method to produce near 100% density [57] [58]. During the sintering of TiH_2 powder, atomic hydrogen is released which also acts as a scavenging agent for oxygen as well as for contaminants such as Cl and Mg [57].

More recently, further developments of the process have been made with the proposal of a partial replacement of magnesium with hydrogen as the reducing agent (Equation 2.5.1) [56]. Utilization of hydrogen aids reduction by shortening the reduction time as well as the following vacuum distillation stage. Distillation temperatures can also be lowered [56]. In 2013 a pilot scale plant was set up with an annual capacity of 113.4 tonnes [59].

$TiCl_4 + (1\text{-}2)H_2 + (1\text{-}2)Mg \rightarrow TiH_2 + (1\text{-}2)MgCl_2 + (0\text{-}2)HCl$ **(Equation 2.5.1)**

Recent published work has shown the production of both Ti-6Al-4V and high strength titanium alloys made using a titanium hydride powders and a blended elemental approach [60] [61]. However, in 2012, a patent was filed for the direct production of alloyed titanium hydride powders, which details the direct production of Ti-6Al-4V powder using the ADMA process [62].

Although this process is capable of reducing the costs of titanium production, the technology used is a derivative of the Kroll process and as such may not be able to provide a large enough reduction in the cost of titanium powder that is required to revolutionise the industry.

2.5.2 The Armstrong Process – Cristal

Revolving around the reduction of $TiCl_4$ using a sodium reductant, the Armstrong process is akin to the Hunter process [50]. However, in contrast to the batch product nature of the Hunter process, the Armstrong process removes the requirement of producing a sponge, offering a continuous route with the potential for significant cost savings [51]. Essentially, $TiCl_4$ in vapour form is sprayed into a stream of molten sodium which react to produce titanium and sodium chloride (Eq. 2.5.2) [50].

$TiCl_4 + 4Na \rightarrow 4NaCl + Ti$ **(Equation 2.5.2)**

After separation via filtration distillation and washing a titanium powder product is retrieved with a high purity (<1000 ppm oxygen and <50ppm chlorine) [51]. A schematic of the process is shown in Fig. 2.5.1. It is also possible to directly produce titanium alloy powder by simultaneously reducing other metal chlorides (Eq. 2.5.3 & 2.5.4) [50].

$AlCl_3 + 3Na \rightarrow 3NaCl + Al$ **(Equation 2.5.3)**

$VCl_3 + 3Na \rightarrow NaCl + V$ **(Equation 2.5.4)**

A major advantage of the low temperature Armstrong process is its continuous nature, which can be extended to include the compaction and rolling of the produced material. Research undertaken by Rivard et. al. [63] demonstrated the consolidation into plate and roll compacted sheet from powder produced directly from the Armstrong process (pure Ti and Ti-6Al-4V). Although the ductility levels produced were not acceptable for the Ti-6Al-4V roll compacted sheet, the paper conveys that a viable product can be produced from the consolidation of the powder [63].

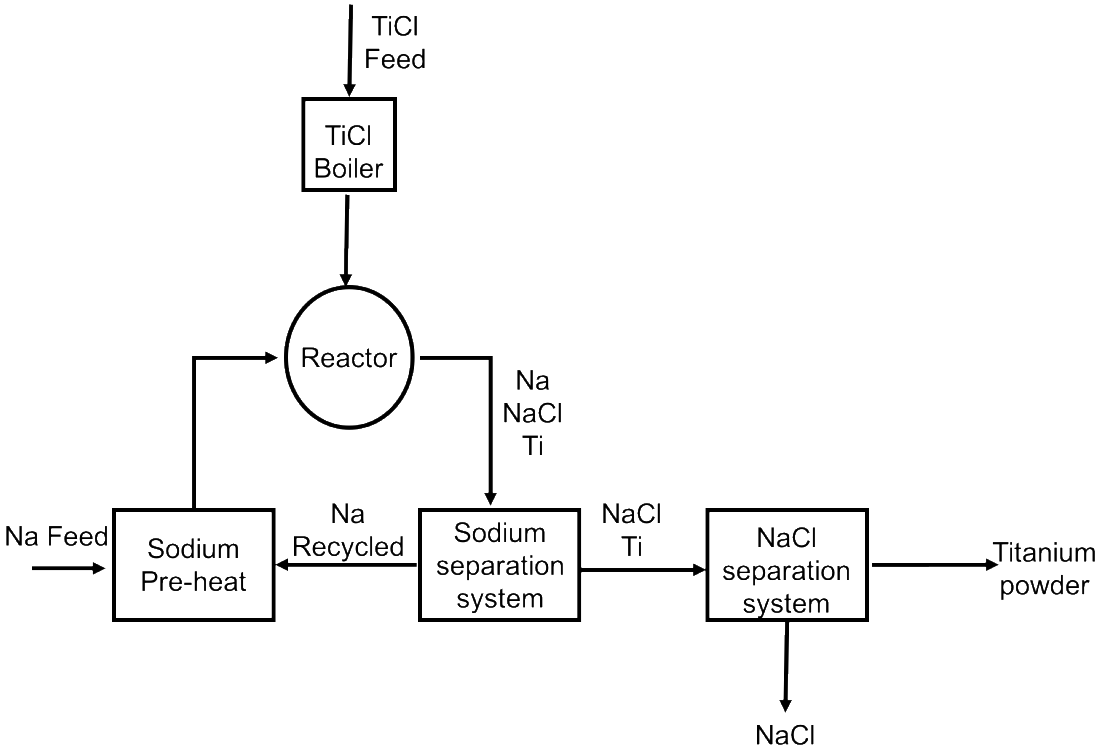

Fig 2.5.1: Schematic diagram of the Armstrong process, redrawn from [63].

However, the high cost of the sodium reductant may limit the cost savings potential of this process. Further, the feedstock required for this process is $TiCl_4$, titanium ores cannot be directly converted using the Armstrong process at present.

2.5.3 MER corporation process

The MER Corporation have been developing an electrolytic reduction process which initially utilises a carbon reductant, over the last 20 years. A range of titanium rich materials (TiO_2, rutile, titanium slags) can be used as the starting material, which are carbothermically reduced to produce the anode, consisting of composite of titanium suboxides and carbon TiC_xO_y [51] shown in Fig. 2.5.2.

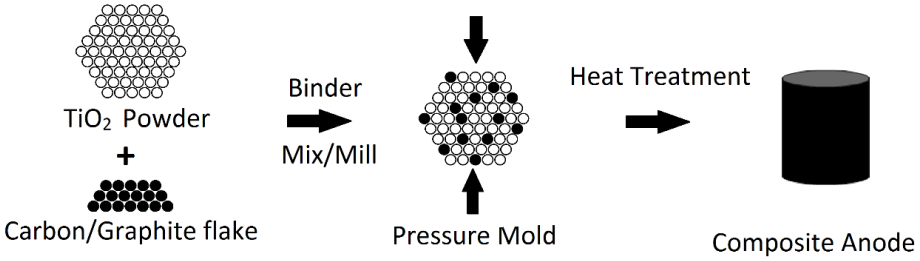

Fig. 2.5.2: Schematic diagram of the MER Corporation process composite anode (TiC_xO_y) production redrawn from Ref [51].

The reduced composite anode is then placed in an electrochemical cell and subjected to elevated temperatures (above 1600°C) [50] [64], resulting in the release of Ti^{2+} ions into the molten electrolyte (typically a salt mixture of alkaline and alkali earth chlorides [64]) which are subsequently collected as solid titanium on the cathode [51]. This reaction is accompanied by the release of carbon oxides at the anode, illustrated in Fig. 2.5.3 [51].

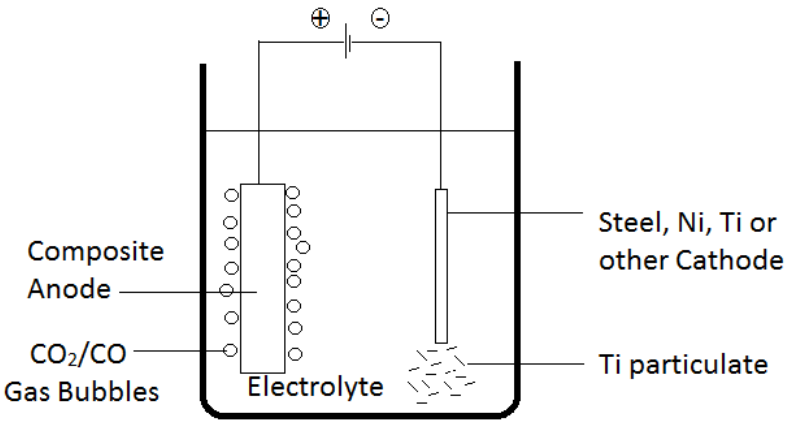

Fig. 2.5.3: Schematic diagram of the MER process, redrawn from Ref [51].

This oxy-carbide technique is also capable of producing titanium powder using impure starting materials such as ilmenite, or titanium slags [64]. However, in comparison with the aims of Metalysis and the work presented in this thesis, the MER process actively removes the alloying elements, such as Fe, Mn, Cr etc present within the starting material [64]. Recent research by Carnegie Mellon University has focused on the ability to remove metallic impurities to produce a pure Ti product [65]. This process has potential, however a review by Hu and Chen noted that the initial carbothermic reduction is relatively difficult and the Ti^{2+} can be oxidised to higher oxidation states during the reduction process [66].

2.5.4 TiRO™ Process

CSIRO's low cost titanium route converts the classic Kroll reactions into a continuous process by utilising a fluidised bed reactor which allows a large reduction in the rate of reaction and operating costs [50]. The process is capable of producing powder of 0.25% oxygen at a throughput rate of 0.2 kg/h [50]. A scale up plant has been built and is currently under development with a designed throughput of 2 kg/h [67].

Initial experiments utilising TiRO powder in conjunction with direct rolling technologies to produce strip have been performed [67]. However, the quality, density and chemical composition of the strip produced was not reported at the time of writing.

2.5.5 Summary of Low Cost Extractive Titanium Processes

Overall there are several different extractive processes currently under investigation and gaining momentum. Of all the alternative extractive processes, it appears the Armstrong process is the most advanced, capable of producing both low oxygen Ti-6Al-4V and CP Ti powders on a pilot plant scale. At this stage, it is difficult to construct a direct cost comparison, due to a lack of economic models for each of the processes, as the true cost of production may not be fully realised until the powder is scaled up and produced at a commercial scale. Table 2.2 summarises each of the processes included within this summary.

Table 2.2: Comparison of low-cost extractive technologies for titanium metal

Process	Description	Advantages	Disadvantages	Production status
FFC	Electrolytic reduction of TiO_2	Can be used for other metals, can use range of starting materials to directly produce alloys.	Batch process at present	Pilot plant 20 tons/year in progress
MER	Oxy-carbide reduction	Can use ore as starting material to produce pure titanium.	Production of composite anode relatively difficult.	
CSIRO	Continuous version of Kroll using a Fluidised bed reactor	Continuous	Kroll based technology	2kg/hour pilot plant
ADMA	Kroll + H_2	Continuous	Kroll based technology	Pilot plant 113 tons/year
Armstrong	Liquid Na reduction of $TiCl_4$ Vapour	Continuous	High cost of Na reductant, use of toxic TiCl4 precursor	Pilot plant (Ottawa plant) 2,000 tons/year

Note, although these extractive processes are seen as 'competitors', it is worth mentioning that a breakthrough into commercial application by any low-cost alternative to Kroll will likely facilitate the qualification and acceptance of other low-cost powders.

In comparison to alternative extraction processes, a major advantage of the FFC process (discussed in detail below) is its unique ability to be applied to a wide range of metals (Ta, Ti, Cr, Zr,) [68] [69] [70] [71], combined with the ability to produce homogeneous alloys in a single, solid state processing step [72] [73].

As such, the Metalysis FFC process holds a key advantage over alternative processes in being able to quickly and easily change course to produce complicated and difficult to produce alloys. For example, recent research from Metalysis has reported the production of high entropy alloys [74]. Typically, high entropy alloys are composed of several (usually five) elements, present in equal mass proportions. Hence, the production of such alloys is complex using conventional processing due to the range in melting points and densities involved.

With respect to titanium, this means the Metalysis has the opportunity to create novel low-cost alloys previously unexplored using conventional processes. An excellent example of which is the production of homogeneous titanium alloys directly from synthetic rutile – an inexpensive feedstock already possessing a range of beta stabilising alloying elements.

2.6 The Fray Farthing Chen (FFC) Process

Since its introduction in 2000 [68], the FFC process has experienced waves of both positive and negative publicity. Initial over speculation invited hotly anticipated results which never quite came to fruition, leading to inevitable disillusionment and disappointment. However, the FFC process has fundamentally proved a theoretical low cost model of producing titanium powder. After gathering increasing investment, technology company Metalysis have been working to improve the process and have managed to produce some promising results. Using the process, Ta production is almost at a commercial level. While Ti production is not yet commercialised, many advances have been made. Titanium powder can now be produced directly from a loose powder, rather than using a pellet, or honeycomb preform. Trials involving the direct reduction of both natural and synthetic rutile have begun, producing positive results, and perhaps most importantly, oxygen levels of under 3000 ppm amount have been successfully produced on a developmental scale (~5 kg batches). Despite these encouraging results, it is important to note that the process is currently still at a technology readiness level of 5. Although this extraction technique is both an exciting and lucrative prospect, many resources, particularly time and capital will be required before it will reach the commercialisation level.

Reported in 2000 by Fray, Farthing and Chen, the electrochemical deoxidation FFC process has allowed the production of metals and alloys – directly from their corresponding oxides [68]. In an electrolyte of molten salt, typically calcium chloride, using a consumable carbon anode, a voltage is applied, resulting in the direct electrochemical reduction of the metal oxide cathode (Fig. 2.6.1). Utilization of this method has led to the successful production of many metals including Zr, Nb, Cr and Ta [69] [70] [71]. Notably, the FFC process has also been applied to lunar regolith simulant material [75] [76]. Despite being applicable to a wide range of metals and alloys, titanium and its alloys appear to have stolen the spotlight, receiving a significant proportion of the attention [48] [50] [72] [73] [77] [78] [79] [80] [81] [82]. Much of this attention has been brought around by the lucrative prospect of the low-cost extraction of titanium, as the current cost of titanium severely restricts its application.

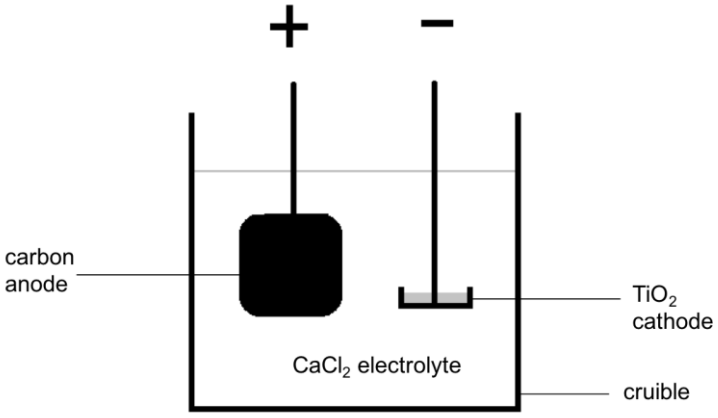

Fig. 2.6.1: Schematic diagram of an FFC cell set up, consisting of a carbon anode, TiO_2 cathode and $CaCl_2$ electrolyte.

2.6.1 FFC Mechanism Studies

Due to its fruitful nature, substantial effort has gone into understanding the reaction pathway and kinetics of the direct electrochemical reduction of titanium dioxide. Schwandt and Fray reported in 2005 the reaction pathway of the reduction of titanium dioxide to titanium metal in molten $CaCl_2$ salt, using a combination of X-ray analysis, gravimetric techniques and electron microscopy [77]. This research reported that the reduction coincides with a number of considerable changes within the microstructure, as well as providing a deduction of a well-defined reaction series, which was split into separate, distinct stages. Further work by the authors re-organised the stages to align with changes in the kinetic and transformational regimes [78]. Beginning with the formation of various titanium suboxides, of composition Ti_xO_y and presence of the calcium titanate, $CaTiO_3$, the reduction proceeds via the chemical reactions outlined below.

$$\mathbf{5TiO_2 + Ca^{2+} + 2e^- = Ti_4O_7 + CaTiO_3} \qquad \textbf{(Equation 2.6.1)}$$

$$\mathbf{4Ti_4O_7 + Ca^{2+} + 2e^- = 5Ti_3O_5 + CaTiO_3} \qquad \textbf{(Equation 2.6.2)}$$

$$\mathbf{3Ti_3O_5 + Ca^{2+} + 2e^- = 4Ti_2O_3 + CaTiO_3} \qquad \textbf{(Equation 2.6.3)}$$

Clearly the reactions proceed chronologically to produce titanium sub oxides of decreasing oxygen content, and it is noted that the reduction most likely proceeded via the Magnéli phases, beginning with Ti_9O_{17} and progressing to Ti_4O_7 [77]. However, as these phases are both

thermodynamically and structurally akin, differentiation between the phases would have been extremely strenuous using XRD analysis [78].

Each of the reactions, represented by Equations 2.6.1, 2.6.2 and 2.6.3 as well as the initial reduction through the Magnéli phases are described as kinetically 'easy'. That is, the transformation required does not require a complete reconstructive approach, hence, resulting in a relatively small kinetic barrier [78]. It is known that the structure of the Magnéli phases exists primarily as a derivative of the standard rutile structure, formed by shearing of the lattice. Therefore, reduction from TiO_2 to the end member of the Magnéli series – Ti_4O_7 occurs with relative ease. Additionally, the structures of Ti_3O_5 and Ti_2O_3 are also very similar to that of the Magnéli phases, hence, can be viewed as an extension of the series of phases, relinquishing the requirement for a reconstructive transformation [78].

Consisting of a face centred cubic structure however, TiO has a distinctly diverse structure than that of its predecessors. Hence, Equation 2.6.4 signals stage 2 of the reduction process, as the shift from the rutile based octahedral to the face centred cubic TiO structure is no longer 'easy' and is associated with a more significant kinetic barrier, resulting in a decreased rate of reduction. A more detailed description of this transformation can be found in the original paper [78].

$$\mathbf{2Ti_2O_3 + Ca^{2+} + 2e^- = 3TiO + CaTiO_3} \qquad \textbf{(Equation 2.6.4)}$$

The third stage of reduction is associated with the diagnostic presence of the calcium dititanate, $CaTi_2O_4$. Two separate reactions were put forward to explain the formation of this compound. The first of which is a chemically driven comproportionation reaction described by Equation 2.6.5 and the second was an electrochemically driven removal of oxygen from $CaTiO_3$, shown by Equation 2.6.6 [77].

$$\mathbf{CaTiO_3 + TiO = CaTi_2O_4} \qquad \textbf{(Equation 2.6.5)}$$

$$\mathbf{2CaTiO_3 + 2e^- = CaTi_2O_4 + Ca^{2+} + 2O^{2-}} \qquad \textbf{(Equation 2.6.6)}$$

It was reasoned that the formation of $CaTi_2O_4$ was more likely to be produced via the chemically driven reaction, as this comproportionation proceeds much more quickly than the alternative electrochemical approach, providing a rationalisation for the large quantities of $CaTi_2O_4$ present, as well as the temporary reduction of TiO throughout this stage [76].

Succeeding the formation of the calcium dititanate, the following stage consists of its subsequent destruction, accompanied by the formation of TiO and release of CaO described in

Equation 2.6.7. Both the formation and deconstruction of the dititanate require quite major reconstruction with respect to the particle morphology and microstructure of the pellets. $CaTi_2O_4$ consists primarily of non-mono crystalline lath shaped needles, illustrated in Fig. 2.6.2, compared to the small cubical and equiaxed shape of the TiO particles formed on the breakdown of the dititanate.

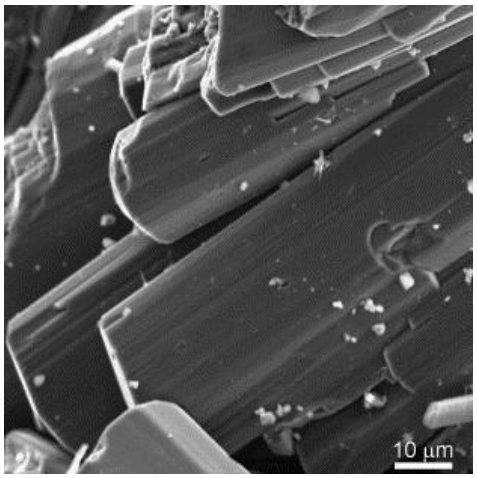

Fig. 2.6.2: Secondary electron image of non-monocrystalline $CaTi_2O_4$ needles. Note the minor facets formed on the major facets, evidence of a non-monocrystalline structure [78].

Following the reformation of TiO, a solid solution of oxygen in titanium $Ti[O]_\delta$ is then produced via the removal of oxygen from the TiO species, which is capable of resulting in a low oxygen titanium product (Equation 2.6.8). Note, δ expresses the concentration of oxygen in solid solution that is in equilibrium with TiO [77].

$$\mathbf{CaTi_2O_4 + 2e^- = 2TiO + Ca^{2+} + 2O^{2-}} \qquad \textbf{(Equation 2.6.7)}$$

$$\mathbf{TiO + 2(1-\delta)e^- = Ti[O]\delta + (1-\delta)O^{2-}} \qquad \textbf{(Equation 2.6.8)}$$

Further details of this reaction pathway were reported in 2009, after a significant rate in reduction was achieved by Schwandt et al [83]. A reduction in reaction time from days to 16 h was attained using a combination of increased concentrations of calcium oxide, which minimises mass transport limitations and the use of an initial voltage ramp, to avoid excessive currents and chlorine production. Although the general reaction pathway remained unaltered, new features were noticed such as the formation of $CaTi_2O_4$ before $TiO/CaTiO_3$. Other differences were noted such as complete conversion to $CaTiO_3$ and TiO is not observed. Additionally, the possibility of $CaTiO_3$ and Ti_2O_3 directly decomposing to TiO on the surface of the pellets was proposed, with the bulk favouring the usual reaction pathway reactions (Equations 2.6.1-2.6.8). This direct

reduction was rendered possible due to the increased oxide ion transport throughout the electrolyte.

Direct reduction of Ti_2O_3, which bypasses the formation of $CaTi_2O_4$, was further investigated by reducing the porosity of the pellets from the usual 25-30% total porosity to ~15% [79]. Throughout these reductions, it was discovered by utilising a dense precursor, the pellet could no longer accommodate the usual porous reaction pathway. A more direct pathway is taken which sees the reduction of Ti_2O_3 to TiO. Initially following the standard porous reduction mechanism, once small amounts of $CaTiO_3$ are formed, the solid volume expands, enough to close all remaining open porosity. Without this porosity, electrolyte flow is blocked and thus, calcium incorporation ceases, leading to the direct reduction of Ti_2O_3 to TiO which is then reduced to a solid solution of oxygen in titanium, Ti-O [79]. Usually, this pathway does not occur as incorporation of calcium ions is both kinetically and thermodynamically favourable [79]. Although a 'direct' reduction seems beneficial, and despite similar times taken to reduce the pellet to a metallic state, decreased current efficiencies were observed and the time taken to reduce oxygen content to below 6500 ppm is more than doubled.

Removal of oxide ions from the solid solution of oxygen in titanium is a rate limiting factor of the FFC process, due to slower diffusion rates in Ti metal than in the oxide. Hence, the high density of the non-porous preform restricts electrolyte flow, slowing the transportation of oxide ions, leading to high oxygen contents compared with porous pellets reduced over similar time spans [79]. As illustrated by the above research, changing the preform of the reduction can have implications on the reaction pathway and may be of importance throughout the alloy design process when using free powder, rather than a preform. Traditionally a preform has been used for the electrochemical deoxidation process, however recent research has led to its elimination, allowing the reduction of loose powder [81].

The main limitation of the aforementioned studies is their ex-situ nature. In 2010 Bhagat et. al studied the reaction mechanism in-situ using synchrotron X-ray diffraction, which determined the formation of $CaTiO_3$ was chemically driven from substoichiometric TiO_2 phases [82]. Further, the formation of Ti_3O_5, alpha TiO and Ti_3O_2 was not observed [82].

2.6.2 FFC Reductions of Rutile

Extraction of titanium directly from its ore, rutile, is possible using the FFC process. Both the quality and composition of the resulting titanium alloy are directly dependant on the type of rutile (natural or synthetic), purity, and the geographical location of the ore source. Prior to this

work only proof of concept experimentation had been completed at Metalysis to demonstrate that the technology was capable of directly reducing ore and ore like material to titanium alloys. However, there is no mechanistic or thorough studies on the reduction pathways prior to this work. Further, there is no data available on the resulting alloy produced from a synthetic rutile feedstock, nor have any mechanical properties been analysed. Hence, this work will provide the baseline understanding of the titanium alloy directly produced from a synthetic rutile feedstock including feedstock analysis, mechanistic studies as well as the resulting mechanical property assessment.

2.6.3 Conclusions to the FFC process

Compared to conventional titanium production, the FFC process offers many significant advantages. Firstly, this electrochemical process directly produces a powder product. Conventionally, to produce a titanium powder, titanium would initially be converted to $TiCl_4$ and reduced to Ti via the Kroll process (section 2.4.1). Following cutting and crushing the titanium sponge produced would then be sent for atomisation or hydride-dehydride processing (section 2.4.3) to produce a powder. As a powder can be directly produced as part of the extraction procedure, costs can be significantly reduced. Powder production is advantageous as up to 47% of the cost of titanium metal production is due to fabrication costs [51]. Many powder metallurgy techniques employ near net shape techniques, which can drastically reduce both machining and wastage costs.

Combining FFC extraction with powder metallurgy techniques to produce a titanium component entirely in the solid state also enables the elimination of costly melting procedures. As well as reducing costs, it is generally the melting stage in which most defects in titanium are produced [17]. The melting stage is particularly expensive in the case of titanium alloys containing alloying elements which are prone to segregation, such as Fe and Mo which require multiple remelts to ensure good homogeneity.

Although substantial research has been undertaken on the electrochemical reduction of pure TiO_2 using the FFC process, there have been no studies investigating the mechanism of a synthetic rutile based precursor. As synthetic rutile is known to contain significant remnant material, particularly iron, it is vital for the mechanism to be reassessed using this feedstock. Further, a full characterisation of synthetic rutile feedstock and corresponding titanium alloy is required to build a complete understanding of the process.

2.7 Powder Metallurgy

Direct production of a titanium powder utilising an extraction process such as the FFC process (section 2.6) vastly expands the potential of powder metallurgy routes. Although powder metallurgy (PM) itself minimises wastage and vastly reduces processing costs, the current cost of powder production often outweighs the benefits provided by powder metallurgy methods. At present, to produce titanium in powder form involves the initial extraction of titanium via the expensive Kroll process (section 2.4.1) followed by further costly powder producing methods via either HDH, GA or PREP techniques (section 2.4.3).

2.7.1 Introduction

PM refers to the processing of metal in particulate form to produce solid metal objects [84]. Although PM is not a new concept, it has had difficulty gaining much traction within the titanium industry. Originally trialled by Kroll throughout the late 1940s – early 1950s, powder metallurgy was of little interest until the 1970's, culminating in the 1980s [84]. Although the following decade yielded little progress [84], following this period, significant advancements have been made such as the refinement and development of field assisted sintering (FAST) [85] [86], continuous rotary extrusion (CRE) [87], metal injection moulding (MIM) and additive layer manufacturing (ALM) [88].

Powder metallurgy offers many advantages over traditional ingot metallurgy. Perhaps most enticingly, is the potential for major cost savings [89]. Inherently, near net shaping processes are optimised to minimise wastage of the expensive titanium metal. Additionally, the production of near net shapes also substantially reduces the need for machining, which is particularly strenuous and costly for titanium. Alongside more effective and efficient use of the material, PM has the ability to produce much more complex shapes, with reduced processing steps [84]. Further cost savings are also envisaged during the scaling up of production to mass produce components [25].

Another major benefit of utilising PM with titanium alloys is the ability to take advantage of alloys which were unsuitable for classic ingot metallurgy. For example, titanium alloys with high contents of elements with either vastly different densities or melting points had the tendency to segregate throughout the melting procedure. However, as powder metallurgy techniques take place below the melting temperature of titanium alloys, this problem is avoided and homogenous alloys can be produced [25].

PM can also be used to produce porous components which can be beneficial within the biomedical industry, due to the decreased Young's modulus (closer to that of bone), as well as the opportunity for bone ingrowth, facilitating both fixation of the implant and transferal of stresses from the implant to the bone [90]. PM can produce lattice structures, which could reduce the mass of weight sensitive applications.

There are two main avenues of powder metallurgy with respect to powders used. The first is a blended elemental (BE) approach in which the individual elemental powders are mixed prior to processing. The second is pre-alloyed (PA) powder in which the powder already possesses the desired composition.

Despite its advantages, the commercialisation of PM has been somewhat limited by the initial cost of producing powder. However, new low cost extraction techniques currently in development such as the Armstrong or FFC process (discussed in sections 2.5.2 and 2.6 respectively), produce a powder directly which could make PM techniques much more viable. Furthermore, as these low-cost titanium production technologies produce a powder directly, PM has an advantage over classic metallurgy as the low-cost titanium powder produced can be directly taken advantage of.

2.7.2 Powder Metallurgy Methods

Powder metallurgy encompasses a wide range of techniques, many of which revolve around the basic principle of sintering. Sintering is the coalescence of powders into a solid mass without surpassing the melting point of the material [91]. The major driving force behind this process is the reduction of surface free energy via the reduction of surface area [91]. Additive layer manufacturing, hot isostatic pressing, field assisted sintering and continuous rotary extrusion all contain aspects of sintering. As the consolidation technique of choice within this work, a more in depth overview of FAST will be provided.

2.7.2.1 Field Assisted Sintering Technique/ Spark Plasma Sintering

Field assisted sintering is a branch of sintering which involves the densification of powders via the application of heat, current and axial mechanical loading [85], shown in Fig. 2.7.1. This technique has a variety of acronyms associated with it including spark plasma sintering (SPS) and pulsed electric current sintering (PECS). Facilitating lower temperatures, shorter processing times and improved comparative properties field assisted sintering offers marked advantages over classic hot pressing techniques [85]. Although popular with ceramics, FAST has only recently gained much attention with respect to titanium [86] [92] [93] [94]. FAST differentiates

itself from the classic sintering technique due to the application of a current and rapid heating rates, however, the exact effect the current has upon the mechanism of sintering is still unclear within the literature [85] [86] [95]. Presence of spark discharges have been disputed, with recent reviews favouring its nonexistence [85]. Further experimentation into the effect of pulsing has been explored, with reports showing neither pulse frequency nor pulse pattern have an effect on consolidation [85].

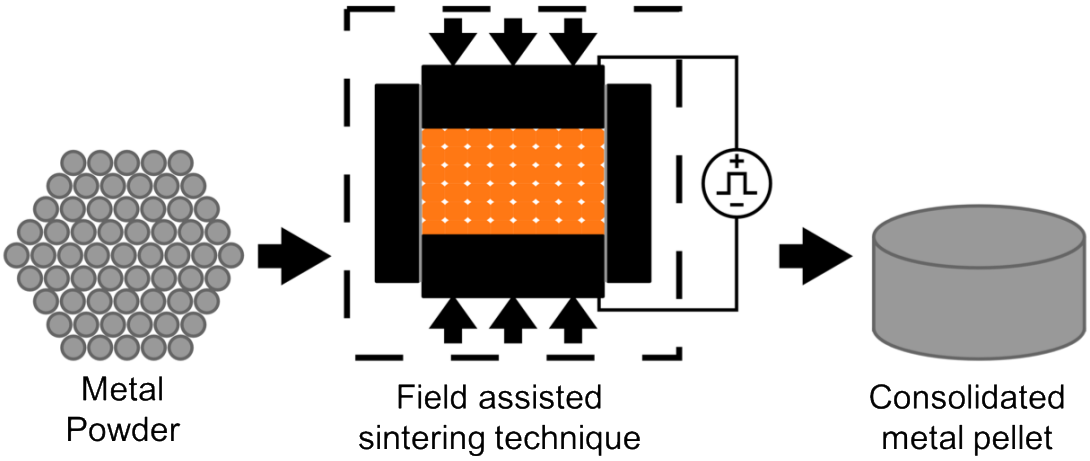

Fig. 2.7.1: Schematic diagram of the field assisted sintering technique [96].

With respect to titanium consolidated via FAST, the data available remained somewhat limited until recently. Weston et al. determined the effects of various process parameters such as dwell time, sintering temperature and heating rate on titanium alloys while other reports have consolidated commercial titanium alloys (principally Ti-6Al-4V and CP titanium powders) and determined their mechanical properties [94] [93]. Both Bolzoni et al. and Yang et al. have investigated the effect of using the BE approach compared to pre-alloyed powders [92] [93]. Both research groups reported good homogenisation using the BE approach. However, both studies investigate Ti-6Al-4V, of which Al and V diffuse at a similar rate as the self-diffusion of titanium within the beta phase [17]. When using elements which are much slower at diffusing, such as Ta or Mo, homogeneity of the final compact may be strongly dependant on the homogeneity of the initial premixed BE powders as shown in work by Liu et al, a two-phase microstructure was observed when consolidating Ti and Ta powders due to insufficient diffusion [97].

Powder size between 38 and 150 µm showed no difference in densification achieved under the same consolidation conditions using either PA or BE techniques [93].

As a final note on the FAST process, Weston et al. have demonstrated upscaling of the process on a 5 kg scale resulting in both homogenous microstructure and full density throughout [86]. Further, their research has also demonstrated the production of shaped consolidated parts which would aid the minimisation of both wastage and machining costs with the titanium production process [98]. Hence, with further investigations, consolidation of titanium on an industrial scale using FAST is a viable prospect.

2.7.2.2 Continuous Rotary Extrusion / Conform Process

Continuous rotary extrusion and variant, the Conform process, are PM consolidation techniques based around the principle of severe plastic deformation [99], with the goal of the continuous production of wire via rotary friction extrusion. Aimed at replacing the current industry standard production route of titanium wire, which consists of multiple energy intensive melting, forging and rolling steps, this is a game-changing technology that has the potential to disrupt current manufacturing routes.

Figure 2.7.2 displays a schematic of the process, which involves the input of feedstock particulate via a hopper. Once entered, the particulate is carried around via a groove in the wheel until diverted by the abutment, where the particulate is forced through a profiled die at temperature, resulting in the consolidation and extrusion of the feedstock [99]. Mechanical friction between the metal particulates and the grooved wheel subjects the particles to sufficient stress to remove oxide layers, hence allowing particle-to-particle bonding to occur [99].

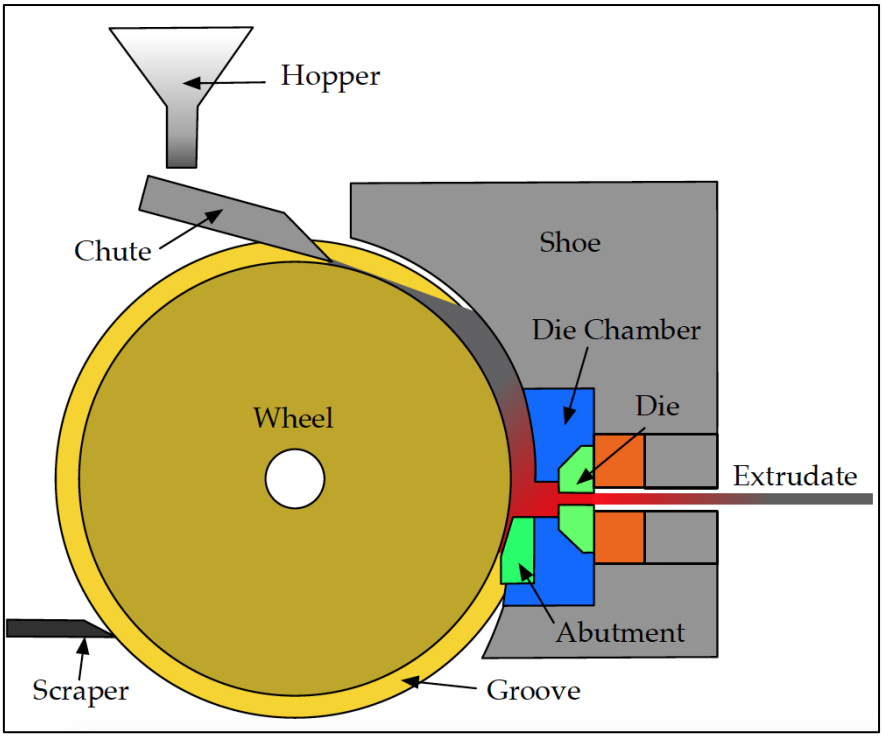

Fig. 2.7.2: Schematic diagram of a conform machine illustrating the continuous extrusion process for powder feedstock [99].

Conform technology has been successful in the extrusion of softer materials such as aluminium alloys and copper alloys [100] [101] [102]. Continuous rotary extrusion of higher strength materials such as that of titanium has been successful, however there is little available data within the literature [99] [103]. Currently, the technology is still known to be under investigation by both the University of Sheffield [87] [99] and CSIRO [104].

2.8 Alloy Development

2.8.1 Introduction

Traditionally, titanium alloy development has been stimulated by the requirement for enhanced properties for increasingly demanding applications. Typically, these alloys have been designed exclusively for markets in which cost is of less concern, such as the aerospace sector and military markets. However, for titanium to expand its current application portfolio into more commercialised markets, such as the automotive industry, minimising expenditure must become a priority.

Providing the link between low cost extraction techniques and cost-effective PM methods, alloy development will play a crucial role within the acquisition of low cost titanium. Production of a titanium alloy directly from synthetic rutile feedstock via the FFC process would allow an efficient streamlined method of alloy production. Furthermore, when fabricated using new downstream consolidation techniques, many processing steps such as melting, could become redundant. Development of such an alloy would aid the simplification of titanium production and hence, facilitate much more affordable and commercialised titanium usage. However, for this to be a viable route to low cost titanium, the alloy powder produced must possess good mechanical properties and therefore, be capable of reaching high sintered densities.

To develop a successful titanium alloy, a fundamental understanding of alloying elements is crucial to avoid any unwanted effects. Both the microstructure and the chemical composition are responsible for the determination of the properties retained by titanium alloys [15]. Chemical composition is predominantly responsible for the volume fraction of phases, as well as the mechanical properties observed. Hence, throughout the process of alloy development, a fundamental understanding of the effects of each alloying element addition is therefore required [105]. This baseline knowledge allows the mechanical properties desired to be obtained, and facilitates the avoidance of unwanted effects.

2.8.2 Alloy Design for Powder Metallurgy

Almost all titanium alloys, particularly commercial titanium alloys, have been designed and intended for use from an ingot metallurgy standpoint. As such, titanium alloy design has been limited to allow for constraints associated with ingot metallurgy, such as severe segregation, a resultant of large differences in melting point or density. Therefore, most of the classic titanium alloys should not necessarily be first choice in demonstrating the capabilities of powder metallurgy. Hence, optimisation of powder design intended for powder metallurgy consolidation has gained interest, with recent research reporting on alloys designed with powder metallurgy in mind [25] [106].

A major difference between designing alloys for solid state titanium production routes (solid state extraction & powder metallurgy) as opposed to classic ingot metallurgy, is the removal of the segregation prone melting procedure, which is known to be the primary source of defects found within titanium [17]. Instead, powder metallurgy consolidation techniques utilise sintering, the process of reducing surface area resulting in the production of a coherent, solid mass via mass transport. As such, in terms of avoiding defects such as segregation within titanium alloys, using a sintering process, properties such as melting point and density are no longer useful indicators. Instead, a major controlling force of creating homogeneous microstructures is the difference in diffusion coefficients between the self-diffusion of the matrix titanium with that of the alloying additions. Slow diffusing alloying elements with respect to the titanium matrix can result in a two-phase structures and/or Kirkendall porosity [97].

An example of segregation caused by differences in diffusion rates is shown by Liu et al. when consolidating a BE mixture of titanium and tantalum powder. Ta has a much lower diffusion coefficient than titanium resulting in its poor homogenisation during consolidation and potentially the formation of Kirkendall porosity [107] [97].

Possible solutions to minimise this problem include:

a) use of a prealloyed powder

b) employment of a more effective mixing technique prior to consolidation

Of the above options, prealloyed powder is usually the more expensive option, as it requires melting to gain homogenisation prior to powder production. An alternative option is capitalise on the extractive technology of the FFC process. By premixing the feedstock powders, uniform,

homogenous alloyed products are possible, such as in the case of Ti-Mo and Ti-W alloys reported by Bhagat et al [72] [73].

Exact alloy composition can affect the behaviour and mechanism of sintering, for example, some alloying elements are capable of influencing the sinterability of Ti alloys, such as fast diffusing iron, which has been reported to enhance the sintering process [106] [108].

Within the beta phase of titanium, both the self-diffusion of titanium as well as diffusion of alloying additions are both significantly faster than within the alpha phase [17]. Further, work by Weston et al. demonstrated the densification mechanism altered when consolidating Ti-64 in comparison to a CP titanium alloy [86].

Effects of powder morphology and size also need addressed during alloy design. Although the effect of particle morphology appears to make minimal difference to the final density achieved using optimal conditions of 1200°C using FAST [86], powder size is still thought to have an effect on the sinterability of powders due to the increased surface area [91]. Hence, while designing alloys for powder metallurgy, new approaches must be taken and the solid state production route must be kept in mind.

As Fe, Mo and Al have been utilised as alloying additions throughout this work, a review of these elements as titanium alloying additions will be given.

2.8.3 Alloying Elements & Effects - Aluminium

Effect of aluminium as an alloying addition within titanium has been well documented. Aluminium is one of the most common alloying elements and can be found within all classes of titanium alloys. Presence of alloyed aluminium can have several effects, such as an increased melting point and beta transus, as well as increasing the solubility of beta stabilising elements in the alpha phase [2]. Additionally, the presence of aluminium is known to widen the α+β processing window [109]. Aluminium is also well known to increase the strength of titanium alloys and is thought to add between 35 to 70 MPa per wt% added [20].

From the Ti-Al phase diagram, illustrated in Figure 2.8.1, it can be seen that a number of intermetallic phases can be formed, such as Ti_3Al, TiAl, and $TiAl_2$. If the content of aluminium surpasses its solubility limit within the alpha phase, the intermetallic Ti_3Al will precipitate out. Formation of this phase, known as α_2, is concerning, as it is known to induce detrimental effects, such as embrittlement. Hence, in practise, most commercially available alloys possess 6 wt% Al or less [17] and less than 9 wt% aluminium equivalency [20].

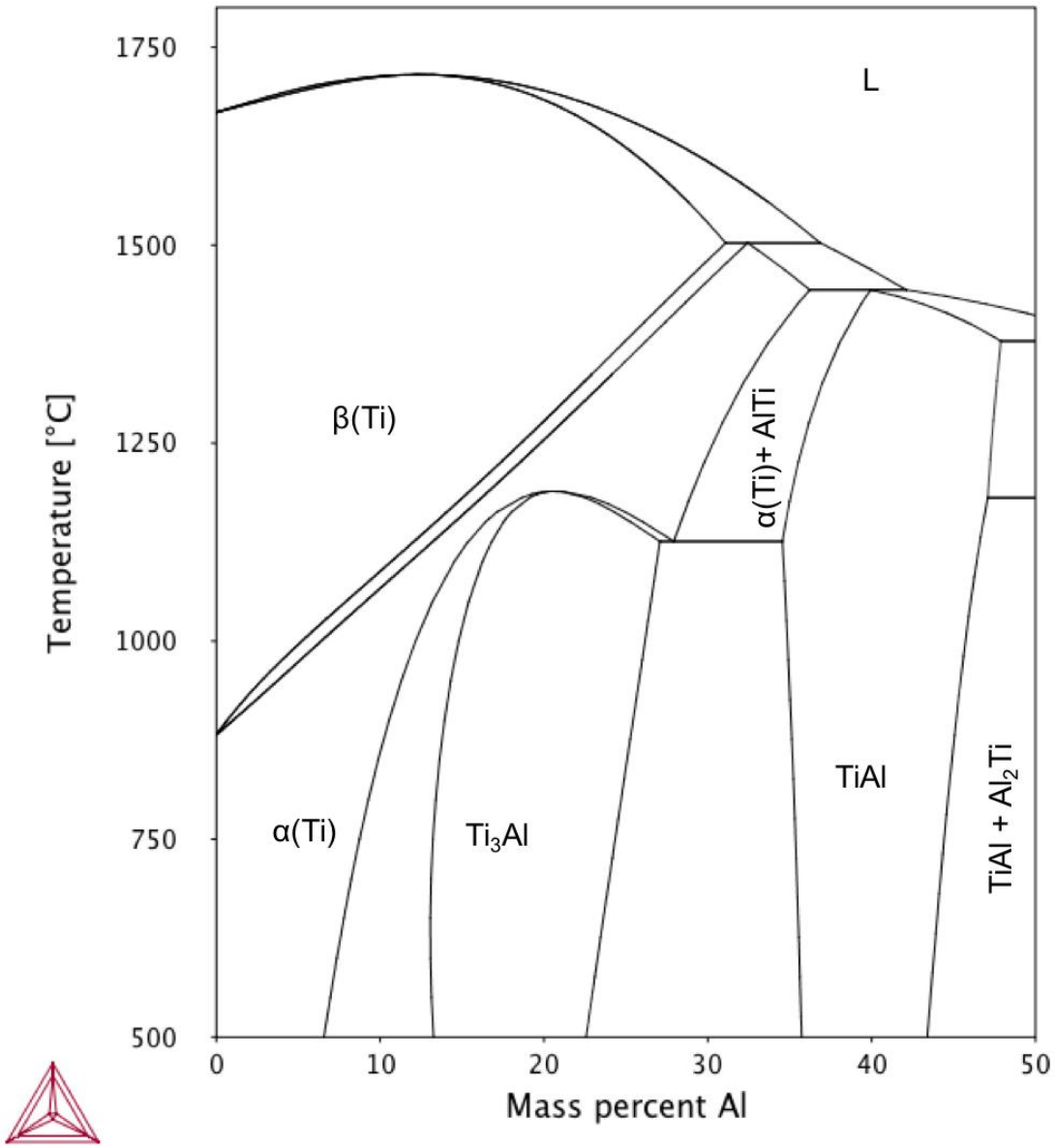

Fig. 2.81: Equilibrium binary phase diagram of Ti-Al drawn using Thermo-Calc software [110].

The only commercial titanium alloy with high aluminium content is Ti-8Al-1Mo-1V (Ti-811). However, due to the high aluminium content and high aluminium equivalency (Eq. 2.8.1), problems with stress corrosion cracking were observed [15] as well as the formation of the brittle α_2 phase at exposure to elevated temperatures [20].

Aluminium is by far the most utilised alpha stabiliser within titanium alloy design. In contrast to aluminium's substitutional position, other alpha stabilisers, O, N and C all occupy interstitial vacancies. Although these elements are also capable of increasing the beta transus, it was quickly established that these alloying elements are embrittling and extremely detrimental to

ductility [111]. Neutral alloying elements, Zr and Hf will act to enforce the alpha phase if aluminium is present, whereas Sn can replace Al within the Ti_3Al α_2 phase [17]. However, these elements are not as potent alpha stabilisers as aluminium as observed within the aluminium equivalency equation [20]:

Al Eq. = 1(Al) + 1/3(Zr) + 1/6 (Sn) +10(O + C +2N) **Equation (2.8.1)**

Note the highly alpha stabilising effect of interstitial O/C/N and relatively weaker effects of Zr and Sn compared to Al.

Aluminium has also been reported to affect the sinterability of titanium alloys. Fig. 2.8.2 displays work by Liu et al. which displays a decrease in relative density corresponding with an increase in aluminium concentration [106]. At 1350°C, a difference of 3% density is observed between Ti-1.5Al and Ti-6Al. Note, the decrease in density with increasing temperature is suggested to be due to expansion of entrapped gas in residual pores following the atomisation of aluminium [106].

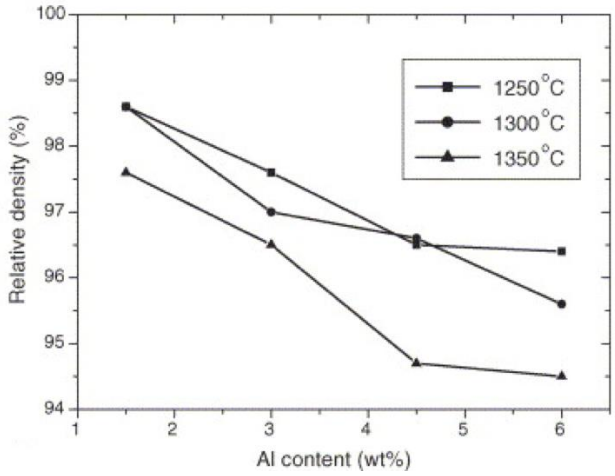

Fig. 2.8.2: Differences in density of Ti-Al alloys sintered for 3h [106].

However, Izui et al. reported an increase in sintered density of Ti-5Al compared with a pure Ti feedstock when utilising FAST [112]. Differences between the two reports could be due to a smaller particle size of aluminium used by Izui (4.9 µm compared with 15.1 µm) and rapid sintering afforded by FAST.

2.8.4 Alloying Elements & Effects – Molybdenum (beta isomorphous)

Of the beta stabilising elements, those with an isomorphous crystal structure to that of titanium are preferred over those without, known as eutectoid stabilisers. Due to their isomorphous disposition, these alloying elements are able to form a continuous solid solution with titanium and thus, do not form intermetallic compounds, unlike eutectoid stabilisers.

Out of the isomorphous alloying additions (Mo, V, Ta,) it is molybdenum which is able to generate the largest increase in hardenability, per weight percent added [113]. As well as increased strength and hardenability, Ti-Mo alloys are noted for their well-established superior corrosion resistance [114] [115] [116] and biocompatibility [117] [118].

Further, Mo is often utilised in applications requiring a low Young's modulus, such as that of springs, or medical implants in which a low Young's modulus can significantly reduce the stress shielding effect [35].

However, the relationship between Young's modulus and Mo is complex as the elasticity of the alloy can depend on the concentration of phases present within the alloy – particularly that of the brittle omega phase [119]. Fig. 2.8.3 illustrates the variation in elasticity with varying Mo content. Alloys containing between 4.5 and 7 at% Mo were found to have a higher value due to the presence of the omega phase [119]. Above 8 at% (14.8 wt%) Mo, only the beta phase was identified and low Young's modulus values were attained. Hence, for low Young's modulus values, avoiding the formation of the omega phase is key.

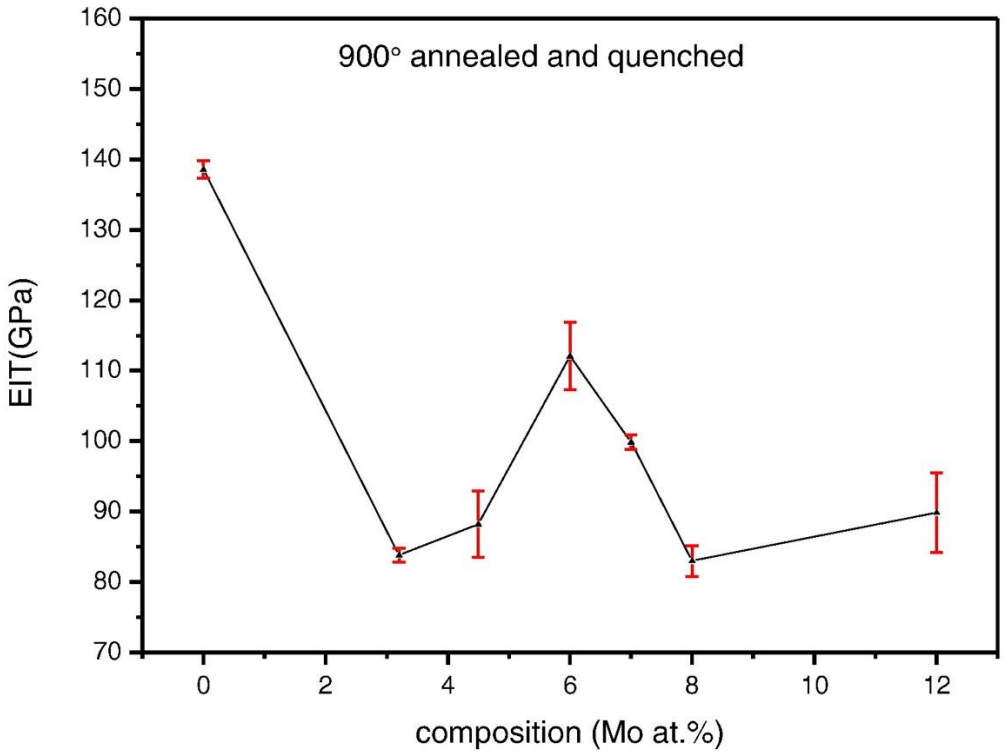

Fig. 2.8.3: Young's modulus of Ti-Mo alloys with various Mo concentration [119].

Despite its advantageous effects, the use of molybdenum has been restricted by its high density (10.22g cm^3), which causes segregation issues during melting procedures. Segregation can be minimised by repeating the melting process and use of smaller ingots, however, this results in a highly expensive procedure.

The effect of Mo as alloying addition throughout the sintering process of Ti alloys has also been studied [106] [120]. Mo appears to be detrimental to the sintering process due to its slow diffusion rates within titanium. As shown in Fig. 2.8.4, an increase in Mo content results in a lower achieved density [106].

In contrast to this work, Izui reported an enhancement in sinterability of Ti-5Mo in comparison to pure Ti. However it is stated that the increased could have be due to the small particle size of the Mo powder utilised. Further, Izui used the FAST as opposed to a standard press and sintering technique [112].

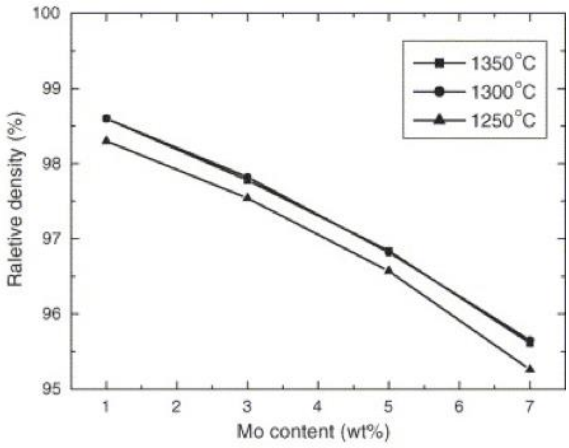

Fig.2.8.4: Differences in density of Ti-Mo alloys sintered for 3h [106].

2.8.5 Alloying elements & effects – Iron (beta eutectoid)

A main attractive property offered by iron alloying additions is cost [25]. More recently, alloys have been designed specifically for markets which are heavily restricted by cost restraints, such as the automotive sector. Some avenues of low cost alloy design have exploited both the potency of Fe as a beta stabiliser and its relatively inexpensive disposition [25]. Low cost Ti-7Fe alloys were specifically designed with the objective of producing lower cost titanium alloys in conjunction with powder metallurgy methods [25]. Use of stainless steel as way of adding iron as well as chromium to titanium alloys has also been explored, resulting in no formation of the undesirable Ti-Fe phase [121].

In contrast to the previously mentioned elemental additions, iron belongs to the beta eutectoids. Traditionally, the use of beta eutectoids has been limited, or avoided to prevent the formation of intermetallic phases. Formation of the Ti-Fe intermetallics can be problematic for titanium alloys, as these phases are known to induce unwanted mechanical properties, such as embrittlement [25]. As can be seen in the phase diagram of Ti-Fe, displayed in Fig. 2.8.5, iron has a very low solubility in the alpha phase and may precipitate out at atomic percentages less than 0.1%. It can also be observed that the intermetallic phase, Ti-Fe is thermodynamically stable under equilibrium conditions at room temperature for a large range of compositions [25].

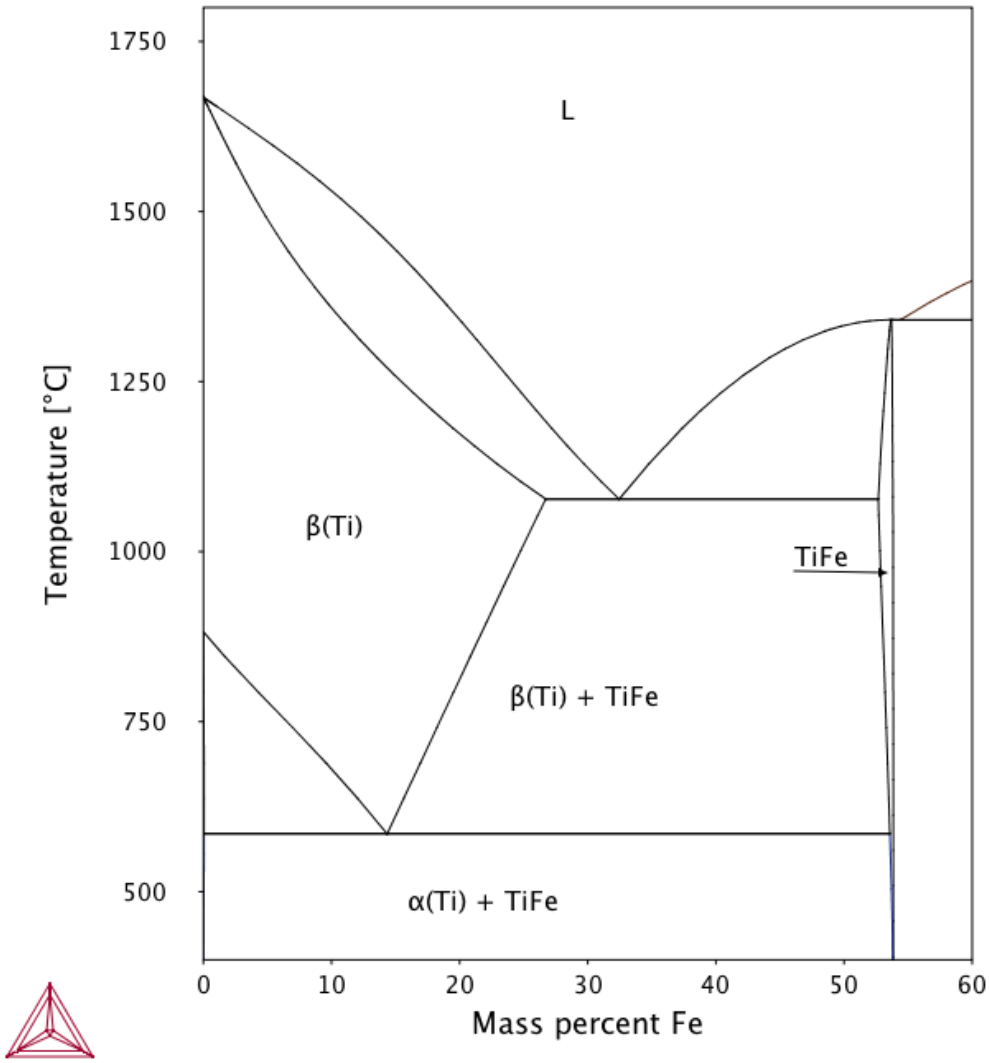

Fig. 2.8.5: Equilibrium binary phase diagram for a Ti-Fe system redrawn from [25] using Thermocalc software [122].

Although the stability of the TiFe phase is well known, iron is still commonly used as an alloying addition. Alloys such as Ti-10-2-3 (Ti-10V-2Fe-3Al), Timetal 125 (Ti-6V-6Mo-5.7Fe-2.7Al), Ti-1-8-5 (Ti-1Al-8V-5Fe) take advantage of iron's potent beta stabilising nature. Incorporation of iron as an alloying element is possible as the formation of its intermetallic phase is known to be very sluggish [123]. As such, TiFe formation can be somewhat controlled during the manufacture of the alloy [25].

However, during conventional processing, titanium alloys containing iron need to be carefully controlled to also avoid the formation of beta flecks. Beta flecks are regions locally enriched with the beta phase which can be difficult to remove once formed [17]. Minimisation of beta flecks can be achieved by producing susceptible alloys in small ingots, however this has a significant

impact on the cost of production [17]. Beta fleck formation may be avoided using PM techniques, however there is currently no data on the large-scale consolidation of iron containing titanium alloys.

Further, recent research has shown that using PM techniques, the formation of Ti-Fe intermetallics is supressed [124]. Ti-7Fe alloys were produced via PM and slow cooled from the sintering temperature without the formation of any Ti-Fe intermetallics. Following this observation, the Ti-7Fe alloys were separately slow cooled following sintering at 1150°C to 740°C (above the eutectoid formation temperature of 595°C) and to 550°C (within α+TiFe phase field Fig. 2.8.5) and held for 24h before furnace cooling to room temperature. While the higher holding temperature produced coarser lamellar with a high content of the beta phase, no Ti-Fe formation was observed in either sample using scanning or transmission electron microscopy. As such, throughout this study the eutectoid reaction (β -> α + TiFe) did not occur while cooling [124]. This work is supported by other research who also report no formation of Ti-Fe intermetallics within Ti-Fe alloys consolidating using a PM technique [25] [125].

As well as intermetallic formation, the effect of iron on the densification process throughout sintering has also been studied [108] [112] [106]. It is agreed within the literature that the addition of iron to titanium results in an enhanced sintering process. Fig. 2.8.6 displays data from research by Liu et al. illustrating the higher relative density achieved by Ti alloys containing higher contents of Fe.

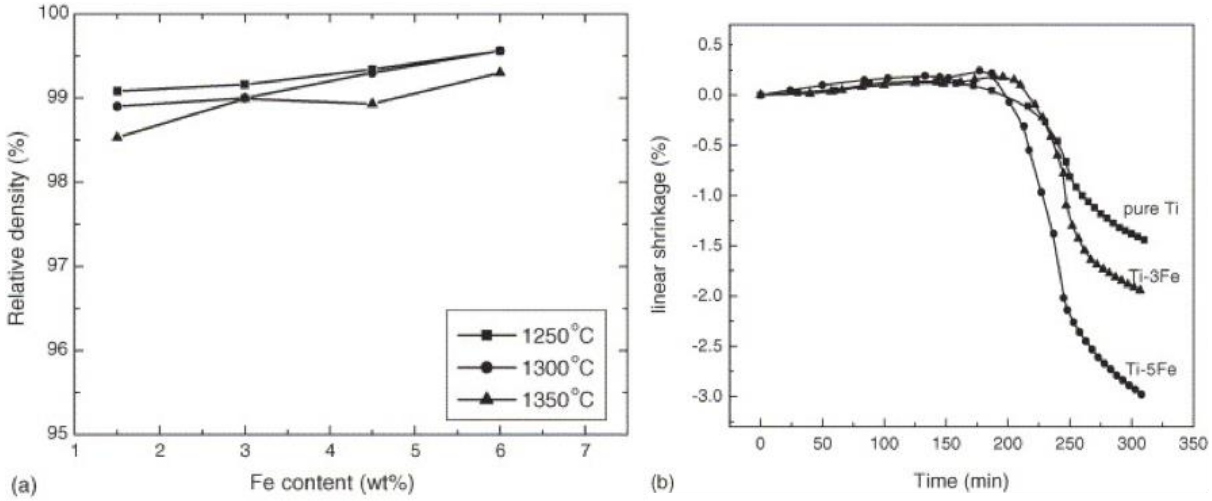

Fig. 2.8.6: a) relative density Fe content of Ti-Fe compacts at various temperatures sintered for 3h and b) Linear shrinkage of pure Ti, Ti-3Fe and Ti-5Fe with time [106].

Increased sinterability is usually ascribed to the fast diffusion of iron within titanium [108]. The exact mechanism of iron diffusion within titanium has been disputed, however, it is generally thought that iron may diffuse via an interstitial mechanism [126].

Hence, with no formation of Ti-Fe intermetallics, an enhanced densification rate and low cost, iron is a particularly promising alloying element for titanium alloys produced via a processing route conducted entirely in the solid state.

References

[1] W. Lowrie, Fundamentals of geophysics 2nd Ed, Cambridge: Cambridge University Press, 2011.

[2] G. Meinhold, "Rutile and its applications in earth sciences," *Earth science reviews,* vol. 102, pp. 1-28, 2010.

[3] T. S. Mackey, "Upgrading ilmenite into a high-grade synthetic rutile," *JOM,* vol. 46, no. 4, pp. 59-64, 1994.

[4] W. Zhang, Z. Zhu and C. Y. Cheng, "A literature review of titanium metallurgical processes," *Hydrometallurgy,* vol. 108, pp. 177-188, 2011.

[5] J. A. Kahn, "Non-Rutile Feedstocks for the Production of Titanium," *JOM,* vol. 7, pp. 33-38, 1984.

[6] N. S. H, "Ilmenite upgrading by the Murso process," in *Light Metals 1972*, New York, AIME-TMS Publications, 1972, pp. 261-274.

[7] E. A. Walpole and J. D. Winter, "The Austpac ERMS and EARS processes for the manufacture of high-grade synthetic rutile by the hydrochloride leaching of ilmenite.," *Proceedings of ChlorideMetallurgy,* pp. 401-415, 2002.

[8] R. G. Becher, "Improved process for the beneficiation of ores containing contaminating iron". Australia Patent 247110, 1963.

[9] Iluka Resouces , "Iluka's Synthetic Rutile Production," 2012. [Online]. Available: https://www.iluka.com/docs/mineral-sands-briefing-papers/iluka%27s-synthetic-rutile-production-june-2012. [Accessed 03 04 2017].

[10] R. G. Becher, R. G. Canning, B. A. Goodheart and S. Uusna, "A new process for upgrading ilmenitic mineral sands.," *Australian inst. Mining. Met. Proc,* vol. 214, pp. 21-44, 1965.

[11] C. Noubactep, "Metallic iron for environmental remediation: Learning from the Becher process," *Journal of Hazardous Materials,* vol. 168, no. 2-3, p. 1609–1612, 2009.

[12] J. B. Farrow , I. M. Ritchie and P. Mangano, "The reaction between reduced ilmenite and oxygen in ammonium chloride solutions.," *HydrometaUurgy,,* vol. 18, pp. 21-38., 1987.

[13] Iluka, "Synthetic Rutile," [Online]. Available: http://www.iluka.com/docs/3.3-operations/synthetic-rutile.pdf. [Accessed 25 09 2015].

[14] H. M. Flower, "Microstructual development in relation to hot working of titanium alloys," *Materials Science and Technology,* vol. 6, pp. 1082-1090, 1990.

[15] C. Leyens and M. Peters, Titanium and titanium alloys, Wiley-VCH, 2003.

[16] M. J. Donachie, Titanium: A technical guide, ASM International , 2000.

[17] G. Lutjering and J. C. Williams, Titanium, Berlin: Springer, 2007.

[18] R. Bhagat, The electrochemical formation of titanium alloys via the FFC cambridge process, Imperial College London: PhD Thesis, 2008.

[19] R. R. Boyer, J. C. Fanning and S. L. Nyakana, "Quick reference guide for beta titanium alloys in the 00s," *Journal of materials engineering and performance,* vol. 14, no. 6, pp. 799-811, 2005.

[20] I. Polmear, Light alloys:, Oxford: Butterworth-Heinemann, 2006 4th Ed.

[21] Z. Xiaohua and L. Daoxin, "Influence of surface coating on Ti811 alloy resistance to fretting fatigue at elevated temperatures," *Rare Metals,* vol. 28, no. 3, p. 266, 2009.

[22] R. Boyer, G. Welsch and E. W. Collings, Materials Properties Handbook: Titanium Alloys, ASM International, 1994.

[23] G. Welsch, R. Boyer and E. W. Collings, Materials Properties Handbook: Titanium Alloys, ASM International, 1993.

[24] S. R. Seagle, K. O. Yu and S. Giangiordano, "Considerations in processing titanium," *Materials Science and Engineering A,* vol. 263, no. 2, p. 237–242, 1999.

[25] P. G. Esteban, L. Bolzoni, E. M. Ruiz-Navas and E. Gorgo, "PM processing and characterisation of Ti-7Fe low cost titanium alloys," *Powder Metallurgy,* vol. 54, no. 3, pp. 242-251, 2011.

[26] P. J. Bania, "Beta titanium alloys and their role in the titanium industry," *JOM,* vol. 46, no. 7, pp. 16-19, 1994.

[27] R. R. Boyer, "An overview on the use of titanium in the aerospace industry," *Materials Science and Engineering A213,* pp. 103-114, 1996.

[28] R. Boyer, "Aerospace applications of beta titanium alloys," *JOM,* vol. 46, no. 7, 1994.

[29] S. Shekhar, R. Sarkar, S. K. Kar and A. Bhattacharjee, "Effect of solution treatment and aging on microstructure and tensile properties of high strength b titanium alloy, Ti–5Al–5V–5Mo–3Cr," *Materials and Design,* vol. In Press, 2014.

[30] H. W. Rosenburg, "Ti-15-3: A New Cold-Formable Sheet Titanium Alloy," *JOM,* vol. 35, no. 11, pp. 30-34, 1983.

[31] R. R. Boyer and R. D. Briggs, "The Use of beta Titanium Alloys in the Aerospace Industry," *Journal of Materials Engineering and Performance,* vol. 14, no. 6, pp. 681-685, 2005.

[32] Y. Kosaka, S. P. Fox, K. Faller and S. H. Reichman, "Properties and Processing of TIMETAL LCB," *Journal of Materials Engineering and Performance ,* vol. 14, no. 6, pp. 792-798, 2005.

[33] P. G. Allen, P. J. Bania, A. J. Hutt and Y. Combres, "A low cost beta alloy for automotive and other industrial applications.," in *Titanium '95 II*, Cambridge, The University Press, 1995, pp. 1680-1687.

[34] D. Kuroda, M. Niinomi, M. Morinaga, Y. Kato and T. Yashiro, "Design and mechanical properties of new beta type titanium alloys for implant materials," *Materials Science and Engineering A234,* pp. 244-249, 1998.

[35] W. F. Ho, C. P. Ju and J. H. Chern Lin, "Structure and properties of cast binary Ti–Mo alloys," *Biomaterials ,* vol. 20, no. 22, p. 2115–2122, 1999.

[36] E. Eisenbarth, D. Velten, M. Muller, R. Thull and J. Breme, "Biocompatibility of beta-stabilizing elements of titanium alloys," *Biomaterials,* vol. 24, pp. 5705-5713, 2004.

[37] A. Takemura, H. Ohyama, T. Abumiya and T. Nishimura, "Development and applications of beta and near beta titanium alloys," in *Beta titanium alloys in the 1990's*, TMS, 1993, pp. 15-26.

[38] O. M. Ivasishin, P. E. Markovsky, Y. V. Matviychuk, S. L. Semiatin, C. H. Ward and S. Fox, "A comparative study of the mechanical properties of high-strength beta(SYMBOL) titanium alloys," *Journal of Alloys and Compounds,* vol. 457, pp. 296-309, 2008.

[39] O. M. Ivasishin and R. V. Teliovich, "Potential of rapid heat treatment of titanium alloys and steels," *Materials Science and Engineering A,* vol. A263, pp. 142-154, 1999.

[40] J. D. Cotton, R. D. Briggs, R. R. Boyer, S. Tamirisakandala, P. Russo, N. Shchetnikov and J. C. Fanning, "State of the art in beta titanium alloys for airframe applications," *JOM,* vol. 67, no. 6, pp. 1281-1303, 2015.

[41] A. I. Nwobu, H. M. Flower and D. R. F. West, "The influence of micrsostructure on the tensile properties of high strength/high toughness Ti-V-Fe-Al alloys," in *Titanium '95*, Cambridge , The University Press, 1996, pp. 1243-1250.

[42] W. M. Parris and H. W. Rosenberg, "High strength titanium alloys". United States Patent 3,802,877, 1974.

[43] A. I. P. Nwobu, H. M. Flower and D. R. F. West, "Constitution of titanium rich alloys of Ti-V-Fe-Al system," *Materials science and technology,* vol. 7, pp. 391-398, 1991.

[44] C. Li, L. Zou, Y. Fu, W. Ye and S. Hui, "Effect of heat treatment on microstructure and property of a high strength/toughness Ti-8V-1.5Mo-2Fe-3Al alloy," *Materials science and engineering A,* vol. A616, pp. 207-213, 2014.

[45] Y. Yulan, W. Weiqi, L. Fengli, L. Weiqing and Z. Yongqiang, "The Effect of Aluminum Equivalent and Molybdenum Equivalent on the Mechanical Properties of High Strength and High Toughness Titanium Alloys," *Materials Science Forum,* Vols. 618-619, pp. 169-172, 2009.

[46] C. L. Li, X. J. Mi, W. J. Ye, S. X. Hui, Y. Yu and W. Q. Wang, "Effect of solution temperature on microstructures and tensile properties of high strength Ti–6Cr–5Mo–5V–4Al alloy," *Materials Science and Engineering A ,* vol. A578, pp. 103-109, 2013.

[47] W. Kroll, "The production of ductile titanium.," *The journal of the electrochemical society ,* vol. 78, no. 1, pp. 35-47, 1940.

[48] M. Jackson and K. Dring, "A review of advances in processing and metallurgy of titanium alloys," *Materials Science and Technology,* vol. 22, pp. 881-887, 2006.

[49] I. Barin, Thermochemical Data of Pure Substances, 3rd Edition ed., Weinheim, Germany: VCH, 1993.

[50] D. J. Fray, "Novel methods for the production of titanium," *International materials review,* vol. 53, no. 1, pp. 79-86, 2008.

[51] *EHK Technologies. Prepared for US Department of Energy and Oak Ridge National Laborator, Summary of emerging titanium cost reduction technologies,* Subcontract 4000023694, 2003.

[52] R. O. Suzuki , K. Teranuma and K. Ono, "Calciothermic Reduction of Titanium Oxide and in-situ Electroylsis in Molten CaCl2," *Metallurgical and materials transactions B,* vol. 34B, pp. 287-295, 2003.

[53] J. C. Withers, "Production of Titanium Powder by an Electrolytic Method and Compaction of the Powder," in *Titanium Powder Metallurgy – Science, Technology and Applications*, Butterworth-Heinemann, 2015, pp. 33-49.

[54] F. Fatollahi-Fard and P. C. Pistorius, "Production of Titanium Oxycarbide from Titania-Rich Mineral Sands," in *EPD Congress 2015*.

[55] I. Mellor and G. Doughty, "Novel and Emerging Routes for Titanium Powder Production-An Overview," *Key Engineering Materials,* vol. 704, pp. 271-281, 2016.

[56] O. Ivasishin and V. Moxson, "Low-cost titanium hydride powder metallurgy," in *Titanium Powder Metallurgy- Science, Technology and Applications*, Oxford, Butterworth-Heinemann, 2015, pp. 117-148.

[57] F. H. Froes, Titanium: Physical Metallurgy, Processing, and Applications, Materials Park, OH: ASM International , 2015.

[58] F. H. Froes, "Titanium Powder Metallurgy: Developments and opportunities in a sector poised for growth," *Powder Metallurgy Review,* vol. 2, no. 4, pp. 29-43, 2013.

[59] V. Duz, M. Moxson, A. Klevtsov and V. Sukhoplyuyev, "ADMA Process for Hydrogenated Titanium Powder Production," in *Materials Science & Technology 2014*, Pittsburgh, 2014.

[60] V. V. Joshi, C. Lavender, V. Moxon, V. Duz, E. Nyberg and K. Scott Weil, "Development of Ti-6Al-4V and Ti-1Al-8V-5Fe Alloys Using Low-Cost TiH2 powder feedstock," *Journal of Materials Engineering and Performance,* vol. 22, no. 4, pp. 995-1003, 2012.

[61] A. Devaraj, V. V. Joshi, A. Sirvastava, S. Manandhar, V. Moxson, V. A. Duz and C. Lavander, "A low-cost hierarchical nanostructured beta-titanium alloy with high strength," *Nature communcations,* vol. 7, pp. 1-8, 2016.

[62] V. S. Moxson, V. A. Duz, A. G. Klevstov, V. D. Sukhoplyuyev, M. D. Sopka, Y. V. Shuvalov and M. Matviychuk, "Method of Manufacturing Pure Titanium Hydride Powder and Alloyed Titanium Hydride Powders By Combined Hydrogen-Magnesium Reduction of Metal Halides". US Patent US 20130315773 A1, 28 November 2013.

[63] J. D. Rivard, C. A. Blue, D. C. Harper, J. O. Kiggans, P. A. Menchhofer, J. R. Mayotte, L. Jacobsen and D. Kogut, "The thermomechanical processing of titanium and Ti-6Al-4V thin gage sheet and plate," *JOM,* pp. 58-61, 2005.

[64] J. C. Withers, F. Cardarelli, J. Laughlin and R. O. Loufty, "Recent Improvements for Electrowinning Titanium Metal from Composite Anodes," in *International round table on titanium production in molten salts*, DRL German Aerospace Center, Cologne, 2008.

[65] F. Fatollahi-Fard and P. C. Pistorius, "Impurity Removal from Titanium Oxycarbide," in *TMS 2017 146th Annual Meeting & Exhibition Supplemental Proceedings*, San Diego, 2017.

[66] D. Hu and G. Z. Chen, "Advanced Extractive Electrometallurgy," in *Springer handbook of Electrochemical Energy*, Berlin, Springer, 2017, pp. 801-834.

[67] C. Doblin, D. Cantin and S. Gulizia, "Processing TiRO™ powder for strip production and other powder metallurgy applications (Presentation)," TiDA International Titanium Powder Processing Conference, Hamilton, New Zealand, 2013.

[68] G. Z. Chen, D. J. Fray and T. W. Farthing, "Direct electrochemical reduction of titanium dioxide to titanium in molten calcium chloride," *Nature,* vol. 407, pp. 361-364, 2000.

[69] G. Chen and D. J. Fray, "A morphological study of the FFC chromium," *Trans. Inst. Min. Metall. C,* vol. 115, pp. 49-54, 2006.

[70] R. Barnett, K. T. Kilby and D. J. Fray, "Reduction of Tantalum Pentoxide Using Graphite and Tin-Oxide-Based Anodes via the FFC-Cambridge Process," *Metalurgical and materials transactions B,* vol. 40B, pp. 150-157, 2009.

[71] D. J. Fray , "Anodic and Cathodic reactions in molten calcium chloride," *Canadian Metallurgical Quarterly,* vol. 41, pp. 433- 429, 2002.

[72] R. Bhagat, M. Jackson, D. Inman and R. Dashwood, "The production of Ti-Mo alloys from mixed oxide precurosrs via the FFC Cambridge process," *Journal of The Electrochemical Society,* vol. 155, pp. E63-E69, 2008.

[73] R. Bhagat, M. Jackson, D. Inman and R. Dashwood, "Production of Ti-W alloys from mixed oxide precursors via the FFC Cambridge process," *Journal of The Electrochemical Society,* vol. 156, pp. E1-E7, 2009.

[74] M. Ellis and G. Doughty , "Solid State Manufacture of High Entropy Alloys-Preliminary Studies," in *MRS Advances*, doi:10.1557/adv.2017.116, 2017.

[75] S. Jiao and D. J. Fray, "Development of an inert anode for electrowinning in calcium chloride- calcium oxide melts," *Metallurgical and Materials transactions B,* vol. 41B, pp. 74-79, 2010.

[76] C. Schwandt, J. A. Hamilton, D. J. Fray and I. A. Crawford, "The production of oxygen and metal from lunar regolith," *Planetary and Space Science,* vol. 74, pp. 49-56, 2012.

[77] C. Schwandt and D. J. Fray, "Determination of the kinetic pathway in the electrochemical reduction of titanium dioxide in molten calcium chloride," *Electrochimica Acta,* vol. 51, no. 1, pp. 66-76, 2005.

[78] D. L. Alexander, C. Schwandt and D. J. Fray, "Microstructural kinetics of phase transformations during electrochemical reduction of titanium dioxide in molten calcium chloride," *Acta Materialia ,* vol. 54, pp. 2933-2944, 2006.

[79] D. T. L. Alexander , C. Schwandt and D. J. Fray, "The electro-deoxidation of dense titanium dioxide precursors in molten calcium chloride giving a new reaction pathway.," *Electrochimica Acta,* vol. 56, pp. 3826-3295, 2011.

[80] B. K. Jackson, M. Jackson, D. Dye, D. Inman and R. J. Dashwood, "Production of NiTi via the FFC Cambridge process," *Journal of the electrochemical society,* vol. 155, pp. E171-E177, 2008.

[81] I. Mellor, L. Grainger, K. Rao, J. Deane, M. Conti, G. Doughty and D. Vaughan, "Titanium powder production via the Metalysis process," in *Titanium powder metallurgy*, Oxford, Butterworth-Heinemann, 2015, pp. 51-67.

[82] R. Bhagat, D. Dye, S. L. Raghunathan, R. J. Talling, D. Inman, B. K. Jackson, K. K. Rao and R. J. Dashwood, "In-Situ Synchrotron Diffraction of the Electrochemical Reduction Pathway of TiO2," *Acta Materialia,* vol. 58, no. 15, pp. 5057-5062, 2010.

[83] C. Schwandt, D. T. L. Alexander and D. J. Fray, "The electro-deoxidation of porous titanium dioxide precursors in molten calcium chloride under cathodic potential control," *Electrochimica Acta,* vol. 54 , p. 3819–3829, 2009.

[84] F. H. Froes, "A historical perspective of titanium powder metallurgy," in *Titanium Powder Metallurgy*, Oxford, Butterworth-Heinemann, 2015, pp. 2-19.

[85] Z. A. Munir, D. V. Quach and M. Ohyanagi, "Electric Current Activation of Sintering: A Review of the Pulsed Electric Current Sintering Process," *Journal of the american ceramic society,* vol. 94, pp. 1-19, 2011.

[86] N. S. Weston, F. Derguti, A. Tudball and M. Jackson, "Spark plasma sintering of Commerical and Development Titanium alloy powders," *Journal of materials science,* vol. 50, no. 14, pp. 4860-4878, 2015.

[87] B. Thomas, F. Derguti and M. Jackson, "Thomas, B., Derguti, F. and Jackson, M. (2016) Continuous Extrusion of Titanium Particulates, in Proceedings of the 13th World Conference on Titanium (eds V. Venkatesh, A. L. Pilchak, J. E. Allison, S. Ankem, R. Boyer, J. Christodoulou, H. L. Fraser, M. A," in *Proceedings of the 13th World Conference on Titanium*, San Diego, 2015.

[88] B. Dutta and F. H. Froes, "The Additive Manufacturing (AM) of titanium alloys," *Powder Metal Report,* vol. 72, no. 2, pp. 96-106, 2017.

[89] F. V. Lenel, Powder Metallurgy - Principles and applications, New Jersey : Metal Powder Industries Federation, 1980.

[90] I.-K. Oh, N. Nomura, N. Masahashi and S. Hanada, "Mechanical properties of porous titanium compacts prepared by powder sintering," *Scripta Materialia,* vol. 49, no. 12, pp. 1197-1202, 2003.

[91] R. M. German, Sintering Theory and Practise, New York: John Wiley & Sons, 1996.

[92] L. Bolzoni, E. M. Ruiz-Navas, E. Neubauer and E. Gordo, "Inductive hot-pressing of titanium and titanium alloys," *Materials Chemistry and Physics,* vol. 131, pp. 672-679, 2012.

[93] Y. F. Yang, H. Imai, K. Kondoh and M. Qian, "Comparison of spark plasma sintering of elemental and master alloy powder mixes and prealloyed Ti-6Al-4V powder," *International journal of powder metallurgy,* vol. 50, no. 1, pp. 41-47, 2014.

[94] R. Chuadhari and R. Bauri, "Microstructure and mechanical properties of titanium processed by spark plasma sintering (SPS)," *Metallography, microstructure and analysis,* vol. 3, pp. 30-35, 2014.

[95] Z. A. Munir, U. Anselmi-Tamburini and M. Ohyanagi , "The effect of electric field and pressure on the synthetsis and consolidation of materials: A review of the spark plasma sintering method," *Journal of Materials Science,* vol. 41, no. 3, pp. 763-777, 2006.

[96] Artwork by Nick Weston.

[97] Y. Liu, S. Xu, X. Wang, K. Li, B. Liu, H. Wu and H. Tang, "Ultra-High Strength and Ductile Lamellar-Structured Powder Metallurgy Binary Ti-Ta Alloys," *JOM,* vol. 68, no. 3, pp. 899-907, JOM, Vol. 68, No. 3, 2016.

[98] N. Weston and M. Jackson, "FAST-forge − A new cost-effective hybrid processing route for consolidating titanium powder into near net shape forged components," *Journal of Materials Processing Technology ,* vol. 243, pp. 335-346, 2017.

[99] B. Thomas , F. Derguti and M. Jackson, "Continuous extrusion of a commercially pure titanium powder via the Conform process," *Materials Science and Technology,* pp. 1-5, 2016.

[100] S. Katsas, R. Dashwood, G. Todd, M. Jackson and R. Grimes, "Characterisation of Conform™ and conventionally extruded Al–4Mg–1Zr. Effect of extrusion route on superplasticity," *Journal of Materials Science,* vol. 45, no. 15, p. 4188–4195, 2010.

[101] C. A. Poblano-Salas, "High temperature properties of Cu–Cr–Zr alloys processed by conventional inverse extrusion of atomised powders and comparison with Conform consolidated powders," *Powder Metallurgy,* vol. 52, no. 2, pp. 124-134, 2009.

[102] J. A. Pardoe, "CONFORM continuous extrusion process – its contribution to energy conservation," *Metals Technology,* vol. 11, no. 1, pp. 358-365, 1984.

[103] M. Duchek, T. Kubina, J. Hodek and J. Dlouhy, "Development of the production of the ultrafine-grained titanium with the conform equipment," *Materials and Technology,* vol. 47, no. 4, pp. 515-518, 2013.

[104] R. S. Wilson, M. Yousuff, N. A. Stone, D. J. B. Ritchie, G. M. D. Cantin, M. A. Gibson and I. C. Thomas, "Extrusion of high temperature formable non-ferrous metals". USA Patent US Patent 2014/0000332 A1, 2 Jan 2014.

[105] J. Lu, G. Peng and Z. Yongqing, "Recent development of effect mechanism of alloying elements in titanium alloy design," *Rare metal materials and engineering,* vol. 43, no. 4, pp. 775-779, 2014.

[106] Y. Liu, L. F. Chen, H. P. Tang, C. T. Liu, B. Liu and B. Y. Huang, "Design of powder metallurgy titanium alloys and composites," *Materials Science and Engineering: A,* vol. 418, no. 1-2, pp. 25-35, 2006.

[107] Y. Liu, K. Li, H. Wu, M. Song, W. Wang, N. Li and H. Tang, "Synthesis of Ti–Ta alloys with dual structure by incomplete diffusion between elemental powders," *Journal of the mechanical behavior of biomedical materials,* vol. 51, pp. 302-312, 2015.

[108] W. Wei, Y. Liu, K. Zhou and B. Huang, "Effect of Fe addition on sintering behaviour of titanium powder," *Powder Metallurgy,* vol. 46, no. 3, pp. 246-250, 2003.

[109] A. I. P. Nwobu, H. M. Flower and D. R. F. West, "Structure/Property Relationships in near beta Ti-V-Fe-Al Based alloys," in *Titanium '92*, Warrendale, TMS, 1993, pp. 531-537.

[110] Thermo-Calc software, *SSOL4 database, V4.9f.*

[111] D. F. Neal, "Alloy Development," in *Titanium '95*, Cambridge, The University Press, 1995, pp. 2195-2204.

[112] H. Izui and G. Kikuchi, "Sintering Performance and Mechanical Properties of titanium compacts prepared by spark plasma sintering," *Materials Science Forum ,* Vols. 706-709, pp. 217-221, 2012.

[113] Z. Zhu, C. Haishan and H. Ruixin, "Near beta Ti-5Mo-5V-2Cr-3Al alloy," in *Titanium '95 Volume III*, Cambridge, TMS, 1995, pp. 2325-2330.

[114] A. Takemura, H. Ohyama, T. Abumiya and T. Nishimura, "Development and applications of beta and near beta titanium alloys," in *Beta alloys in the 1990's*, TMS, 1993, pp. 15-26.

[115] R. W. Schutz and J. S. Grauman, "Fundamental Corrosion Characterization of High Strength Titanium Alloys," in *Industrial Applications of Titanium and Zirconium*, Philadelphia , ASTM, 1986, pp. 130-143.

[116] J. S. Grauman, "Effct of aircraft hydraulic fluid on Timetal 21S," in *Beta Titanium Alloys in the 1990's*, Pennsylvania, TMS, 1993, pp. 127-135.

[117] Y. Li, C. Yang, H. Zhao, S. Qu, X. Li and Y. Li, "New Developments of Ti-Based Alloys for Biomedical Applications," *Materials,* vol. 7, no. Yuhua Li, Chao Yang *, Haidong Zhao, Shengguan Qu, Xiaoqiang Li and Yuanyuan Li, pp. 1709-1800, 2014.

[118] M. Niinomi, "Recent research and development in titanium alloys for biomedical applications and healthcare goods," *Science and Technology of Advanced Materials,* vol. 4, pp. 445-454, 2003.

[119] W. D. Zhang, Y. Liu, H. Wu, M. Song, T. Y. Zhang, X. D. Lan and T. H. Yao, "Elastic modulus of phases in Ti–Mo alloys," *Materials Characterization ,* vol. 106, pp. 302-307, 2015.

[120] Y. Liu, W. F. Wei, K. Zhou, L. F. Chen and H. P. Tang, "Microstructure and mechanical behaviour of PM Ti-Mo alloy," *Journal of Central South University of Technology,* vol. 10, no. 2, pp. 81-86, 2003.

[121] L. Bolzoni, E. Herraiz, E. M. Ruiz-Navas and E. Gordo, "Study of the properties of low-cost powder metallurgy titanium alloys by 430 stainless steel addition," *Materials and Design,* vol. 60, pp. 628-636, 2014.

[122] Thermo-Calc software, *TTTI3 database, V3.1.*

[123] R. I. Jaffee, "The physical metallurgy of titanium alloys," *Progress in Metal Physics,* vol. 7, pp. 65-163, 1958.

[124] B. Y. Chen, K. S. Kwang and K. L. Ng, "Effect of cooling process on the alpha phase formation and mechanical properties of sintered Ti–Fe alloys," *Materials Science and Engineering A,* vol. 528, pp. 4556-4563, 2011.

[125] L. Bolzoni, E. M. Ruiz-Navas and E. Gordo, "Understanding the properties of low-cost iron-containing powder metallurgy titanium alloys," *Materials and Design,* vol. 110, pp. 317-323, 2016.

[126] R. A. Perez, H. Nakajima and F. Dyment, *Materials Transactions,* vol. 44, no. 1, pp. 2-13, 2003.

Chapter 3:

Experimental Methods

3.0 Experimental Methods

Experimental methods utilised throughout this work are detailed within this Chapter.

3.1 FFC Process Reductions at R&D Scale

Reduction of synthetic rutile samples (150-212 µm) supplied by Iluka Resources were achieved at both R&D scale, with quantities of approx. 20 g and development scale, approx. 5 kg. Partial reductions were completed at an R&D scale with powder for consolidation of the baseline SR derived alloy obtained from developmental scale reductions.

The R&D cells consist of a stainless steel retort and lid. Cathode and anode rods are inserted into the lid in addition to a thermocouple. 20 g of each synthetic rutile sample was placed into a steel basket, which was lined with a stainless steel mesh. A connecting rod was attached to the basket, which screwed into the cathode rod. A carbon anode was screwed into the anode rods. 1.6 kg of dried $CaCl_2$ salt contained in a ceramic crucible was placed in the retort before the lid was attached and the retort sealed. Exhaust and water pipes were attached to the lid to allow removal of heat and gases produced. Finally, an argon line is attached to ensure the reaction occurs under an inert atmosphere. Figure 3.1 displays the experimental set up utilised for R&D experiments.

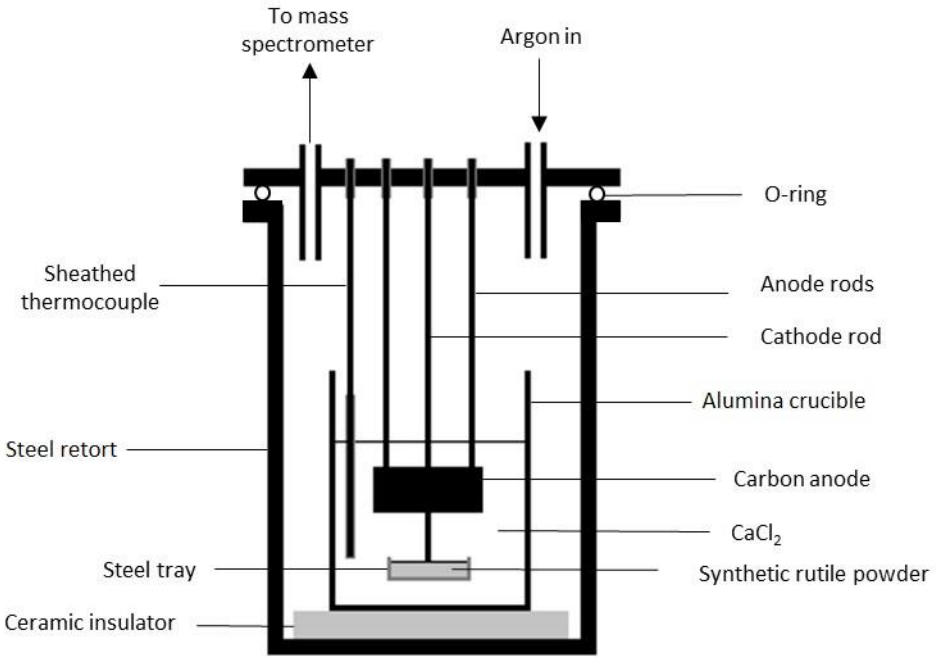

Fig. 3.1.1: Experimental set up of an R&D reduction cell.

After the cell had been sealed, the temperature was ramped to above 900°C. A salt sample was taken by dipping a rod into the molten salt via a viewing port. The CaO content of the salt was then determined using an acid-base titration, facilitated by an autotitrator (Mettler Toledo autotitrator T50). Cathode and anodes were then lowered into the molten calcium chloride electrolyte. The depth of the anode and cathode into the salt can be controlled by measuring the protrusion of the rods in the lid and was kept constant throughout the experiments. Experiments were run at constant current, with an initial current ramp in place to avoid excessive voltages and chlorine formation. Each experiment was timed from the end of the ramp period. Off gases produced by the reaction (CO and CO_2) were monitored by mass spectroscopy. Full reductions were ground and washed until the water ran clear to remove any remaining salt. After washing the samples were dried, sieved and weighed.

Partial reductions were interrupted before completion by terminating the applied current and lifting the cathode tray out from the salt into the cooler upper section of the retort. After electrolysis, the partially reduced samples were washed in water and lightly ground before being soaked in hydrochloric acid (1M). Samples were again washed with water and dried in air at around 80°C. Due to the powdered nature of the product and mechanical fragility of some phases, great care was taken to minimise material loss.

Once clean and dry, samples were analysed using X-ray diffraction techniques outlined below, followed by microstructural studies, with the exception of the 2 h partial, in which microstructure studies took place from a repeated non ground sample due to the mechanical fragility of the Ca_2TiO_4 needles. Each of the time intervals were completed at least twice.

3.2 Calcination of Synthetic Rutile

Synthetic rutile was calcined at a temperature of 1000°C for 2 h with a ramp rate of 3°C/minute in static box furnaces.

3.2.1 Calcination of Doped Samples

Al doped SR samples were mixed in a Turbula for 4 h before being calcined for 4 h at a temperature of 1300°C with a ramp rate of 3°C/min in a tube furnace (see section 5.3.1 for discussion of the calcination temperature). Note, a Turbula is a mechanical mixing machine used for powder blending or mixing, shown in Fig. 3.2.1.

Fig. 3.2.1: Photograph of a Turbula machine. Samples are inserted into closed containers and placed inside the vessel which is filled with soft padding.

As some oxides of Mo are known to sublime, none of the Mo samples were calcined after mixing. Instead, MoO_2 was mixed with pre-heat treated SR (calcined SR). For the pseudo tertiary SR alloys, SR and Al_2O_3 were mixed for 4 h before heat treatment of 1350°C for 4 h in a tube furnace at a ramp rate of 3°C/min took place. After this calcination, MoO_2 was mixed in with the powder using a Turbula for a further 4 h. To provide clarity on the various heat treatments the powders underwent prior to reduction, Table 3.1 lists the powders within this thesis and the heat treatment conducted prior to reduction. R&D scale typically uses 20 g of titanium oxide while developmental scale reduces 5 kg.

Table 3.1: Heat treatment and reduction scale of all samples within this thesis.

Chapter(s)	Sample(s)	Heat treatment/Preparation	Reduction scale
4	SR partials	-	R&D
4	SR partial- full reduction	-	R&D
4,5,6	SRA 1	1000°C 2h	Development
5	Pseudo binary SR-Al alloys	SR + Al 1350°C 4h	R&D
5	Pseudo binary SR-Mo alloys	SR 1000°C then mixed with MoO_2	R&D
5	Pseudo ternary SR-Al-Mo alloys	SR + Al 1350°C 4h then mixed with MoO_2	R&D
6	Spring Alloys	SR + Al 1350°C 4h then mixed with MoO_2/Fe_2O_3	R&D

3.3 Morphology Studies

Following mounting in conductive Bakelite, samples were subjected to standard metallographic preparation techniques. Grinding consisted of intervals of 320, 800 and 1200 silicon grit papers for a minute each. After the grinding stage, an MD-Largo polishing plate was used with 9 µm diamond paste for 8 minutes. Following this, an MD-Dac polishing plate was used with 3 µm diamond paste for 15 minutes. The final stage of polishing utilised a MD-Chem polishing plate with a 1:1 solution of Struers OPS-solution and water for 10 minutes, and a further 5 minutes with only water. Following polishing, samples were dried using compressed air.

Scanning electron microscopy images were taken using a JEOL-JSM649OLV using an acceleration voltage of 20 keV.

3.4 Characterisation Techniques

3.4.1 X-ray Diffraction Analysis

Powder samples were ground before X-ray diffraction analysis using a Bruker D2 phaser and Cu-Kα radiation. Samples were scanned throughout the range of 10-80°. Phase analysis was completed using the ICDD (International Centre for Diffraction Data) database and ICDD PDF-4+/SIeve+ software, with the following PDF (Powder Diffraction File) cards being utilized: Ti_2O_3 (01-074-0324), Ti_3O_5 (04-008-8183), $CaTiO_3$ (04-012-0563), TiO (04-004-9041), $CaTi_2O_4$(04-010-0703), Ti_2O (04-005-4357), α-Ti (04-008-4973), Al_2O_3 (04-006-9730), Al_2TiO_5 (00-026-0040).

3.4.2 Powder Characterisation Techniques

Particle size distribution (PSD) measurements were attained using a Malvern Mastersizer 2000. Apparent bulk density tests were conducted on the feedstock by filling a 100 cm^3 graduated cylinder to the brim, measuring the mass and calculating the density.

3.4.3 Chemical Analysis

Oxygen content was measured using an Eltra ON-900. Error associated with this method is known to be +/- 80 ppm for samples with an oxygen concentration of less than 1960 ppm. For samples over 1960 ppm oxygen, a sample of 2912 ppm oxygen was tested ten times to determine the error which was found to be +/- 240 ppm, shown in the Appendix. Further, as the machine is calibrated for low levels of oxygen, the larger oxygen contents of the partial reductions will have a significantly larger error associated with them. X-EDS (X-ray Energy Dispersive Spectroscopy) was performed using INCA software on the aforementioned scanning electron microscope. Inductively Coupled Plasma-Mass spectrometry (ICP-MS) analysis was performed by Metalysis using a Thermo X series 2. Carbon analysis was conducted using an Eltra CS-800 with the error known to be ± 8 ppm.

3.4.3.1 XRF Spectroscopy

Initial X-ray fluorescence (XRF) spectroscopy (Chapter 4) was conducted via an external company using a Phillips PW 2404. Later analysis (Chapters 5 &6) was completed at the university using a Panalytical Zetium, fitted with a Rh X-ray tube. Powder samples were measured in a He atmosphere and bulk measurements were made under vacuum. Measurements were taken from a solid sample of 10 mm diameter. Each reported value was measured 3 times and an average value taken.

3.5 Consolidation via the Field Assisted Sintering Technique

Consolidation was achieved via a field assisted sintering technique using a FCT Systeme GmbH spark plasma sintering furnace type HP D 25 (Fig 3.5.1). 20 mm pucks were created using 17 g of powder placed into a 20 mm diameter graphite ring mould with two pistons, lined with graphite foil. A carbon jacket was added to prevent heat loss and maximise current density [1]. Once loaded into the FAST machine, the sample underwent a predetermined sintering cycle, involving a ramp rate of 100°C/min, an applied force of 15 kN (48 MPa) and a dwell time of 30 minutes at 1200 °C. Temperature was controlled via a pyrometer positioned

directly above the mould set up. Any remaining graphite paper was removed by grit blasting to yield a 10mm x 20 mm consolidated synthetic rutile pellet.

Fig. 3.5.1: Photograph of FCT Systeme GmbH field assisted sintering machine

A small-scale testing technique was developed and is discussed in detailed (Section 5.1), involving the production of 11 mm moulds, shown within the FAST machine in Fig. 3.5.2. 4.2 g of SR derived titanium powder was placed into these 11 mm moulds lined with a graphite foil to produce solid pellets of approximately 11 mm diameter by 10 mm height. Thermocouple control was used as the small size of the set up did not allow for pyrometric control. A small 1.1 mm diameter hole drilled 1.3 mm deep into the mould wall allowed for K type thermocouple insertion. Again, a predetermined sintering cycle was utilised, consisting of a ramp rate 100 °C/min an applied force of 5 kN (53 MPa) and a dwell time of 30 minutes. Any remaining carbon foil was removed via grit blasting.

Fig. 3.5.2: Photograph of 11 mm FAST moulds with attached K-type thermocouple attached within the FAST machine.

3.6 Porosity Measurements

Porosity was determined using image software, Image J. An average of at least 3 images was taken to determine the porosity of consolidated alloys.

3.7 Physical Property Testing

3.7.1 Beta Transus Testing

9 mm radius samples of material were painted with a glass lubricant to minimise oxidation before being placed in a box furnace and left for 1 h to ensure homogenisation before quenching took place in a beaker of room temperature water. Samples were then mounted and the percentage of beta phase was determined by analysing SEM images of the microstructure using analysis software Image J [2].

3.7.2 Hardness Testing

Hardness values were obtained using a CV-100KS Vickers hardness tester which took 3 measurements per sample.

3.8 Compression Testing

Compression testing was undertaken using the ThermoMechanical Compression machine (TMC). All tests were undertaken at room temperature with a strain rate of 0.1 s^{-1}

3.9 Modelling Software

Production of the predictive model using multiple regression analysis was possible using the statistical software, Minitab [3]. Prediction of beta transus values and drawing of phase diagrams was done using the thermodynamic phase diagram software Thermo-Calc using database TTTI V3.1 [4]. Database SSSOL4 was used to draw the Ti-Al phase diagram found in chapter 2.

References

[1] N. S. Weston, F. Derguti, A. Tudball and M. Jackson, "Spark plasma sintering of Commerical and Development Titanium alloy powders," *Journal of materials science,* vol. 50, no. 14, pp. 4860-4878, 2015.

[2] *W. S. Rasband: ImageJ, U.S National Institutes of Health, Bethesda, Maryland, USA, 435 http://imagej.nih.gov/ij/, 1997..*

[3] Minitab, "Minitab V17," All such material remains the exclusive property and copyright of Minitab Inc. All rights reserved.

[4] ThermoCalc. Software, *TTT Titanium alloys database.*

Chapter 4:

Characterisation of Synthetic Rutile Derived Titanium Alloys

Work from this chapter formed the basis of the following publications:

L.L. Benson, I. Mellor and M. Jackson. "Direct reduction of synthetic rutile using the FFC process to produce low-cost novel titanium alloys" Journal of Materials Science. vol 51, pp 4250–4261, 2016.

L.L. Benson, I Mellor and M Jackson. "Solid State Extraction and Consolidation of Titanium Alloys Direct from Synthetic Rutile" in Proceedings of the 13th World Conference on Titanium, San Diego, 2016.

Work from this chapter contributed towards the following publication:

L. Benson Marshal, L.L. Benson, N.S. Weston, S.E. Repper, M. Jackson and I. Mellor. "Development of Titanium Alloy Powders Produced Via the Metalysis Process" in proceedings of the European Powder Metallurgy Conference, Milan, 2018.

4.0 Characterisation of Synthetic Rutile Derived Titanium Alloys

To begin alloy development, a full understanding of the physical and chemical properties of the starting material feedstock must be obtained. To achieve this, a wide range of experimental characterisation techniques were employed such as X-ray diffraction (XRD), spectroscopy, particle size distribution measurements (PSD), X-ray fluorescence (XRF), spectroscopy, carbon analysis, bulk density measurements and scanning electron microscopy (SEM). It is imperative to note that despite the in-depth analysis given here, other samples of synthetic rutile (SR) may differ in chemical composition as well as the morphology and PSD. This variation is due to differences in the morphology, PSD or chemical composition of the starting ilmenite feedstock, as well as differences in the specific method used to extract the synthetic rutile (Becher, Laporte etc). However, the ability to tailor the synthetic rutile feedstock by changing the starting ilmenite or alter the extraction method may prove to be a valuable tool in designing an alloy – enabling upstream alterations may minimise the need for downstream master alloy additions.

In addition to the characterisation of the synthetic rutile feedstock, the properties of the synthetic rutile derived titanium alloy were also analysed. Consolidation of this initial alloy allowed mechanical data to be obtained, establishing baseline properties for synthetic rutile derived titanium alloys.

Finally, a full understanding and characterisation of synthetic rutile derived titanium alloys produced via the FFC process would not be complete without a thorough understanding of the reaction mechanism throughout the reduction procedure. Hence, partial reductions and their subsequent analysis have been completed.

This chapter is aimed at fully understanding the reduction behaviour of synthetic rutile as well as characterising its baseline properties. From physical and chemical properties of the synthetic rutile feedstock, to the mechanical properties obtained from the consolidated synthetic rutile derived titanium alloy. The synthetic rutile characterised and utilised within this thesis was produced from ilmenite sourced from multiple locations with Western Australia and produced via the Becher process by Iluka Resources North Capel Operation, Western Australia. The feedstock fraction size analysed and reduced was 150-212 µm. which had been sieved from a bulk sample at Iluka Resources.

4.1 Synthetic Rutile Feedstock Characterisation

4.1.1 Synthetic Rutile X-Ray Diffraction

Synthetic rutile produces a complicated X-ray diffraction spectrum, shown in Figure 4.1.1. Despite its nomenclature, SR contains only a small quantity of the rutile phase, (TiO_2). Dominant phases present are reduced rutile phases ($TiO_{(2-x)}$) and pseudobrookite (M_3O_5). Minor quantities of remnant metallic iron are also present. The quantity of these titanium phases vary with the degree of rutile reduction in the kiln and whether sulphur was injected into the kiln to control the Mn content of the SR [1] [2]. Further, the presence of some trace elements such as Al, Mn, Fe and Mg will actively stabilise the pseudobrookite phase [3].

Reduced rutile phases, produced during the Becher process have compositions in the range $TiO_{1.9}$-$TiO_{2.0}$ [4] cannot be determined via XRD analysis, as there are no available structural models for these phases, required to fit the XRD patterns and hence estimate the phase composition. Models are only available for the Magneli reduced rutile phases with compositions in the range $TiO_{1.75}$ (Ti_4O_7) to $TiO_{1.89}$ (Ti_9O_{17}).

However, previous sponsored research developed a method to estimate the reduced rutile compositions based on the adjacent XRD peak separation distance (Δ2θ - CuKα) between 27.8° and 30.0° [3]. For the synthetic rutile used in this work, the reduced rutile phase composition was estimated to be around $TiO_{1.933}$ [5].

Only small quantities of rutile are present within SR, as rutile has mostly been reduced to the reduced rutile phases, with many of the rutile peaks overlapping with the reduced rutile peaks. A small quantity of remnant metallic iron from the Becher process is also observed in the XRD pattern. Presence of iron oxides are known, as total Fe measured via XRF is larger than the quantity of metallic Fe present, measured via titration using a copper sulphate method at Iluka Resources. The iron oxide present within SR will be within the M_3O_5 phase ($FeTi_2O_5$-Ti_2O_5 solid solution) [5].

The M_3O_5 phase, present within the synthetic rutile, consists of a solid solution containing Fe, Mn, Mg, Cr, Al and Ti oxides [3] in a highly distorted octahedral M_3O_5 structure [6]. Ferric pseudobrookite (Fe_2TiO_5) crystallographic data was used to determine the M_3O_5 peaks within the synthetic rutile XRD spectrum, see Appendix 3. Synthetic rutile produced in the Becher process normally contains between 12 and 18 wt% of Ti^{3+} which is responsible for the black colouration of the synthetic rutile. Ti^{3+} is found in both the reduced rutile and M_3O_5 phases

[5]. However this phase does not appear in the XRD spectrum as it is present within the other phases such as pseudobrookite ($Ti_2O_3.MO_2$) and the reduced rutile phases.

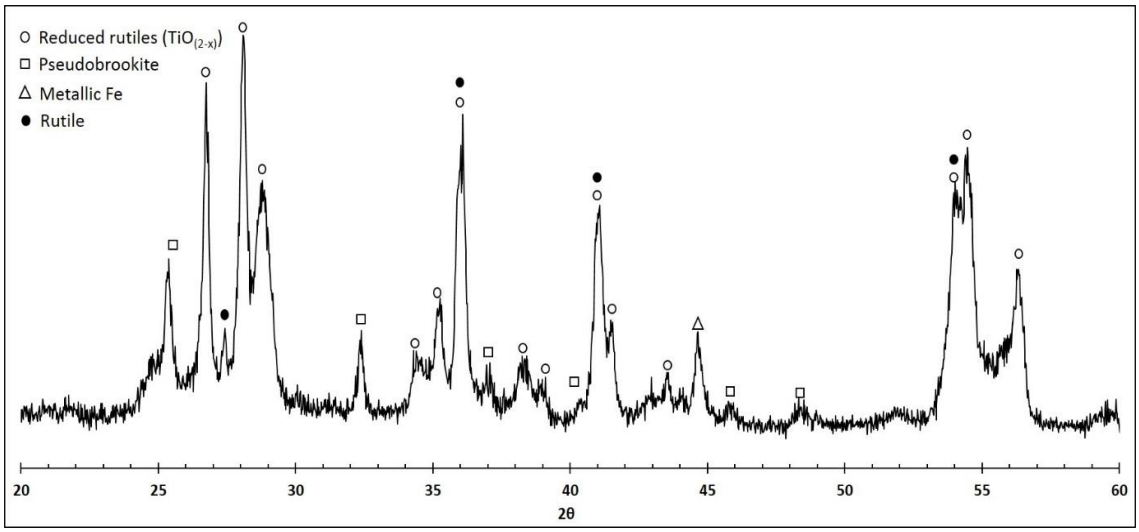

Fig. 4.1.1: XRD pattern of synthetic rutile produced via the Becher process containing rutile, TiO_2 (●), reduced rutiles, $TiO_{(1.933)}$ (○), pseudobrookite, M_3O_5 (□), and metallic Fe, (Δ).

In almost all cases, the black synthetic rutile feedstock goes through a heat treatment process, known as calcination, prior to extraction via the Metalysis FFC process. Within this work, the heat treatment of the baseline SR samples consisted of heating at 1000°C for 2 h. This process removes most of the carbon present with the SR by oxidising it to CO_2. Further, both the reduced rutile phases and pseudobrookite phases are oxidised to TiO_2 (rutile phase structure), producing a sand coloured powder.

An XRD spectrum was recorded of this powder, known as calcined rutile (CR) and is shown below in Fig. 4.1.2. As expected, the XRD spectrum now contains predominantly rutile (TiO_2), with a small quantity of ferric pseudobrookite (Fe_2TiO_5).

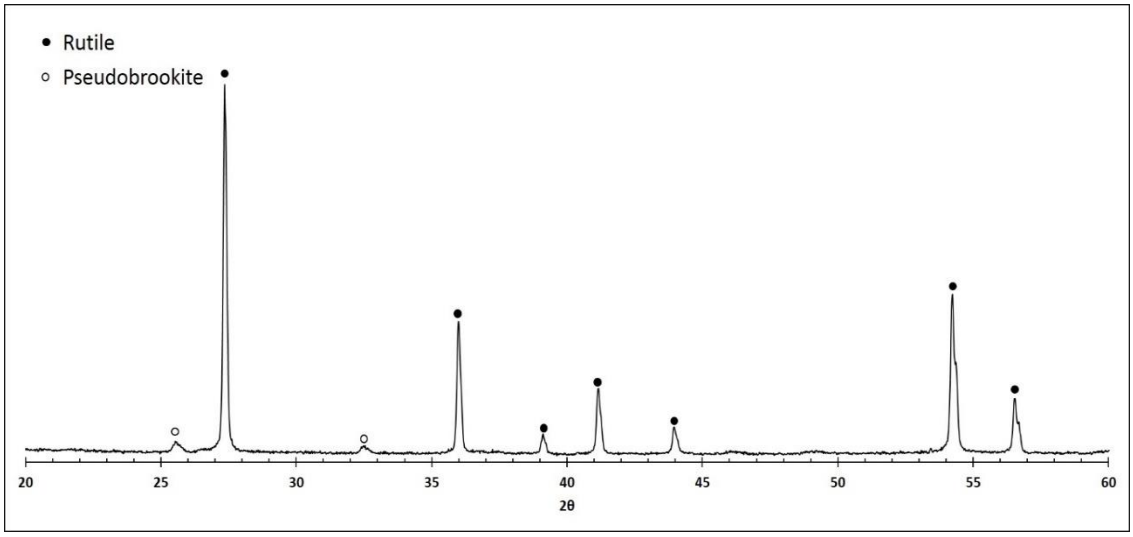

Fig. 4.1.2: XRD spectrum of calcined rutile (synthetic rutile heated at 1000 °C for 2 h containing rutile, TiO_2 (●) and small amounts of pseudobrookite, M_3O_5 (○)

4.1.2 Elemental Analysis

A full elemental analysis was undertaken to gain insight into the chemical composition of the synthetic rutile feedstock, with Table 4.1 listing the analysis via XRF spectroscopy. Note Nb was not included in the XRF analysis but measured using inductively coupled plasma mass spectrometry (ICP-MS).

Table 4.1: Elemental composition of synthetic rutile and calcined rutile feedstock (wt%).

	Al	Cr	Fe	Mn	Mo	S	Si	V	Zr	Nb
Synthetic rutile	0.48	0.08	2.77	0.82	<0.05	0.36	0.28	0.16	0.05	0.50
Calcined rutile	0.49	0.03	2.83	0.67	<0.05	0.01	0.33	0.12	0.05	0.11

From Table 4.1, synthetic rutile contains around 4.5 wt% transition elements and has 0.48 wt% of alpha stabilising aluminium. Hence, when the rutile is reduced, the resulting titanium alloy produced will contain a significant amount of beta stabilisers, which from a commercial standpoint, could reduce the dependency on master alloys further downstream. Carbon analysis was completed separately to reveal a content of around 4400 ppm. Elemental analysis was also completed on the calcined rutile, which is also shown in Table 4.1. Although most elements measured show similar values, there are some differences. The sulphur value in the calcined rutile was significantly decreased as this is oxidised during the heat treatment. Likewise, the carbon value was determined to be 45 ppm, significantly reduced from the synthetic rutile value as the carbon has oxidised to CO_2 during calcination. Other values may

differ slightly as their metal has been oxidised. Other differences may be due to errors within the analysis method or slight inhomogeneity of the sample.

4.1.3 Microstructural Analysis

The morphology and microstructure of synthetic rutile were studied using scanning electron microscopy. As received synthetic rutile is shown in Figure 4.1.3a-c. A very porous powder is apparent, with a range of irregular shapes being observed, typically with rounded edges. Porosity is a diagnostic feature of synthetic rutile, formed as a result of the leaching of oxidised iron during the Becher process [7]. A wide range of pore shapes and sizes are observed, ranging from small and abundant porosity in some particles, to large and sparse in others. Elongated pores are also observed and in some extreme cases, hollow particles can be observed.

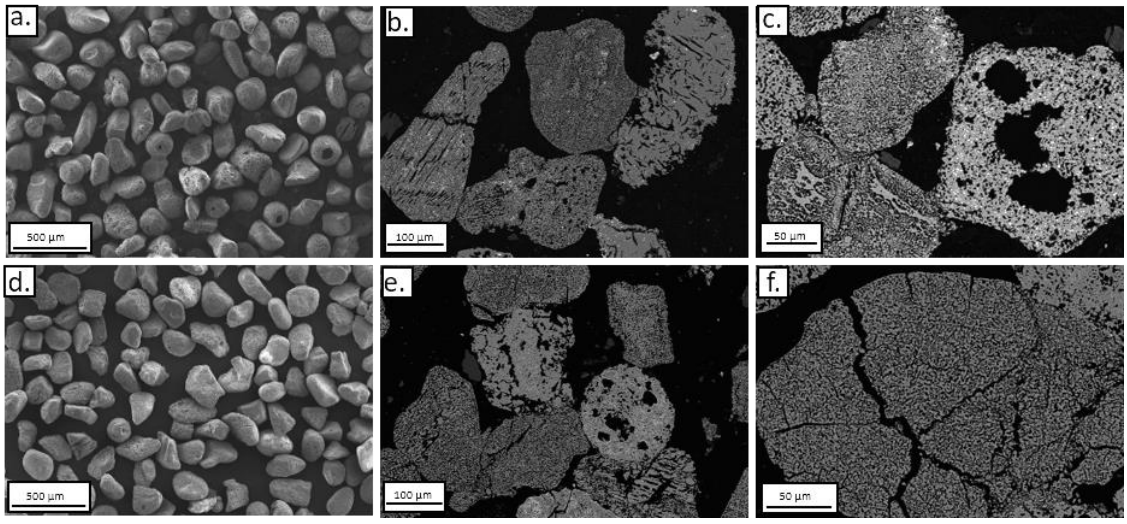

Fig. 4.1.3: Electron microscopy images of synthetic rutile a) secondary electron b) and c) backscattered electron and electron microscopy images of calcined rutile d) secondary electron, e) and f) backscatered electron imaging.

Remnant metallic Fe from the Becher process can be observed as bright white particles under the Z contrast in backscattered imaging, shown in an enlarged image in Fig. 4.1.4. Iron in oxide form is also present [5], but is more homogeneously dispersed and does not appear as a bright phase. Most of the other remnant elements found are well distributed, however occasionally a rare particle consisting of Zr and Si or Al/Si/O can be found.

Microstructual studies were also undertaken on the heat treated synthetic rutile, known as calcined rutile, shown in Figure 4.1.3d-f. Similar particle shapes were found compared to that of synthetic rutile, generally the pores appeared to be smaller and more finely distributed, though large pores are still common. Bright spots consisting of metallic iron are now much rarer, due to the metallic iron oxidising to iron oxide during the heat treatment, which is not observed as a bright phase.

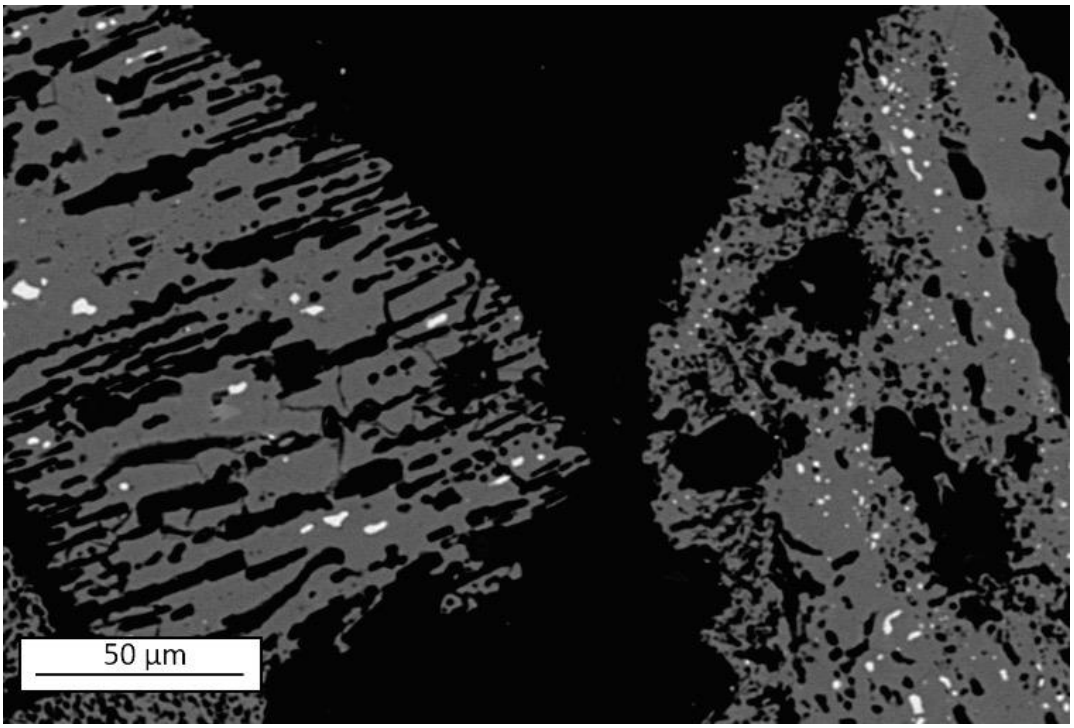

Fig. 4.1.4: Backscatter electron image of synthetic rutile feedstock. Bright white spots are areas of remnant iron leftover from the Becher process.

X-ray energy dispersive spectroscopy (X-EDS) analysis of the SR feedstock revealed a slight inhomogenity on a local scale with respect to iron concentration. Iron inhomogenity is expected as SR is produced from an ore which will have a local variation of iron concentration from particle to particle. Further, the removal of iron from each particle will be slightly different.

4.1.4 Physical Properties Characterisation

In many powder metallurgy applications, particle size and size distribution (PSD) play significant roles. In some applications, a uniform shape and narrow PSD is required such as in electron beam melting (EBM). However, other applications are more lenient and can utilise a larger size distribution. For example, continuous extrusion techniques can accommodate a wide PSD, which can be beneficial in ensuring a better packing density parameter, and thus achieving improved consolidation [8]. Other applications require a particular particle size range, for example, small particle sizes (< 30 μm) are preferred for metal injection moulding (MIM). Hence, an important parameter to monitor is the particle size distribution before and after reduction.

The PSD of 150-212 μm fraction size synthetic rutile was measured to reveal a D_{50} of 207 μm (Fig. 4.1.6). This value is larger than expected and may be due to agglomeration of the particles. It has previously been reported that the FFC process is capable of producing a similar PSD of the feedstock used; hence a degree of control can be maintained over the PSD [9].

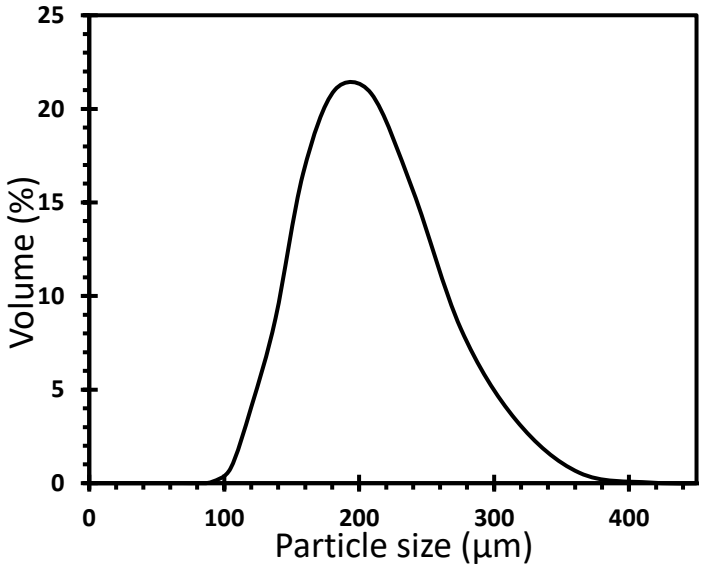

Fig. 4.1.6: Particle size distribution data of synthetic rutile as received (~150-212 μm)

Bulk density of the synthetic rutile was also measured and was found to be 1.42 g cm^{-3} (apparent) and 1.59 g cm^{-3} (tapped). Compared with that of 95% purity non-porous natural rutile, 2.28 g cm^{-3} (apparent) and 2.56 g cm^{-3} (tapped), these are relatively low values. Low bulk density values are observed due to synthetic rutile's high internal porosity, inherent

from the Becher process. Additionally, the size range 150-212 µm is relatively narrow, resulting in large pores between the particles, reducing the bulk density values.

4.2 Partial Reductions of Synthetic Rutile

Alongside the characterisation of synthetic rutile and its subsequent alloy, an understanding of how it behaves throughout the reduction process is of high priority. As such, the reduction behaviour and mechanism was determined via the analysis of partial reductions. Partial reductions consisted of the standard reduction procedure, which was stopped at set timed intervals and the resulting powder analysed. Note, there are associated limitations with this experimental set up. Clearly the most limiting aspect is the ex-situ nature of the analysis. Due to the set-up of the experimentation, analysis of the partially reduced powder was not possible in-situ. As such, further crystallographic transformations are possible during the cooling of the powder from cell temperature (950°C), to room temperature. One such transformation is the formation of Ti_2O, which is formed from the cooling of Ti-O. Additionally, the growth of crystals may also occur throughout the cooling down period, particularly the $CaTi_2O_4$ needles. However, the experimental set-up does allow for direct comparison to previous work which investigated the reduction mechanism of pure TiO_2 [10].

The reduction mechanism of pure TiO_2 has been well researched [10] [11] [12] [13] [14] and an in depth review of the FFC mechanism can be found in section 2.6. Here, partial reduction of synthetic rutile has allowed an insight into its reaction pathway and behaviour throughout reduction. Previous partial reductions, undertaken to understand the reaction mechanism of the FFC process, utilised 99.5% pure TiO_2 pressed preform pellets of 25–30% porosity, with an average particle size of 1-2 µm [10] [12] [13]. This set of experiments utilises loose synthetic rutile feedstock, of particle size 150–212 µm, which has been reduced and the mechanism compared with the original pure TiO_2 work [10]. In this work, particular attention is paid to the pathway of the iron, which is the most prevalent of the remnant elements within synthetic rutile. Samples were taken at 0.5 h, 1 h, 2 h, 8 h, 12 h and 16 h and a combination of chemical analysis techniques (oxygen analysis, XRF) were utilised to determine the composition as well as undergoing XRD analysis to determine the phases present. SEM studies were performed to resolve the morphology and topography throughout the reduction.

4.2.1 General Observations of Partially Reduced Synthetic Rutile

Generally, the partially reduced powders were dark in colour with exception of the SR reduced for 0.5 h. This powder was a brown-orange colour which reverted back to black after soaking in 1 M HCl for 16 h. The colour is thought to be due to iron precipitating out of solid solution and rusting on exposure to air, which is removed during the acid washing process. Both 4 h and 8 h samples required two 16 h washes in acid to remove the high levels of CaO and $CaCO_3$ present within the samples.

In some cases, the addition of acid to the partially reduced material resulted in the formation of a frothy scum layer on top of the aqueous phase. After 1 h a gold scum formed containing Cl, O, Ti and Fe, as determined by X-EDS. After 4 and 8 h a silver scum formed, consisting of C, O and Ca. It is likely that the silver scum contains a combination of free C, CaO and $CaCO_3$. $CaCO_3$ has been previously observed by Bhagat et al. who suggested its formation was due to the reaction of CO_2 bubbles with O^{2-} released by the reducing cathode via Equation 4.2.1 [15].

$$\boldsymbol{CO_2 + O^{2-} \rightarrow CO_3^{2-}} \qquad \textbf{(Equation 4.2.1)}$$

4.2.2 XRD & SEM of Partially Reduced Synthetic Rutile

Each of the partial samples were subjected to XRD analysis, with a good reproducibility of the phases being found. Detection of phases was restricted by the limited sensitivity of the XRD technique, with only major phases being detected (>5 wt%). Furthermore, the complex Ti-O system contains many suboxides, producing similar crystallographic peaks, (e.g. Ti_3O and Ti_6O) which can make identification of some phases strenuous [10]. Figure 4.2.1 shows the XRD patterns produced from the reductions.

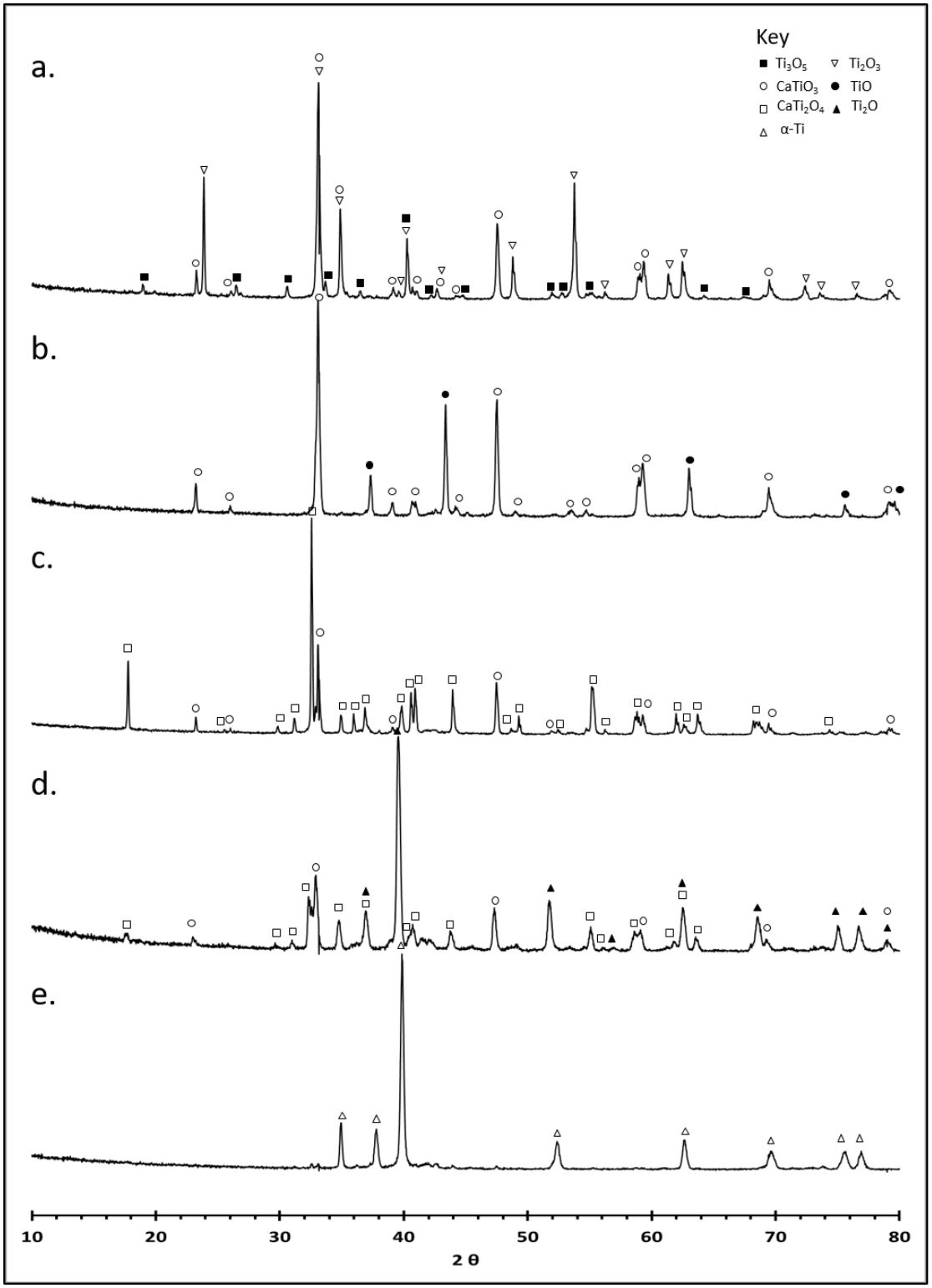

Fig. 4.2.1: X-ray diffraction spectrum of partially reduced samples of synthetic rutile at various timed intervals a) 0.5 h showing Ti_3O_5, Ti_2O_3 and $CaTiO_3$ b) 1 h showing TiO and $CaTiO_3$ c) 2 h showing $CaTiO_3$ and $CaTi_2O_4$ d) 4 h showing Ti_2O, $CaTiO_3$ and $CaTi_2O_4$ e) 8 h showing α-Ti.

After 30 minutes of electrodeoxidation, XRD revealed major phases of Ti_3O_5, Ti_2O_3 and $CaTiO_3$ (Figure 4.2.1). Requiring minimal atomic reconstruction, these phases have previously been observed by Schwandt et al, following the reaction pathway via equations 2.6.2 and 2.6.3, section 2.6 [10] [16]. This work [10] [16], also deduced that the initial step of the reduction is the incorporation of Ca into the cathode, which is highlighted by the increase in Ca content and decrease in Ti content after 30 minutes of polarisation, as illustrated by Figure 4.2.2. Figure 4.2.2 also displays the oxygen content throughout the reduction process. Note, at high levels of oxygen these numbers are indicative values only, as the instrument is calibrated for low levels of oxygen content.

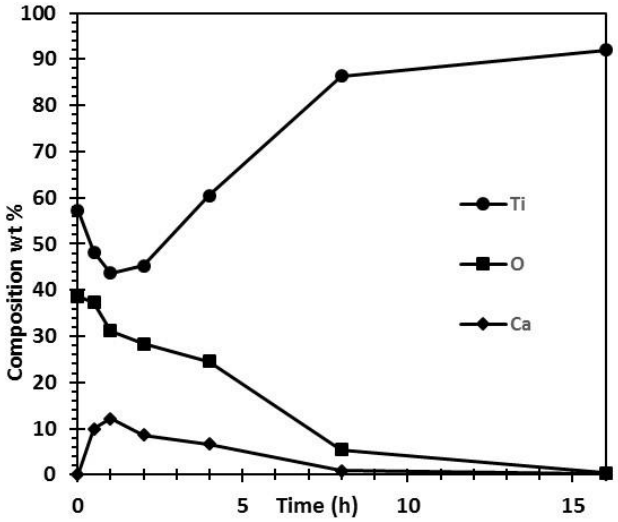

Fig. 4.2.2: Chemical composition in wt% of titanium, calcium and oxygen throughout the reduction of synthetic rutile as measured by XRF analysis. Calcium levels at 0 h and 16 h were measured by ICP due to low concentrations.

The brown orange colour residue observed after 30 minutes of reduction, following removal of the salt, is postulated to be due to the presence of iron, which had precipitated out of solid solution. Once washed in acid, the iron was removed, reverting to a black powder with a substantially reduced iron content. Iron is a beta stabiliser and rapidly diffuses within titanium [17]. Furthermore, from a thermodynamic consideration, iron oxide reduces more readily than titania via the FFC process. Hence, as iron has precipitated out after 30 minutes of polarisation, evidence from this work suggests that iron has reduced within this time frame and has migrated out of solid solution.

Morphology of the particles after 30 minutes of reduction shows two distinct phases. Larger solid appearing areas have been analysed to reveal calcium, titanium and oxygen content. Therefore, these areas have been identified via X-EDS analysis, as the $CaTiO_3$ phase, shown

in Figure 4.2.3b. Smaller pieces with a more fragmented appearance show a decreased presence of calcium and consist mainly of titanium and oxygen. Therefore, these areas have been identified as a combination of the titanium suboxide phases.

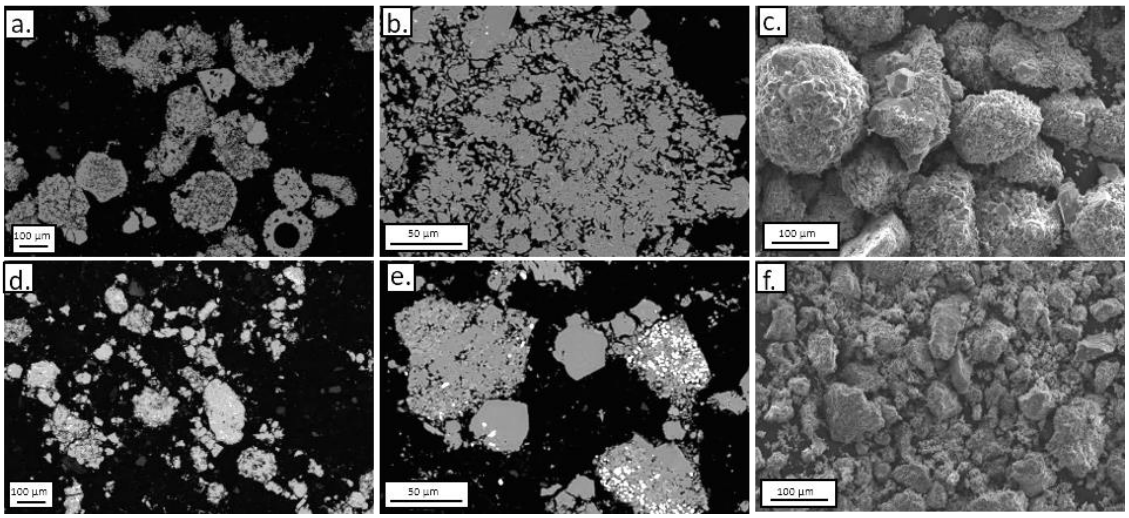

Fig. 4.2.3: Partially reduced synthetic rutile a) and b) show backscattered electron images of partially reduced synthetic rutile morphology after 0.5 h at 950°C and d and e after 1 h at 950°C c) and f) represent secondary electron images after 0.5 h and 1 h of reduction at 950°C respectively.

After reducing synthetic rutile for 1 h, the iron has clearly reduced, as can been seen in Figure 4.2.3e. The bright, iron rich phase has formed discrete particles which have diffusion bonded to the surrounding suboxide phase. Identification of the phase using X-EDS analysis was limited due to the large interaction volume with respect to the low volume fraction of the iron containing phase. The stoichiometry of this intermetallic phase shows a wt% ratio of roughly 30:70 (Ti:Fe). Thus, it can be deduced that the intermetallic $TiFe_2$ phase has formed. $TiFe_2$ was not detected by XRD due to its low concentrations. Only two major phases, consisting of cubic TiO and $CaTiO_3$ were detected by XRD at this point in the reduction (Figure 4.2.3b). Again, the formation of the TiO phase is in agreement with the reaction mechanism outlined earlier by Schwandt et al, shown in Equation 2.6.4, section 2.6 [10]. At this stage in the reduction, a kinetic barrier is expected as the lattice crystal structure shifts from edge sharing Ti_2O_3 octahedra, to cubic titanium oxide [16]. Figure 4.2.3d-f depicts the morphology observed at this stage in the process, illustrating the formation of agglomerate particles consisting of TiO and $CaTiO_3$.

Following the formation of TiO, the reaction proceeds to the formation of calcium dititanate at around 2 h of polarisation. This stage features the largest reconstructive transformation

throughout the reduction, with the formation of the lath shaped acicular $CaTi_2O_4$ (Eq 2.6.5, section 2.6). Due to the low mechanical stability of the dititanate phase, a further repeated partial reduction halted at 2 h was performed in order to observe the needles before the sample was ground for XRD analysis. Backscattered electron images clearly show the presence of both titanates; the needle like $CaTi_2O_4$ and the more faceted $CaTiO_3$, shown in Figures 4.2.4b and 4.2.4c. Formation of $CaTi_2O_4$ has previously been reported to grow in a "star burst" manner, which was also observed and shown in Fig. 4.2.4c. This star burst pattern has previously been explained as a result of limited nucleation and fast anisotropic growth at low angles of misorientation [16]. Figure 4.2.4c also highlights an enlarged image of a faceted $CaTiO_3$ particle.

Presence of the iron as discrete $TiFe_2$ particles is still clear at this point in the reduction. However, occasionally, a thin layer of a less bright phase coats the $TiFe_2$ phase. It is thought that as the reaction proceeds, the iron within the $TiFe_2$ particles begins to diffuse into surrounding suboxides to form a thin layer of TiFe around the $TiFe_2$ core. Formation of the TiFe phase is discussed in more detail at 4 hours of reduction.

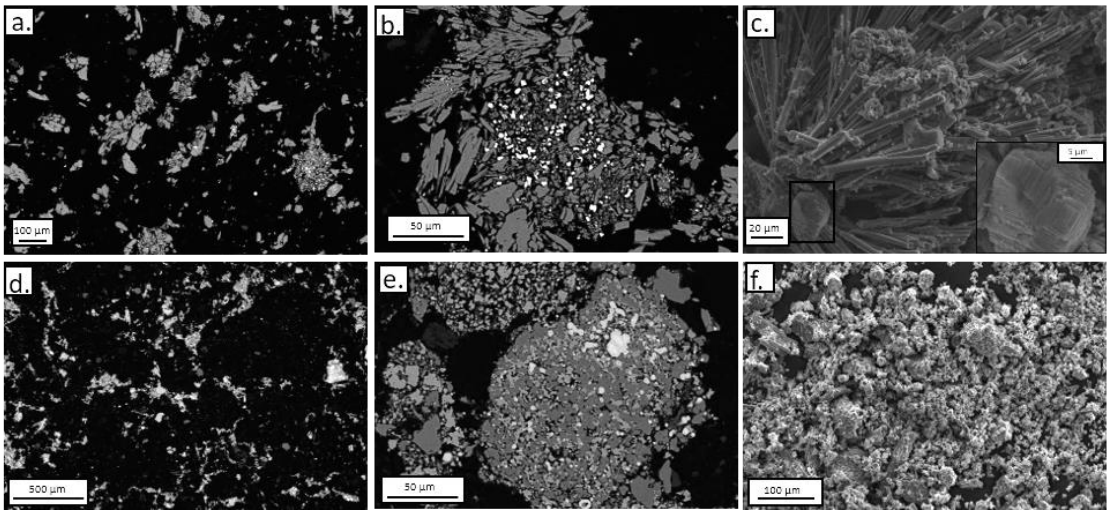

Fig. 4.2.4: Partially reduced synthetic rutile a) and b) show backscattered electron images of partially reduced synthetic rutile after 2 h at 950°C and d) and e) after 4 h at 950°C c) and f) represent secondary electron images after 2 h and 4 h at 950°C of reduction respectively.

After 4 h, both titanates are still present, alongside newly formed Ti_2O (Figure 4.2.4d). It has previously been reported that the Ti_2O phase is a product of the cooling of the Ti-O phase [13], which can be observed in the Ti-O phase diagram shown in Fig. 4.2.5. During this stage of the reduction, destruction of the dititanate produces oxide ions alongside Ca^{2+}, resulting in the high content of CaO throughout the sample (Eq.2.6.6). Hence, extra acid washing was required at this stage to remove the calcium oxide. The morphology of the particles at this point is somewhat mixed, with some particles showing little resemblance to the initial spherical style particle they evolved from. Secondary electron images reveal nodular growth of a globular nature.

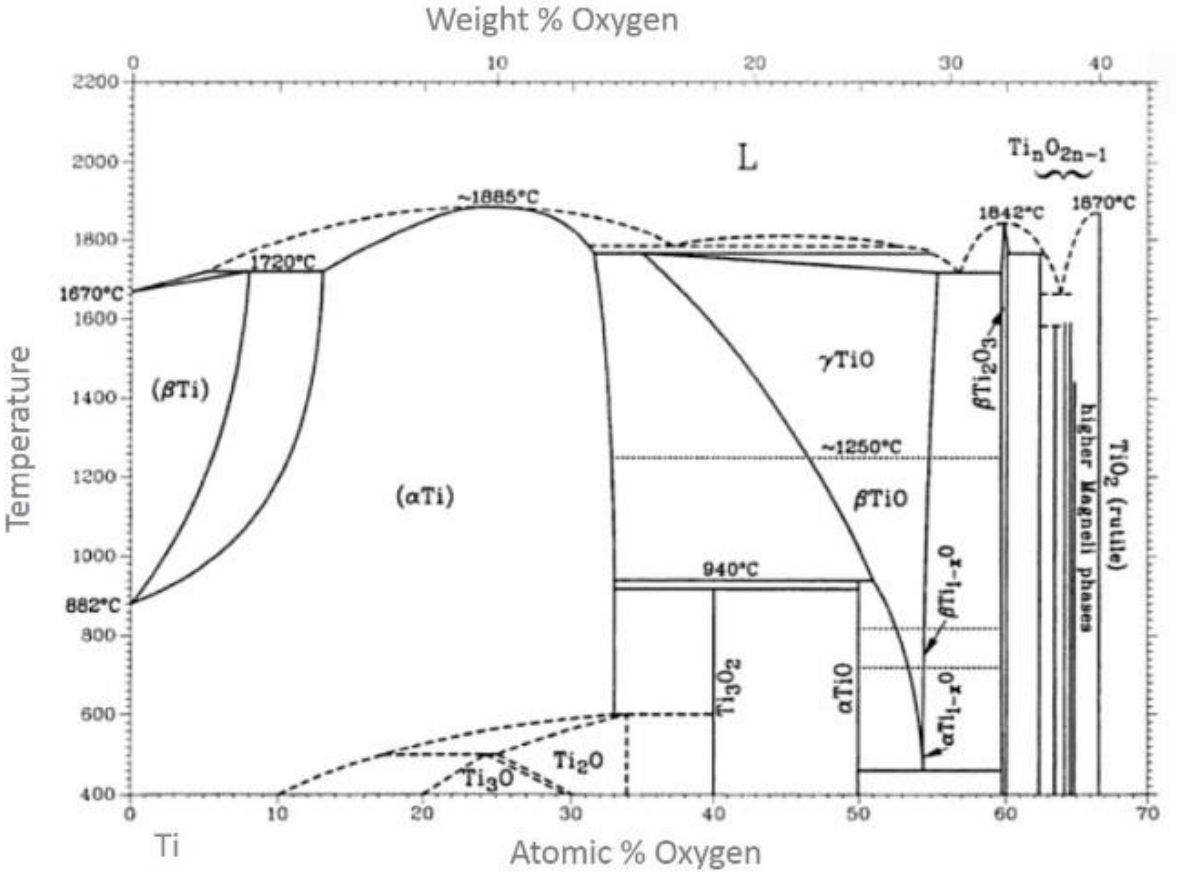

Fig. 4.2.5 Equilibrium binary phase diagram of Ti-O [18].

Additionally, at 4 h of reduction, bright, highly concentrated areas of iron begin to noticeably reduce in size and intensity. Areas of high iron concentration now display two clear phases, easily identifiable due to the difference in contrast. Porosity around the phase edges also affirm the formation of a second iron containing phase. Again, identification of this second iron-containing phase (TiFe) using X-EDS analysis was limited due to the large interaction volume with respect to the low volume fraction of the phase.

However, it appears the core $TiFe_2$ remains, with the second coating phase containing a lower concentration of iron. From the Ti-Fe-O phase diagram (Figure 4.2.6), the limited X-EDS data available and SEM images, it is plausible that the TiFe phase has formed a layer surrounding the $TiFe_2$ core. A more in-depth discussion of the iron intermetallics can be found in Section 4.2.3.

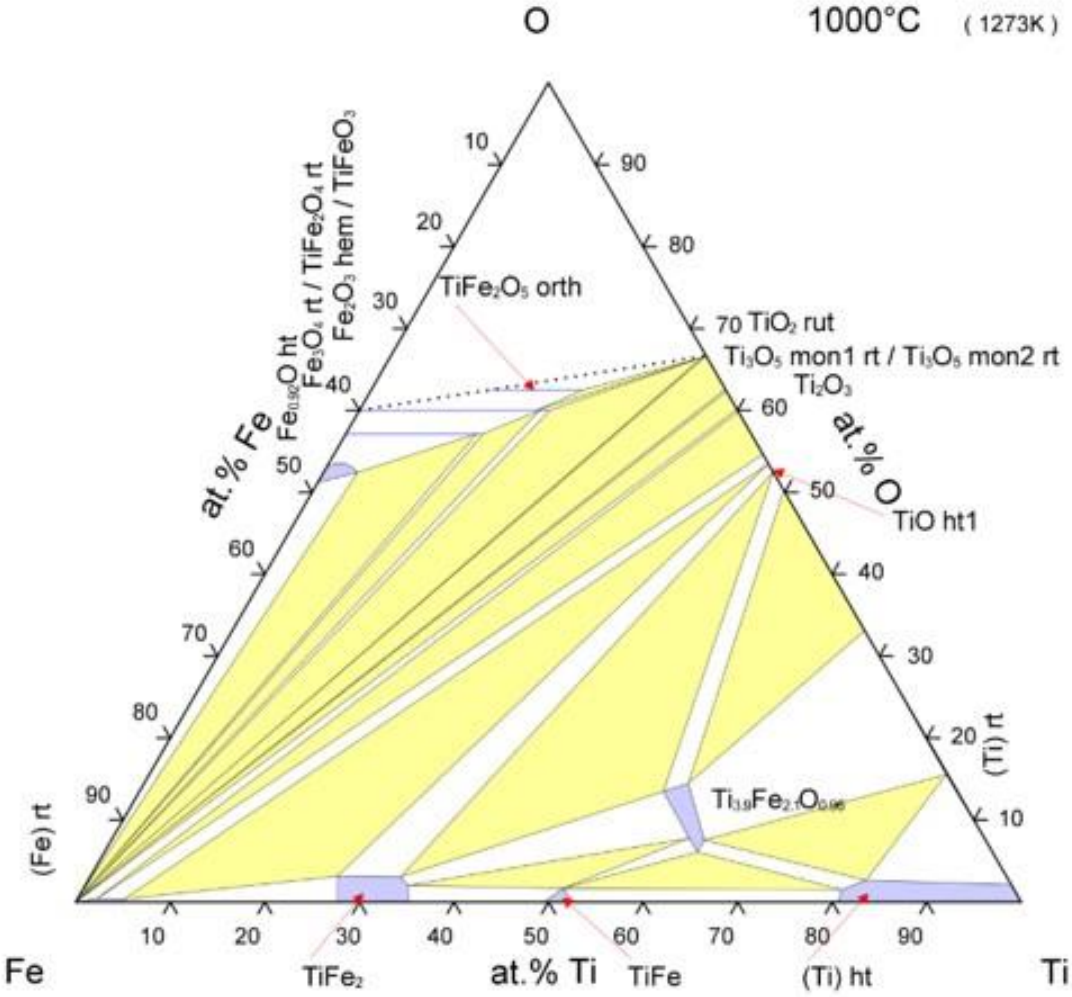

Figure 4.2.6: Equilibrium isothermal section of Ti-Fe-O at 1000°C [19] [20].

After just 8 h, α-Ti is identified as the major phase by XRD analysis (Figure 4.2.1). Note, α-Ti can accommodate up to 15 wt% oxygen [21] (Figure 4.2.5) and as shown by Figure 4.2.2, at 8 h, this sample contains around 5 wt% oxygen. Other phases may be present, as shown by the presence of 2θ peaks at 32.5°, 36° and 42° mentioned earlier, which were unable to be identified. An interconnected porous system is beginning to take shape, shown in Figure 4.2.7b which exhibits two separate phases, identified as alpha and beta titanium, an enlarged image more clearly showing the two phases can be found in the appendix. At this point in the

reduction the final morphology begins to evolve, which is comparable to that of the final product shown in Figures 4.2.7b and 4.2.7c. It is imperative to note at this stage in the reduction, no intermetallics or areas of excessive iron content can be found; the iron has fully dispersed throughout each particle.

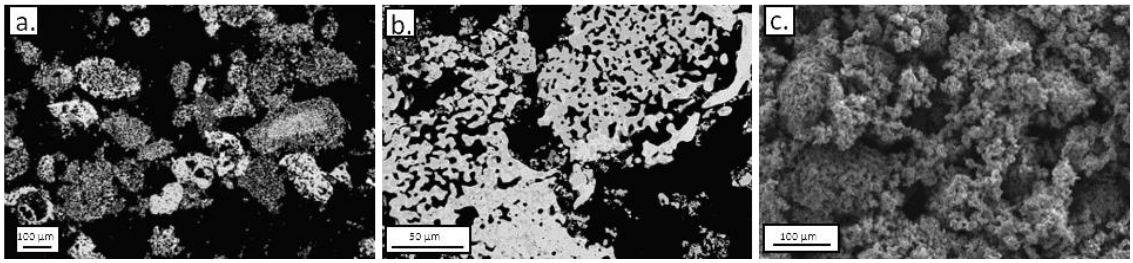

Fig. 4.2.7: Partially reduced synthetic rutile a) and b) show backscattered electron images of partially reduced synthetic rutile after 8 h at 950°C c) illustrates secondary electron images after 8 h of polarisation at 950°C.

After 16 h the powder was fully reduced and is discussed in section 4.3. However, subsequent work undertaken has shown that a fully reduced titanium powder (3038 ppm oxygen) is produced under the same experimental conditions after 12 h, shown below in Figure 4.2.8. Currently the reduction process is not optimised towards the reduction of synthetic rutile and there is opportunity to further increase the efficiencies of the process. Although beyond the scope of this work, further work may also investigate the kinetic effects the reduction of synthetic rutile in comparison to that of pure TiO_2. Particularly as iron is capable of stabilising the beta phase at higher concentrations of oxygen (compared with pure titanium), aiding faster reduction. Faster reduction is achieved as oxygen is known to diffuse at least two orders of magnitude faster in the beta phase than the alpha phase.

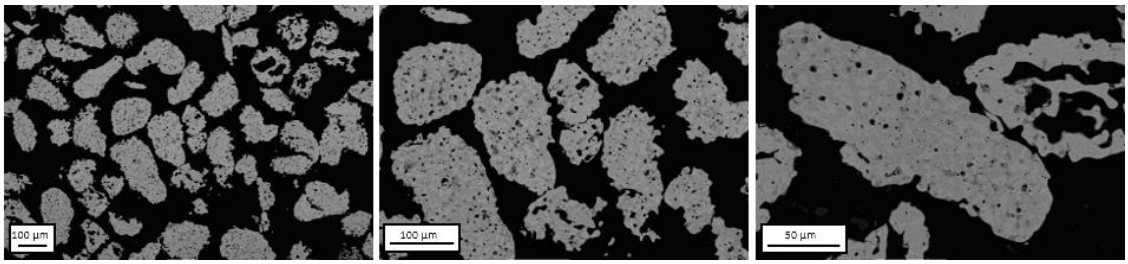

Fig. 4.2.8: Backscatter electron images of fully reduced synthetic rutile achieved after 12 h of polarisation at 950°C.

4.2.3 Overview of Partial Reductions of Synthetic Rutile

Overall it appears the reaction pathway of synthetic rutile is in agreement with that previously reported by Schwandt et al in 2005 [10], however, there are some significant differences in this system warranting further discussion. A new major feature is apparent in the formation and subsequent reduction of iron intermetallic phases. Initially iron present within the synthetic rutile is reduced to metallic Fe after 30 minutes of reduction. Following the reduction of iron oxide is the formation of the intermetallic $TiFe_2$ as compact discrete particles, easily identifiable as the bright phase in backscattered images (Figure 4.2.9a). As the reduction progresses, the iron diffuses into the surrounding titanium suboxides, giving rise to TiFe. A coexistence of these phases can be seen in the titanium-iron phase diagram (Figure 2.8.5). Both intermetallic phases can be observed in Figures 4.2.9b and 4.2.9c, with the bright core of the iron based particle consisting of $TiFe_2$ and the outside exhibiting the less bright TiFe phase.

Further dispersion of the concentrated iron occurs with further diffusion of iron into surrounding suboxides. A solid solution of iron in titanium begins to appear with high contents of iron (up to 60Ti:40Fe) confirming its diffusion into the surrounding titanium (Figure 4.2.9c). Note, concentrations of ~60Ti:40Fe could suggest the formation of a titanium rich intermetallic such as Ti_2Fe.

Formation of the Ti_2Fe phase has been previously investigated, of which a concise review can be found [22]. Initially, existence of the Ti_2Fe phase was disputed [22] [23] [24]. However subsequent work found X-ray spectra of oxygen containing titanium rich Ti-Fe compounds (Ti_3Fe_3O or Ti_4Fe_2O) to be almost identical to that of early Ti_2Fe reports [22]. As such, it is generally believed that the Ti_2Fe phase does not form, unless in the presence of oxygen, hence, this phase is excluded from Ti-Fe phase diagrams.

During reduction, the TiFe phase formed is surrounded by a substantial amount of oxygen, hence, it is plausible that a titanium rich Ti-Fe compound Ti_2Fe or Ti_2FeO could form. However, Polnis and Par have expressed a view that the formation of the Ti_2Fe phase is somewhat sluggish and hence, may not form in the timeframe of the reduction process [22] [25]. Further, none of the X-EDS analysis of the titanium rich Ti-Fe particulates displayed any oxygen, this could be due to the low concentrations of oxygen and limited resolution of this spectroscopy technique. Therefore, without further investigation, it is unclear if a Ti rich phase (Ti_2Fe/Ti_2FeO) forms during the reduction process.

Formation of iron intermetallics throughout the reduction process results in the formation of high local concentrations of iron. As a potent beta stabiliser, high local concentrations of iron leads to a widening of the α+β and beta phase field at the expense of alpha phase field in the Ti-O phase diagram (Figure 4.2.5). Widening of these phase fields allows a faster reduction within these areas, due to the presence of beta titanium, in which oxygen diffuses at least two orders of magnitude faster than within alpha titanium [26]. Occasionally, rare particles of high oxygen titanium metal are observed at 4 h (Figure 4.2.9d). The formation of titanium at this early stage in the reduction process is likely to be due to the particles containing high quantities of iron, allowing the formation of the high oxygen beta phase and faster diffusion process. Particles containing reduced titanium at 4 h of reduction often contained significant quantities of the beta phase.

Iron continues to disperse throughout the reducing titanium metal and after 8 h of reduction, no observable intermetallic compounds are found. Iron is found to be evenly dispersed throughout the beta phase of the resulting reduced particles. However, an observation was made that particles containing higher proportions of the beta phase (appearing lighter under backscatter electron imaging) were clearly more sintered than particles that were alpha dominant, as can be seen in Figure 4.2.9e. This enhanced sintering is due to the faster diffusion rate of oxygen within beta titanium and as such, slightly faster reduction. However, at the end of reduction, most particles are sintered to a similar extent, with iron fully dispersed throughout the beta phase of each particle (Figure 4.2.9f).

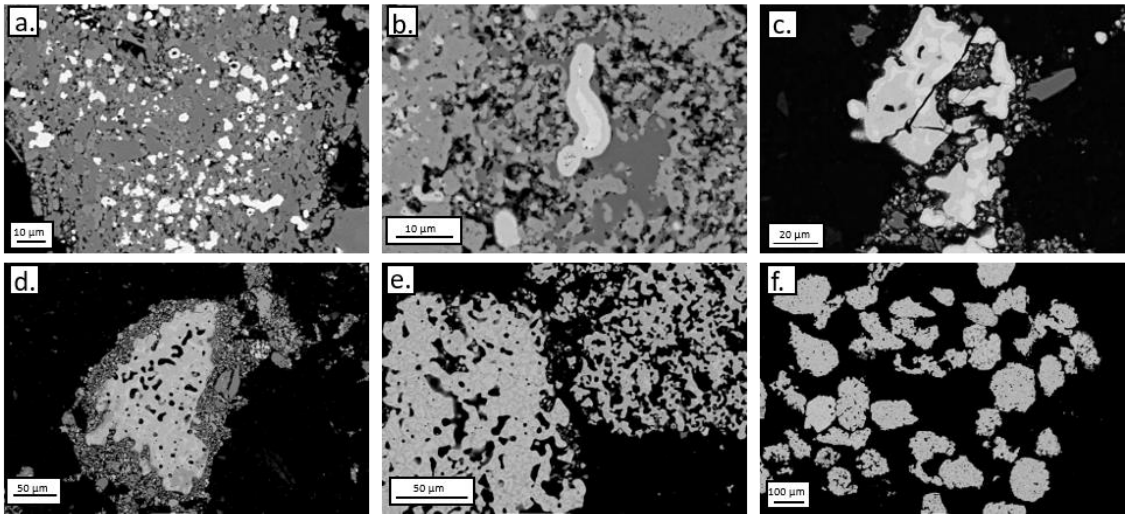

Fig. 4.2.9: Backscattered electron images of a partial reduced synthetic rutile samples a) After 1 h of reduction at 950°C, highlighting the bright $TiFe_2$ phase b, c, and d) After 4 hours of reduction at 950°C with b) showing a $TiFe_2$ core surrounded by a TiFe layer c) Illustrates a bright $TiFe_2$ surrounded by titanium with iron content ranging from 40-50 wt% d) Rare particle showing the first formation of titanium metal consisting mostly of beta titanium, surrounded by titanium suboxides and $CaTiO_3$ e) Particles after 8 h of reduction at 950°C, left particle is beta rich and slightly more sintered whereas the right particle is alpha dominant and is less sintered f) Fully reduced material showing beta phase is well dispersed within final particles.

4.3 Synthetic Rutile Derived Titanium Alloy

Once fully reduced, the resulting titanium alloy exhibits an α+β microstructure, as shown in Figure 4.3.1b. The powder morphology is angular in nature with inherent internal porosity, characteristic of material derived via the FFC process. Fully reduced synthetic rutile usually contains a significant amount of carbon (~0.3 wt% up to 1 wt%), due to carbon found in the feedstock. If the SR is heat treated prior to reduction (calcined rutile), the resulting titanium alloy generally has a much lower carbon concentration, typically around 0.1 wt% carbon.

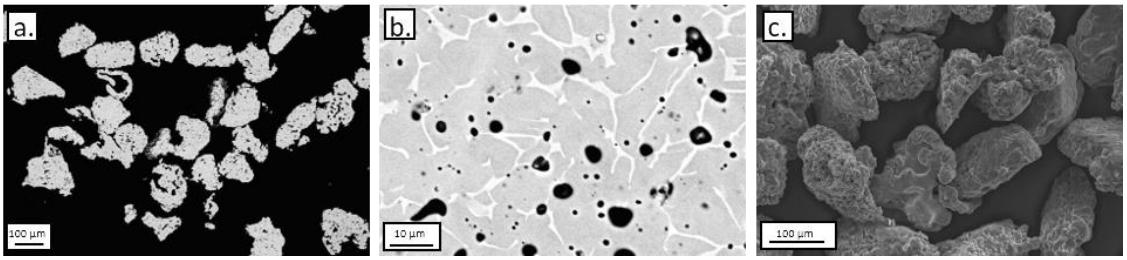

Fig. 4.3.1: a) and b) backscattered electron images of fully reduced synthetic rutile feedstock after 16 h of polarisation at 950°C (ca. 4000 ppm oxygen) c) secondary electron microscope image of the same powder.

The elemental composition of the reduced synthetic rutile feedstock was analysed via XRF spectroscopy and is given below in Table 4.3.

Table 4.3: Elemental composition of synthetic rutile derived titanium alloy (shown Figure 4.3.1) in wt% measured via XRF (except Nb measured via ICP-MS)

	Al	Cr	Fe	Mn	Mo	S	Si	V	Zr	Nb
SR derived titanium alloy	0.78	1.19	2.47	0.25	<0.05	<0.05	0.38	0.28	0.05	0.36

The high concentration of iron provides an effective beta stabiliser, which may lower the dependence for master alloy additions further downstream. Further, the presence of small quantities of other beta stabilisers (V, Nb, Mn, Cr) provide substantial solid solution strengthening, which is highlighted in section 4.6 by the high compressive yield strengths achieved.

In terms of chemical homogeneity, on a particle-to-particle basis some inhomogeneity is found, which is apparent from the slight variations within the microstructure. In SR derived titanium alloy powder produced on a developmental scale, the microstructures of each particle appeared more homogeneous than on an R&D scale. Fig. 4.3.2 illustrates the

difference in microstructure observed in some SR derived titanium alloys produced on a developmental scale. Differences in microstructure are likely to be due to slight differences in iron concentration, although slight differences in interstitials may also alter the microstructure.

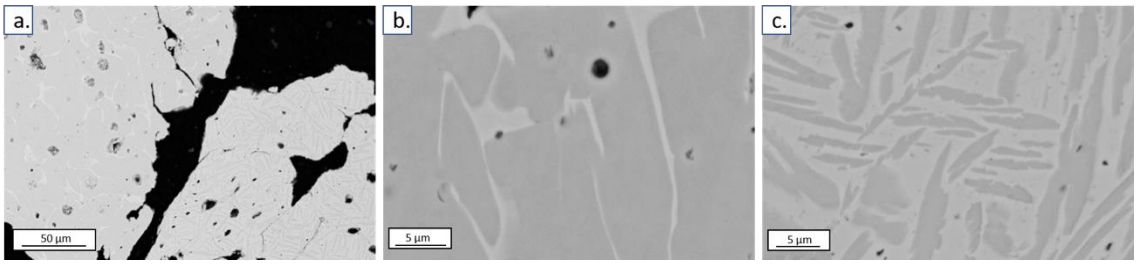

Fig. 4.3.2: Backscattered electron images of SR derived titanium alloy (SRA 1) a) Particle on the left showing a more alpha stabilised microstructure compared to the lamellar microstructure in the right particle b) higher magnification of left particle in Fig.4.3.2a c) high magnification of right particle in image Fig 4.3.2a.

In terms of bulk repeatability on a batch to batch basis, some elements remain consistent such as V, Si, Nb and Zr. However, elements such as Fe, Mn and Cr exhibit more variability from batch to batch due to contamination from materials of construction in the FFC reduction cell (stainless steel). At an R&D scale there were differences in the oxygen and carbon concentration, which could be due to slight differences in the post processing technique, variations in CaO concentration of the salt, inhomogeneity of the starting feedstock or slight variation from cell to cell. As noted earlier, the process is still in the developmental stages and has not yet been entirely optimised in terms of efficiency or repeatability with respect to synthetic rutile.

4.4 Consolidation of Synthetic Rutile Derived Titanium Alloy Powder

Field assisted sintering technique (FAST) also known as spark plasma sintering (SPS) or pulsed electric current sintering (PECS) within the field was chosen to consolidate the reduced synthetic rutile powder. Using this technique, powder is inserted into a graphite mould and under the application of a DC pulsed current, elevated temperature and pressure, the powder is allowed to sinter [27]. FAST has been utilized for a wide range of materials, however, until recently [28], there was relatively little reported data available on the field assisted sintering of titanium and its alloys. Weston et al. have previously consolidated FFC pigment derived pure titanium powders, however the consolidation of synthetic rutile derived alloys has not been previously attempted [28].

At an R&D scale, only small amounts of powder are produced (~9 g) hence, calcined rutile reduced at a developmental cell scale (~5 kg) was used for the following consolidation and subsequent forging which shall now be referred to as synthetic rutile alloy 1 (SRA 1). Figure 4.4.1 and Table 3 display the microstructure and elemental composition of SRA 1 respectively.

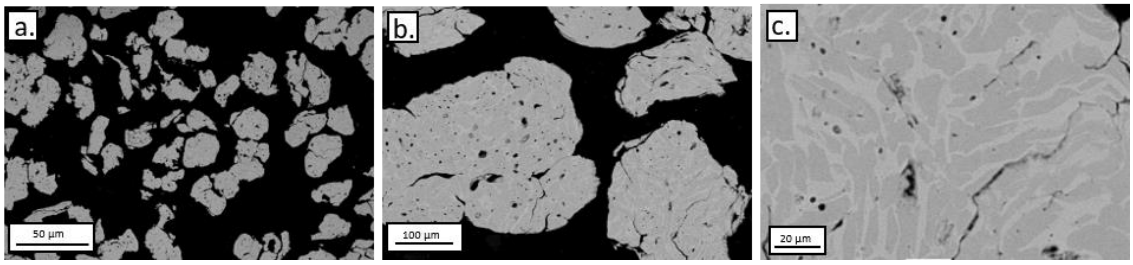

Fig. 4.4.1: Backscatter electron microscope images of fully reduced SR derived titanium alloy composition shown in Table 4.3 (SRA 1).

Table 4.4: Elemental composition of SR derived titanium alloy (SRA 1) shown in Figure 4.4.1 determined by a combination of XRF (elements above 0.6 wt%) and ICP (element below 0.6 wt%).

	Al	Cr	Fe	Mn	Mo	S	Si	V	Zr	Nb
SRA 1	0.10	0.10	2.57	0.54	<0.05	<0.05	0.33	0.16	0.08	0.51

Note there are differences in both microstructure and chemical composition compared to the powder produced at an R&D scale described in section 4.3. These differences are due to the up scaled process undertaking an altered set of experimental conditions and post

processing techniques that are only applicable to high volumes of powder. The exact experimental detail and post processing techniques cannot be detailed, as this information is of a sensitive nature. SRA 1 was determined to have 3528 ppm oxygen and 1041 ppm carbon.

To determine the amount of SR derived titanium alloy powder required to produce a puck of a height of X cm, the following equation is used:

Equation 4.3.1:

$$\text{Powder (g)} = \text{Density (g cm}^{-3}) \times \text{Sample height (cm)} \times \pi \times \text{radius}^2 \text{ (cm)}$$

Hence, 17 g of synthetic rutile derived titanium alloy powder was consolidated into a 10 mm height by 20 mm diameter pellet. Microstructures produced are shown below in Figure 4.4.2. A density of 98.6% was achieved, as determined by software Image J [29]. Although this is lower than the >99% achieved in commercial titanium alloys [28], the FAST conditions used were not optimised. Previous work by Weston et al. investigating the consolidation of titanium alloys via FAST has shown that material containing internal porosity of a spongy nature is slightly more difficult to consolidate [28]. Weston et al. also postulated that an increase in pressure and hold time would allow the removal of the final porosity.

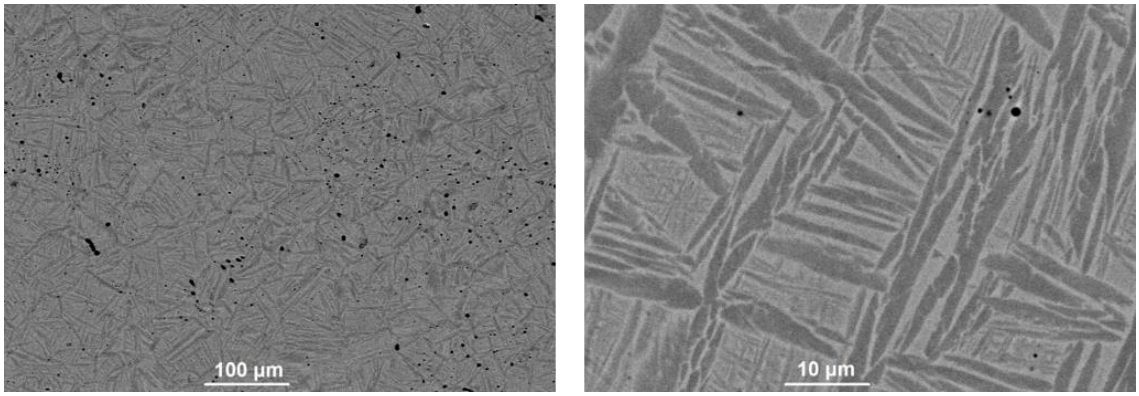

Fig. 4.4.2: Backscatter electron image of the consolidated synthetic rutile derived titanium alloy (SRA 1) ca. 3500 ppm oxygen.

As shown in Figure 4.4.2 a homogenous microstructure is achieved despite the slight local variations of Fe found both within the feedstock and within the resulting SR derived titanium powder. As previously shown in Table 4.3, SR contains a significant quantity of alloying elements. Of these, iron is the most prevalent. Previous work has shown that iron acts to increase the sinterability of titanium alloys due to its fast rate of interdiffusivity [30]. Compared with the self-diffusion of titanium, the diffusion of iron is an order of magnitude

faster [31]. Hence, despite the local inhomogeneity of iron within the particles of the starting powder feedstock, during consolidation, a complete diffusion of iron is observed, which has the benefit of producing a homogeneous microstructure. Further, no intermetallics are formed during the consolidation of the SR derived titanium powder. Iron intermetallic compounds are avoided during consolidation via FAST due to their sluggish formation and the fast diffusion rate of iron [32].

4.5 Determination of the Beta Transus via Experimental and Modelling Methods

Determination of the beta transus reveals at what temperature the titanium alloy exists entirely in the β phase. This value is of significance as it is typically used to determine the temperature of various processing techniques such as homogenisation, deformation, recrystallization and ageing [31].

Initially the beta transus of SRA 1 was determined via modelling software, Thermocalc [33], which predicted a transus value of 909.4°C. This value was then validated experimentally. To experimentally determine the β transus, consolidated synthetic rutile derived titanium alloy (SRA 1) underwent various heat treatments followed by microstructural analysis. Samples of the titanium alloy were heated to the following temperatures for approximately 1 h: 810°C, 835°C, 860°C and 885°C before quenching in water. Resulting microstructures of the various heat treatments are shown in Figure 4.5.1 below.

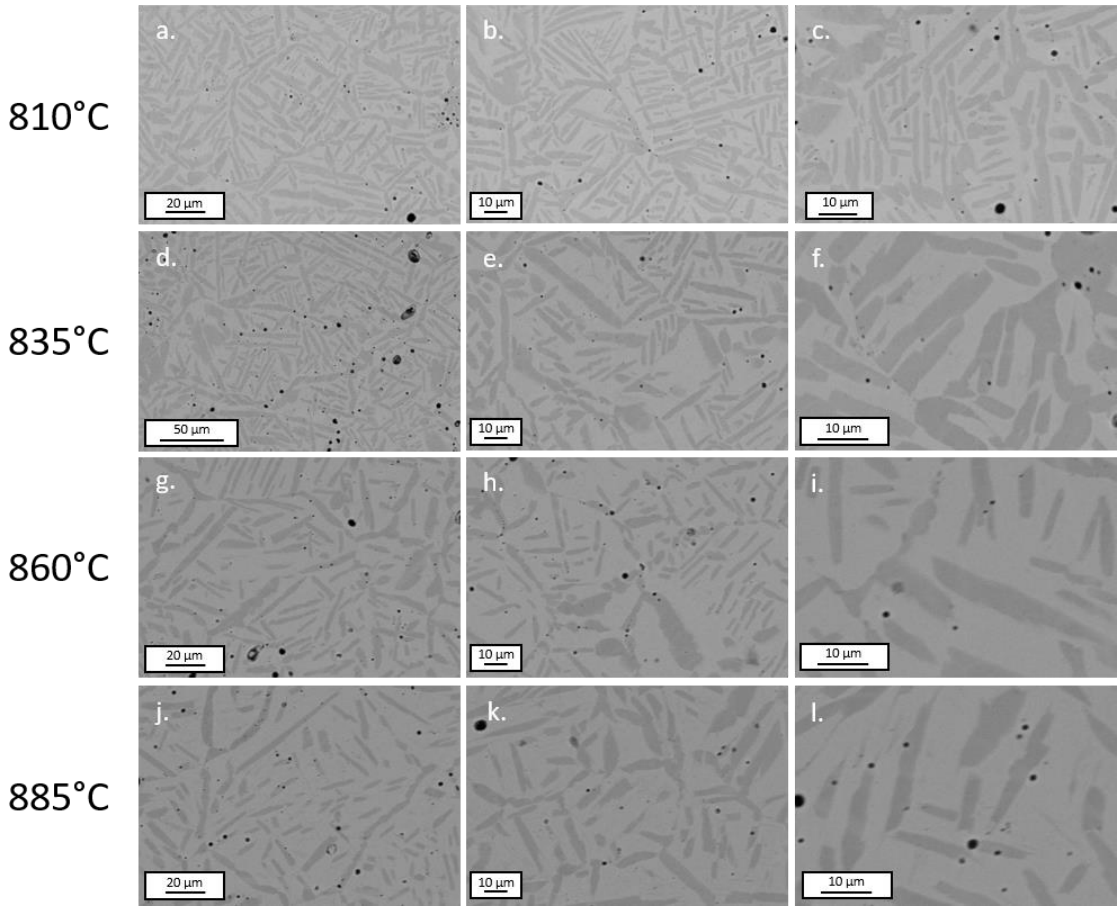

Fig. 4.5.1: Backscatter electron images illustrating microstructure of SRA 1 with composition listed in Table 4.3. Dark phase shows alpha concentrations, light phase reflects beta content. a-c) heated treated at 810°C d-e) heat treated at 835°C g-I) heat treated at 860°C j-l) heat treated at 885°C.

Using image software, Image J [29], the microstructures observed at each heat treatment temperature were analysed to determine the percentage of beta phase present. Figure 4.5.2 illustrates the resulting beta approach, which was extrapolated to determine an approximate beta transus temperature. Using the given equation of the line of best fit, y = 0.4678x – 336.25 (R^2= 0.986), an approximate beta transus temperature of 934.7°C was determined. In comparison to the value predicted by the modelling software (909.4°C) this gives a difference of 2.71% which is within the range of experimental error, providing confidence within the modelling software.

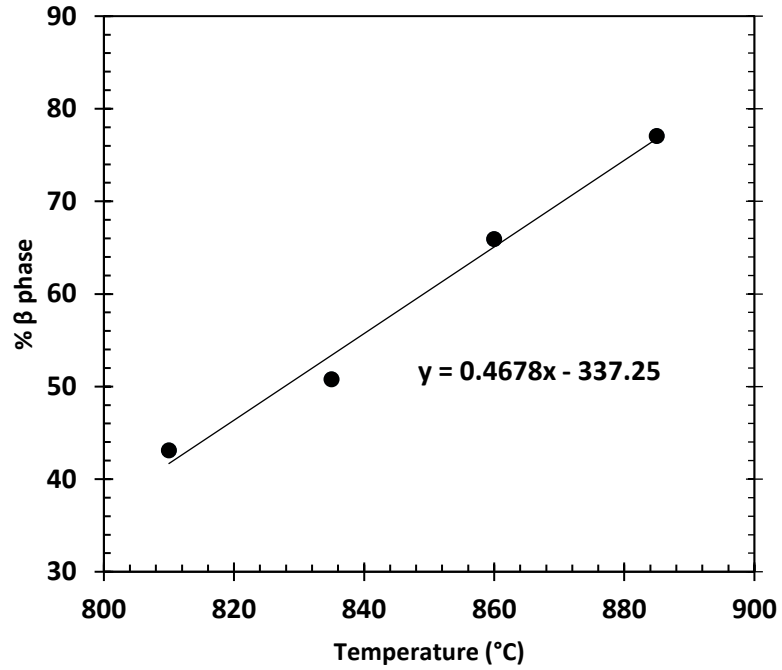

Fig. 4.5.2: Percentage of β phase present at various heat treatment temperatures.

4.6 Mechanical and Physical Data of Synthetic Rutile Derived Titanium Alloy

Following the consolidation of the synthetic rutile derived alloy, initial physical tests including compression and hardness testing, were conducted in order to determine the baseline mechanical properties such as compressive yield strength, hardness and flow stress of the alloy produced.

Hardness values of the consolidated synthetic rutile derived titanium alloy (SRA 1) were obtained using a CV 100KS Vickers hardness tester and determined to be 328.25 HV. This value is comparable to the hardness of the Ti-6Al-4V alloy [34].

Compression testing of the synthetic rutile derived titanium alloy was completed using the Thermo Mechanical Compression (TMC) machine. This machine is capable of replicating the forging procedure and allows mechanical data, such as compressive yield strength and flow stress to be measured.

Initial testing was completed at room temperature using material consolidated via FAST using the small-scale set up which is detailed and validated in Section 5.1. Note, using the small-scale set up produced a slightly lower density of the SR derived Ti alloy due to a reduction in temperature which is discussed in Chapter 5. Three repeats of SRA 1 baseline alloy were conducted with the resulting flow stress curves displayed in Figure 4.6.1.

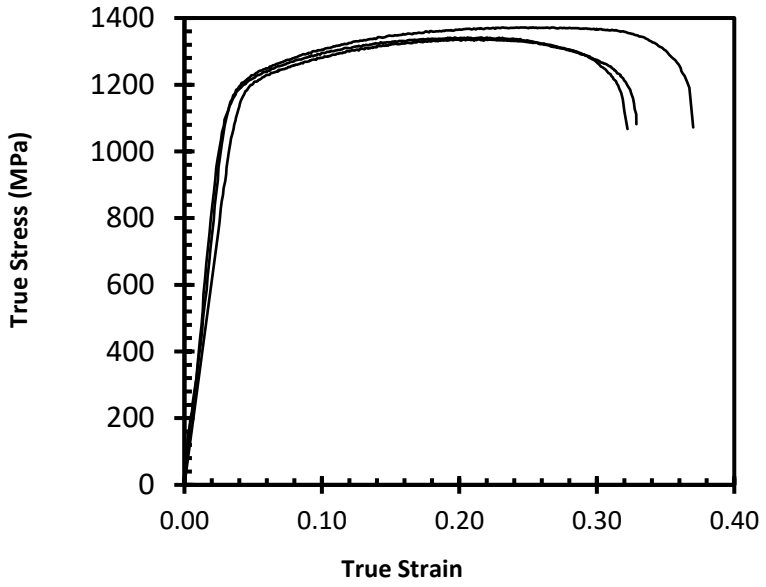

Fig. 4.6.1: Compressive true stress-true strain graphs of three repetitions of SR baseline alloy (SRA 1) at a strain rate of 0.1 s^{-1} and room temperature.

Despite its synthetic rutile origins, the three repeats produced similar 0.2% yield strength values of 1061 MPa, 1099 MPa, 1109 MPa, a variation of less than 4.5%. A larger strain to failure was observed in one of the repetitions, which is not an unusual occurrence when testing materials, as depending on their mechanism of failure and fracture point, the strain to failure value may be slightly different.

Failure of the synthetic rutile derived alloy was investigated via microscopic studies. Fig. 4.6.2 displays microstructure close to the fracture line. Plastic deformation is observed, however, there is no evidence of the formation of shear bands. Evidence from the micrographs suggest the sample has failed prematurely, due to coalescence of porosity. Hence, it is not unreasonable to expect improved strain to failure values once full consolidation is achieved.

Even with significant porosity, both the compressive yield strength and the strain to failure observed are similar to that of popular workhorse alloy Ti-6Al-4V, which is discussed in more detail in chapter 5.

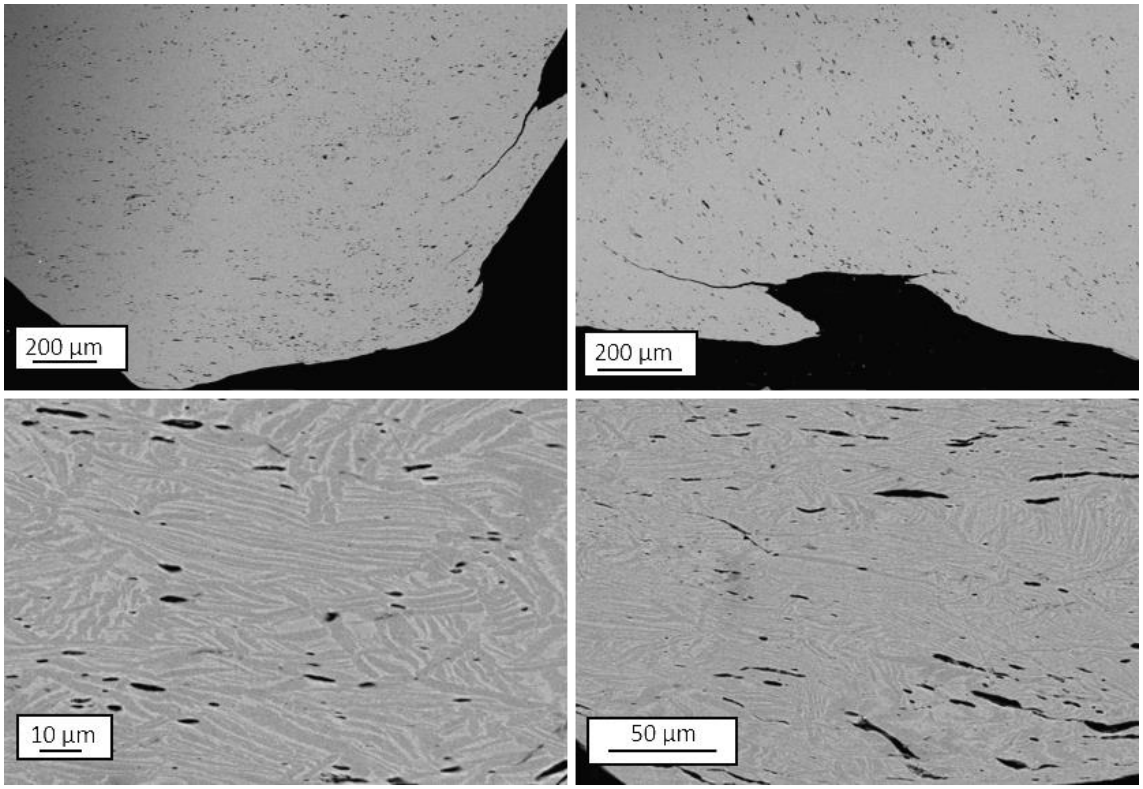

Fig. 4.6.2: Backscatter electron images of the fracture surface of failed synthetic rutile derived alloy compressed at room temperature at a strain rate of 0.1 s^{-1}.

4.7 Large Scale Mechanical Properties of Synthetic Rutile Derived Titanium Alloy

Although further mechanical properties need to be investigated, such as tensile yield and fatigue strength these results are promising for the use of a synthetic rutile derived alloy as a low-cost alternative, particularly in the cost-conscious industries such as the automotive sector. Following this work, new research projects set-up following investment from both automotive and aerospace companies has led to the up-scaling and production of 100 mm diameter pucks, which will allow both tensile and fatigue tests to be conducted.

4.8 TiC Formation in SR Derived Titanium Alloys

Due to the relatively high starting concentrations of carbon within synthetic rutile, when reduced, the carbon content can be as high as 1 wt%. This level of carbon is enough to produce a considerable amount of the intermetallic compound TiC. However, the carbon level can be significantly reduced to values below 0.1 wt% provided the SR is heat treated prior to reduction. Note, (with the exception of the partials work, section 4.2) all of the titanium alloys were produced using heat treated feedstock unless otherwise stated.

Within the synthetic rutile derived titanium alloys powder, carbon is predominantly present in four ways:

1. **As scum particles:** 'Scum particles', shown in Fig. 4.8.1a and 4.8.1b are particles heavily contaminated with carbon, typically with significant quantities of TiC around the edges of the particle. Following reduction, the top of the lightly sintered Ti alloy cake is typically covered in a thin layer of 'cathode scum' consisting mainly of carbon. Hence, the scum particles observed are likely to have been near the top of the cathode, nearest to the carbon anode during reduction and should be removed from the powder with adequate post processing techniques. Concentration of scum particles is dependent on the rigour of the post processing technique, typically, powders from development scale contained significantly fewer than at R&D scale. Often no scum particles were identified using SEM of development scale powder following post processing techniques.

2. **As discrete, coarse precipitates:** When large concentrations of carbon (roughly >0.1%) are present in the bulk powder, the powder exhibits discrete precipitates of the TiC phase, shown in Fig 4.8.1. The coarse phase tends to precipitate near areas of alpha or the edge of particles. If the SR is not heat treated to remove the carbon prior to reduction, a significant amount of carbon is found in the resulting titanium alloy (~0.8 - 1 wt%). As such, significant precipitation of the TiC phase is observed within most particles, as shown in Fig. 4.8.1e and 4.8.1f. If the SR is heat treated prior to reduction to remove this carbon, the resulting alloy contains typically less than 2500 ppm carbon (at R&D scale, lower at development scale due to improved post processing technique). Hence, these carbon precipitates are much rarer, see Fig. 4.8.1d. Generally, with decreasing carbon content, the less TiC precipitation is found. Using X-EDS analysis, these coarse particles are typically between 16-20 wt% carbon,

however, some particles contained ~5 wt% carbon, shown and discussed further in Appendix 3. Due to the limitation of X-EDS and small size of the precipitates, more work may be required to determine the exact stoichiometry of the forming carbides.

3. **Within solid solution, stabilising the alpha phase:** Under equilibrium conditions, the alpha phase does not possess any solubility for carbon at room temperature. However, the SR derived titanium powder was not produced under equilibrium conditions. When the electrolysis is stopped, the cathode is pulled from the salt to the upper, cooler area of the retort, hence the sample will cool under non equilibrium conditions. (Note, the sample is protected by a layer of electrolyte, $CaCl_2$, which helps to prevent oxygen pickup when the sample is taken out of the argon atmosphere within the cell). As such, carbon may also be present in solid solution, illustrated by Fig. 4.8.2. Additionally, with the presence of remnant elements, the SR derived titanium alloy will deviate significantly from the previously determined phase diagram. It is predicted that the α+β phase field will widen and the precipitation of TiC may occur at lower temperatures at equilibrium. However, it is still predicted that carbon will be present within solid solution within the α+β phase at temperature, and retained within solid solution when cooled under the conditions described above to room temperature.

4. **Coating the particles:** Free carbon may also be present coating the particles, both around the edges and within the pores. However, this is difficult to confirm as Bakelite is a strong source of carbon. Hence this cannot be confirmed using SEM/optical microscopy when the samples are mounted in Bakelite. Further work is required to both confirm and quantify the presence/amount of carbon present within the powder in this manner.

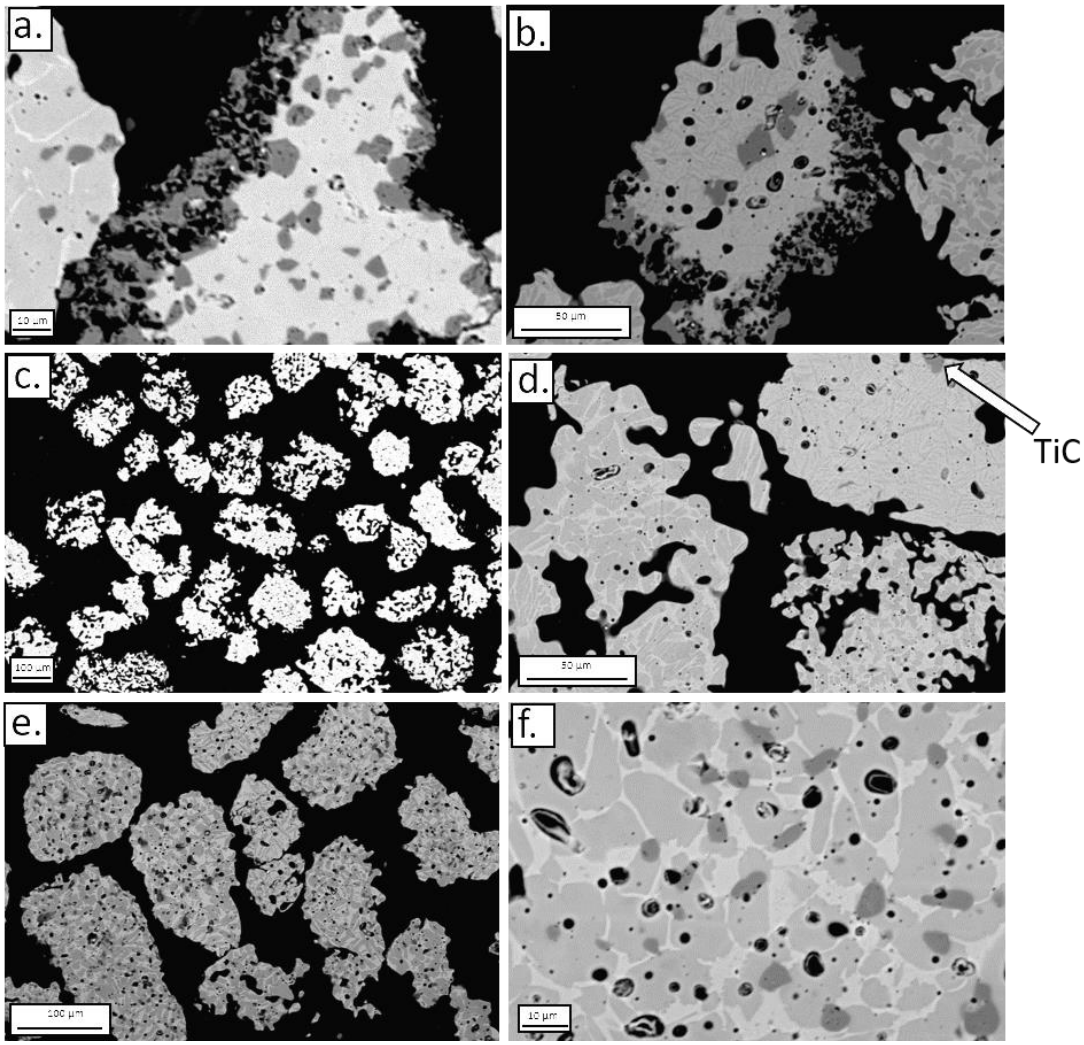

Fig. 4.8.1: a) and b) backscattered electron images of a carbon rich “scum particle” found within SR derived titanium alloy a) baseline SR sample not calcined prior to reduction b) sample calcined prior to reduction containing 0.28 wt% C c and d) synthetic rutile derived titanium alloy showing 3 phases – dark/light α/β titanium matrix and small coarse carbon precipitate 3rd phase TiC particle low in C (alloy Al2- appendix) (0.05 wt% C) e) and f) Non calcined baseline SR derived titanium alloy, hence carbon rich (0.72 wt%) – significant quantity of TiC precipitate.

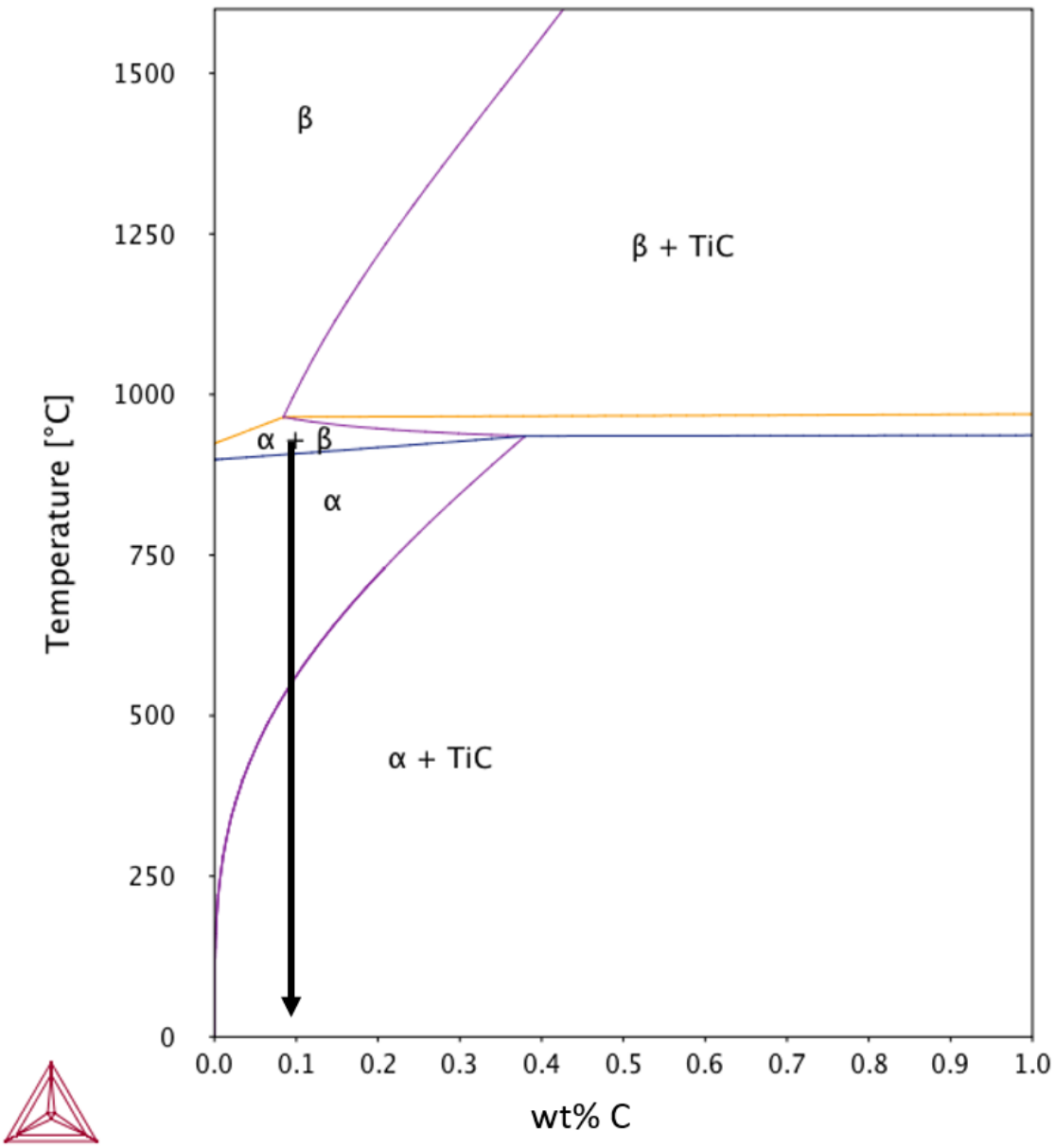

Fig. 4.8.2: Binary phase diagram of Ti-C illustrating super saturated solid solution formation calculated using Thermo-Calc software [33], with composition Ti-0.35O-0.1C. Note, the full composition of SR was not used due to the complexity of the system resulting in the prediction of many phases not relevant to this particular discussion.

4.8.1 TiC formation in Consolidated Synthetic Rutile Derived Alloys with Low Carbon (<0.3 wt %)

Following consolidation, scum particles have largely remained intact and are easy to identify in the consolidated microstructure (Fig. 4.8.3a). In the powder, the scum particles typically contained high concentrations of carbon on the edges of the particles. Once consolidated, the scum particles are apparent as the prior particle shape is clear (Fig. 4.8.3a). These pockets of high carbon are detrimental to the properties of the alloy as stress initiators, however these particles are rare, especially when the powder has been post processed on scales larger than R&D. Further, with scaling up and improved post processing techniques, these particles should be eradicated entirely.

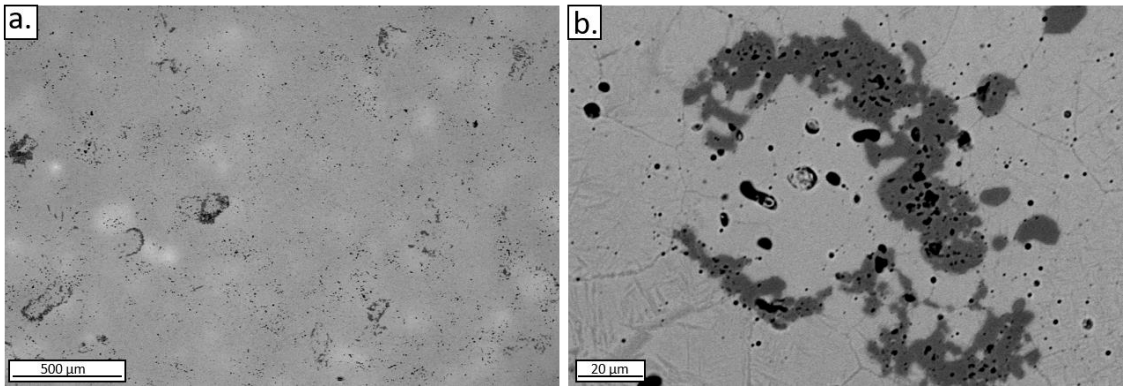

Fig. 4.8.3: a) Backscattered SEM images of consolidated alloy with a) 0.1 wt % carbon in the bulk (alloy T3 - appendix) and b) 0.21 wt% carbon in the bulk (alloy Al6), illustrating the retention of 'scum' particles following consolidation (both alloys calcined prior to reduction).

Within the carbon perimeter of the defect, occasionally there is notable porosity (Fig. 4.8.3b). Due to the high carbon concentration found in scum particles, these edges are more difficult to diffusion bond with the surrounding titanium resulting in higher porosity.

Coarse individual precipitates of carbon found prior to consolidation (Fig. 4.8.1c and d) are also found following consolidation via FAST (Fig. 4.8.4). These are generally found along grain boundaries; however, it is unclear if these particles remain throughout the sintering process or are redistributed.

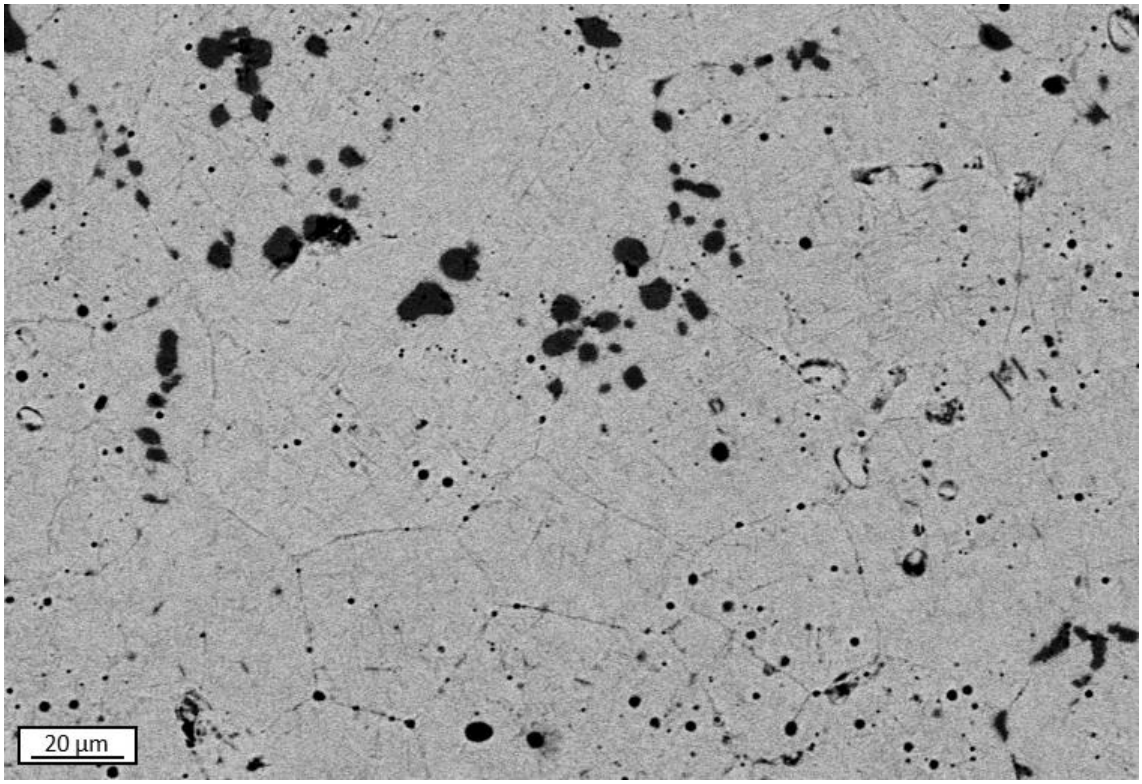

Fig. 4.8.4: Backscattered electron image of individual carbon precipitates within a consolidated SR derived titanium alloy of 0.25 wt% C.

Finally, also observed in the consolidated titanium alloy are fine lath like TiC ppts. These are fine and difficult to identify, though typically they are more apparent, or easier to identify within the beta phase. These fine precipitates are not present within the starting titanium alloy powder and have formed during a solid-state transformation. Previous work in beta stabilised alloys of 0.2 wt% C has ascribed their formation due to the decreasing solubility of carbon in beta titanium as temperature decreases during cooling, forcing the partitioning of the TiC phase as fine acicular laths [35].

However, in this work, using SR derived titanium alloys, it is thought there is carbon present within the titanium microstructure at room temperature as a solid solution. During heat up in FAST consolidation, It is possible that the TiC precipitation also occurs as the alpha phase diminishes. As C is more soluble in the alpha phase than the beta phase (Fig. 4.8.2), once the crystal structure transforms α->β, solubility of C decreases, resulting in TiC precipitation. Therefore, the lath like TiC precipitates do not precipitate on grain boundaries, as they are formed separately prior to alpha stabilisation. The production of the lath like TiC precipitates is a complex case which requires significant further investigation.

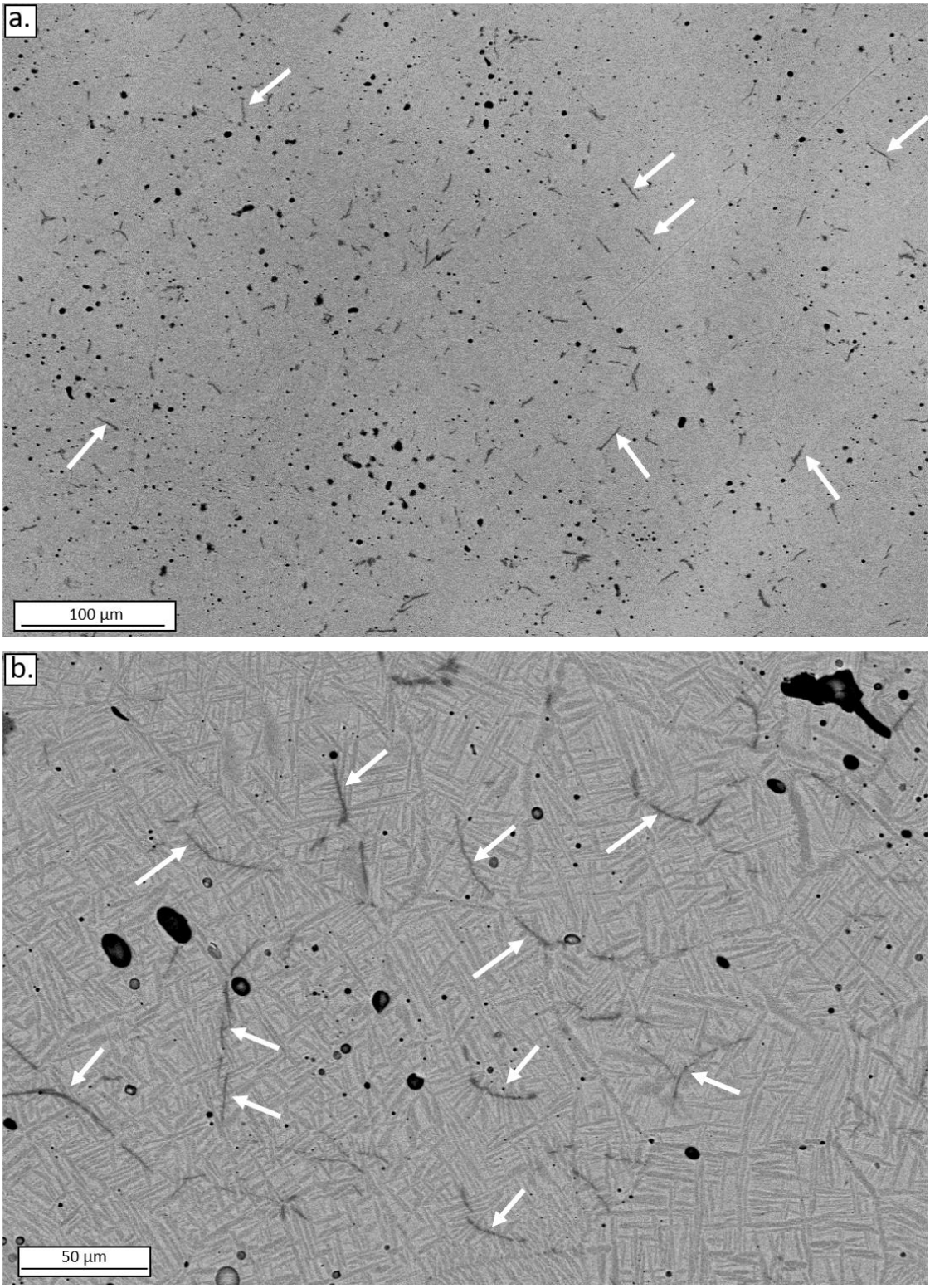

Fig. 4.8.5: Backscattered electron image of a) beta stabilised region of an SR derived titanium alloy (calcined prior to reduction, SR-4Mo containing 0.22 wt% C b) α+β region of a baseline SR derived alloy containing 0.1% wt C. White arrows point to precipitated TiC laths.

Fig. 4.8.5b) also shows the formation of TiC lath precipitates with an α+β region. Note these TiC laths were usually more difficult to identify within α/β regions than β regions. The sample in Fig. 4.8.5b) was prepared using standard metallographic techniques (section 3.3) but without the polishing MD-Dac stage. By removing 15 minutes of polishing, the TiC phase appeared more prominent under the SEM. It is thought that the longer polishing stages effectively wore down the TiC precipitates faster than the Ti matrix, as the thickness and hence, concentration of the TiC phase is decreased and the difference in contrast is not as obvious.

However, the presence of the TiC laths do affect the surrounding microstructure, as shown in Fig 4.8.6. Diffusion of carbon into the surrounding titanium matrix is observed, resulting in the stabilisation of alpha.

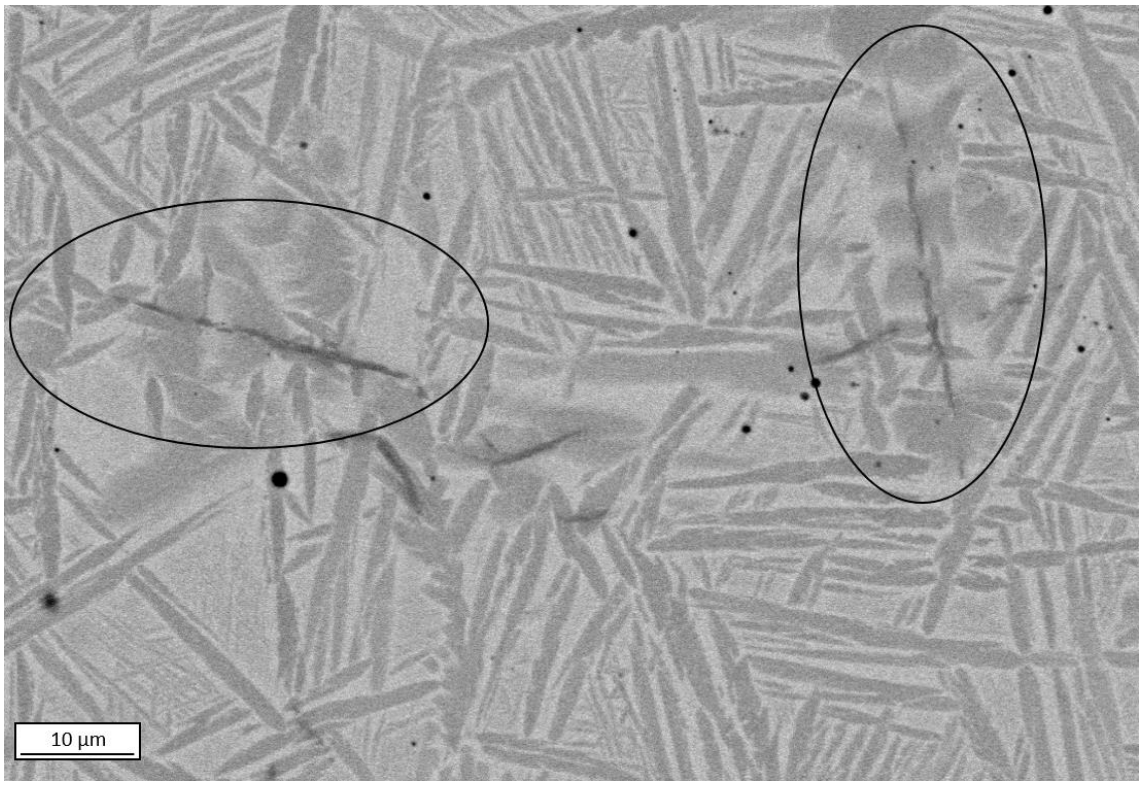

Fig. 4.8.6: Backscattered electron image of TiC ppt laths within abaseline SR derived titanium alloy of 0.1 wt% C. Areas of alpha stabilisation are encircled.

4.8.2 TiC Formation summary

In summary: TiC is present within the Ti powder as scum particles, coarse ppts and possibly dissolved within the α phase in a super saturated solid solution. Free carbon may also be present coating the edges and pores of the particles, however more work is required to confirm this. Following consolidation, the scum particles remain and are apparent from their prior particle shape and porosity within the carbon rich particle perimeters. Coarse carbon precipitates are also still present within the consolidated alloy, though it is not clear if these particles remain throughout the process or are redistributed and reformed. Finally, within the consolidated alloys is also the formation of fine acicular TiC laths. These laths are thought to form throughout the solid-state transformation during the FAST consolidation process, however, the formation of laths during consolidation may also be a manifestation of free carbon coating the outside/pores of the initial powder.

4.9 Formation of Metal Matrix Composites - TiC Formation in Consolidated Synthetic Rutile Derived Alloys with High Carbon (>0.5 wt %)

Although small additions of carbon can be beneficial to titanium alloys if they are finely distributed and pinning the grain boundaries, precipitates of TiC are generally seen as detrimental, as they can lead to decreased ductility and premature failure. However, the use of TiC particulates in titanium alloys as a strengthener, has also been investigated extensively and are known as Metal Matrix Composites (MMCs) [36] [37] [38] [39]. TiC reinforced titanium alloys are known to produce high strengths and stiffness levels.

NASA has previously investigated the strength and stiffness of MMC containing TiC particulates for space propulsion applications, with the resulting microstructure shown in Fig. 4.9.1 [36]. Although such material lead to a loss in ductility, significant increases in strength and stiffness were observed in comparison to the unreinforced Ti-6Al-4V. Also of note is that the low cycle fatigue testing of Ti-6Al-4V reinforced with particulate in comparison of unreinforced Ti-6Al-4V led to similar results [36].

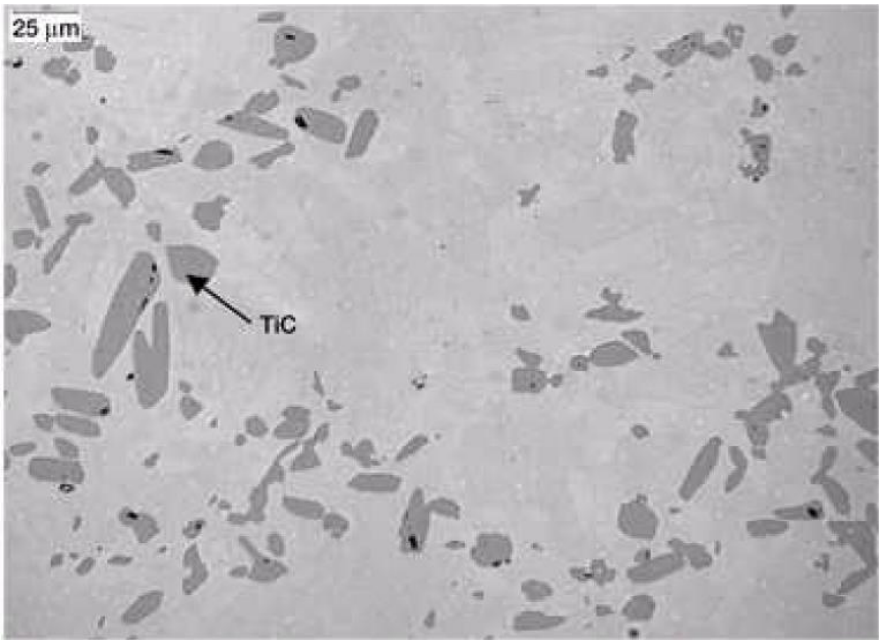

Fig. 4.9.1: TiC particulates (10 wt %) reinforcing a Ti-6Al-4V matrix [36].

If synthetic rutile feedstock is not heat treated prior to reduction, the resulting alloy will have considerable carbon content, resulting in coarse carbon precipitates throughout most particles, shown in Fig. 4.9.2a.

Following consolidation, the resulting microstructure exhibits the same coarse TiC particles shown in Fig 4.9.2a. Precipitating on grain boundaries (Fig. 4.9.2b), the TiC particulates are generally well distributed and are typically between 5 and 15 μm in size. The microstructure produced is similar to that of a particulate reinforced titanium alloy metal matrix composite. In comparison to the microstructure produced by NASA, SR derived TiC MMC's appear to have a more uniform distribution of the particulate.

Although on the macro scale the precipitate seems well distributed (Fig. 4.2.9a), there are areas of clustering and TiC lean areas, as exemplified in Fig. 4.9.2c and d. Fig. 4.9.2e also shows occasionally, prior particles can be identified by the precipitate of TiC along the grains.

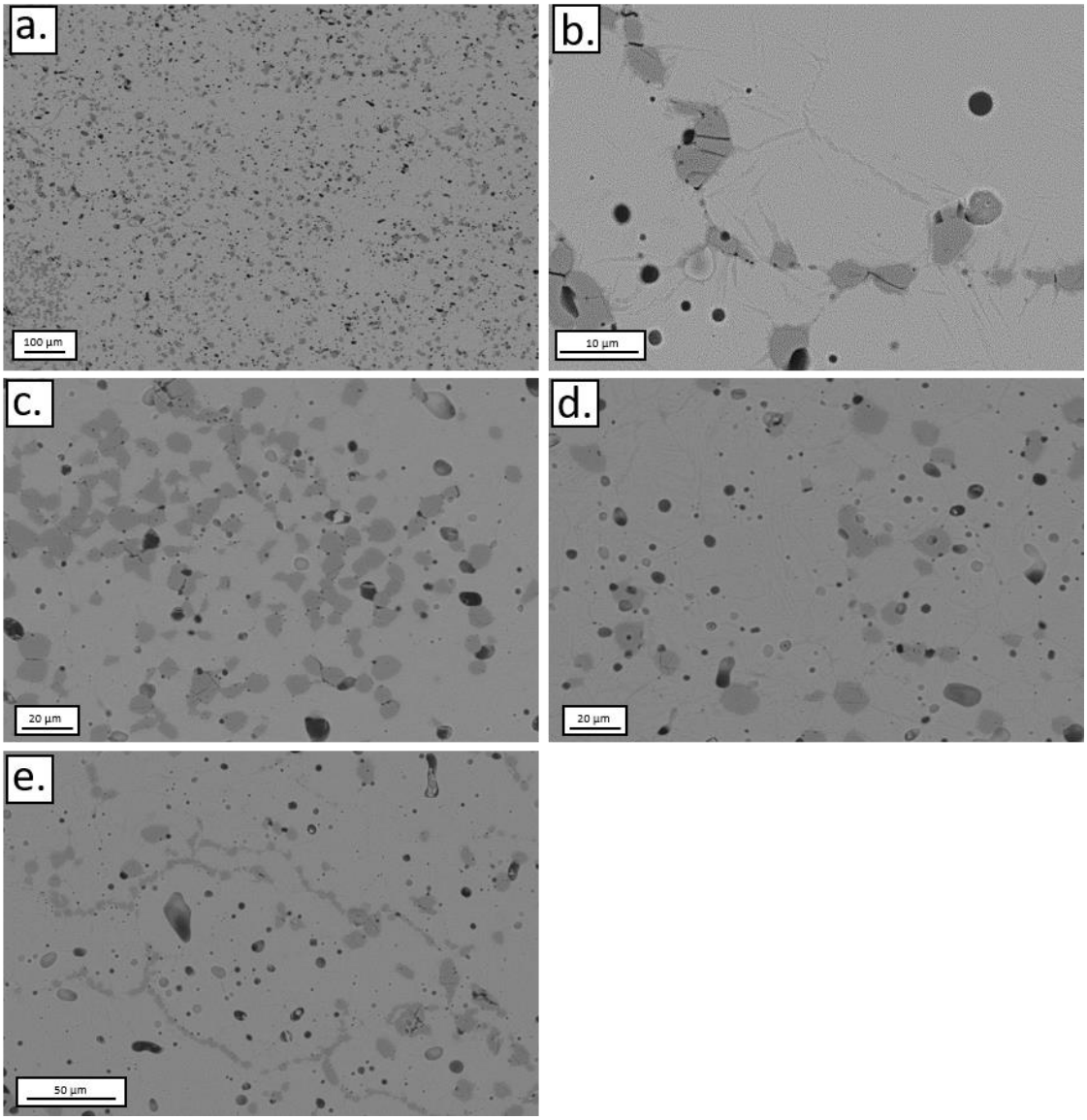

Fig. 4.9.2: Backscattered electron images of a SR derived titanium alloy containing 0.9 wt% C. a) Overall distribution of TiC particles and b) TiC precipitation along grain boundaries c) Clustering of TiC precipitates d) TiC lean area e) TiC formation along prior particle boundary. Note this particular sample is more heavily beta stabilised than SRA 1with a Mo Eq of 13.7 containing 1.25 wt% Mo an 3.9 wt% Fe, however the precipitation of TiC is thought to be the same.

The production of TiC particulate reinforced MMCs via the FFC process directly from synthetic rutile is an interesting prospect, especially as no additions need to be made. However, an in-depth analysis is out of the scope of this thesis and it will be considered in the future work section.

4.10 TiC Avoidance

TiC formation can be avoided in the first instance by calcining the synthetic rutile feedstock (1000°C, 2 h). As it is known that increased levels of TiC are found when the reduction process is overrun, TiC formation can also be reduced by proper control of the reduction process. With the respect to the consolidation technique, it has previously been reported that titanium samples consolidated via FAST picked up an average of 150 ppm carbon, when measured at the centre of the sample using the combustion method (ELTRA C/S 800) [28]. An in-depth report by by Mackie et. al showed significant carbon contamination when consolidating a SmCo based material using FAST, however, highly elevated carbon levels were limited to depths of around 10 µm from the sample surface when analysed using electron probe micro-analysis [40]. Hence, most of the carbon pick up occurs at the edge of the sample, which will typically be removed during machining. . Mackie et. al also suggest machining away the edges of the sample prior to any further processing . Hence, FAST is not seen as a source of significant carbon pick up, particularly when the outer surface layer is removed.

Finally, a rigorous post processing/washing procedure also minimises the carbon levels within the resulting alloy. Research is currently ongoing at Metalysis to optimise the post processing procedure.

Note, the less carbon found in the bulk sample measurement of the powder, the less of the coarse carbon ppt is observed. The SRA 1 sample used for the determination of the mechanical properties of the SR derived Ti alloy had 0.1 wt% C. No scum particles were found with minimal amounts of rare discrete carbon precipitate.

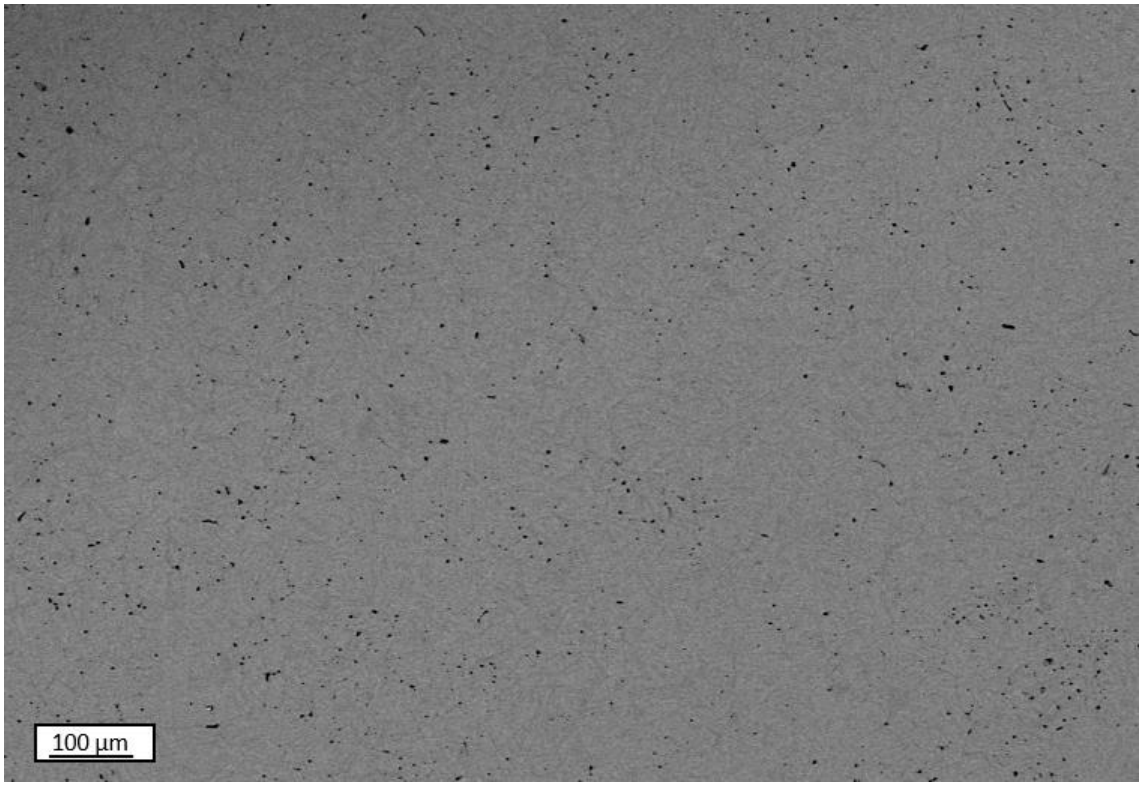

Fig. 4.10.1: Backscattered electron image of SRA 1 following consolidation via FAST at 1200°C with a dwell time of 30 minutes.

References

[1] I. E. Grey and A. F. Reid, "Reaction sequences in the reduction of ilmenite: 3-reduction in a comercial rotary kiln; an X-ray diffraction study," *Trans. Instn. Min. Metall. (Sect C: Mineral Process. Extr. Metall).,* vol. 83, pp. C39-46, 1974.

[2] Iluka Resources Operation, "Australasian Mining and Metallurgical Operating Practises," in *Monograph 28*, 3rd Edition ed. The Sir Maurice Mawby Memorial Volume, AusIMIM, 2013, pp. 1695-1707.

[3] I. E. Grey, L. M. D. Cranswick, C. Li, T. J. White and L. A. Bursill, "New M3O5- anatase intergrowth structures formed during low-temperature oxidation of anosovite," *Journal of solid state chemistry,* vol. 150, no. 1, pp. 128-138, 2000.

[4] R. G. Becher, R. G. Canning, B. A. Goodheart and S. Uusna, "A new process for upgrading ilmenitic mineral sands.," *Australian inst. Mining. Met. Proc,* vol. 214, pp. 21-44, 1965.

[5] J. Bultitude-Paull, Iluka Resources Limited, (personal communication), 2015.

[6] A. F. Wells, Structural Inorganic Chemistry, Oxford: Oxford university press, 1984 5th Edition.

[7] Iluka, "Synthetic Rutile," [Online]. Available: http://www.iluka.com/docs/3.3-operations/synthetic-rutile.pdf. [Accessed 25 09 2015].

[8] B. Thomas, F. Derguti and M. Jackson, "Continuous extrusion of a commercially pure titanium powder via the Conform process," *Materials Science and Technology,* pp. 1-5, 2016.

[9] I. Mellor, L. Grainger, K. Rao, J. Deane, M. Conti, G. Doughty and D. Vaughan, "Titanium powder production via the Metalysis process," in *Titanium powder metallurgy*, Oxford, Butterworth-Heinemann, 2015, pp. 51-67.

[10] C. Schwandt and D. J. Fray, "Determination of the kinetic pathway in the electrochemical reduction of titanium dioxide in molten calcium chloride," *Electrochimica Acta,* vol. 51, no. 1, pp. 66-76, 2005.

[11] G. Z. Chen, D. J. Fray and T. W. Farthing, "Direct electrochemical reduction of titanium dioxide to titanium in molten calcium chloride," *Nature,* vol. 407, pp. 361-364, 2000.

[12] D. T. L. Alexander, C. Schwandt and D. J. Fray, "Microstructural kinetics of phase transformations during electrochemical reduction of titanium dioxide in molten calcium chloride," *Acta Materialia,* vol. 54, pp. 2933-2944, 2006.

[13] C. Schwandt, D. T. L. Alexander and D. J. Fray, "The electro-deoxidation of porous titanium dioxide precursors in molten calcium chloride under cathodic potential control," *Electrochimica Acta,* vol. 54 , p. 3819–3829, 2009.

[14] D. T. L. Alexander , C. Schwandt and D. J. Fray, "The electro-deoxidation of dense titanium dioxide precursors in molten calcium chloride giving a new reaction pathway.," *Electrochimica Acta,* vol. 56, pp. 3826-3295, 2011.

[15] R. Bhagat, M. Jackson, D. Inman and R. Dashwood, "The production of Ti-Mo alloys from mixed oxide precurosrs via the FFC Cambridge process," *Journal of The Electrochemical Society,* vol. 155, pp. E63-E69, 2008.

[16] D. L. Alexander, C. Schwandt and D. J. Fray, "Microstructural kinetics of phase transformations during electrochemical reduction of titanium dioxide in molten calcium chloride," *Acta Materialia ,* vol. 54, pp. 2933-2944, 2006.

[17] H. Nakajim and M. Koiwa, "Diffusion in Titanium," *ISIJ International,* vol. 31, no. 8, pp. 757-766, 1991.

[18] J.A Murray and H.A Wriedt IN, R. R. Boyer, G. Welsch and E. W. Collings, Materials properties handbook: titanium alloys, Ohio: ASM International, 1994.

[19] V. Raghavan, "The Fe-O-Ti (Iron-Oxygen-Titanium) System, Phase Diagrams Ternary Iron Alloys.," *Indian Inst. Met.,* vol. 5, pp. 300-325, 1989.

[20] V. Raghavan , "Ti-O-Fe Phase Diagram. ASM Alloy Phase Diagrams Database, P. Villars, editor-in-chief; H. Okamoto and K. Cenzual, section editors," *http://www1.asminternational.org/AsmEnterprise/APD,* pp. Materials Park, OH, 2006.

[21] E. L. Molchanova, Phase diagrams of titanium alloys, Jerusalem : Isreal program for Scientific translations, 1965.

[22] A. D. McQuillian and M. K. McQuillian, Titanium, London: Butterworths Scientific Publications, 1956.

[23] F. Laves and H. J. Wallbaum, *Naturwissenschaften,* vol. 27, p. 674, 1939.

[24] H. W. Worner, *Journal of the institute of metals,* vol. 79, p. 173, 1951.

[25] D. H. Polonis and J. G. Parr, *Transactions of the american institute for mining and metallurgy engineers,* vol. 200, p. 1148, 1954.

[26] I. Polmear, Light alloys:, Oxford: Butterworth-Heinemann, 2006 4th Ed.

[27] Z. A. Munir, U. Anselmi-Tamburini and M. Ohyanagi , "The effect of electric field and pressure on the synthetsis and consolidation of materials: A review of the spark plasma sintering method," *Journal of Materials Science,* vol. 41, no. 3, pp. 763-777, 2006.

[28] N. S. Weston, F. Derguti, A. Tudball and M. Jackson, "Spark plasma sintering of Commerical and Development Titanium alloy powders," *Journal of materials science,* vol. 50, no. 14, pp. 4860-4878, 2015.

[29] *W. S. Rasband: ImageJ, U.S National Institutes of Health, Bethesda, Maryland, USA, 435 http://imagej.nih.gov/ij/, 1997..*

[30] Y. Liu, L. F. Chen, H. P. Tang, C. T. Liu, B. Liu and B. Y. Huang, "Design of powder metallurgy titanium alloys and composites," *Materials Science and Engineering: A,* vol. 418, no. 1-2, pp. 25-35, 2006.

[31] G. Lutjering and J. C. Williams, Titanium, Berlin: Springer, 2008.

[32] P. G. Esteban, L. Bolzoni, E. M. Ruiz-Navas and E. Gorgo, "PM processing and characterisation of Ti-7Fe low cost titanium alloys," *Powder Metallurgy,* vol. 54, no. 3, pp. 242-251, 2011.

[33] Thermo-Calc. Software, *TTT Titanium alloys database.*

[34] RTI. Metals, "RTI Titanium alloy guide," 01 2000. [Online]. Available: http://www.rtiintl.com/Titanium/RTI-Titanium-Alloy-Guide.pdf. [Accessed 02 08 2016].

[35] Z. Q. Chen, Y. G. Li and M. H. Loretto, "Role of alloying elements in microstructures of beta titanium alloys with carbon additions," *Materials Science and Technology October 2003 Vol. 19 1391,* vol. 19, pp. 1391-1398, 2003.

[36] J. C. Thesken, B. A. Lerch, J. Rodney Ellis and S. M. Arnold, "Particulate Titanium Matrix Composites Tested--Show Promise for Space Propultion Applications," 2003. [Online]. Available: https://ntrs.nasa.gov/archive/nasa/casi.ntrs.nasa.gov/20050215252.pdf. [Accessed 02 02 2017].

[37] S. C. Tjong and Y. W. Mai, "Processing-structure-property aspects of particulate- and whisker reinforced titanium matrix composites," *Composites Science and Technology,* vol. 68, pp. 583-601, 2008.

[38] D. B. Miracle, "Metal matrix composites – From science to technological significance," *Composites Science and Technology 65 (2005) 2526–2540,* vol. 65, pp. 2526-2540, 2005.

[39] S. C. Tjong and Z. Y. Ma, "Microstructural and mechanical characteristics of in situ metal matrix composites," *Materials Science and Engineering,* vol. 29, pp. 49-113, 2000.

[40] A. J. Mackie, G. D. Hatton, G. C. Hamilton, J. S. Dean and R. Goodall, "Carbon uptake and distribution in Spark Plasma Sintering (SPS) processed Sm(Co, Fe, Cu, Zr)z," *Materials Letters,* vol. 171, pp. 14-17, 2016.

Chapter 5:

Alloy Development of Synthetic Rutile Derived Alloys

Work from this chapter formed the basis of the following publication:

L.L. Benson, L. Benson Marshall, N. Weston, I. Mellor and M. Jackson. “On a Testing Methodology for the Mechanical Property Assessment of a New Low-Cost Titanium Alloy Derived from Synthetic Rutile” Metallurgical and materials transactions A. vol 48, pp 5228–5232, 2017.

5.0 Alloy Development of Synthetic Rutile Derived Alloys

Alloy development is a key component in the acquisition of low cost titanium alloy powder. Traditionally, titanium alloys have been designed to be produced via conventional processing routes (Kroll, VAR etc section 2.4). However, by virtue of increased interest in low cost titanium production routes and the advent of extraction routes capable of producing powder directly, novel alloys, designed specifically for solid state production routes has begun to be explored [1]. Throughout much of this research, low cost alloy design remains a prominent feature. By directly producing alloys from a synthetic rutile source, further cost savings are made viable.

Mechanical properties exhibited by the baseline titanium alloy derived from synthetic rutile (SR), determined in Chapter 4 have shown promising results, with a compressive yield strength and strain to failure similar to that of the widely Ti-6Al-4V alloy. As such, SR derived alloys have the potential to be commercially utilized without further alloying additions. However, for specific applications such as that of springs, where a low Young's modulus is required, the baseline alloy can be altered. By the addition (or reduction) of individual alloying elements, the subsequent mechanical properties can be adapted to the application's specific requirements. To be able to successfully tailor the alloy, the synthetic rutile baseline alloy requires a thorough understanding of how it behaves with the addition of each of the individual alloying elements.

As synthetic rutile derived alloys have not been previously created, it is important to understand how the inclusion of additional alloying elements will affect the mechanical, chemical and physical properties of the baseline alloy. Particularly as the baseline synthetic rutile derived alloy may not necessarily follow the pattern of pure titanium alloys, due to the distinctive presence of a range of remnant alloying elements.

Previous work has established that the addition of alloying elements influence microstructure evolution as well as mechanical properties when utilizing solid state fabrication techniques. Alteration of the rate of densification is one such effect, which may have significant consequences for the production route [1]. Other impacts include changes in compaction/consolidation behaviour, altered beta transus and the potential to form Kirkendall porosity [2] [3]. Furthermore, it is known that the addition of alloying elements may alter the reduction process. For example, the addition of molybdenum has been reported to aid a faster reduction process of titanium [4]. Effects of key alloying additions on consolidation, microstructure and mechanical properties will be studied throughout this chapter.

In the initial stages of this study, two pseudo binary synthetic rutile titanium alloys were created using chosen elements, Al and Mo in varying concentrations. Al is an effective α stabiliser and is commonly used throughout many commercial titanium alloys. Mo is an isomorphous β stabiliser, hence creates no intermetallic phases. Despite Mo's effectiveness as a β stabiliser, it has found little success in commercial titanium alloys in concentrations of greater than 6 wt% due to difficulties with segregation during the VAR stage. However, as the extraction and powder fabrication routes will both occur in the solid state, severe segregation effects can potentially be avoided, offering a competitive commercial advantage. A more detailed review of Mo additions to titanium alloys can be found in section 2.8.4.

Once created and of sufficient quality (oxygen and carbon below 0.4 wt% and 0.25 wt% respectively), the pseudo binary alloys were consolidated using field assisted sintering technologies (FAST) and mined for a range of mechanical data such as compressive yield strength and hardness values.

Note, it is imperative to understand the limitations associated with the study. Due to the batch product nature and small volumes produced at an R&D scale, variations in materials of construction (Fe, Cr and Al) and interstitial elements (O and C) were present between the alloys produced. Such variations made a true quantitative analysis unattainable. Although every effort was made to keep C and O values consistent, each alloy will have an optimised reduction profile and the optimisation of the reduction process was not deemed worthwhile during this initial exploratory stage of alloy development, leading to a standardised reduction process. Further, variation in O and C levels are observed from batch to batch at an R&D scale. Another source of variability between alloy powders was the degree of consolidation. Although all the alloys tested contained a similar amount of porosity (between 1-2%) the variation in porosity adds another layer of complexity when analysing the mechanical data. As such the data gained from these experiments act as guideline values in assisting the down-selection of alloys for specific applications. This data was intended to act as an orientative tool to aid the alloy design process rather than a quantitative analysis technique.

To assess the mechanical properties of the small quantity of powder created at an R&D scale, a small-scale testing approach needed to be designed. The small-scale approach consisted of consolidation via FAST and subsequent axi-compression testing using a thermomechanical compression machine (TMC). Validation of the small-scale approach was achieved by testing commercially available alloys and comparing them to both literature and modelled values using

modelling software JMatPro [5]. Testing of commercial alloys also provided a benchmark to directly compare against SR derived titanium alloys.

Bespoke graphite moulds were designed to produce a small 10 mm height by 11 mm diameter "pellet" from just 4.2 g of powder. This puck allowed the production of a thin disc for physical and chemical analysis and a small cylindrical compression sample to be machined. Prior to testing the SR derived alloys, the small-scale testing technique was validated using commercially available alloys: Ti-6Al-4V, Ti-5553 and Beta-C.

Following the harvesting of mechanical data, a model was designed using a multiple regression technique to aid and refine future alloy design, which is discussed in Chapter 6.

This chapter details the production and subsequent analysis of synthetic rutile derived titanium alloys doped with Al or Mo. Mechanical assessment of these alloys was achieved using a small-scale assessment technique. The development of the small-scale testing technique is provided within this chapter alongside the mechanical assessment of the enhanced synthetic rutile derived titanium alloys.

5.1 Small-Scale Testing Approach

At an R&D scale only small amounts of powder are produced (~9 g). To maximise the data yielded from these small quantities, a small-scale testing approach was specifically designed. Initially the powders were consolidated via the emerging FAST, chosen for its fast consolidation rates, minimal interstitial pick-up and ability to consolidate small volumes of material [2]. Following consolidation, small axi-compression samples were machined to allow the extraction of mechanical data from small quantities of powder.

However, the smallest standard set up of the FAST machine utilized a 20 mm diameter puck, which requires 9.9 g (Eq. 4.3.1) of powder to produce enough sample to machine out a small (6 mm diameter by 9 mm height) compression sample. Typical runs at R&D scale (20 g oxide) averaged around a 75% yield which produced around 9 g of powder. Of the powder produced, typically 3 g were used for analysis techniques granting around 6 g for consolidation. Hence, a new set of bespoke moulds were designed which allowed small quantities of powder to produce a solid pellet large enough for a variety of mechanical testing.

The solid pellet produced was designed to be sliced to yield a thin disc, used for microscopic studies, hardness testing and nanoindentation. The remainder of the puck was machined into a small 6 mm diameter by 9 mm height cylindrical axi-compression sample. Axi-compression

samples were compressed using the thermomechanical machine (TMC) at the University of Sheffield. Commercial alloys Ti-6Al-4V, Ti-5553 and Beta-C were also subject to the same consolidation and compression testing to i) validate the accuracy and reliability of the small-scale testing rig and ii) be directly comparable to the newly developed alloys. Although mechanical properties of commercial alloys consolidated via FAST can be found [6] [7] [8], tensile values are usually reported, or the samples have been produced under different consolidation conditions making direct comparisons invalid.

5.1.1 Small-Scale Mould Design

The initial prototype was designed to produce a 9 mm diameter by 11 mm height sample. Fig. 5.1.1 illustrates the specifications of prototype 1. A design flaw was found in using spacers (Fig. 5.1.1bii and 5.1.1bv) to fit into standard 20 mm platens. Unfortunately, the spacers could not withhold the load due to the holes in the standardised platens (required for pyrometric control) and failed upon loading. An additional design flaw of the first prototype was the small diameter size proved difficult to insert the graphite protective lining.

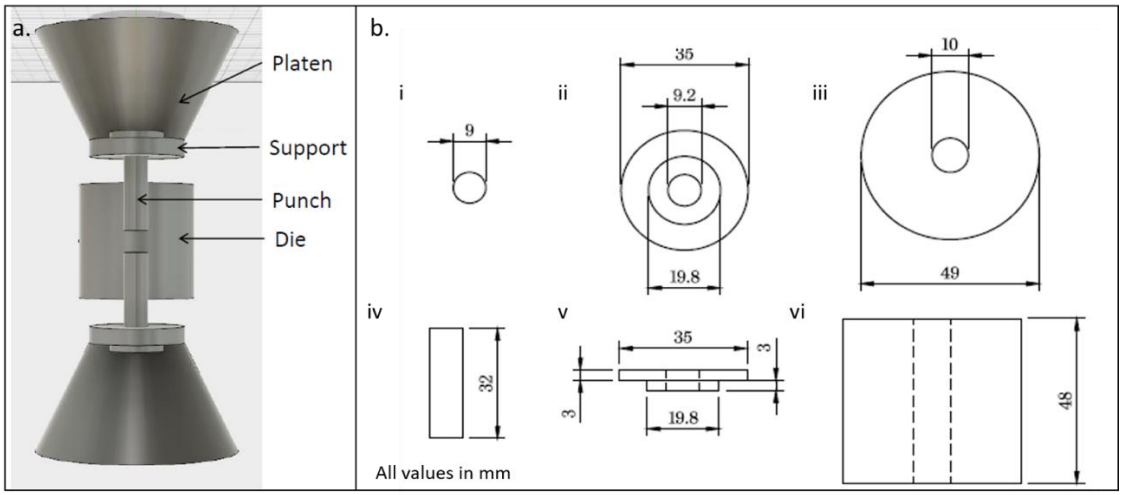

Fig. 5.1.1: a) CAD diagram of FAST mould set up and b) specifications for 9 mm diameter moulds (prototype 1): Top view of i) punch ii) support and iii) die. Side view of iv) punch v) spacer and vi) die [9].

Following the failure of the initial prototype, the moulds were redesigned. A second prototype was developed with slightly larger dimensions, possessing an 11 mm diameter (Fig. 5.1.2). To circumvent the spacer failure of the prior prototype, the spacers were made thicker and new solid platens used instead.

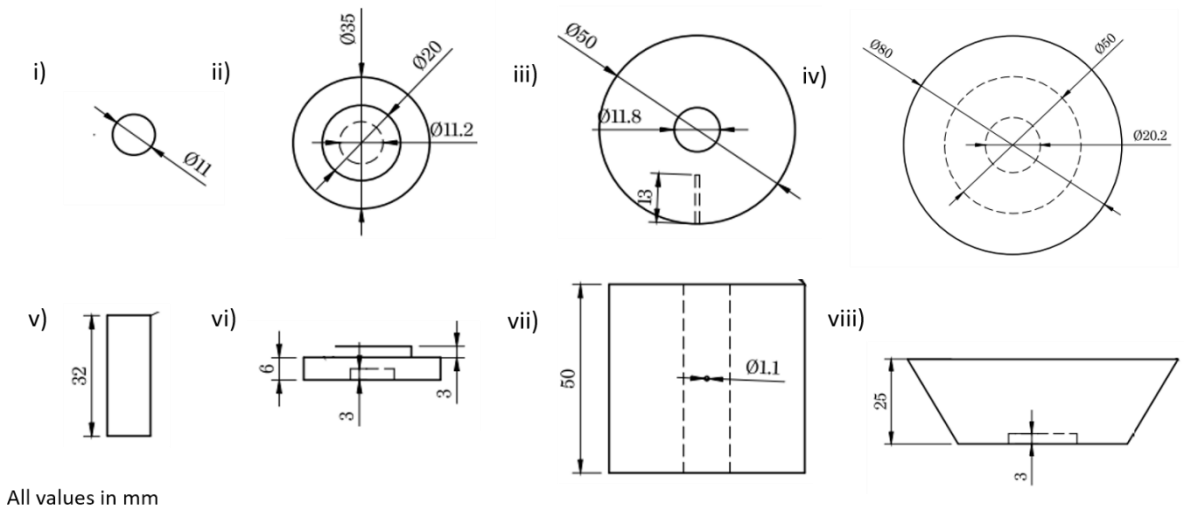

Fig. 5.1.2: Drawing of 11 mm graphite mould specifications i) ii) iii) and iv) top view of punch, spacer, die and support v), vi) vii) and viii) side view of punch, spacer die and support [9].

Utilizing prototype 2, 4.2 g of powder produced a pellet of 11mm diameter by 10 mm height, allowing the production of a 1-2 mm thick disc and a 6 x 9 mm compression sample (Fig. 5.1.3). The larger diameter size also made insertion of the graphite lining more straightforward. This design proved successful and a photograph of the mould and machined compression sample are shown in Fig. 5.1.4. However, due to the small size of the mould set-up, the usual axial pyrometer control could not be used. Instead, a 1.1 mm diameter hole drilled 1.3 mm deep allowed for K-type thermocouples to monitor the temperature. Inside of the die was lined with a graphite foil, before powder was added. Following consolidation, the graphite layer was removed via grit blasting.

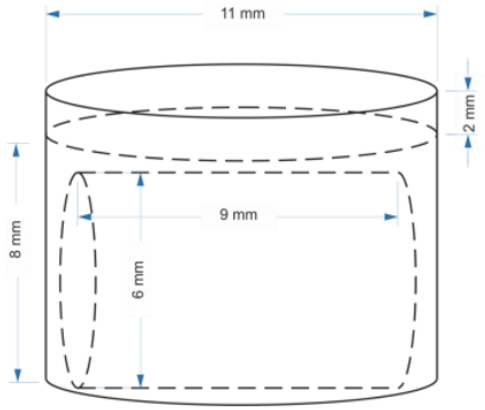

Fig. 5.1.3: Drawing of 11 mm diameter x 10 mm height pellet [9].

For each sample, FAST consolidation conditions were kept the same. Using thermocouple control, temperatures were limited to 1090°C. An applied pressure of 53 MPa (5 kN) was used with a 100°C/min ramp rate and a dwell of 30 minutes. Consolidation was executed under vacuum rather than an argon atmosphere to prevent entrapment of argon in the pores.

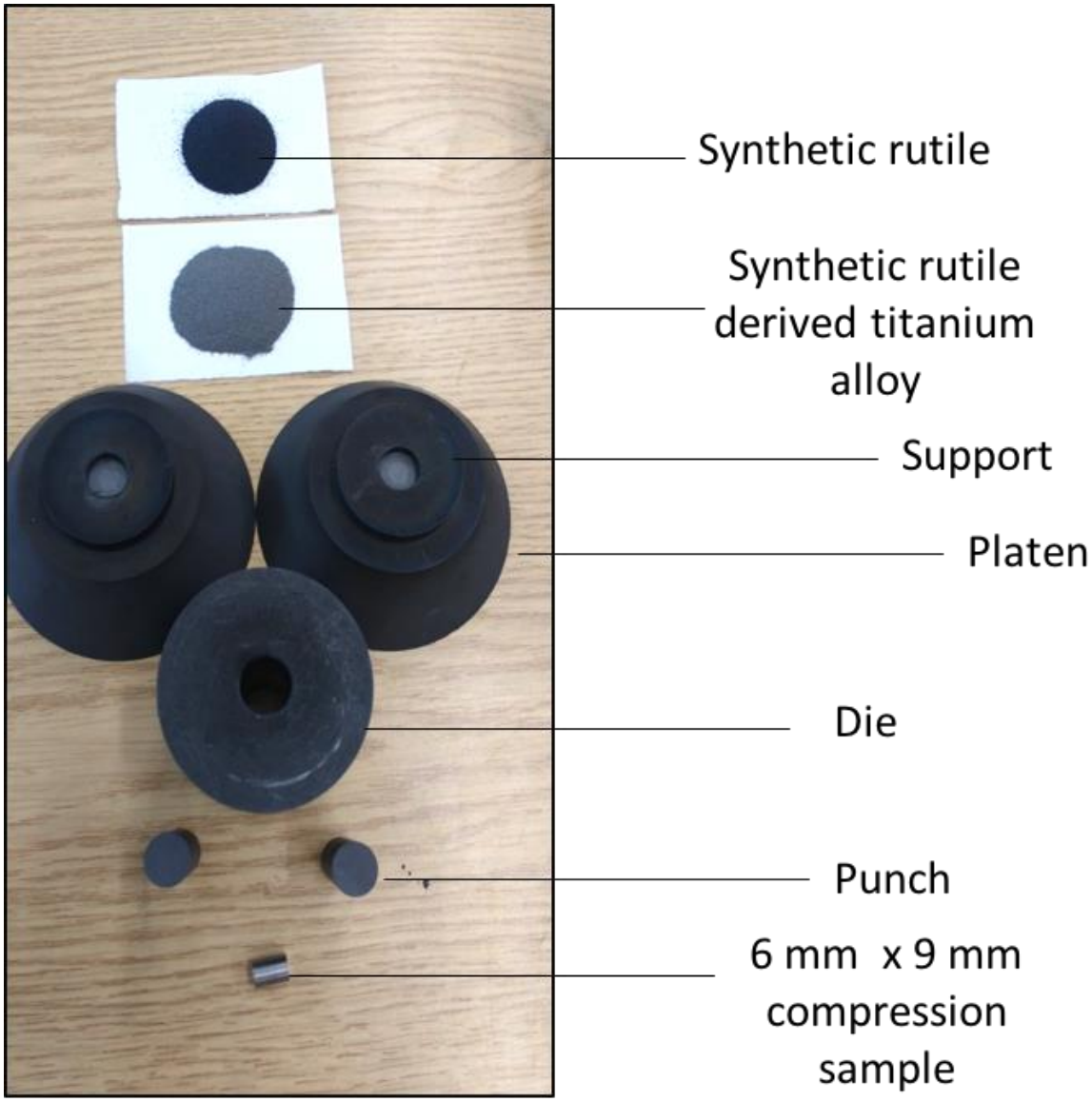

Fig. 5.1.4: Photograph of synthetic rutile, synthetic rutile derived titanium alloy, 11 mm FAST moulds and 6 mm x 9 mm machined compression sample.

5.1.2 Validation of the Small-Scale Testing Approach Using Commercial Alloys

Commercial samples Ti-6Al-4V, Ti-5553 and Beta-C underwent the small-scale consolidation and compression testing to both validate the approach and be directly comparable to synthetic rutile derived alloys. Table 5.1 details information of commercial powders used within the trials in comparison to the SR derived alloy.

Table 5.1: Morphology, oxygen content and particle size range of powders prior to consolidation and their microstructure and density following FAST consolidation.

Alloy	Morphology	Oxygen (ppm)	Particle size range (µm)	Density (%)	Microstructure
SR	Angular, spongy	3500	212-500	97.5	α/β lamellar
Ti-6Al-4V	Angular	2067	60-225	99.9	α/β lamellar
Ti-5553	Spherical	2972	20-150	99.9	β grains
Beta-C	Spherical	1613	20-150	99.9	β

Both Ti-5553 and Beta-C are typically unavailable in powder form. As such these alloys were gas atomised from forged and billet material respectively, yielding a spherical morphology. In comparison, Ti-6Al-4V was produced via HDH processing yielding an angular powder similar to the angular nature of FFC derived titanium (Fig. 5.1.5). However, FFC derived powders contain inherent internal porosity which slightly inhibits the densification process; previous work by Weston et al. has shown that when FFC derived powders are spheroidised and internal porosity removed, full density is achievable [2]. Note, spheroidisation also removes volatile Cl (present within FFC produced powders in small quantities), which is also known to hinder densification [10].

Generally, between the commercial powders, the size range was similar, between 20-225 µm, with Ti-6Al-4V possessing a larger fraction size than Beta-C and Ti-5553. However, the synthetic rutile derived titanium powder used was of a higher size fraction than the commercial alloy powders, which is also thought to impede the densification process [11].

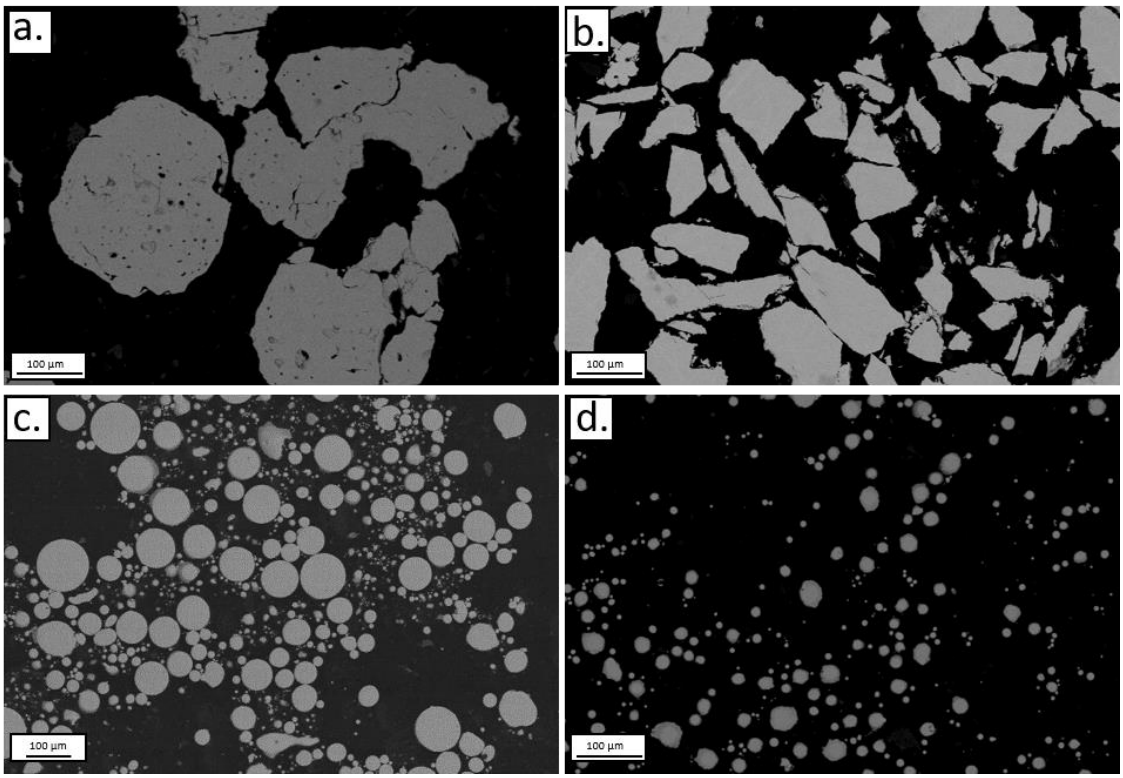

Fig. 5.1.5: Backscatter electron images of commercial alloy powders a) SR derived titanium alloy (SRA 1) b) Ti-6Al-4V c) Ti-5553 and d) Beta-C.

Full consolidation was achieved for all of the commercial titanium alloys using the small scale set up (Table 5.1). As the small-scale testing approach was limited to 1090°C due to using thermocouple control, slightly less consolidation of SRA 1 was achieved than when using the standard 20 mm set up (section 4.4). However, the microstructure achieved was similar, exhibiting a beta rich α+β lamellar morphology (Fig. 5.1.6), similar to that of α+β titanium alloy Ti-6Al-2Sn-4Zr-6Mo. Ti-6Al-4V exhibited a similar lamellar microstructure, somewhat finer than that observed of consolidated SRA 1 (Fig. 5.1.6). Consolidation of Ti-5553 produced large β grains of approximately 60 µm. Beta-C also existed as metastable beta phase at room temperature, no alpha was found under SEM (Fig. 5.1.6).

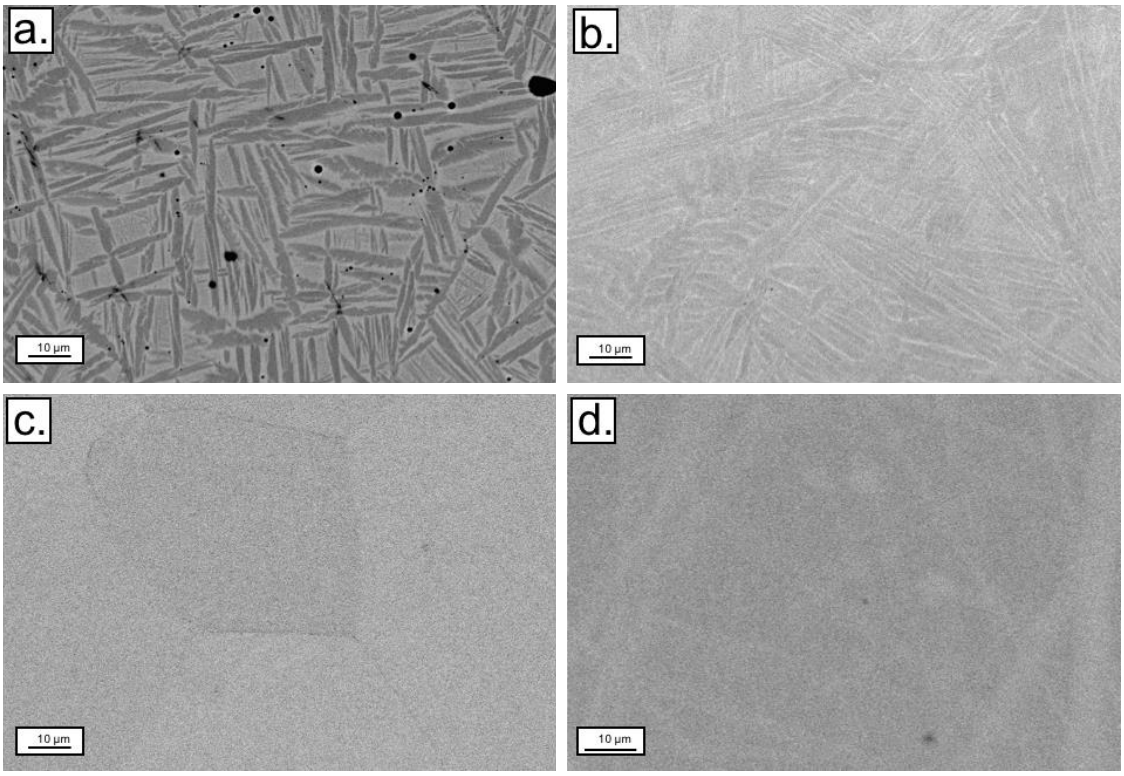

Fig. 5.1.6: SEM Backscatter electron images of consolidated a) SR derived alloy b) Ti-6Al-4V c) Ti-5553 and d) Beta-C.

Following consolidation, commercial alloy samples were compressed at room temperature to generate mechanical data such as compressive yield strength and strain to failure. Each of the alloys were consolidated and compressed three times to determine the repeatability of the approach.

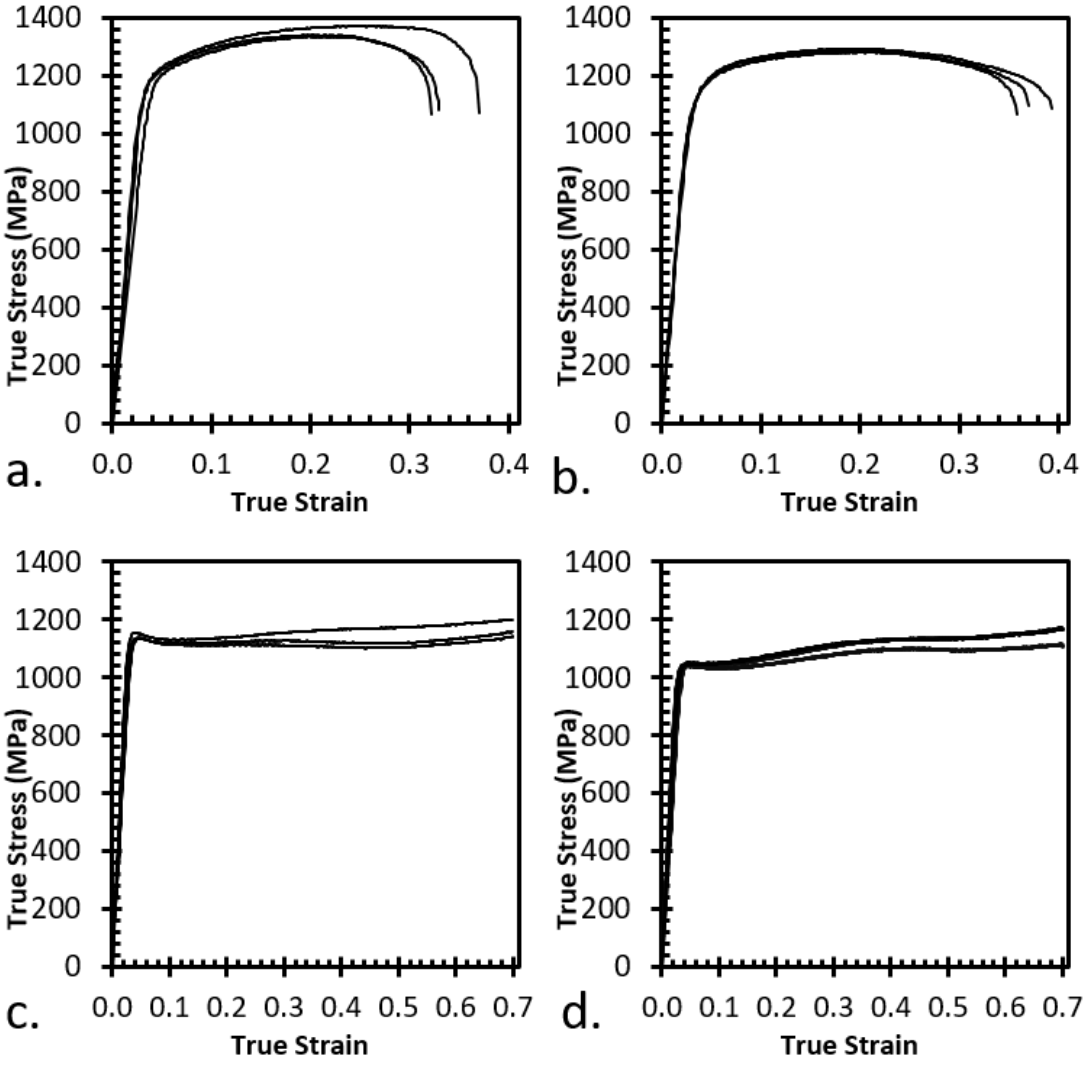

Fig. 5.1.7: True stress-true strain graphs at room temperature with a strain rate of 0.1 s^{-1} to a final strain of 0.7 a) SR derived titanium alloy (SRA 1) b) Ti-6Al-4V c) Ti-5553 d) Beta-C

Detailed descriptions of good practise for conducting axi-compression tests have been reported by Roebuck [12] and these were followed as closely as possible. The 6 mm diameter by 9 mm high sample size maintained the recommended aspect ratio of 1.5. Temperature was not recorded as tests were conducted at room temperature. Further, the addition of thermocouple holes in the samples would be significantly detrimental to the yield behaviour, due to the size of the hole compared with the sample height (>10 %). A constant strain rate of 0.1s^{-1} was applied up to a final strain of 0.7. Load, time, velocity and displacement were recorded throughout the experiments. Each alloy was tested three times to assess repeatability, with the resulting true stress-true strain curves shown in Fig. 5.1.7.

Each of the repeated compression test yield strength values are reported in Table 5.2. A variation of less than 4.5% was found between the values giving confidence in the reliability of the small-scale testing approach. To assess the accuracy of the test, the compressive yield strength values achieved were compared with values found in the literature for commercial alloys in a solution treated condition, typically as cast and HIPed (Table 5.2). Further validation was provided by use of modelling software, JMatPro [5]. This software predicts mechanical data based on the composition of the alloy. Note, this software is predicting tensile yield strength, however in the commercial titanium alloys tested there is usually less than 15% difference between the compressive and tensile values.

As seen in Table 5.2, the literature values are within 15% of the values achieved via the small-scale testing approach, providing confidence in the accuracy of the approach. It is also a sign of quality of the FAST technique which is capable of mimicking compressive yield strength values compared with traditionally fabricated titanium alloys. Values predicted by the modelling software are also similar, providing confidence in both the technique and the software.

Table 5.2: Experimentally determined compressive yield strength, literature yield strength and theoretical yield strength as determined by modelling software JMatPro [5]

Alloy	0.2% compressive yield strength experimental (MPa)	Compressive yield strength Literature (MPa)	J Mat Pro (grain size)
SR	1061, 1099, 1109	-	1016 (5 µm)
Ti-6Al-4V	991, 991, 1009	855-979 annealed [13] 897 cast and HIP'd [14] [15]	1058 (5 µm)
Ti-5553	1047, 1050, 1085	1138 cast and HIP'd [14] [15]	1154 (60 µm)
Beta-C	1025, 970, 971	1070-1110 ST and aged [13]	1016 (5 µm)

5.1.3 Comparison of Commercial Alloys and SR Derived Titanium Alloy

Following validation of the small-scale testing approach, the data produced from the commercial alloys is now directly comparable to the synthetic rutile derived titanium alloy. Figure 5.1.8 shows the true stress-true strain curves of the commercial alloys as well as the SR derived alloy.

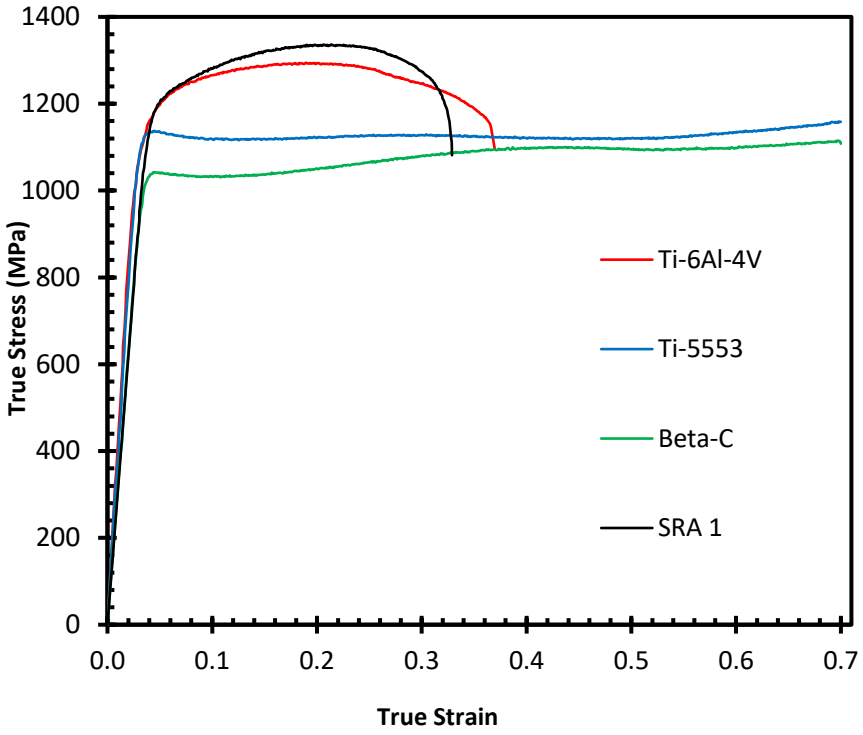

Fig. 5.1.8: True stress-true strain curve comparison of SR derived titanium alloy (SRA 1), Ti-6Al-4V, Ti-5553 and Beta-C

Due to the high levels of ductility afforded by large quantities of the β phase within both Ti-5553 and Beta-C alloys, neither sample fractured throughout compression testing to a strain of 0.7. Ti-5553 exhibited a higher yield strength compared to Beta-C with Ti-6Al-4V possessing the highest yield strength of all the commercial alloys. The synthetic rutile derived alloy achieved yield strength values almost identical to that of Ti-6Al-4V as well as experiencing failure at a similar strain (Fig. 5.1.8). Both alloys have chemistries resulting in the formation of beta rich α+β alloys. Microstructures displayed by both Ti-6Al-4V and SRA 1 are similar, with both alloys exhibiting a lamellar α+β structure. As such, the alloys possessed enhanced strength levels, but poorer ductility compared to the highly beta stabilised alloys.

5.2 Pseudo Binary SR Alloys (SR-Al and SR-Mo) Introduction and Limitations

Following validation, the small-scale testing approach can be exploited within the alloy development process. By creating a range of pseudo binary SR derived titanium alloys, the effects of individual alloying elements were able to be assessed. As SR derived alloys have not previously been studied in detail, it was important to understand the effects of additional alloying elements. The data generated from the production of pseudo binary SR derived alloys could then be used to create a predictive model using linear regression software. Once the effects of alloying elements Al/Mo were determined, this data could then be used to aid the design of alloys for specific applications which is detailed within Chapter 6.

However, before a comparison of physical and mechanical properties of the newly developed pseudo binary synthetic rutile alloys can be made, it is important to be aware of limitations associated with the study. First, it is difficult to directly contrast and compare many of the powders due to differences in C/O values as well as differences in the concentration of Fe/Cr which can vary due to contamination from the materials of construction. Hence, these values must be taken into consideration when evaluating the mechanical properties.

Density is also a source of transgression within this study as it has been previously reported that both Al and Mo have a detrimental effect on the sintering behaviour of titanium alloys, whereas Fe is known to enhance the sinterability of titanium alloys [1] [[16] [17]. Therefore, changes in the concentration of the Fe and/or alloying additions may result in differing degrees of sintering resulting in amounts of porosity following consolidation. Porosity was determined by analysing backscattered electron images using the image analysis software Image J [18]. It was found that there was a variation in porosity values between all consolidated alloys of 1%. Increased porosity is known to result in the premature failure of samples. Note, improved density values may be obtained by optimising the FAST process parameters for each individual alloy – however, in this study the process parameters were kept uniform for each individual consolidation.

As well as impacting densification rates, differences in rates of diffusion also influence the distribution of the alloying element during consolidation. As some alloys produced did not achieve full homogenisation (mostly SR-Mo alloys) after consolidation, this is another source of error and must be considered when analysing the mechanical data produced from the alloys. Table 5.3 lists the diffusion rates of Al, Mo and Fe within β-titanium.

Table 5.3: Average diffusion rates of Al, Mo and Fe within β-titanium [19]

Average rate of diffusion ($x10^{-13}$ m^2 s^{-1}) in β-Ti

Temp (°C)	Al	Mo	Fe
1250	~12.5 ± 7.5	3.25 ± 1.25	~300
1020	1 ± 0.2	0.33 ± 0.15	~30

Although aluminium has a relatively slow diffusion rate within titanium compared to Fe, it is often cited as a 'fast' diffuser [19]. Aluminium is not technically a fast diffuser, however, due to its high solubility in both phases of titanium, aluminium is not subjected to the same segregation issues as the β stabilisers and as such, aluminium rapidly distributes itself throughout the alloy [19]. Therefore, although aluminium is a relatively slow diffuser, it is a fast distributor.

Note, mechanical properties obtained from this study will be compared with that predicted by modelling software JMatPro. However, the software assumes 100% density which is not accurate. Further, the software is also unable to take account for Mn or Cl content, however these values are fairly consistent.

5.3 Aluminium alloy powder Introduction

Effects of aluminium on the synthetic rutile baseline alloy were chosen for further study as aluminium is the only non-interstitial alpha stabiliser and is commonly found in the majority of commercially successful titanium alloys. A more in depth analysis of the effect of aluminium in titanium alloys can be found in section 2.8.3. There is little published data available on the behaviour of aluminium as an alloying element throughout the FFC reduction process, although Metalysis have successfully produced Ti-6Al-4V powders. Aluminium enhanced synthetic rutile was made by mixing synthetic rutile with Al_2O_3 for 4 hours in a Turbula mixer before firing at 1350°C for 4 h.

5.3.1 Pseudo Binary SR-Al Feedstock Production

The feedstock powder was mixed for 4 h as this was thought to be a sufficient amount of time to allow for complete mixing of the powders. Prior to selecting the heat treatment temperature of 1350°C, the equilibrium phase diagram of rutile and corundum (TiO_2-Al_2O_3) was consulted (Fig. 5.3.1). At temperatures above 1200°C, the Al_2TiO_5 phase is known to form. This phase then decomposes in a eutectoid reaction to produce the constituting TiO_2 and Al_2O_3 phases. By incorporating Al_2O_3 into the synthetic rutile feedstock (rather than coating the particles), it was thought a more homogeneous distribution of the alloying aluminium would be achieved in the resulting alloy.

*Note, 1350°C was selected to ensure the temperature was firmly in the TiO_2 + Al_2TiO_5 region as other work has noted Al_2TiO_5 is only thermodynamically stable above 1280°C [20] [21]. The equilibrium phase diagram was used as a guide only, as it is also known that the presence of other oxides such as SiO_2, ZrO_2, Fe_2O_3 and MgO can influence the rate of decomposition of Al_2TiO_5 [21] [22]. Additionally, the equilibrium phase diagram is that of TiO_2 and Al_2O_3. Synthetic rutile, as discussed in Chapter 4, is predominantly made of reduced rutile phases ($TiO_{1.933}$) as well as containing pseudobrookite and some metallic Fe (section 4.1). The presence of pseudobrookite (Fe_2TiO_5) may have a considerable impact on the production and decomposition of Al_2TiO_5, as these phases are isomorphous [21]. Iron has also been previously shown to stabilise the Al_2TiO_5 phase [23], and can also form an M_3O_5 solid solution between Fe_2TiO_5 and Al_2TiO_5 [24].

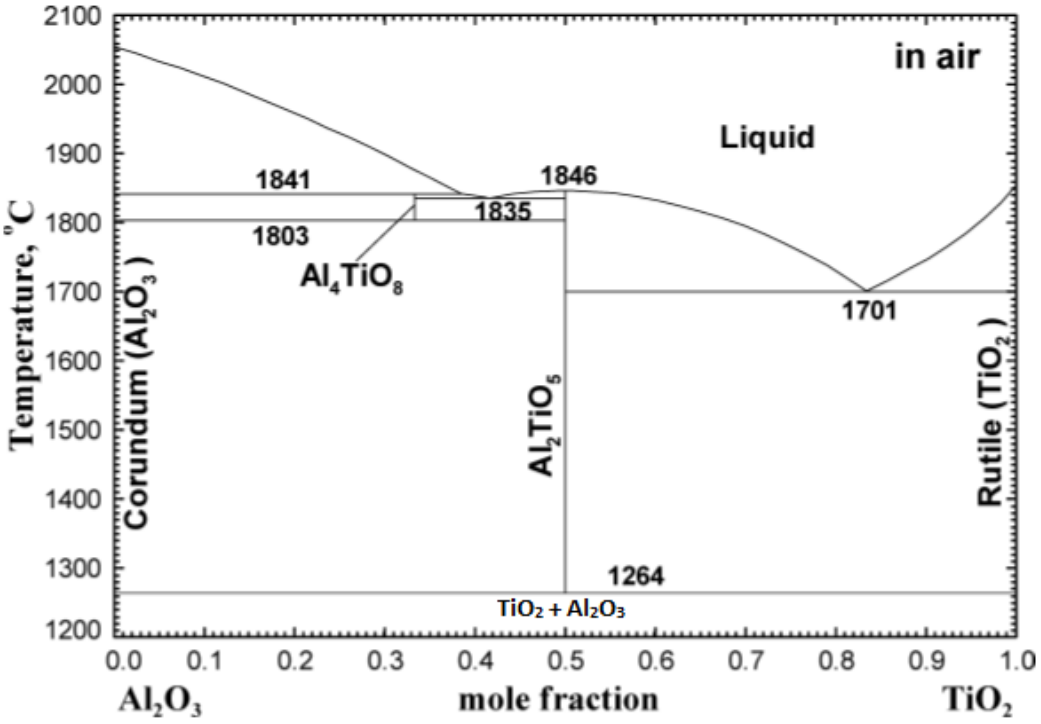

Fig. 5.3.1: Calculated Equilibrium phase diagram of TiO_2-Al_2O_3 [25].

Two feedstocks were created; both consisted of synthetic rutile with 6 wt% Al_2O_3 and were mixed for 4 h in the Tubula. The first sample (Al1100) was then heat treated in air at 1100°C for 4 h, below the temperature of Al_2TiO_5 formation. Whereas the second sample (Al1350) was heat treated in air at 1350°C.

Figure 5.3.2 displays backscattered electron images of samples of SR feedstock + 6 wt% Al_2O_3, heat treated at 1100°C and 1350°C. Al1100 shows the presence of aluminium oxide coating the SR particles and is observed as a darker phase under SEM. Enlarged images can be found in Appendix 2. Al_2O_3 appears darker in comparison to the synthetic rutile due to its lower atomic number. Note, most particles are coated, although the thickness of the coating does vary and is not homogeneous. In comparison, sample Al1350 does not show the presence of a consistent Al_2O_3 coating. It is therefore deduced that the aluminium is likely dispersed throughout the synthetic rutile, although it is unclear if the aluminium is present as Al_2TiO_5, Al_2O_3 (from a eutectoid-like decomposition of Al_2TiO_5) or if the aluminium has substituted into pseudobrookite present in the synthetic rutile.

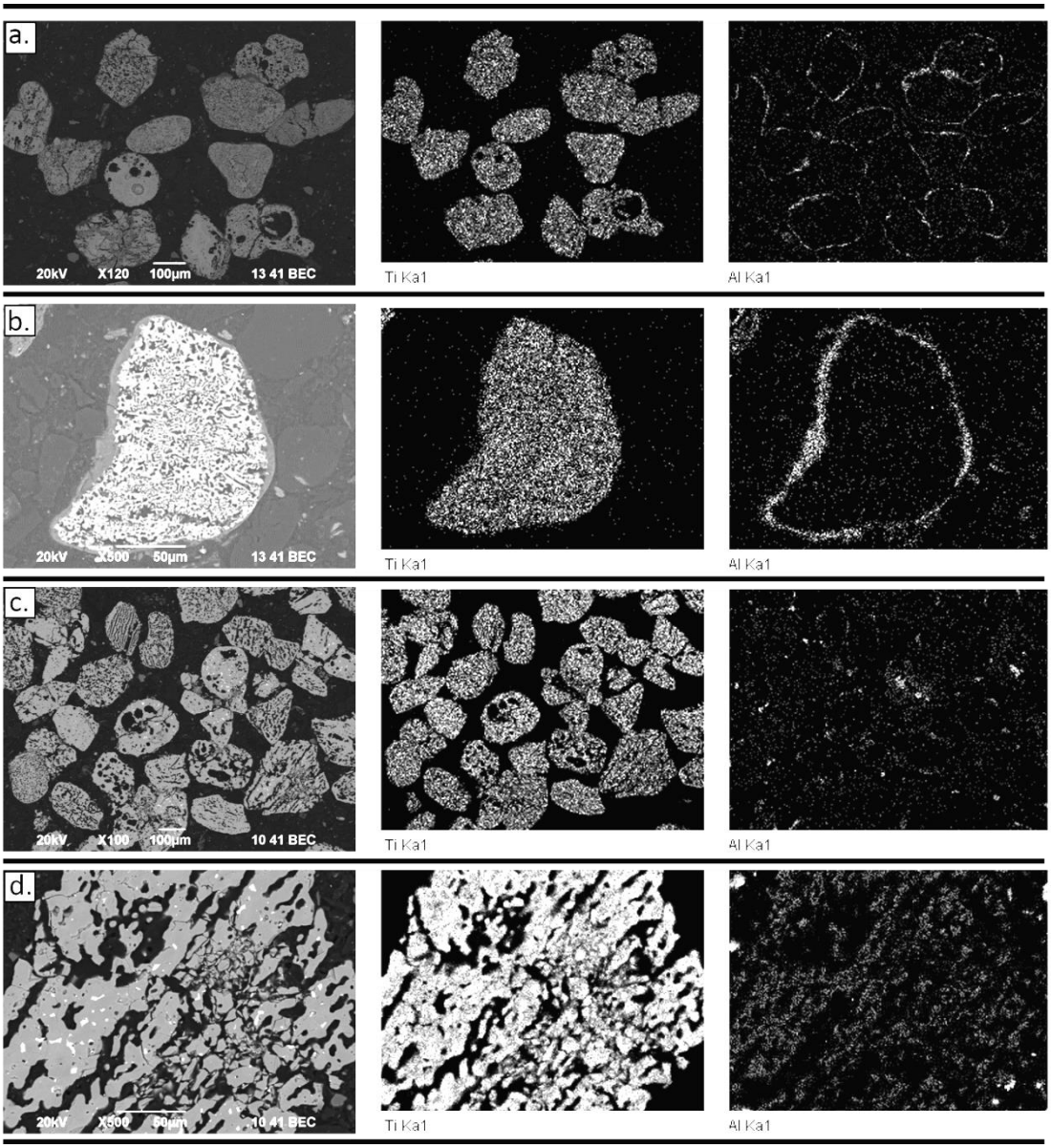

Fig. 5.3.2: Backscatter electron images and corresponding X-EDS map of a) and b) SR+ 6wt Al_2O_3 feedstock heat treated at 1100°C 4h c) and d) SR + 6wt% Al_2O_3 feedstock heat treated at 1350°C 4h.

Hence, XRD analysis was performed to aid the determination of phases present on a sample of SR + 33 wt% Al_2O_3, separately heat treated to 1100°C and 1350°C. As the Al_2TiO_5 phase is known to undergo a eutectoid decomposition (Fig. 5.3.1) the high amount of Al_2O_3 was chosen in an attempt to retain some of the Al_2TiO_5 phase. Fig. 5.3.2 shows the XRD spectrum produced.

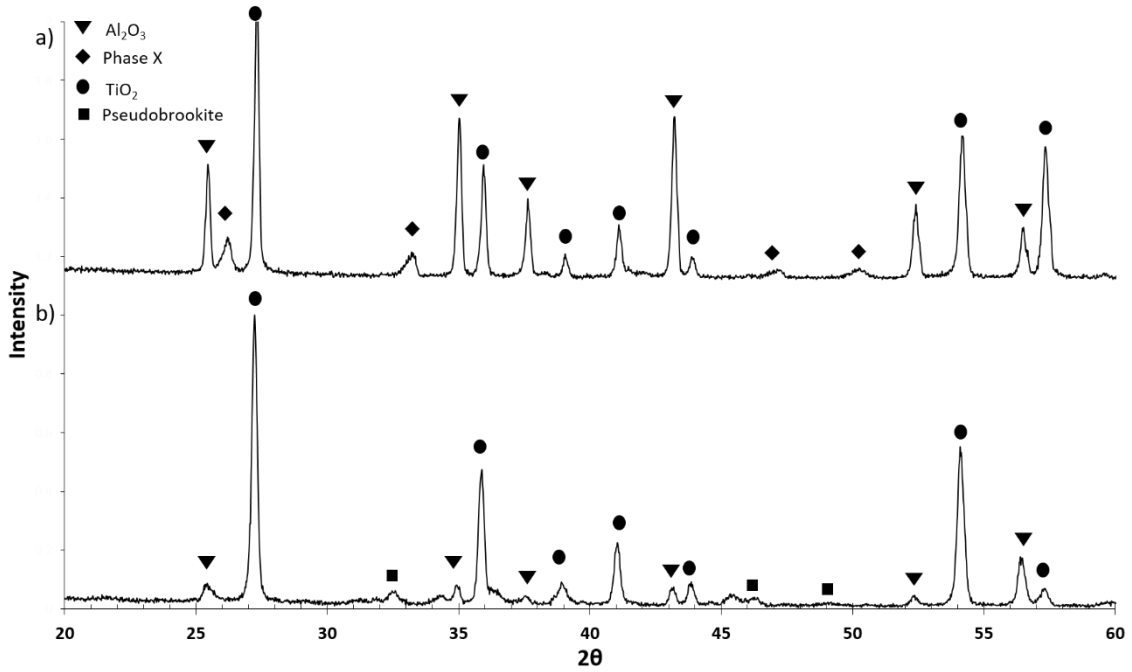

Fig. 5.3.2: XRD spectra produced of a) SR-33 wt% Al heat treated at 1350°C for 4 h b) SR-33 wt% Al heat treated at 1100°C for 4h.

In the sample heat treated to 1100°C, the XRD spectrum displayed (Fig. 5.3.2) only TiO_2 (rutile) and Al_2O_3 (corundum). The SR + 33wt Al_2O_3 heated to 1350 however, contains additional peaks to the TiO_2 and Al_2O_3 found in the Al1100, labelled as 'Phase X' in Fig. 5.3.2. The additional peaks are similar to that of Al_2TiO_5 but slightly shifted to the right, or pseudobrookite but shifted to the left. The shift could be due to impurity present within the compound, such as the inclusion of Fe into the structure. Alternatively, the peaks also correlate with those of the pseudobrookite (Fe_2TiO_5), if shifted slightly to the left. Fig. 5.3.3 shows a magnified area of the XRD spectrums of SR heat treated at 1350°C (4 h) and SR +33 wt% Al_2O_3 also heat treated at 1350°C (4 h) and the simulated plot of Al_2TiO_5 to more clearly demonstrate the shift observed.

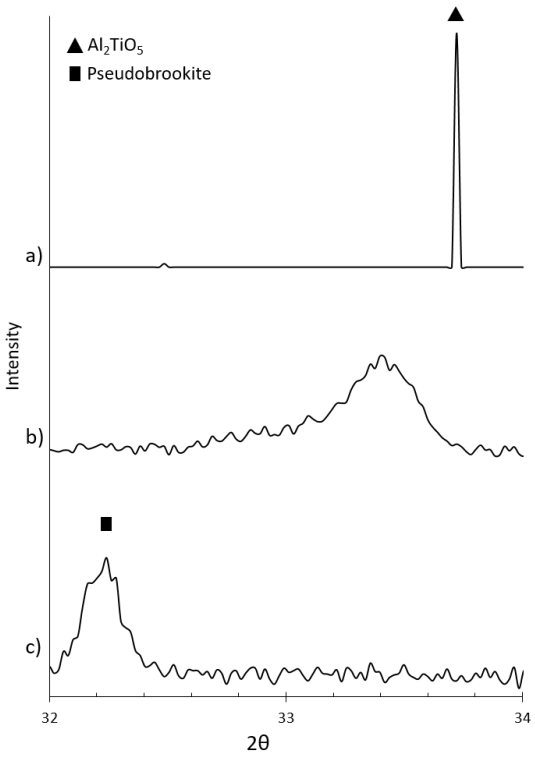

Fig. 5.3.3: XRD spectrum of a) Simulated plot of Al_2TiO_5 b) 33 wt% Al_2O_3 in SR heat treated to 1350°C for 4h and c) SR heat treated at 1350°C for 4 h.

With the aid of Rietveld analysis [26], it was shown that the shifted peaks observed in the SR + 33 wt% Al_2O_3 aligned most closely with that of a $FeAlTiO_5$ phase.

As an additional observation, within the SR + 6wt% Al_2O_3 feedstock, areas of high aluminium content occasionally corresponded with areas of high iron concentration as shown in Fig. 5.3.4. Areas of increased concentrations of Fe and Al suggests the presence of the M_3O_5 phase, containing either Al_2TiO_5 with substituted Fe or pseudobrookite, M_3O_5, with incorporated aluminium. It may also be the presence of a solid solution, formed between Fe_2TiO_5 and Al_2TiO_5 or the presence of $FeAlTiO_5$ in small quantities.

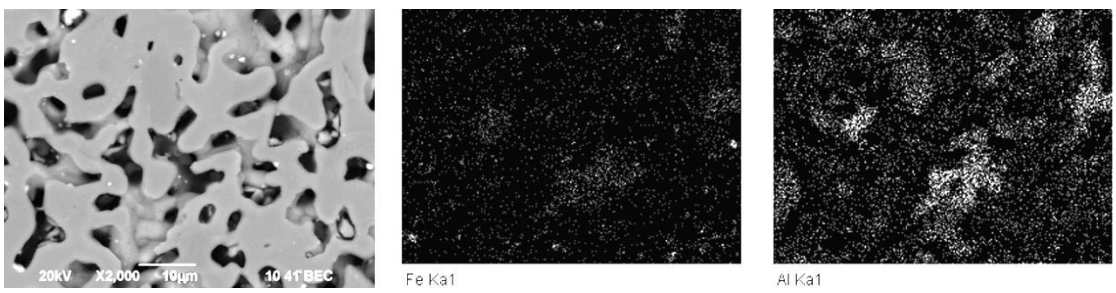

Fig. 5.3.4: Backscatter electron images and corresponding X-EDS maps of a SR + 6wt% Al_2O_3 feedstock heat treated at 1350°C for 4 h.

Both pseudobrookite and Al_2TiO_5 have the general formula of M_3O_5 and are known to be isomorphous [20]. Further, substitution of Al into the pseudobrookite structure is known, with solid solutions of $Al_{2-2x}Fe_{2x}TiO_5$ (where $0 < x < 1$) being reported [27]. A higher resolution technique would be required to determine the exact phase that has formed within Al1350. Possibilities include Al substitution into the pseudobrookite or Fe substitution into the Al_2TiO_5 or, an M_3O_5 solid solution has formed, resulting in phases such as that of $AlTiFeO_5$.

Note, the Al1350 sample contains 33 wt% Al_2O_3, as such it is likely the peak produced is shifted further to the right than in the feedstocks used to create SR derived titanium alloys (~6 wt%). Hence, a further sample of a much lower Al_2O_3 content (SR + 10 wt% Al_2O_3) was analysed and did not exhibit the $AlTiFeO_5$ phase, however, the phase may have been present in quantities undetectable via XRD. Interestingly, the peaks observed within the SR +10 wt% when analysed via Rietveld analysis [26], indicated the presence of both Fe_2TiO_5 and a smaller quantity of Al_2TiO_5. The presence of Al_2TiO_5 at lower concentrations of Al_2O_3, and the presence of $AlTiFeO_5$ at higher concentrations of Al_2O_3, indicates that the concentration of Al_2O_3 affects the phases that form throughout the heat treatment however, in situ experiments are required to fully understand the phases formed throughout the calcinations.

Hence, at the higher heat treatment temperature, aluminium is no longer solely on the outside of the SR particles, along with the XRD data, which shows that the formation of an Al containing M_3O_5 phase is feasibly formed at 1350°C, it is likely that an Al_2TiO_5 phase (or variation thereof) is formed at the higher heat temperature. However, the extent of its decomposition to TiO_2 and Al_2O_3 is unclear and further in-depth investigation would be required to determine this.

Therefore, the SR-Al binary alloys made throughout this work have been produced by mixing SR and varying quantities of Al_2O_3 for 4 h prior to a heat treatment of 4 h in air at 1350°C. This specific heat treatment was chosen to aid the distribution and retention of the aluminium throughout the reduction process.

5.4 Pseudo Binary SR-Al Titanium Derived Alloys Powder Analysis Following Reduction

In comparison to the plain synthetic rutile derived titanium alloy, SR derived titanium alloys with enhanced aluminium concentrations tend to exhibit a spongier microstructure, despite having similar oxygen levels (Fig. 5.4.1).

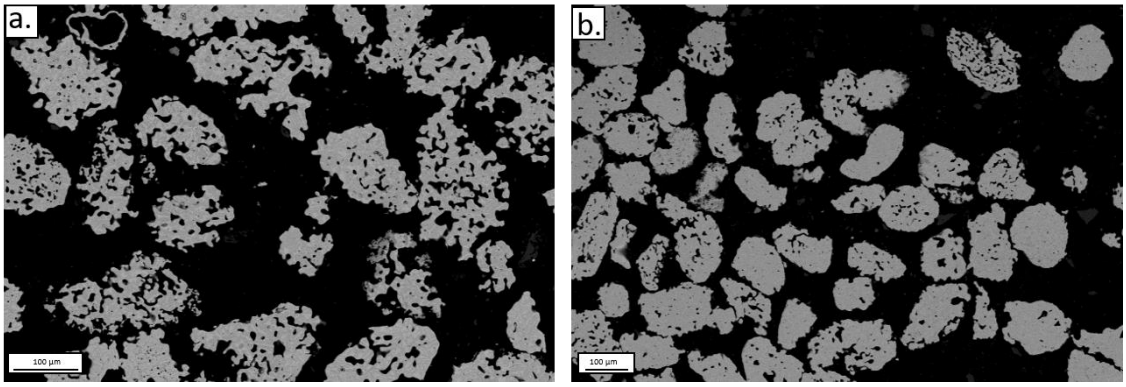

Fig. 5.4.1: a) Backscattered electron images of 5.3 wt% Al doped SR derived titanium alloy powder with 2030 ppm oxygen and b) Plain SR derived titanium alloy with 2155 ppm oxygen, both alloys reduced for 16 h.

Prior research has been undertaken to understand the effect aluminium has on the sintering behaviour of titanium [1] [28][30]. During the sintering of titanium alloys containing aluminium alloying additions (using a blended elemental technique), an increase in the compact size is observed once the sintering temperature surpasses that of the melting point of aluminium [29]. Previous work has determined this behaviour to be linked to the formation of Kirkendall voids formed by the diffusion of aluminium in titanium, as well as the formation of Ti_3Al [29] [31]. However, the formation of Kirkendall porosity following consolidation of the SR-Al alloys in this work was not observed and may require more in-depth investigation.

The morphology observed of fully reduced Al enhanced SR (5.3 wt% Al) are comparable to that of partially reduced plain SR alloys with higher oxygen concentrations (~5 wt% O 8 h). The less sintered appearance of the particles (despite low oxygen levels) could be due to the detrimental effect aluminium is known to have upon the sinterability of titanium alloys [1]. Alternatively, or in addition to this effect, aluminium raises the beta transus and generally requires longer reduction times compared to that of undoped synthetic rutile. As such, the powder has been fully reduced for less time after 16 h and has had less time to sinter. Note plain baseline SR achieved low oxygen levels (<4000 ppm) after 12 hours of reduction Fig. 4.2.8.

Note, although the aluminium enhanced powders generally display a more porous microstructure, enhanced sintering afforded by iron is still observable. The mapping images shown below in Fig. 5.4.2 illustrate more porous particles may have an increased aluminium content, however a decreased iron content is sometimes also found in these particles in comparison to the more heavily sintered particles.

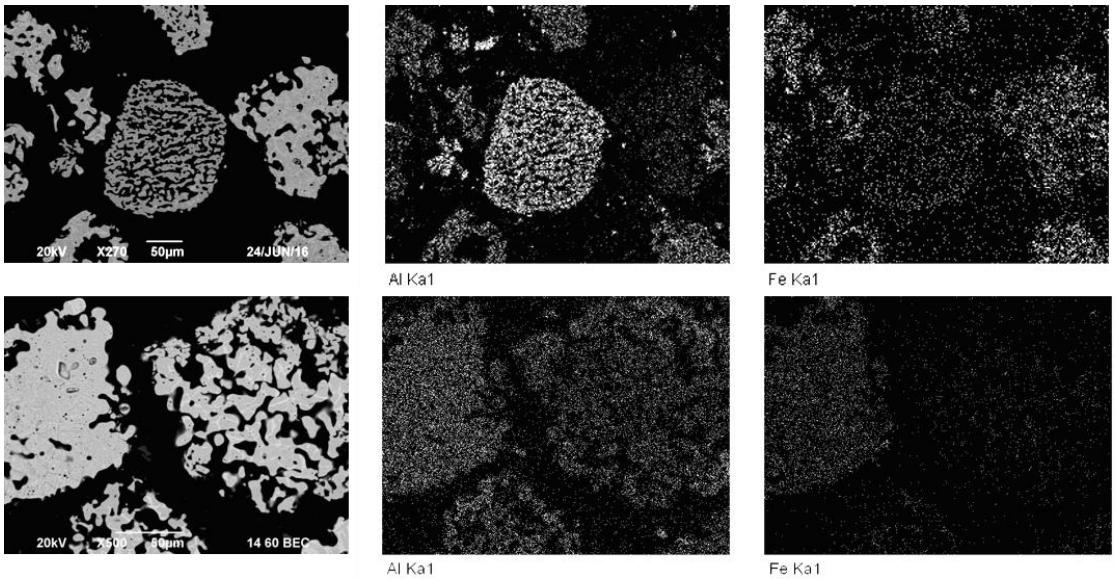

Fig. 5.4.2: Backscatter electron X-EDS mapping images of relative Al and Fe concentrations in a sample with 5.3 wt% Al in the bulk powder. More sintered particles show an increased iron content.

Pseudo binary SR-Al alloys all exhibited some inhomogeneity in terms of distribution of aluminium. A slight local variation in the concentration of iron had already been observed from the initial reductions of the plain synthetic rutile (section 4.3). Aluminium distribution inhomogeneity is also apparent, with some particles displaying a more heavily alpha stabilised microstructure than others (Fig. 5.4.3a). Figures 5.4.3a and 5.4.3b display a particle heavily alpha stabilised, containing around 14.5 wt% Al in the alpha phase, determined by X-EDS. Figure 5.4.3b shows the Al rich particle is not entirely alpha stabilised and does contain small regions of the beta phase.

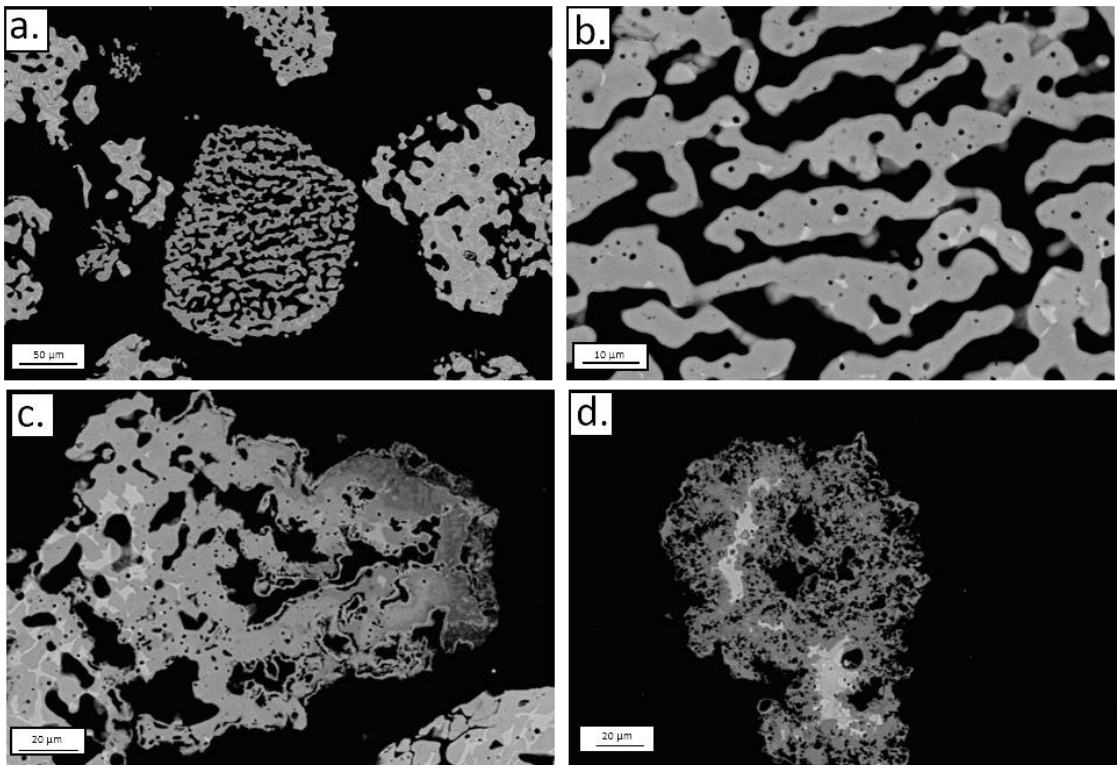

Fig. 5.4.3: Backscatter electron images of a) 5.3 wt% Al enhanced synthetic rutile powder illustrating local variations in Al content as apparent by difference in contrast/ extent of sintering b) close up of particle containing 14.5 wt% Al c) particle containing 35-55 wt % Al on RHS, LHS highly alpha stabilised d) Particle exhibiting 10 wt% C phase outer region with high Al (8 wt%) and Fe (13 wt%) centre.

In some extreme cases, particles were found with exceptionally high aluminium contents, leading to the possible formation of undesirable titanium aluminides (Fig. 5.3.4c). Although all of the SR-Al alloys powder bulk contained less than 6 wt% aluminium, high local concentrations of aluminium led to the formation of extremely high aluminium concentrations in some particles. Improved mixing technique and sieving of the aluminium oxide prior to mixing (to reduce clumps and/or clumping) would lead to improved homogenisation prior to reduction, avoiding the formation of such particles.

In addition to particles with excessively high Al content, other undesirable particles were also observed. Fig. 5.3.4d displays the presence of carbon rich particles, although these particles are also observed in the reduction of plain SR (section 4.8), whereas the outer darker layer consists of a light carbon rich layer (~10-15 wt% C, ~5 wt % Si, bal Ti). The centre of these particles typically exhibit high aluminium and iron contents. The high content of carbon within these particles suggests they are 'scum' particles which have originated from the top of the cathode sample and should have been removed during post processing.

Titanium carbide precipitates were also observed within the SR-Al powders, even when the carbon content was less than 0.15 wt% C. Formation of titanium carbides has been discussed in more detail in Section 4.8.

Although there are a range of undesirable particles produced, these particles were produced in small quantities, which would be further reduced when producing powders at a larger scale. Formation of most of these defect particles can be avoided. Careful mixing techniques would reduce or eliminate the formation of highly Al rich particle as well as produce a more homogeneous distribution of Al. Carbon rich scum particles would be removed during post processing procedures of which Metalysis are currently developing but are of a commercially sensitive nature. TiC precipitation can be controlled/avoided by initial calcination of synthetic rutile feedstock followed by an improved post processing procedure to remove particles of high carbon content (Section 4.10).

After characterisation of the SR-Al powders, Table 5.4 lists all the aluminium enhanced powders chosen for consolidation, listed in order of increasing Mo equivalency with the exception of Al7 as this alloy had anomalous properties which is further discussed in section 5.4.1. Selection criteria for SR-Al alloys to be mechanically tested were alloys with aluminium content between 1-5.5 wt%, oxygen lower than 4000 ppm and carbon below 2600 ppm.

Table 5.4: Mo. equivalent and chemical composition (Al, Fe, Cr O, C) of pseudo binary SR + Al alloys

Alloy	Al wt%	Fe wt%	Cr wt%	Oxygen (ppm)	Carbon (ppm)	Mo Eq.
Al1	2.8	2.2	0.7	2572	2562	5.6
Al2	2.4	2.2	0.9	3779	485	6.1
Al3	5.3	3.4	0.4	2030	1065	6.1
Al4	3.4	3.	0.5	2828	1004	7.1
Al5	3.6	3.9	1.0	3235	2261	10.3
Al6	2.7	3.9	1.4	2030	2111	11.8
Al7	2.4	3.4	0.4	1532	2467	9.1

Table 5.4 includes elements containing the most variation. Other measured alloying elements (Si, V, Mn, Nb, Ta, Zr) remained fairly constant between all alloys and a full composition of each of the produced alloys can be found in Appendix 1. Fe and Cr values differed due to contamination from the materials of construction (stainless steel). Variation in carbon values were also observed but typically did not exceed 0.26 wt%. Table 5.4 also includes the corresponding Mo equivalent of the alloys produced, as determined via Equation 2.3.1. Alloyed samples produced varied in aluminium content from 2.4-5.3 wt%, with SRA 1 containing 0.1 wt% Al. Cl values were also measured as it is known that the presence of Cl can be problematic within powder metallurgy due to the formation of Cl_2 gas throughout consolidation. Pores formed from Cl_2 gas formation are then difficult to close [10]. Typically, Cl values were around 0.2 wt%.

5.4.1 SR-Al Consolidation and Mechanical Testing

Of the Al enhanced SR titanium alloys, generally good homogenisation was achieved following consolidation via FAST despite some local heterogeneity found within the starting powder feedstock. Although aluminium does not have a fast diffusion co-efficient within beta titanium (Table 5.3), its high solubility in both alpha and beta phases facilitates its fast distribution throughout the alloy. Hence, homogeneity issues were generally avoided.

Similar microstructures were observed throughout the entirety of the SR-Al consolidated pellets produced, with the exception of sample Al6 (Fig. 5.4.4). Al6 displays areas of the typical lamellar microstructure as well as areas of more heavily stabilised beta. This sample also contained a higher than normal content of Cr and Fe, likely from contamination of materials of construction.

Generally, the major defect found within these alloys was remnant porosity and the presence of titanium carbides, mainly from incorporation of scum particles not removed during post processing (Section 4.8). It is important to bear in mind such defects when assessing the mechanical properties, both porosity and the presence of clustered TiC are likely to lead to the premature failure of the material. Additionally, excessive concentrations of TiC will increase the yield strength. Removal of such defects is discussed in Section 4.9.

Fig. 5.4.4. displays the microstructure of the titanium alloys produced following consolidation via FAST.

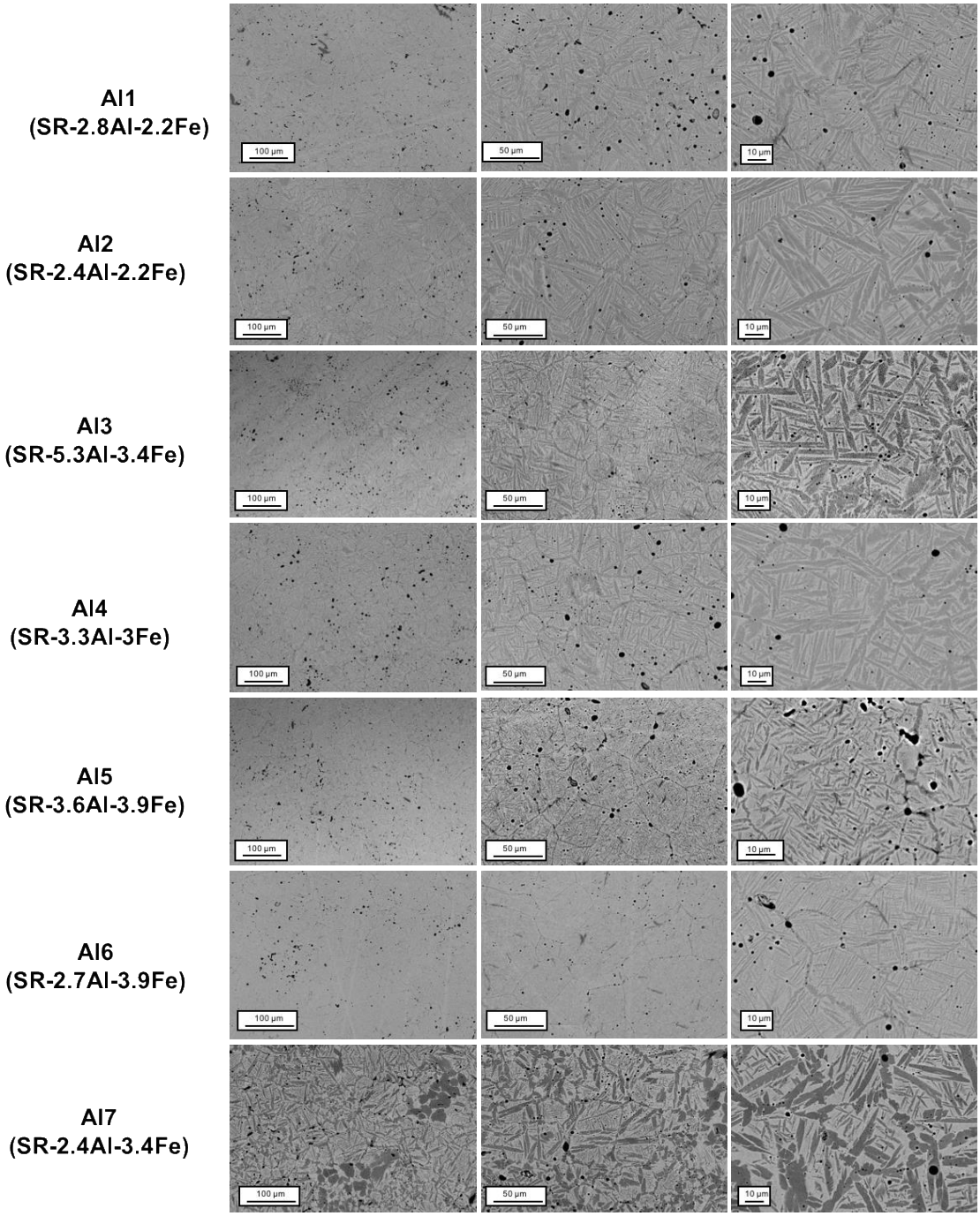

Fig. 5.4.4: Backscatter electron images of consolidated synthetic rutile derived titanium alloy powders enhanced with varying aluminium content.

Alloy Al7 appears to be an anomaly, exhibiting an anomalous microstructure. Large areas of block like alpha dominate and can be found throughout the microstructure. Unlike the fine lamella usually achieved by SR derived alloys, Al7 displays much larger lamelle and particularly thick sections of the alpha phase. An X-EDS spectrum of the area reveals high carbon content in some of the thicker alpha regions, with aluminium concentrations not exceeding 3 wt%. It is plausible that the thick sections of alpha are stabilised by local areas of high carbon content. However, it is unclear what has caused this microstructure to form as the alloy chemistry is not unusual, showing no excessive levels of either aluminium, carbon or oxygen. Following compression testing, the alloy displayed behaviour more akin to metal matrix composite materials - exceptionally high compressive yield strength (1612 MPa) coupled with the corresponding drop in sample ductility (0.127 strain to failure). As such, this alloy will not be directly compared against the other SR derived alloys as will be treated as an anomaly.

5.4.2 Mechanical Properties and Microstructure of Pseudo Binary SR-Al Alloys

All of the SR-Al alloys underwent mechanical testing using the small-scale testing approach (Section 5.1). Following consolidation, a small axi-symmetric compression sample was machined and compressed using a TMC. Fig. 5.4.5 illustrates the resulting true stress-true strain curves whereas Table 5.5 details the compressive yield strength achieved by each alloy as well as the strain to failure value.

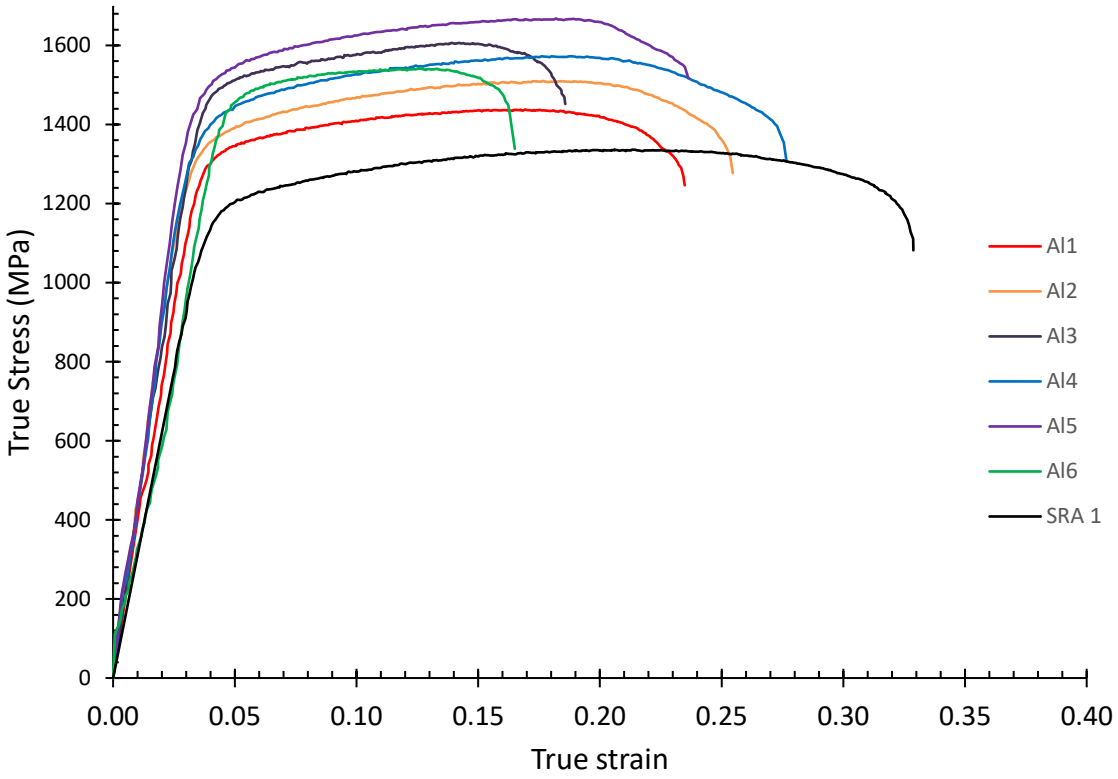

Fig. 5.4.5: True stress-true strain curve produced from small-scale testing approach of pseudo binary SR-Al titanium alloys undertaken at room temperature at a strain rate of $0.1s^{-1}$.

Table 5.5: 0.2% compressive yield strength, strain to failure and density achieved of consolidated pseudo binary SR-Al titanium alloys.

Alloy	0.2 % Compressive yield strength (MPa)	True strain to failure	Density (%)
SRA 1	1090 (av. of 3)	0.339 (av. of 3)	97.63
Al1	1257	0.239	98.2
Al2	1282	0.248	98.5
Al3	1402	0.184	98.6
Al4	1348	0.264	98.4
Al5	1416	0.234	98.0
Al6	1397	0.165	98.6

As shown in Fig. 5.4.5 and Table 5.5, all of the alloys with increased aluminium content produced an increase in strength as would be predicted in pure Ti alloys. Unfortunately, of the alloys produced, only alloy Al4 had a similar baseline composition (similar Fe, O, C and remnant element concentrations, excluding Al) to that of SRA 1 (Table 4.4). In particular, differences in Fe concentration make direct comparisons markedly difficult due to the potent beta stabilisation provided by the element. Hence, due to the differences in Fe (as well as smaller differences in O, C and Cr concentrations), a direct comparison of the alloys produced to determine the exactly effect of changing the aluminium content is challenging. However, the data obtained can be used in combination with a multiple regression technique to take into account all of the variables and will be discussed in Chapter 6.

Here, the discussion will focus primarily around general trends and specific alloys of interest. In general, despite fluctuations in Fe concentration, all of the alloys exhibited a lamellar basketweave structure similar to that achieved by the baseline SRA 1 and Ti-6Al-4V. Alloys with higher aluminium content did not necessarily contain more alpha content. This alpha variation is due to variation in iron concentration which is a potent beta stabiliser as well as oxygen concentration differences which is a potent alpha stabiliser.

Excluding aluminium content, alloy Al4 has the closest baseline chemical composition to that of the baseline SRA 1 in terms of iron, oxygen and carbon concentrations. Alloy Al4 has an increased 0.2% compressive yield strength of 258 MPa compared to SRA 1, with some loss in ductility. However, compared to the other Al enhanced alloys, alloy Al4 has managed to retain a significant proportion of its ductility. Initially it appears unclear why some of the SR-Al alloys retain larger proportions of their ductility, however a relationship between the Al:Fe ratio and strain to failure has been identified as a possible cause and is discussed in more detail in Section 5.4.3.

5.4.3 Al:Fe Relationship in Pseudo Binary SR-Al Titanium Alloys

Despite the variations in baseline compositions, a strong correlation between the aluminium to iron ratio and strain to failure was found. If the aluminium and iron ratio is between 0.9 and 1.3, generally a higher strength (compared to a ratio outside these values) and more ductile alloy was achieved. Table 5.6 gives the Al:Fe ratio and corresponding strain to failure values while Fig. 5.4.6 plots this data graphically.

Table 5.6: Al:Fe ratio of pseudo binary SR-Al alloys and strain to failure values

Alloy	wt% Al /wt% Fe ratio	Strain to failure
Al1	1.25	0.239
Al2	1.11	0.248
Al3	1.57	0.184
Al4	1.11	0.264
Al5	0.93	0.234
Al6	0.70	0.165

As shown in Fig. 5.4.6, the most favourable ratio of Al:Fe concentration appears to be around 1.1. Although this is preliminary data, considering the amount of variables within the data, the existence of a trend suggests there is a significant correlation between the Al:Fe ratio and the strain to failure ratio. Hence, this is a trend worthy of further investigation.

Of the SR-Al alloys tested, alloys Al1, Al4, Al5 and Al2 exhibited an Al:Fe value of close to 1.1, all falling between 0.93 and 1.25. These alloys saw a significant increase in strength from the baseline SRA 1 with good retention of ductility. Alloys Al6 and Al3 had an Al/Fe value further from the ‘ideal’ 1.1 value and showed a significant decrease in the ductility retained. Further, the higher iron content, the better strength achieved, if the Al/Fe relationship was maintained.

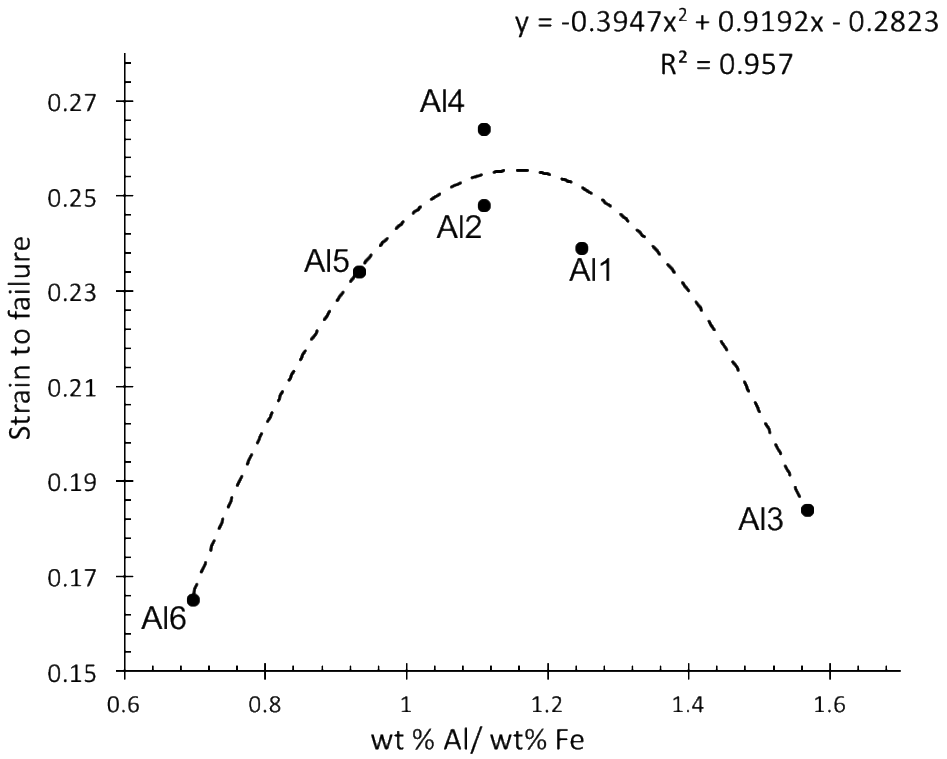

Fig. 5.4.6: Ratio of wt% Al / wt % Fe and corresponding strain to failure value in pseudo binary SR-Al titanium alloys.

Finally, it was observed that the SR-Al alloys retained or picked up more iron than either baseline SR alloys or SR-Mo alloys (Section 5.5). While this may be entirely coincidental and entirely a product of contamination of the powder from materials of construction in the FFC reduction cell, it would be worthwhile conducting partial experiments in the future to rule out the possibly formation of a finely dispersed aluminium-iron based intermetallic.

The favourable properties observed by obeying the Al:Fe ratio are not currently understood. However, one possibility is the formation of Al-Fe intermetallics. Intermetallics FeAl and Fe_3Al are known to form in Ti-Al-Fe systems [27]. Tertiary Al-Fe-Ti intermetallics have also been reported [27]. Formation of such compounds would explain why specific Al:Fe values lead to improved mechanical properties and perhaps explain the higher rate of retention of iron in SR derived alloys enhanced with Al. Although no intermetallic compounds could be found using SEM, such intermetallics may be present as small precipitates. TEM studies would be required to assess these alloys for the formation of such compounds.

5.5 Mo alloy powder production introduction

Mo was chosen for further investigation as an alloying element within synthetic rutile derived alloys for a variety of reasons. Firstly, Mo is an isomorphous β stabiliser and does not produce any intermetallic compounds. Mo was chosen over V, also an isomorphous beta stabiliser, as its oxide is less detrimental to the environment and safer to handle than vanadium's V_2O_5. The beneficial effects of Mo addition to titanium alloys are well known, with additions of 3-4 wt% Mo resulting in an increase in strength of 25-30%, with minimal to no change in ductility [29]. Mo is also known to be able to decrease the elastic modulus of titanium alloys by stabilising the beta phase, which would be beneficial for applications such as springs and biomedical [18] [30] [31].

Despite the many advantages Mo offers, its use within commercial titanium alloys is often severely restricted due to large differences in both density and melting temperature (Table 5.7). These differences cause segregation to occur during the melting procedure. Hence, several melting operations are required to produce a homogeneous alloy which is both costly and time consuming [32].

Table 5.7: Density and melting point of Ti and Mo [33]**.**

	Density (g cm^{-3})	**Melting point (K)**
Ti	4.5	1943
Mo	10.28	2896

By extracting titanium alloy powders directly using the FFC process and taking advantage of downstream consolidation routes, a complete solid state production route from powder to product is realised.. Hence, Mo additions offer a commercial advantage, as these alloys are difficult to produce in an economical manner via traditional means. A further commercial advantage is found in the increased reduction rates of alloys containing Mo within the FFC process. By favouring the +2 and +4 valence states, Mo can avoid initial titanium suboxides (Ti_4O_7, Ti_3O_5 and Ti_2O_3) by directly reducing via Equation 5.1 [4]. Titanium suboxide phases Ti_4O_7, Ti_3O_5 and Ti_2O_3 contain Ti in either the +3 valence state or mixed valence states. By stabilising the +2 and +4 valence states, the oxide can bypass these phases and directly reduce to TiO.

$$\mathbf{TiO_2 + 2e^- \rightarrow TiO + O^{2-}} \qquad \textbf{(Equation 5.1)}$$

Throughout the reduction of Ti-15Mo, no mention is made of the observation of the $CaTi_2O_4$ phase [4]. This may also be due to titanium being present in the +3 valence state within this titanate phase. Additionally, it is also suggested that the presence of Mo in solid solution with TiO – [(Ti,Mo)O] improves the conductivity of the phase, further increasing the rate of reduction of the process. Finally, the presence of Mo also acts to stabilise the beta phase, which is particularly beneficial throughout the final and slowest stage of reduction – deoxidation. Deoxidation is known to be the slowest part of the reduction process due to the slow diffusion rates of oxygen within titanium. However, it has also been established that the diffusion of oxygen in β titanium is at least an order of magnitude faster than within α titanium. High local concentrations of beta stabilising elements can stabilise the beta phase, allowing the oxygen to be removed more efficiently, speeding up the process [4].

Mo enhanced powders were made by pre-mixing calcined rutile with MoO_2 oxide powder for 4 h in a Turbula mixer. Calcined rutile was used to avoid any loss of Mo by firing the powder and to ensure minimum carbon content. The baseline calcined rutile (CR) data is given in Table 4.1.

5.5.1 Mo doped SR Powder Production

After reduction of SR feedstock mixed with MoO_2 powder, low oxygen (< 3000 ppm) titanium alloys were attained, although there were difficulties in producing an even distribution of the alloying Mo. Microstructures of the Mo enhanced CR powder displayed a significant amount of segregation as shown in Fig. 5.5.1. Areas of Mo segregation were easily identifiable due to differences in Z contrast under the SEM. Mo rich areas appeared bright due to high concentration of the heavy Mo, in some cases concentrations of Mo were found to be in excess of 20 wt% in a sample with a bulk Mo value of 4.3 wt%. It is thought that this segregation arises primarily from an insufficient mixing method prior to the FFC reduction.

Additionally, diffusion of molybdenum in titanium is notoriously slow; molybdenum is known to diffuse an order of magnitude slower than the self-diffusion of titanium in the beta phase [34]. Hence, any inhomogeneity present within the feedstock struggles to homogenise within each of the individual particles, throughout the reduction.

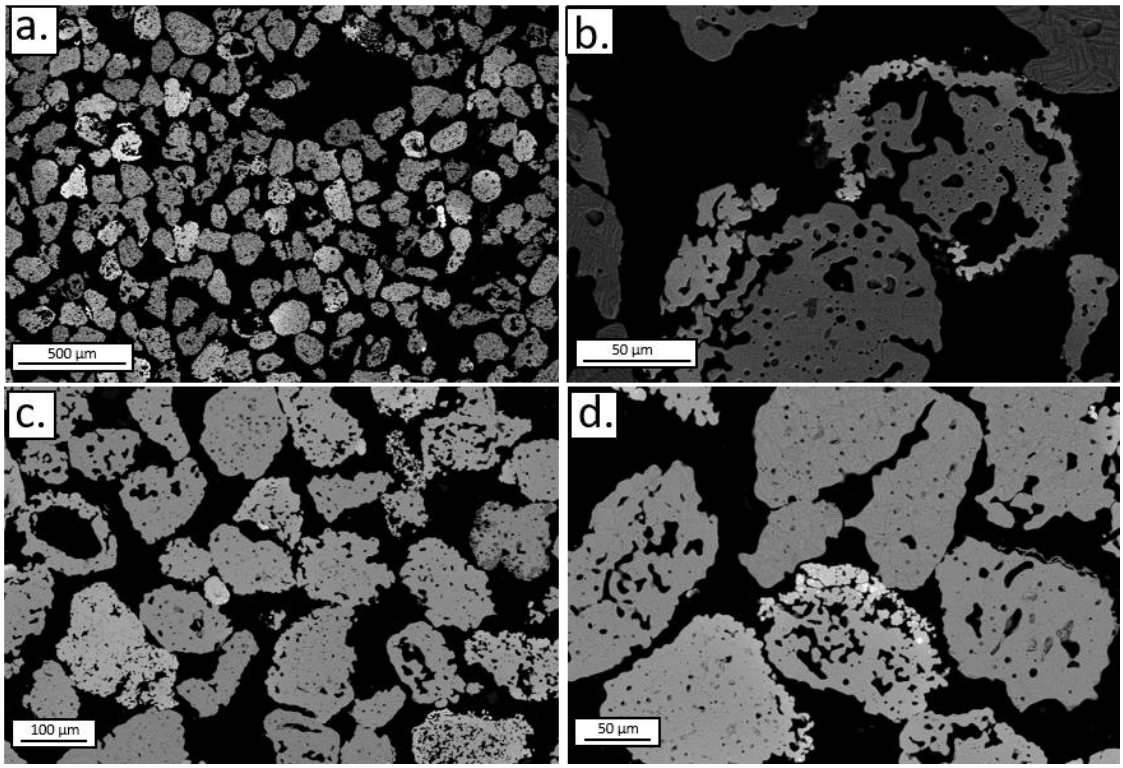

Fig. 5.5.1: Backscatter electron images of reduced Mo enhanced SR derived titanium alloy powders illustrating Mo segregation a) 4.3 wt% Mo in bulk (SR-4Mo) b) 8.3 wt% Mo in bulk (SR-8Mo) c) and d) 9.5 wt% Mo in bulk (Alloy SR-4.5Fe-9.5Mo). Full compositions of the alloys can be found in Appendix 1.

Mo enhanced powders appear to be more sintered than the Al enhanced powders, but more porous than the baseline SR samples. Previous work has suggested Mo is detrimental to the sintering process [1], however Mo is also known to increase the rate of reduction [4]. The combination of these effects may lead to the observed microstructures.

Similarly, to the baseline SR derived alloy (Section 4.8) and Al enhanced SR derived alloys (Fig. 5.4.3d), Mo enhanced powders also exhibit the formation of small amounts of coarse and lath like TiC precipitates within the particles.

As molybdenum possesses an isomorphous crystal structure to β titanium, there is no thermodynamic drive for the formation of Mo intermetallic phases, leaving segregation as the main source of imperfect/defect particles. Although the degree of segregation is significant within the Mo enhanced powders (due to slow diffusion and high quantity of alloying addition), it is thought an improved mixing technique or prior heat treatment would allow the production of a more uniform distribution of the Mo within the titanium alloy powder.

The composition of the SR-Mo alloys created and selected to compare directly to the baseline unalloyed SR derived titanium alloy are listed in Table 5.8. Full chemical analysis of these alloys can be found in Appendix 1. These alloys exhibit Fe concentrations similar to both the baseline SR and each other. Variation in O and C values in these alloys are relatively low, however these fluctuations will be still be taken into account during the analysis of the alloys.

Table 5.8 Chemical composition (Fe, C, O) and Mo equivalency of pseudo binary SR-Mo alloys.

Alloy	Mo (wt%)	Fe (wt%)	O (ppm)	C (ppm)	Mo Equiv.
SRA1	0	2.6	3528	1041	8.7
SR-4Mo	4.3	2.2	2195	2221	12.4
SR-6Mo	5.6	2	2723	2176	13.6
SR-8Mo	8.3	2	2380	1336	15.9
SR-17Mo	17.2	2.2	2833	1062	26

5.5.2 Consolidation of SR-Mo Powders

Fig. 5.5.2 displays the microstructure of the pseudo binary (SR-Mo) alloys post FAST. Density achieved can be found in Table 5.9.

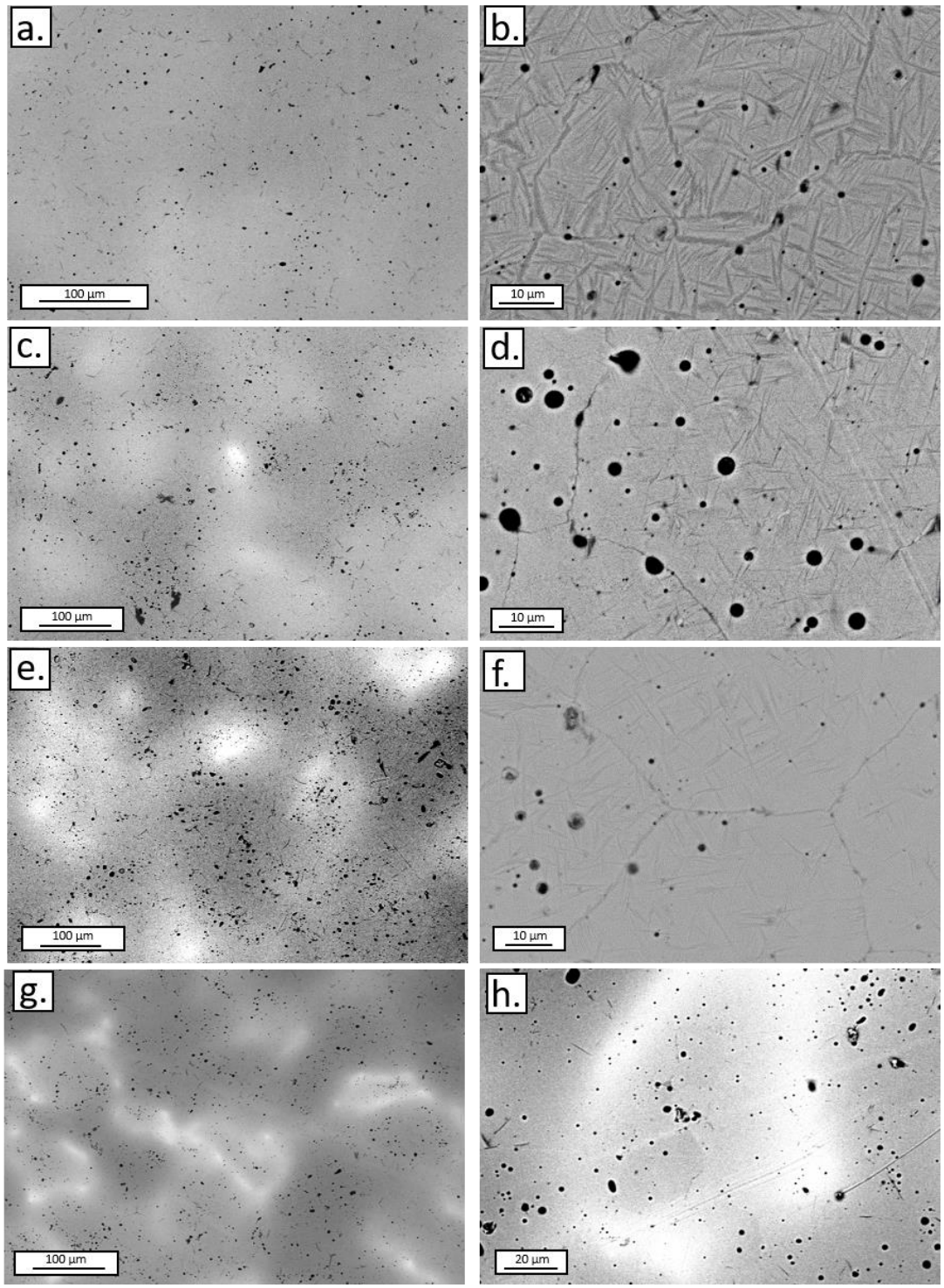

Fig. 5.5.2: Backscatter electron images of consolidated pseudo binary SR+Mo alloys (composition listed in Table 5.8) a) and b) SR-4Mo c) and d) SR-6Mo e) and f) SR-8Mo g) and h) SR-17Mo.

As previously discussed, the diffusion of Mo in titanium alloys is notoriously slow (Table 5.3). Therefore, inhomogeneity present within the initial powder is present within the consolidated microstructure (Fig. 5.5.2). Areas of high molybdenum concentrations are clear in the low magnification SEM images as bright areas, due to the high atomic weight of Mo. X-EDS data highlights this inhomogeneity within sample SR-17Mo, shown in Fig. 5.5.3. Mo concentration varies from 42.76 wt% Mo to 8.65 wt% Mo.

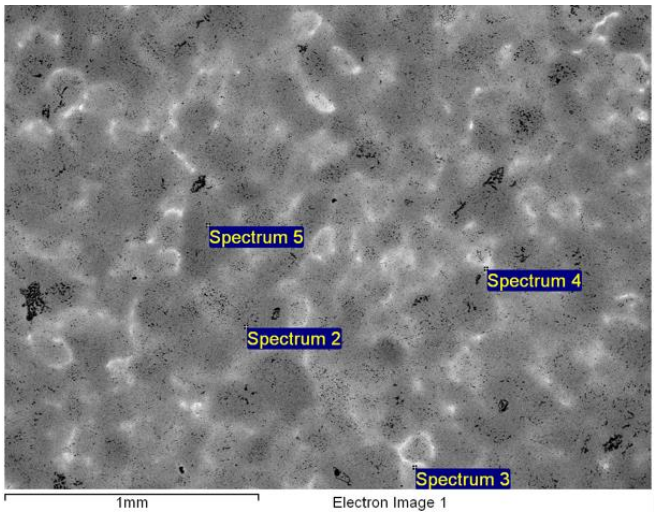

Spectrum	Si	Ti	Cr	Fe	Mo	Total
Sum Spectrum	0.68	77.08	1.24	2.69	18.32	100
Spectrum 2	0.75	81.43	0.98	3.59	13.25	100
Spectrum 3	0.53	65.47	-	1.38	32.62	100
Spectrum 4	-	56.05	-	1.19	42.76	100
Spectrum 5	0.59	83.64	4.19	2.92	8.65	100

Fig. 5.5.3: X-EDS data from a consolidated sample of SR-17Mo.

Under the current FAST conditions, the slow diffusion rate of Mo has not allowed for a full homogenisation to take place. With increasing Mo content, the severity of segregation in the Mo enhanced powders quickly becomes apparent. Although there is segregation, it should be noted that on a macro scale (x 100 magnification), the microstructures are relatively homogeneous, displaying a two-phase, or 'dual' microstructure consisting of Mo rich and Mo lean areas.

However, with optimised processing conditions, improved mixing of MoO_2 and the synthetic rutile feedstock or incorporation of MoO_2 during the upstream production of synthetic rutile, it is thought a much more homogeneous alloy would be obtained. Further, in the case of severe plastic deformation PM processes such as continuous extrusion [35], it is envisaged that such mixing and particle shearing would enhance the homogenisation process. It is also imperative to note that FAST is seen as an intermediate technique, which would be followed by a hot forging step to obtain final microstructures.

The dual structure produced in all pseudo binary (SR-Mo) alloys due to insufficient diffusion has been observed before by Liu et al. in Ti-Ta alloys [36] [3]. Interestingly, the two-phase microstructure reported in Ti-Ta alloys was reported to have enhanced strength and ductility following hot swaging, which was ascribed to the dual nature of the microstructure [3].

With additions of 4 wt% Mo, areas of stabilised beta are found, alongside areas containing significant quantities of alpha in a basketweave structure as shown in Fig. 5.5.2. As Mo concentrations are raised to 6 wt%, areas of alpha laths are less common and the alpha becomes thinner. At 8 wt% Mo, the alpha phase is largely supressed, however areas of α+β lamellar can be found in Mo lean areas. At 17 wt% Mo, the β phase is now heavily stabilised, although there are some areas with small quantities of α in Mo lean areas, although these are rare.

Table 5.9 indicates the density achieved by each of the SR-Mo alloys. Mo has previously been reported to have a deleterious effect on the sintering process of titanium alloys [1]. Although there is some difference in density between the SR-Mo alloys, there does not seem to be a linear pattern as reported by Liu et al [1]. However, the present research was completed using FAST, in which the sintering process is significantly faster. Additionally, there was difficulty accurately measuring the porosity values due to the presence of carbides, which can sometimes be mistaken for porosity and vice versa.

5.5.3 Kirkendall Effect in SR-Mo Alloys

It is possible not all of the porosity observed in the SR-Mo alloys is residual. Within binary substitutional alloys, if the diffusion coefficients of each component are not equal, uneven mass transfer can occur, resulting in the formation of porosity [37]. This phenomenon is known as partial diffusion or the Kirkendall effect and has been previously observed in Ti binary alloys [3] [36] [38].

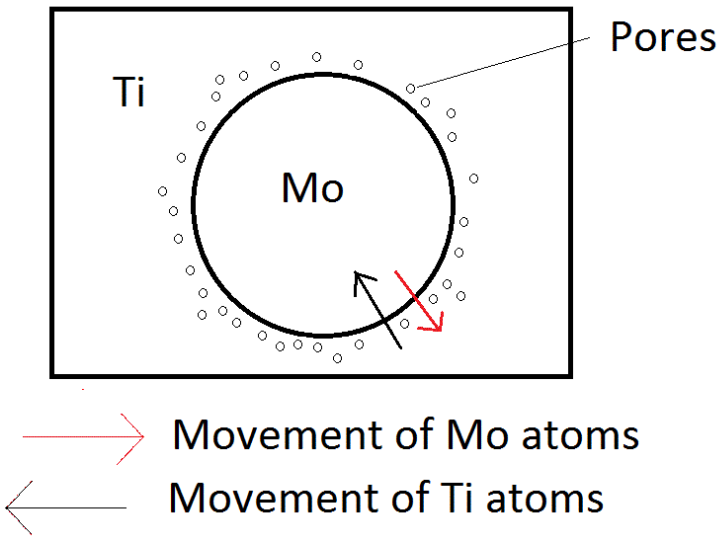

Fig. 5.5.3: Schematic illustrating the Kirkendall effect in binary Ti-Mo solid solutions.

In the case of SR-Mo alloys, the rate of diffusion of Mo is significantly slower than that of the self-diffusion of Ti. Hence, there is a greater mass transfer of Ti into Mo rich areas than Mo into Ti rich areas, resulting in the formation of porosity within Mo lean areas. This is portrayed in the schematic shown in Fig. 5.5.3 and observed in the SEM images. Although areas of higher porosity can be found in the baseline SR alloy, the distribution appears generally homogenous on a global scale. Within the high Mo samples, porosity is often localised in areas lean in Mo.

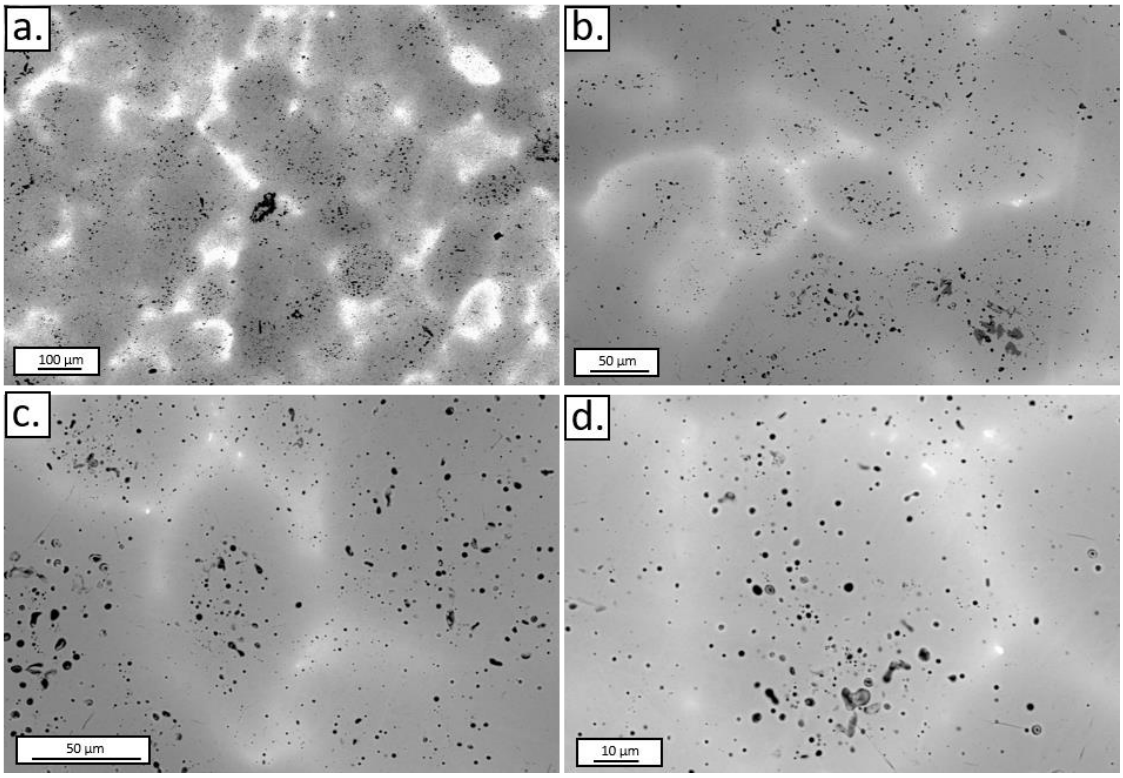

Fig 5.5.4: Backscatter electron images of SR-17Mo showing enhanced porosity in Mo lean areas.

Hence, it is possible that Kirkendall diffusion is occurring within these samples. However, significantly more evidence is required to make a conclusive judgement, which is out of the scope of this work.

5.6 Mechanical Testing of SR-Mo Alloys

The pseudo binary SR-Mo alloys were mechanically tested using the small-scale approach to determine compressive yield strength and strain to failure values as shown in Table 5.9 and Fig. 5.6.1.

Table 5.9: 0.2% Compressive yield strength, strain to failure and density of SR-Mo alloys.

Alloy	0.2 % Compressive yield strength (MPa)	Strain to failure	Density (%)
SRA 1	1090 (av. of 3)	0.339 (av. of 3)	97.5
SR-4Mo	1341	0.183	98.8
SR-6Mo	1365	0.148	98.2
SR-8Mo	1333	0.185	97.9
SR-17Mo	1285	0.376	98.0

All of the alloys gained significant increases in strength over the baseline SR, with SR-6Mo achieving the largest increase of 23%. However, the SR-Mo alloys, apart from SR-17Mo also express a significant decrease in ductility, a reduction of more than half in SR-6Mo. Note, the SR-Mo alloys have increased carbon content in comparison to SRA 1, which may exacerbate the decrease in ductility, however, it is unlikely that this is the sole cause. Also, SR derived titanium alloys with similar carbon levels and significantly improved ductility have been observed.

This decrease in ductility initially appears counter intuitive, as adding molybdenum to pure titanium alloys is known to generally result in an increased ductility due to retention of the ductile beta phase at room temperature. However, the base SR already contains a significant quantity of beta phase at room temperature. Further, it is known that the formation of the omega phase can cause embrittlement of the alloy which may be the cause of the reduced ductility [34]. To determine if the omega phase is present, in depth transmission electron spectroscopy studies are required which is out of the scope of this work.

Omega precipitates can act as potent nucleation sites for alpha precipitation, hence if the alloys have formed the omega phase, following carefully selected heat treatments, the alloys may develop improved properties.

As a ‘black box’ technique was used to consolidate the alloys, each of the alloys are expected to further improve with careful control of consolidation parameters and heat treatments to produce fully dense alloys with optimised microstructures.

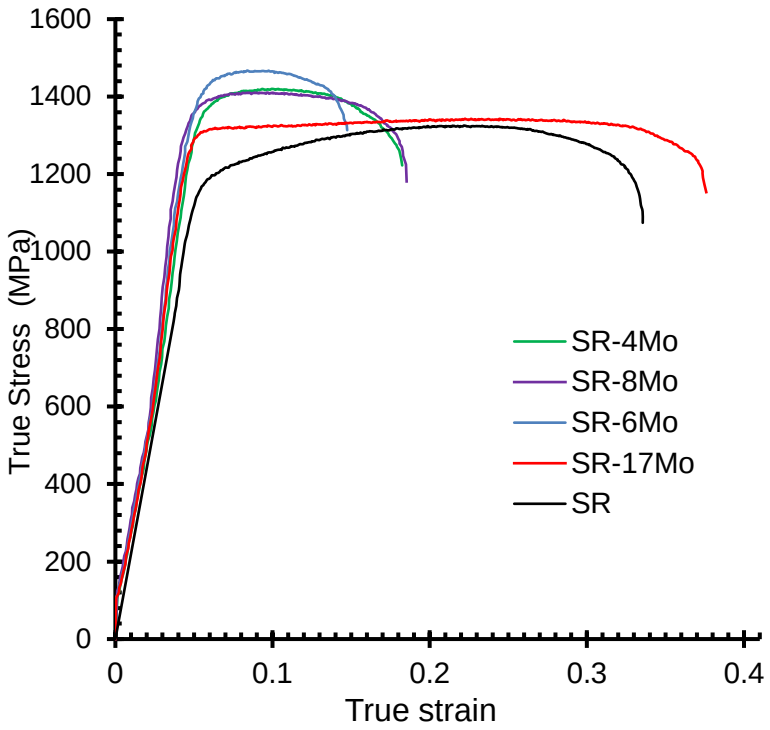

Fig. 5.6.1: True stress-true strain curve of SRA 1 and SR-Mo pseudo binary alloys with varying Mo content.

Interestingly, in alloys SR-4Mo and SR-8Mo, which apart from the 4 wt% Mo content difference anda 0.1 wt% difference in carbon, the alloys behave almost identically with respect to their resistance to plastic deformation at room temperature. This behaviour is not fully understood. Differentiation between the two alloys may occur following heat treatment if omega is present, resulting in the precipitation of the alpha phase.

The high molybdenum content within the SR-17Mo alloy afforded almost the entire microstructure of the alloy to be beta stabilised, with only small amounts of grain boundary alpha being found in Mo lean areas. Stabilisation of the more ductile beta phase allows the improved ductility compared to baseline SRA 1 observed within this alloy. A higher strength is also found in comparison to SRA 1, which is due to the addition of Mo.

Table 5.10 lists the tensile strength of Ti-Mo alloys throughout the literature. There is limited data available on Ti-Mo, particularly compressive strength values, hence the data presented is tensile yield strength as a rough guide to the strengths achieved by standard Ti-Mo alloys. Although the yield strength values found within the literature are tensile yield strength values, typically the difference between compressive and tensile strengths are less than 15%. Hence, the values can be used as a rough guide.

Most of the data available is of Ti-15Mo as this is a commercially produced alloy typically used for orthopaedic applications [39]. Ti-15Mo has the closest Mo content to SR-17Mo, however the Mo equivalency (15) is closer to that of SR-8Mo (15.9). Ti-15Mo has a distinctly low yield strength in the solution treated or β annealed condition, similar to that of grade 4 CP Ti [40]. However, upon annealing in the α+β region, a significant quantity of the alpha phase is retained, improving the strength of the alloy [41].

Table 5.10: Tensile yield strength of Ti-15Mo alloys and Ti-3Mo

Alloy	Oxygen wt %	Condition	Tensile yield strength (MPa)	Notes
Ti-15Mo	0.09	ST	400 [42]	Literature
Ti-15Mo	0.09	CR	750 [42]	Literature
Ti-15Mo	-	annealed	544 [39] [40]	Literature
Ti-15Mo	0.2	β anneal	483 [41]	Technical data sheet
Ti-15Mo	0.2	a+β anneal	800 [41]	Technical data sheet
Ti-15Mo	0.2	α+β anneal + aged	1050 [41]	Technical data sheet
Ti-3Mo	-	PM (sintered)	875 [43]	94% density
Ti-3Mo	-	PM (FAST)	860 [44]	99.8% density

Compared to conventionally produced Ti-Mo binary alloys, pseudo binary SR-Mo alloys all exhibit large increases in strength. In particular, the presence of iron as well as other remnant elements found throughout the SR derived titanium alloys are thought to provide substantial solid solution strengthening. Higher interstitial content found within the pseudo-binary alloys will also contribute to the higher strengths achieved.

Using powder metallurgy techniques, Ti-3Mo has been produced [43], and gives a yield strength much lower than any of the SR-Mo alloys produced within this thesis, of which SR-4Mo has the closest Mo content. Inhomogeneity found within the SR-Mo alloys was also found in work completed by Izui et al. using a blended elemental technique [44].

5.7 Low Cost Alloy Design – Replacement of Mo with Fe

Although SR-17Mo produces a stronger, more ductile alloy than the baseline SRA 1, the cost of the alloying addition Mo may hinder this alloy in low cost applications. Alternatively, an alloy was developed to retain the high Mo equivalency of SR-17Mo but with a significantly reduced Mo content. Iron was chosen to replace Mo as Fe is a potent beta stabiliser, lighter than Mo and could potentially be beneficial from a commercial and economic standpoint.

As a beta stabiliser, Fe is three times more powerful than Mo (Equation 2.1.3). Hence, by replacing ~7.8 wt% Mo with ~2.5 wt% Fe and additional Cr, a Mo equivalency of ~26 is retained, producing an alloy with composition Ti-4.5Fe-9.5Mo, as shown in Table 5.11.

Table 5.11: Chemical composition and mechanical data of SR-17Mo and SR-4.5Fe-9.5Mo

Alloy	Mo (wt%)	Fe (wt%)	Cr (wt%)	O (ppm)	C (ppm)	Mo Equiv.	0.2% Compressive yield strength (MPa)	Strain to failure
SR-17Mo	17.2	2.2	1.1	2833	1062	26	1285	0.376
SR-4.5Fe-9.5Mo	9.41	4.59	1.9	1740	1648	26.1	1222	0.368

Fig. 5.7.1 displays the true stress-true strain of the high Mo alloy, SR-17Mo and SR-4.5Fe-9.5Mo. Although the concentration of Mo has decreased by 7.8 wt%, the increased ductility has been retained. Strength of the alloy has slightly decreased by 5%. However, this alloy would be significantly cheaper due to the vast reduction in Mo content.

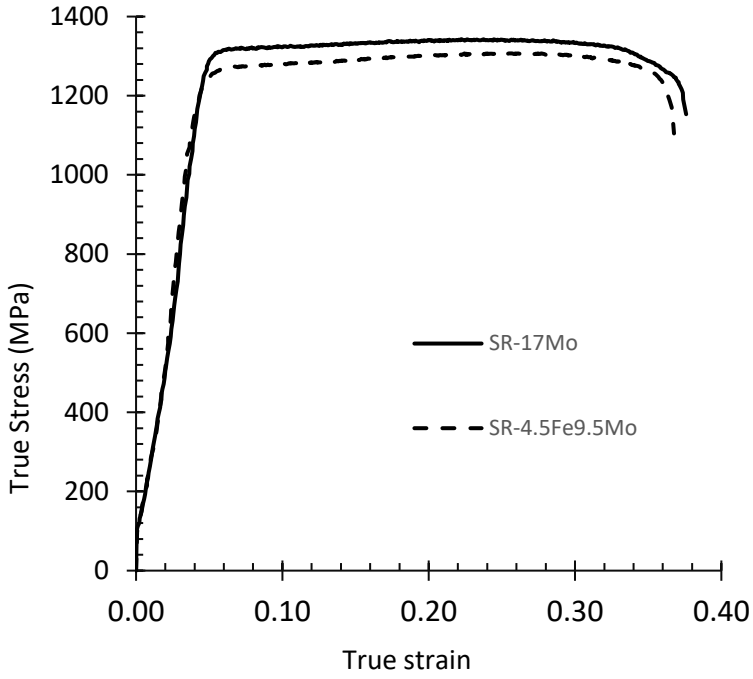

Fig. 5.7.1: True stress-true strain curve of enhanced SR titanium derived alloys SR-17Mo and SR-4.5Fe-9.5Mo conducted at room temperature at a strain rate of $0.1s^{-1}$.

Microstructures of the two ductile alloys are shown in Fig. 5.7.2. As expected, a reduction in the Mo content (in alloy SR-4.5Fe-9.5Mo) has led to a noticeable reduction in segregation within the microstructure.

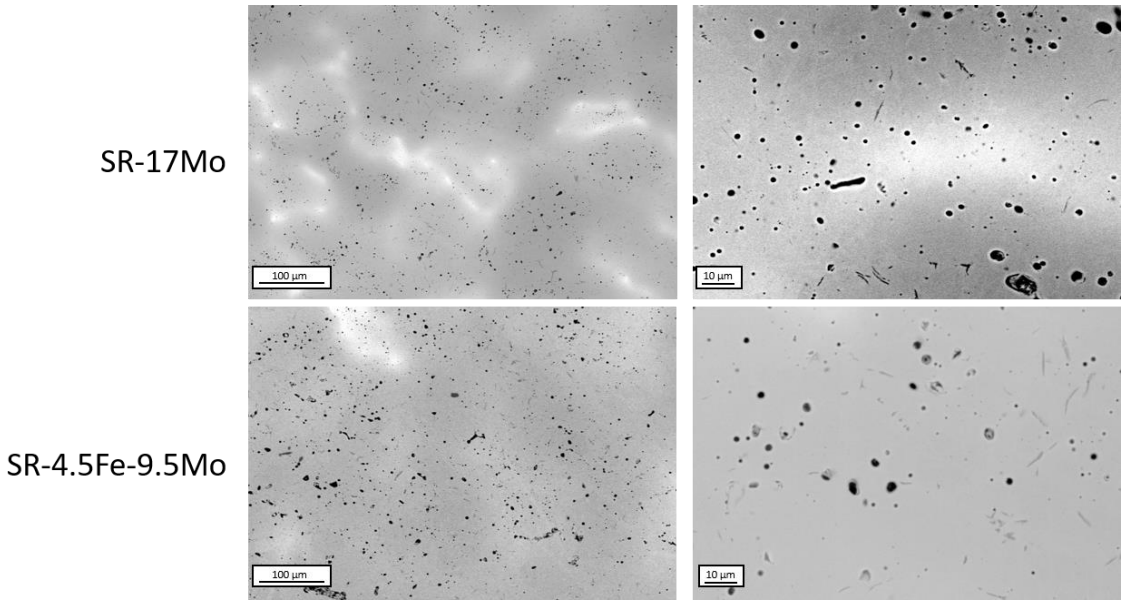

Fig. 5.7.2: Backscatter electron images of modified SR derived titanium alloys, SR-17Mo and SR-4.5Fe-9.5Mo

Using the conventional ingot metallurgy route, alloys with high iron concentrations are typically avoided due to segregation issues and the formation of beta flecks. However, when utilising an extraction and processing technique entirely in the solid state, segregation issues are avoided. Further, as iron is a particularly fast diffuser within titanium, it is unlikely to form unwanted intermetallic compounds when concentrations are relatively low. Throughout this work no intermetallic compounds have been observed with iron concentrations up to 4.6 wt% using SEM and X-EDS analysis. The use of iron as a cheap alloying element has also been explored by Esteban et al., who used up to 7 wt% Fe and reported no observed presence of intermetallic phases [16].

Hence, alloy SR-4.5Fe-9.5Mo is a good starting point for the development of low cost spring alloys intended for automotive application, as explored in Chapter 6.

5.8 Pseudo Ternary Alloys (SR-Al-Mo)

For completion, pseudo ternary alloys containing a SR baseline alongside Al and Mo additions were assessed using the same small-scale testing approach. The pseudo ternary alloys were created via the incorporation of MoO_2 and Al_2O_3 oxides prior to reduction (see section 3 for details). The pseudo ternary alloys produced are listed in order of increasing Mo equivalency in Table 5.12, with full chemical compositions listed in Appendix 1.

Table 5.12: Chemical composition, Mo. Equivalency and Al:Fe ratio of pseudo ternary SR derived titanium alloys (SR-Al-Mo)

Alloy	Al (wt%)	Mo (wt%)	Fe (wt%)	Oxygen (ppm)	Carbon (ppm)	Mo Eq.	wt% Al/ wt% Fe ratio
T1	3.47	1.54	1.53	4143	1155	4	2.27
T2	3.11	1.70	2.18	2804	1846	6	1.43
T3	2.80	5.91	1.47	2477	1037	9.1	1.90
T4	1.76	2.71	2.40	1922	1438	9.3	0.73
T5	1.93	7.31	1.40	3409	2167	11	1.38
T6	3.27	7.22	2.18	2750	2389	12.6	1.50
T7	2.83	7.94	2.76	3481	2502	14.2	1.03
T8	0.93	6.99	2.44	3879	1443	15.6	0.38

The compositions were initially made to study combinations of high and low concentrations of Al and Mo with >2.5 wt% classified as high for Al, and >6 wt% classified as high for Mo.

By selecting a range of high Al-low Mo/low Al-high Mo/low-low and high-high a wide range of alloy compositions was ensured to be assessed as shown in Fig. 5.8.1. However, clearly this is not a full set of data as higher concentrations of Al >5 wt% were not assessed.

All of the alloys assessed were within 1 wt% Fe of each other apart from alloy T7. However, as iron is potent beta stabiliser, this does make comparison to each other difficult. As such, the alloys will not be individually compared and contrasted. However, the data obtained was useful in gaining initial insights into the behaviour of pseudo ternary SR alloys and the production of a predictive model, outlined in Chapter 6.

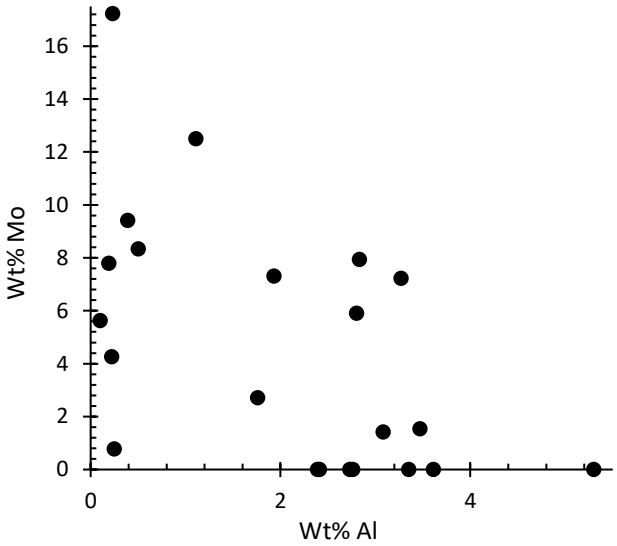

Fig. 5.8.1: Graph of pseudo binary (SR-Al and SR-Mo) and pseudo terrnary alloys (SR-Al-Mo) produced and mechanically assessed within this thesis.

As with SR-Mo alloys, areas of high and low Mo are observed, resulting in a two-phase microstructure. Also akin to SR-Mo alloys, segregation appears more severe with increasing Mo content (Fig. 5.8.2). Areas of stabilised beta with grain boundary alpha can be found in all alloys, as well as areas of the lamellar α+β structure. Note, alloy T7 exhibited an excessively high amount of coarse TiC precipitation.

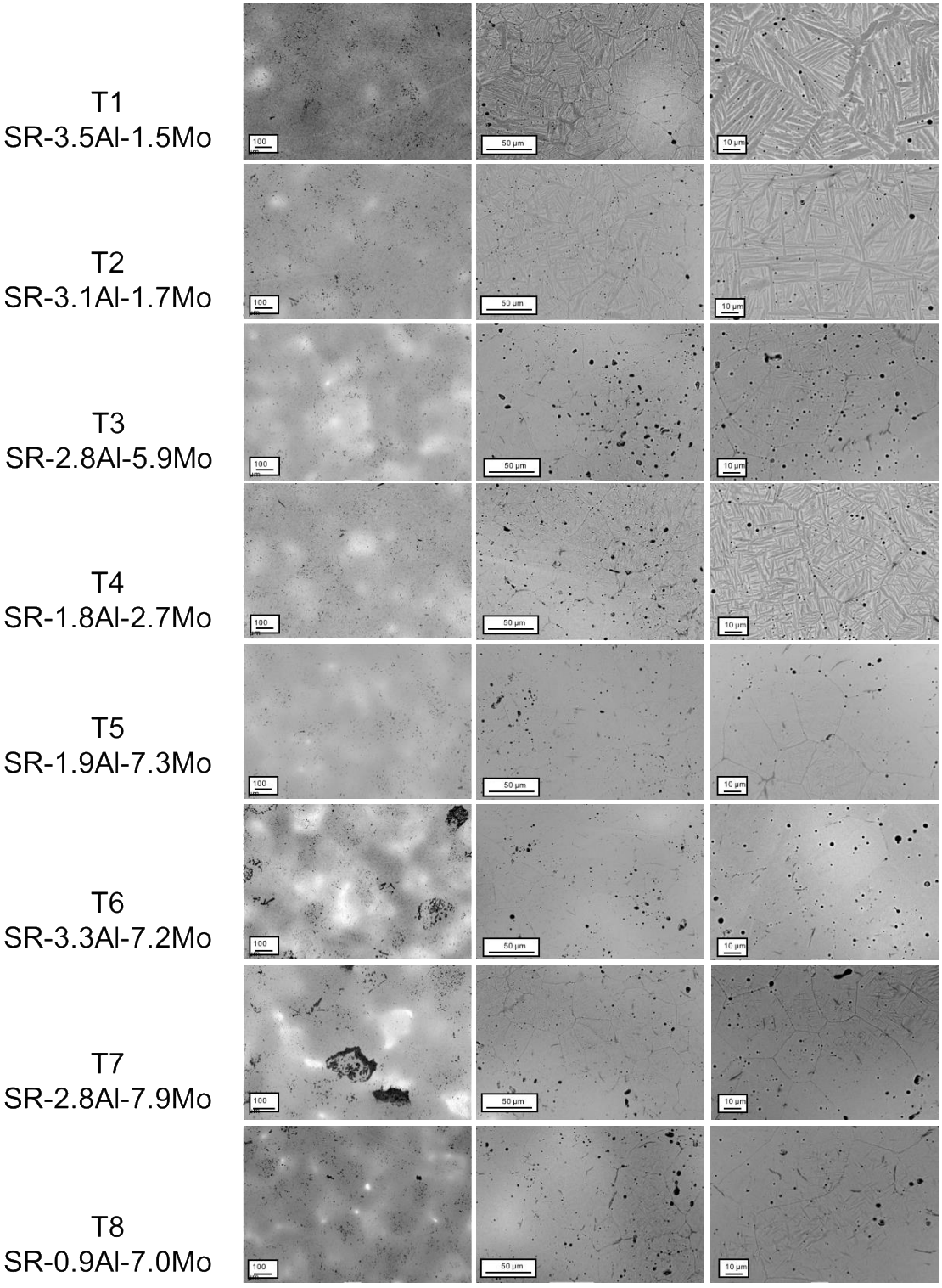

Fig. 5.8.2. Backscatter electron images of pseudo tertiary SR alloys (SR-Al-Mo). Note alloys have been presented in order of increasing Mo equivalency.

As shown in Fig. 5.8.2, the dual phase structure is observed with relatively low Mo contents, as in alloys T1 and T2. Fig. 5.8.3 highlights the bright spots within alloy T1 as a product of Mo inhomogeneity despite a low bulk Mo content of 1.5 wt% and relatively high Al contents of 3.47 wt%. As shown in Fig. 5.8.3, the Mo content increases within the bright areas. While the Al concentration does decrease and contribute to the inhomogeneity observed within the microstructure, it is not as substantial as the Mo segregation observed.

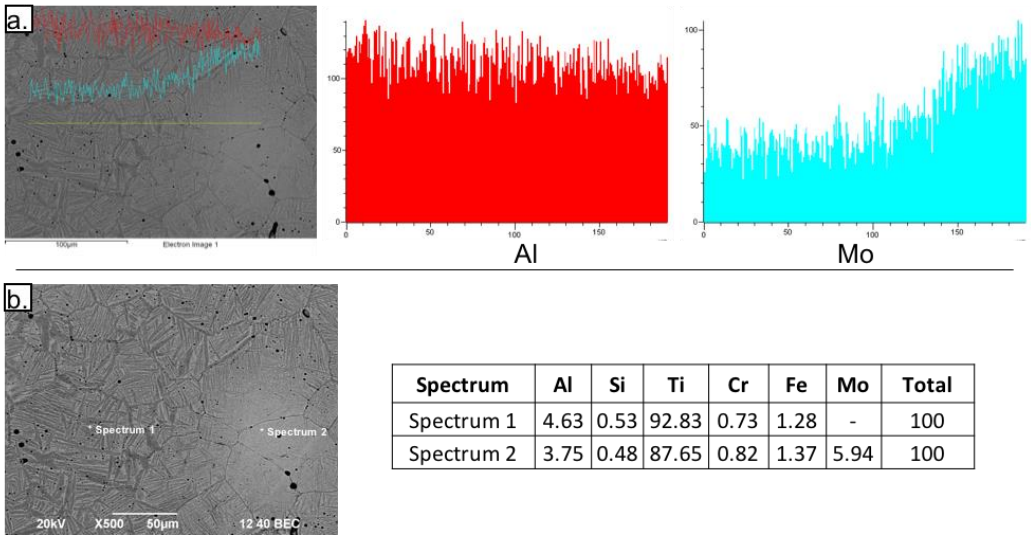

Spectrum	Al	Si	Ti	Cr	Fe	Mo	Total
Spectrum 1	4.63	0.53	92.83	0.73	1.28	-	100
Spectrum 2	3.75	0.48	87.65	0.82	1.37	5.94	100

Fig. 5.8.3: X-EDS data of alloy T1 a) Line scan of Al and Mo concentrations b) point spectrum of Mo lean and rich areas. Values listed in wt%.

5.8.1 Small-scale testing of pseudo tertiary SR alloys (SR-Al-Mo)

Fig. 5.8.4 displays the true stress-true strain curves produced via small-scale testing of the pseudo ternary alloys. In comparison with baseline SRA 1, the alloys produced were generally less ductile, all achieving a strain to failure value of between 0.17 and 0.218. As with the SR-Mo alloys, it is unclear why the addition of Mo does not result in improved ductility. Possible explanations include the differences in interstitial values, the formation of the omega phase, or the presence of Al, however more experimentation is required to experientially determine such theories.

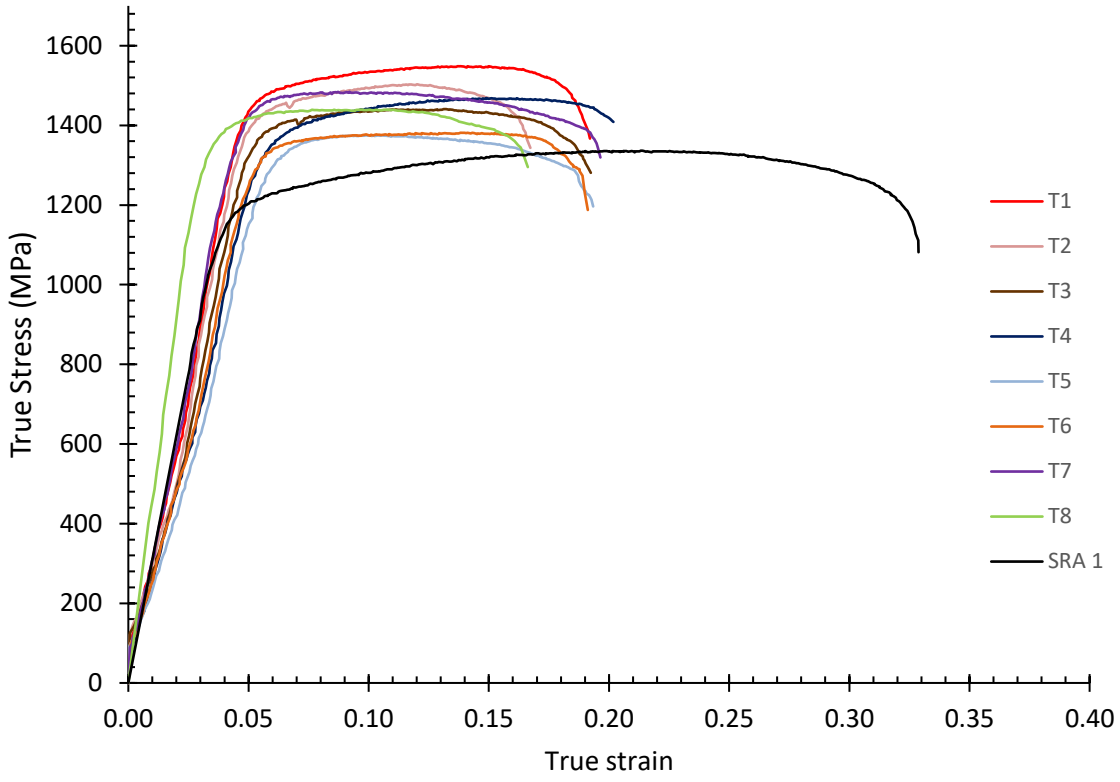

Fig. 5.8.4: True stress-true strain of pseudo tertiary SR alloys (SR-Al-Mo) and baseline SR (SRA 1) conducted at room temperature at a strain rate of $0.1s^{-1}$.

All the pseudo tertiary alloys displayed similar behaviour and strain to failure values. Differences in strain to failure varied by just 5%. The only major difference between the alloys was the yield strength, which varied from 1249 MPa to 1383 MPa. Alloy T1 achieved the highest yield strength, despite relatively low iron levels. However, this alloy possesses the highest aluminium content and oxygen values. Again, due to variations in baseline compositions, it is difficult to accurately assess the individual effects of each alloying element and the combined effect of binary additions to the SR baseline. However, the data was applied to a multiple regression technique to gauge a basic understanding of the additions Chapter 6.

Table 5.13: 0.2% Compressive yield strength, strain to failure and density of pseudo ternary SR derived titanium alloys (SR-Mo-Al)

Alloy	0.2% Compressive yield strength (MPa)	Strain to failure	Density (%)
T1	1383	0.192	98.4
T2	1334	0.170	98.8
T3	1299	0.205	98.8
T4	1257	0.218	98.7
T5	1258	0.204	98.9
T6	1249	0.191	98.3
T7	1355	0.196	98.9
T8	1290	0.162	98.4

It is thought these alloys would begin to differentiate from each other following heat treatments and further precipitation of the alpha phase. If omega is present, this can act as a nucleation site for finely dispersed alpha precipitates, similar to GP zones in Al alloys.

5.8.2 Effect of Mo on Al:Fe – Strain to Failure Relationship

Of the pseudo-ternary SR alloys, only one alloy maintained the Al:Fe ratio, (between 0.9 and 1.3) thought to promote favourable properties. Although Alloy T7 had an Al:Fe ratio of 1.03, the alloy did not retain enhanced ductility as observed in the SR-Al alloys (Fig. 5.8.5). Presence of Mo may disrupt the favourable Al:Fe ratio. However, this alloy also contained a larger amount of TiC precipitates (highest C content of the alloys tested), which could also be the cause of the brittle behaviour of the alloy. As the nature of the Al:Fe – strain relationship is not fully understood it is therefore difficult to assess the effect Mo has on the relationship, without an in-depth analysis, which is out of the scope of this thesis. However, this is an interesting preliminary result worth mentioning and warrants further investigation.

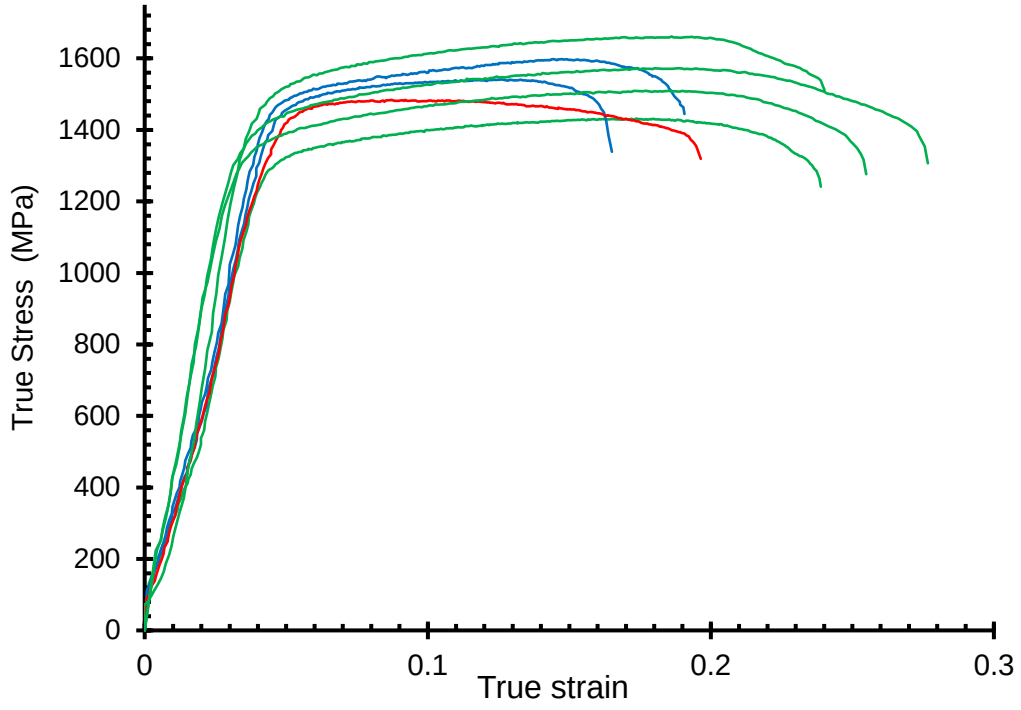

Fig. 5.8.5: True stress-true strain curve conducted at room temperature at a strain rate of 0.1 s^{-1} of pseudo binary SR derived titanium alloys (SR-Al). Alloys with a Al:Fe ratio 0.9-1.3 shown in green and outside of this ratio shown in blue. Pseudo ternary derived alloy T7 with Al:Fe ratio between 0.9-1.3 and containing 7.9 wt% Mo is shown in red.

5.9 Alloy Development of Synthetic Rutile Derived Alloys Conclusions

This work has detailed the development and validation of a small-scale testing approach designed to obtain mechanical properties from small volumes of powder (~4.2g) Further, this work has highlighted two clear pathways for producing tailored, useable alloys from SR feedstock using Al and Mo as alloying additions as shown in Fig. 5.9.1. Although SR derived alloys produce good properties, applications requiring a low Young's modulus, increased strength or increased stiffness may require alterations to the feedstock.

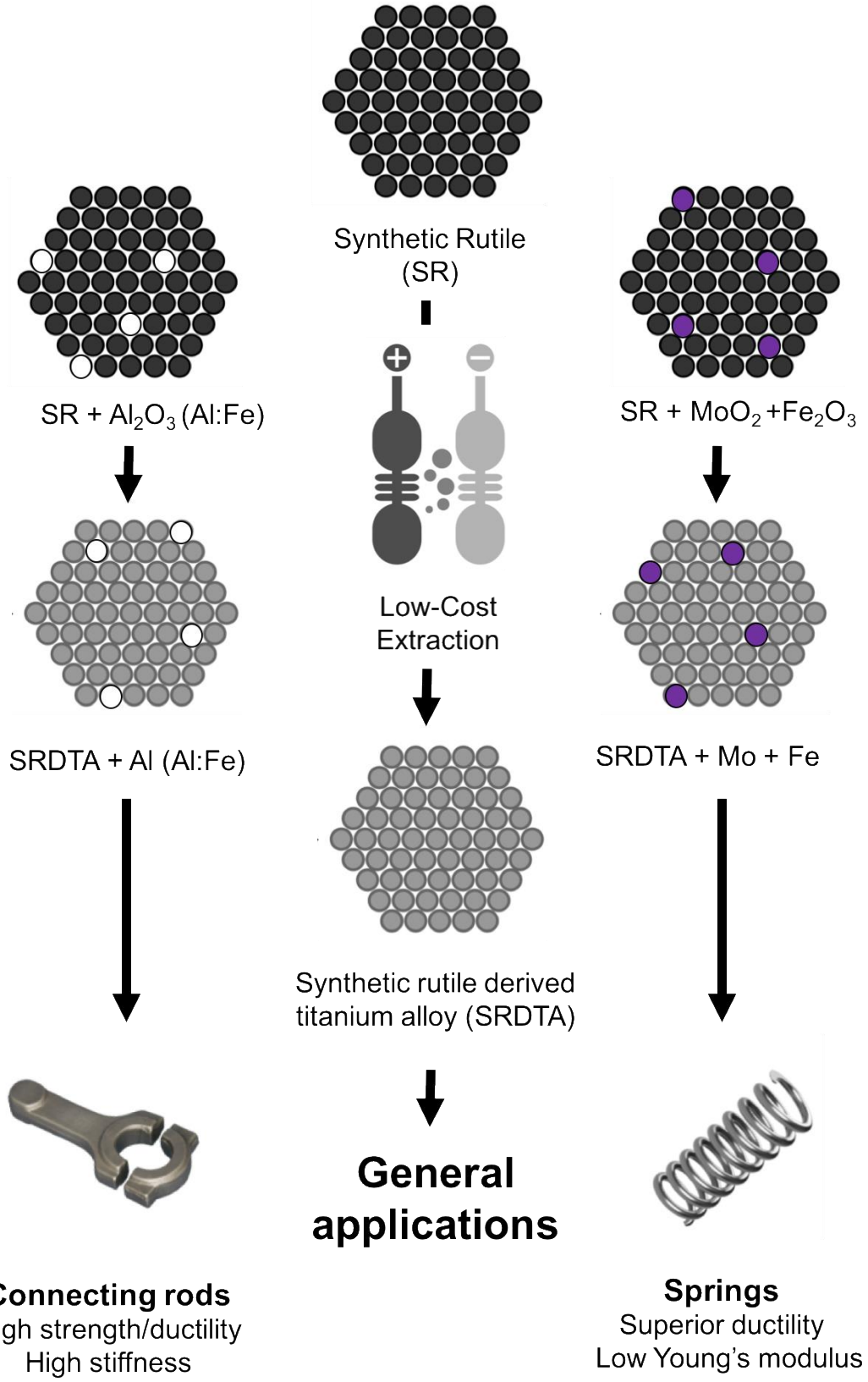

Fig. 5.9.1: Schematic of potential routes to make useable tailored alloys from a SR baseline feedstock.

The addition of aluminium in quantities near equivalency in wt% to that of the iron present result in strong, stiff alloys with good ductility which would be suitable for applications such as connecting rods. Specifically, alloys producing an Al:Fe ratio of 1.1 ± 0.2 produced enhanced ductility, compared to the SR-Al alloys not falling within this range. Further, in pseudo ternary alloys (SR-Al-Mo), the presence of Mo appears to disrupt this favourable relationship.

The other route is to produce low Young's modulus alloys, with low ductility for spring applications – achievable via high stabilisation of the beta phase, via either high Mo addition or by partially replacing Mo content with Fe additions. This alloy development pathway is further explored in Chapter 6.

Fig. 5.9.2 displays all of the SR derived titanium alloys mechanically assessed within this Chapter. Alloys with an Al/Fe value of 0.9-1.3 are represented by the blue curves, these alloys would be most applicable to applications requiring reasonable ductility, high stiffness and high strengths, such as connecting rods. Green curves are alloys with enhanced ductility, achieved by dual-phase structures and high concentrations of beta stabilisers. Red curves are other alloy combinations which did not have a high Mo equivalency (>16) or Al/Fe ratio between 0.9-1.3. Baseline SRA 1 is present as the black curve for reference.

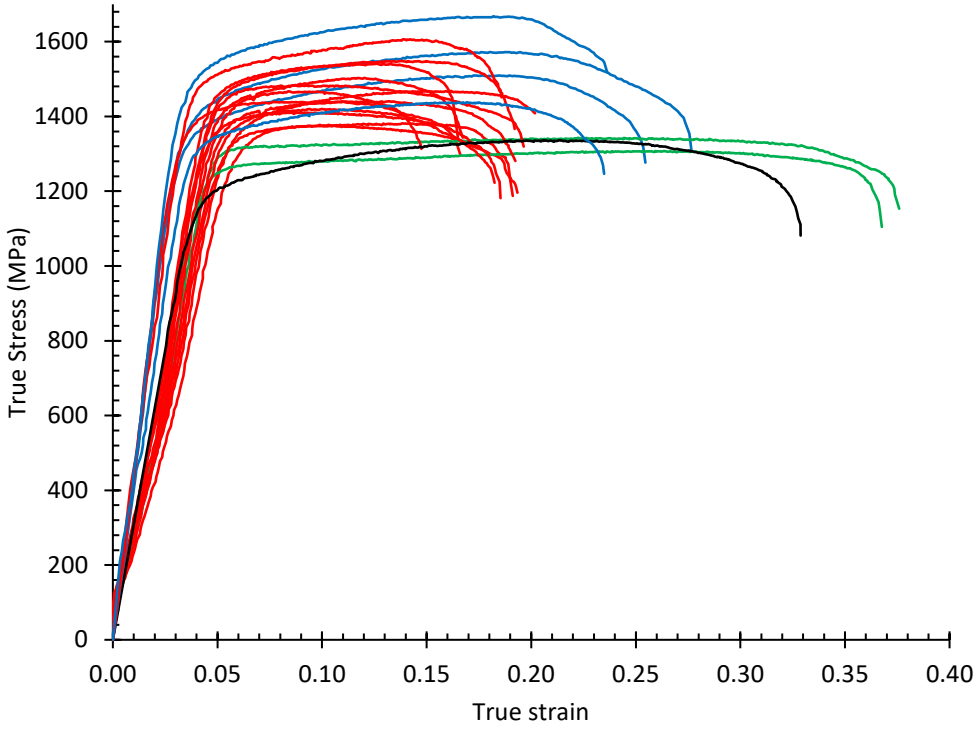

Fig. 5.9.2: True stress- true strain curves conducted at room temperature and a strain rate $0.1s^{-1}$ of all of the SR derived titanium alloys mechanically assessed. Blue = Al:Fe ratio between 0.9-1.3. Green – high Mo Equivalency (>16). Red = Alloys not obeying either of the aforementioned requirements. Black = baseline synthetic rutile derived titanium alloy.

The remainder of this work begins to explore the development of low Young's modulus alloys, with the aim of producing an alloy useable for spring applications within the automotive industry in Chapter 6.

References

[1] Y. Liu, L. F. Chen, H. P. Tang, C. T. Liu, B. Liu and B. Y. Huang, "Design of powder metallurgy titanium alloys and composites," *Materials Science and Engineering: A,* vol. 418, no. 1-2, pp. 25-35, 2006.

[2] N. S. Weston, F. Derguti, A. Tudball and M. Jackson, "Spark plasma sintering of Commerical and Development Titanium alloy powders," *Journal of materials science,* vol. 50, no. 14, pp. 4860-4878, 2015.

[3] Y. Liu, S. Xu, X. Wang, K. Li, B. Liu, H. Wu and H. Tang, "Ultra-High Strength and Ductile Lamellar-Structured Powder Metallurgy Binary Ti-Ta Alloys," *JOM,* vol. 68, no. 3, pp. 899-907, JOM, Vol. 68, No. 3, 2016.

[4] R. Bhagat, M. Jackson, D. Inman and R. Dashwood, "The production of Ti-Mo alloys from mixed oxide precursors via the FFC cambridge process," *Journal of the electrochemical society,* vol. 155, no. 6, pp. E63-E59, 2008.

[5] Senate Software. Ltd, *JMatPro,* V8, 2016.

[6] R. Chaudhari and R. Bauri, "Microstructure and mechanical properties of titanium process by spark plasma sintering," *Metallorgaphy, microstructure and analysis,* vol. 3, pp. 30-35, 2014.

[7] Y. F. Yang, H. Imai, K. Kondoh and M. Qian, "Comparision of spark plasma sintering of elemental and master alloy powder mixe and prealloyed Ti-6Al-4V powder," *International Journal of Powder Metallurgy,* vol. 50, no. 1, pp. 41-47, 2014.

[8] M. Zadra, F. Casari, L. Girardini and A. Molinari, "Microstructure and mechanical properties of cp-titanium produced by spark plasma sintering," *Powder Metallurgy,* vol. 51, no. 1, pp. 59-65, 2008.

[9] Image drawn by Luke Marshall.

[10] R. J. Low, M. Qian and G. B. Schaffer, "Chloride impurities in titanium powder metallurgy- A review," in *Proceedings of the 12th World Conference on Titanium*, Beijing, 2011.

[11] R. M. German, Sintering theory and practise, New York: Wiley-Interscience, 1996.

[12] B. Roebuck, J. D. Lord, M. Brooks, M. S. Loveday and C. M. Sellars, "Measurement Good Practice Guide No 3: Measuring Flow Stress in Hot Axisymmetric Compression Tests," 2002.

[13] R. Boyer, G. Welsch and E. W. Collings, Materials Properties Handbook: Titanium Alloys, ASM International, 1994.

[14] R. R. Boyer and R. D. Briggs, "The Use of beta Titanium Alloys in the Aerospace Industry," *Journal of Materials Engineering and Performance,* vol. 14, no. 6, pp. 681-685, 2005.

[15] S. Veeck, D. Lee, R. Boyer and R. Briggs, "The castability of Ti-5553 alloy: Its microstructure and properties," *Journal of advanced materials,* vol. 37, no. 4, pp. 40-45, 2005.

[16] P. G. Esteban, L. Bolzoni, E. M. Ruiz-Navas and E. Gorgo, "PM processing and characterisation of Ti-7Fe low cost titanium alloys," *Powder Metallurgy,* vol. 54, no. 3, pp. 242-251, 2011.

[17] W. Wei, K. Liu, K. Zhou and B. Huang, "Effect of Fe addition on sintering behaviour of titanium powder," *Powder Metallurgy 2003,* vol. 46, no. 3, pp. 246-250, 2003.

[18] *W. S. Rasband: ImageJ, U.S National Institutes of Health, Bethesda, Maryland, USA, 435 http://imagej.nih.gov/ij/, 1997..*

[19] A. Carman, L. C. Zhang, O. M. Ivaishin, D. G. Saavakin, M. V. Matviychuk and E. V. Pereloma, "Role of alloying elements in microstructure evolution and alloying elements behaviour during sintering of a near beta titanium alloy," *Materials science and engineering A,* Vols. 1686-1693, pp. 1686-1693, 2011.

[20] R. D. Skala, D. Li and I. M. Low, "Diffraction, structure and phase stability studies on aluminium titanate," *Journal of the european ceramic society,* no. 29, pp. 67-75, 2009.

[21] I. M. Low, Z. Oo and B. H. O'Conor, "Effect of atmospheres on the thermal stability of aluminium titanate," *Physica B,* pp. 502-504, 2006.

[22] M. Ishitsuka, T. Sato, T. Endo and M. Shimada, "Thermal Stability of Aluminum Titanate Solid Solutions," *Journal of the American Ceramic Society ,* vol. 70, pp. 69-71, 1987.

[23] T. L. Lekanova, Y. I. Ryabkov, O. A. Sevabo and V. V. Viktorov, "hase Relations in the Systems Al2TiO5–Fe2O3, Al2O3–TiO2–Fe2O3 , and Al2TiO5–Cr2O3," *Inorganic Materials. Translated from Neorganicheskie Materialy, Vol. 40, No. 11, 2004, pp. 1355–1359,* vol. 40, pp. 1191-1194, 2004.

[24] M. I. Powceby, K. K. Constanti-Carey and M. Fischer-White, "Subsolid Phase relationships in the system Fe2O3-Al2O3-TiO2 between 1000 and 1300C," *Journal of the American Ceramic Society,* vol. 86, pp. 975-980, 2003.

[25] I.H. Jung, G. Eriksson, P. Wu and A. Pelton, "Thermodynamic Modeling of the Al2O3–Ti2O3–TiO2 System and Its Applications to the Fe–Al–Ti–O Inclusion Diagram," *ISIJ International,* vol. 49, no. 9, pp. 1290-1297, 2009.

[26] J. Bultitude-Paull, *Perosnal Communcations (unpublished),* vol. Capel Western Australia, p. 2017, Iluka Resources Limited .

[27] M. Palm and J. Lacaze, "Assessment of the Al–Fe–Ti system," *Intermetallics,* vol. 14, no. 10-11, pp. 1291-1303, 2006.

[28] T. Fujita, A. Ogawa, C. Ouchi and H. Tajima, "Microstructure and properties of titanium alloy produced in the newly developed blended elemental powder metallurgy process," *Materials Science and Engineering A213,* pp. 148-153, 1996.

[29] V. M. Anokhin, O. M. Ivasishin and A. N. Petrunko, "Structure and propeties of sintered titanium alloyed with aluminium, molybdenum and oxygen," *Materials science and engineering A,* vol. 243, pp. 269-272, 1998.

[30] M. Long and H. J. Rack, "Titanium alloys in total joint replacement—a materials science perspective," *Biomaterials,* vol. 19, pp. 1621-1639, 1998.

[31] W. F. Ho, C. P. Ju and J. H. Chern Lin, "Structure and properties of cast binary Ti–Mo alloys," *Biomaterials,* vol. 20, pp. 2115-2122, 1999.

[32] R. Bhagat, M. Jackson, D. Inman and R. Dashwood, "The production of Ti-Mo alloys from mixed oxide precurosrs via the FFC Cambridge process," *Journal of The Electrochemical Society,* vol. 155, pp. E63-E69, 2008.

[33] Webelements, "Titanium: the essentials, Molybdenum: the essentials," [Online]. Available: www.webelements.com. [Accessed 22 05 2017].

[34] G. Lutjering and J. C. Williams, Titanium, Berlin: Springer, 2008.

[35] B. Thomas, F. Derguti and M. Jackson, "Continuous extrusion of a commercially pure titanium powder via the Conform process," *Materials Science and Technology,* pp. 1-5, 2016.

[36] Y. Liu, K. Li, H. Wu, M. Song, W. Wang, N. Li and H. Tang, "Synthesis of Ti–Ta alloys with dual structure by incomplete diffusion between elemental powders," *Journal of the mechanical behavior of biomedical materials,* vol. 51, pp. 302-312, 2015.

[37] R. E. Reed-Hill, Physical Metallurgy Principles, New York: D.Van Nostrand Company, 1973.

[38] Y. He, Y. Jiang, N. Xu, J. Zou, B. Huang, C. T. Liu and P. K. Liaw, "Fabrication of Ti–Al Micro/Nanometer-Sized Porous Alloys Through The Kirkendall Effect," *Advanced*

Materials, vol. 19, no. Yuehui He, Yao Jiang, Nanping Xu, Jin Zou,* Baiyun Huang, Chain T. Liu, and Peter K. Liaw, pp. 2102-2106, 2007.

[39] K. Wang, "The use of titanium for medical applications in the USA," *Materials Science and Engineering ,* vol. A213, pp. I34- I37 , 1996.

[40] M. Niinomi, "Mechanical properties of biomedical titanium alloys," *Materials Science and Engineering A,* vol. 243, pp. 231-236, 1998.

[41] ATI, "ATI 15Mo™ Titanium Alloy," 2014. [Online]. Available: https://www.atimetals.com/Products/Documents/datasheets/titanium/alloyed/ati_15Mo_Titanium_Alloy_en_v4%20final.pdf. [Accessed 01 03 2017].

[42] X. Zhao, M. Niinomi, M. Nakai and J. Hieda, "Beta type Ti–Mo alloys with changeable Young's modulus for spinal fixation applications," *Acta Biomaterialia,* vol. 8, no. 5, pp. 1990-1997, 2012.

[43] Y. Liu, W. Wei, K. Zhou, L. Chen and H. Tang, "Microstructures and mechanical behavior of PM Ti-Mo alloy," *Journal of Central South University of Technology,* vol. 10, no. 2, pp. 81-86, 2003.

[44] H. Izui and G. Kikuchi , "Sintering Performance and Mechanical Properties of Titanium Compacts Prepared by spark plasma sintering," *Materials Science Forum,* Vols. 706-709, pp. 217-221, 2012.

[45] D. Goldberg, *Revue International Des Hautes Temperatue et Des Refractaires,* vol. 5, pp. 181-194, 1968.

[46] G. Eriksson, A. D. Pelton, E. Woermann and A. Ender, "Measurement and thermodynamic evaluation of phase equilibria in the Fe-Ti-O system," *Berichte der Bunsengesellschaft/Physical Chemistry ,* vol. 100, no. 11, pp. 1839-1849, 1996.

[47] I. E. Grey, L. M. D. Cranswick, C. Li, T. J. White and L. A. Bursill, "New M3O5-Anatase intergrowth structures formed during low temperature oxidation of Anosovit," *Journal of Solid State Chemistry ,* vol. 150, pp. 128-138, 2000.

Chapter 6:

Spring Alloy Design from a Synthetic Rutile Baseline

6.0 Spring Alloy Design from a Synthetic Rutile Baseline

6.1 Introduction

With the advent of new game-changing technology, capable of extracting titanium alloys from ore like material, or producing near net shapes in a single processing step, it is time to reassess the current titanium alloys. The most widely used titanium alloy, Ti-6Al-4V was developed in the 1950's and has largely remained unchallenged, despite numerous alloys displaying superior properties. Some of the commercial success of Ti-6Al-4V is down to the alloy possessing a well-rounded set of properties, faring well in most applications. Additionally, with 65+ years of mechanical data, corrosion and engine tests, it is difficult to compete with the well-established alloy, even before taking into account the high cost of new alloy qualification [1].

By designing an alloy specifically for new low cost technologies, the significant cost savings potential of new alloys makes further investigation, and potentially qualification, markedly worthwhile.

The work in this Chapter looks specifically at the development of an alloy intended for spring applications within the automotive sector. Automotive springs are an application that would greatly benefit from the high strength to weight ratio and low Young's modulus offered by titanium [2] [3], but have previously eluded the vast majority of vehicles due to the cost-conscious nature of the industry.

A major outcome from Chapter 5 revealed that the enhanced ductility afforded by high molybdenum content, could be replicated with lower Mo contents by simeltaniously increasing the Fe concentration. Previously, high iron containing titanium alloys (typically >3 wt% iron) have been avoided due to segregation effects during the melting procedure, particularly the formation of beta flecks. As FFC derived titanium alloys have been designed to be produced and processed in the solid state, there is no associated melting procedures. As such, high iron concentrations can be taken advantage of. Further, work in Chapter 4 has demonstrated the fast and homogeneous distribution of iron during both the reduction and consolidation processes. Effective homogenisation of iron is afforded by the fast diffusion rate of iron within titanium (Table 5.3).

Based on alloys SR-17Mo and SR-4.5Fe-9.5Mo (section 5.7), a range of pseudo ternary alloys were designed with the intention of producing high strength, low modulus spring candidate alloys. Alloy compositions were explored around compositions of 3-4.5 wt% Fe and 6-12.5 wt% Mo with the intention of replacing costly Mo with inexpensive Fe. Small additions of Al were also added to increase strength/ductility. The combination of Al and Mo was attempted to achieve an alloy with both high strength and substantial ductility; both of which are prerequisite requirements of spring alloys. Unlike the pseudo ternary alloys produced in Section 5.8, these alloys were designed with a higher Mo equivalency, aiming to stabilise a higher proportion of the beta phase at room temperature, with the aim of retaining ductility while still producing high strength levels.

All spring candidate alloys went through the same small-scale testing and characterisation processes (Section 5.1) as the previously assessed pseudo binary/tertiary alloys, to determine microstructure, chemistry and corresponding mechanical properties. The data attained was then used with linear regression software, Minitab [4]. Use of the multiple linear regression software enabled the production of a primitive model for roughly predicting the strength of alloys with a baseline SR composition.

Finally, in the long term, it is expected for the alloying additions to be incorporated into the feedstock further upstream, during the production of SR. As such, Iluka resources supplied 3.2 kg of modified synthetic rutile feedstock which was characterised within this work. Future work will consist of the subsequent reduction, consolidation and mechanical testing of this feedstock.

In summary, this Chapter aims to collate all of the prior research on SR derived titanium alloys to produce a prototype low-cost titanium alloy, specifically designed for solid state processing for spring applications. Full development and commercialisation of a titanium alloy ready for application is a long and laborious process, vastly beyond the scope of this work. Instead, this work endeavours to provide the basis for future alloy development. Firstly through the development of initial prototype spring alloys. Secondly, via the production of an empirical model using data obtained throughout this work. Such a model can be utilised as the basis for determining rough concentrations of Al/Mo/Fe to be added to achieve the required approximate compressive yield strength values in modified SR derived titanium alloys. Finally, characterisation of a modified synthetic rutile baseline intended to directly produce a spring alloy has been achieved, ready for the next stages of development.

6.2 Background on Spring Alloys

Within the automotive industry, replacing high strength steel with titanium allows substantial improvements in both the performance of the vehicle and efficiency of the engine. By virtue of titanium's low Young's modulus, fewer coils are required to hold the same load, hence, in combination with the high strength to weight ratio offered by titanium, substantial weight savings – up to 70% can be achieved by replacing high strength steels with titanium [5].

Fewer coils also have the additional benefit of reducing volume, which is useful in the tight confines of an engine. Further benefits can be found in utilising titanium springs as the corrosion resistance of titanium is excellent and does not require the use of coatings – unlike steels [5].

Within the aerospace industry, where usage of high cost materials can be justified by increased performance, application of titanium wire has been implemented as up and down lock springs on the landing gear, door counter balance springs, flight control springs, pedal return springs for the brakes and hydraulic return springs [6] [7].

In comparison, within the automotive industry, both valve springs and suspension springs have been identified as possible applications for titanium wire. However, despite the advantages of using titanium as a spring material with the automotive industry, the expense of extracting and processing the material has largely inhibited its widespread usage. Low cost titanium alloys have been developed to address this issue, such as the Low Cost Beta alloy (Timetal LCB), Ti-1.5Al-6.8Mo-4.5Fe, which was introduced into approximately 200 units of the Volkswagen Lupo FSI in 1999 [8]. Timetal LCB initially required the same expenditure as CP-Ti to produce, due to the low cost of ferro-molybdenum. However, the cost of ferro-molybdenum increased beyond levels affordable by the automotive industry, leading to the usage of Timetal LCB to be scraped from the Lupo's design [9]. Further, Timetal LCB only addresses the high cost of beta titanium alloys, (in comparison to α+β/alpha alloys) due to the expensive isomorphous alloying additions, rather than the high cost of titanium extraction and downstream processing.

However, by utilising a modified version of the SR derived titanium baseline alloy produced via the low-cost extraction FFC process, in combination with low cost solid state consolidation techniques, affordable titanium spring alloys could become a reality. Fig. 6.2.1 displays the current production route for titanium wire. As explained in Section 2.4.1, the extractive metallothermic Kroll process, is a long, laborious process. Further, following extraction,

numerous procedures are required in addition to produce titanium wire including rolling, drawing and annealing.

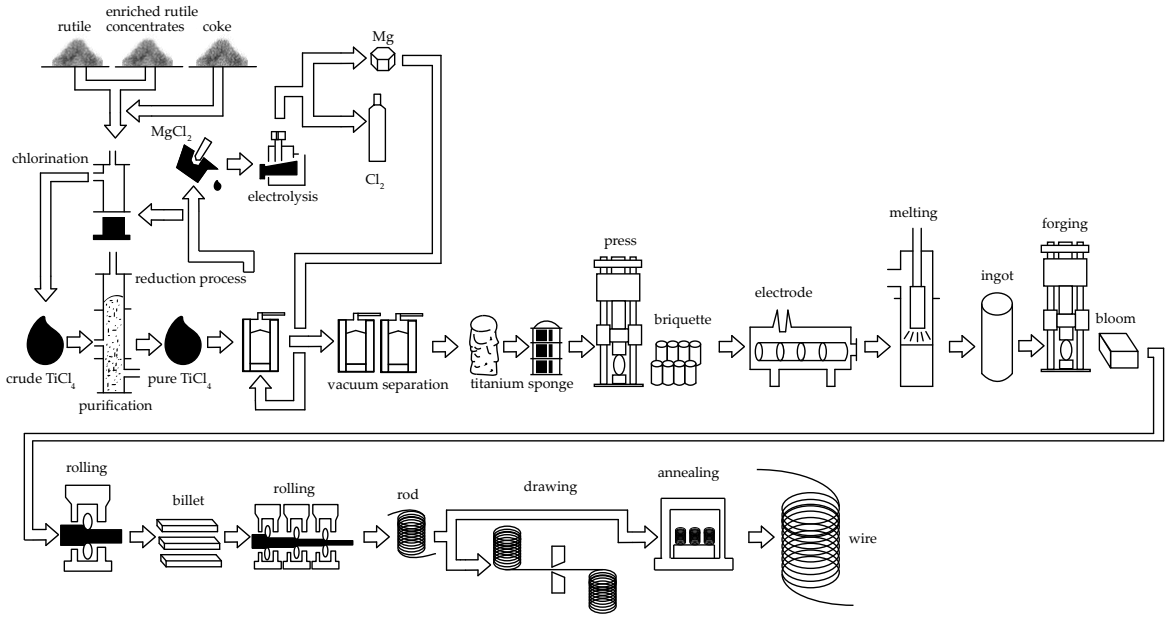

Fig. 6.2.1: Current manufacturing route to produce titanium wire using conventional titanium processing [10].

In comparison, the production of titanium wire via a combination of low cost extractive FFC process and continuous extrusion, as shown in Fig. 6.2.2, can significantly reduce the number of steps required, simplifying the process and allowing substantial cost reductions to be made.

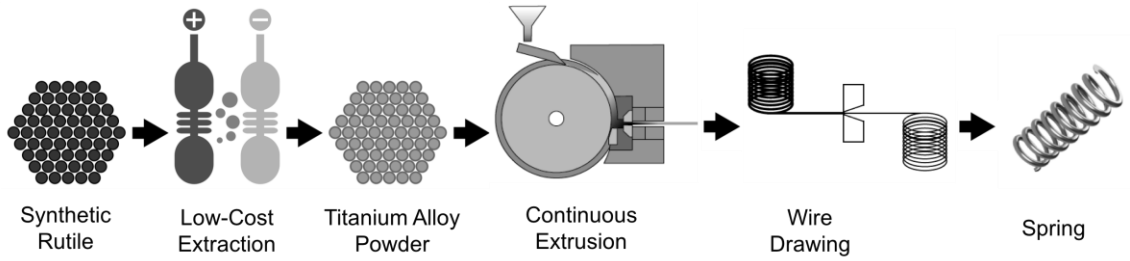

Fig. 6.2.2: Production route of titanium wire from synthetic rutile using a combination of low-cost extraction and continuous extrusion, some images from [11].

Further, by utilising the ore like synthetic rutile as a starting feedstock to the FFC process, an alloy is directly produced. Alterations to this initial feedstock are discussed in this Chapter, with the aims of directly producing an alloy intended for automotive spring applications.

6.3 Synthetic Rutile Derived Spring Alloy Candidates

Alloy SR-17Mo (Section 5.5.2) was identified as a possible spring alloy candidate due to its enhanced strength and ductility compared to that of the baseline SR derived titanium alloy. However, molybdenum is a notoriously expensive alloying addition [12]. Further, addition of molybdenum to SR feedstock prior to reduction led to an inhomogeneous distribution of Mo within the titanium alloy powder produced. This inhomogeneity was retained during consolidation via FAST at 1200°C with a dwell time of 30 minutes, due to Mo's slow rate of diffusion within titanium. Hence, a two-phase microstructure was produced, consisting of Mo rich and Mo lean areas. Improved homogenisation may be achieved by using a smaller Mo powder size, implementing an improved mixing technique of the feedstock powders, hot forging following consolidation, or during the continuous extrusion process via severe plastic deformation. However, a reduction in the amount of Mo in the final alloy is beneficial from an economic standpoint.

By replacing some of the Mo present with iron, high stabilisation of the beta phase can be retained. Further, higher concentrations of iron are both inexpensive and easy to implement during the production of the SR feedstock. As the alloys will be downstream processed using a solid-state powder consolidation route, the fast diffusion rate of iron within titanium is advantageous, enhancing homogenisation of the alloy chemistry. Iron intermetallic precipitates are avoided due to their sluggish formation and the fast diffusion of iron within titanium [12].

Hence, compared to SR-17Mo an alloy with increase iron and decrease molybdenum was created (SR-4.5Fe-9.5Mo, Section 5.7). This alloy showed similar flow stress behaviour to SR-17, with a similar compressive yield strength and strain to failure. SR-4.5Fe-9.5Mo also displayed a lower Young's modulus of 107±3 GPa compared with 130±4 GPa of SR-17Mo. The production of similar properties compared to SR-17Mo prompted a new investigation to examine several spring candidate alloys, with the aim of reducing the Mo content while retaining both strength and ductility.

Changes made to the compositions, compared to the initial SR-17Mo, all reduced Mo concentration. Iron concentrations were increased (from 2.25 wt% in SR-17Mo) and aluminium was added to increase strength and aid precipitation of the alpha phase during post consolidation heat treatments. Table 6.1 lists the spring candidate (SC) alloys in order of descending Mo equivalency.

Table 6.1: Chemical composition and molybdenum equivalency of spring alloy candidate alloys

Alloy	Al (wt%)	Mo (wt%)	Fe (wt%)	Oxygen (ppm)	Carbon (ppm)	Mo eq.
SR-4.5Fe-9.5Mo	0.39	9.40	4.59	1740	1648	26.1
SR-17Mo	0.23	17.2	2.25	2833	1062	26.0
SC 1	1.48	9.90	4.53	2980	2126	25.2
SC 2	3.57	12.7	2.77	4071	2233	20.2
SC 3	1.92	8.83	2.61	2473	1342	18.1
SC 4	1.86	8.06	3.00	3039	1608	17.2
SC 5	2.89	6.16	3.90	2454	2053	16.5
SC 6	2.27	6.19	3.16	2855	1920	16.0

As with the previously assessed SR alloys, variation in oxygen and carbon values was observed which will be taken into account when assessing the alloys.

6.3.1 Consolidation and Mechanical Testing of Spring Candidate Alloys

Figure 6.3.1 displays the microstructures observed by the spring alloy candidate alloys. Note the microstructures of the initial SR-17Mo and SR-4.5Fe-9.5Mo can be found in Section 5.7. Although the majority of the spring alloy candidate alloys consisted of metastable beta phase, fine scale alpha was found within all samples

Segregation is more severe for alloys with higher Mo content (SR-17Mo, SC2), as would be expected due to the slow diffusivity of Mo in Ti, exemplified in Sections 5.5.2 and 5.5.3. Despite the differences in Mo concentration, similar densities were produced with at least 98% density in all spring candidate alloys.

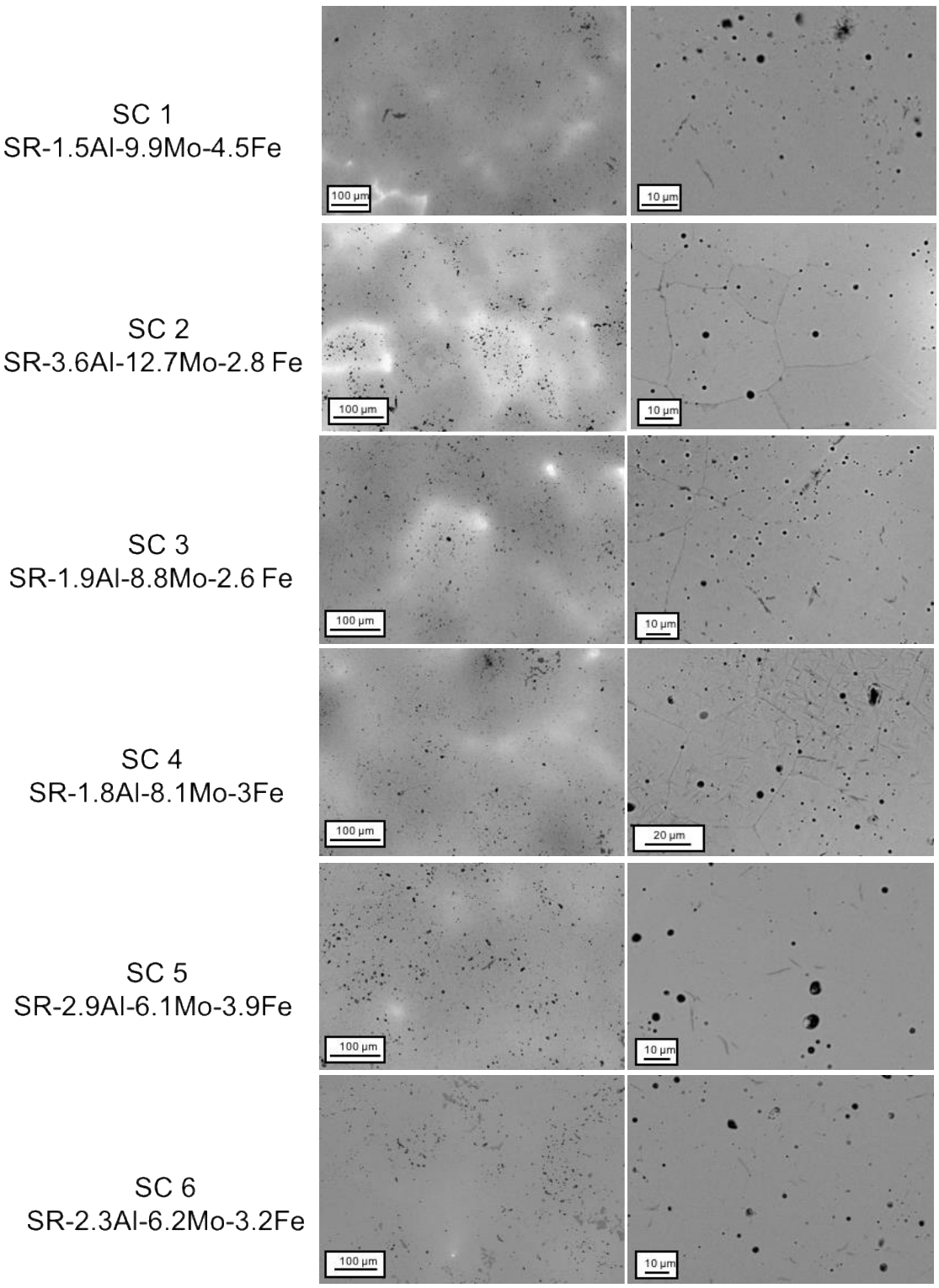

Fig. 6.3.1: Backscattered electron images of modified SR derived titanium candidate spring alloys.

To mechanically asses the alloys, the small-scale testing approach, developed in Section 5.1 was utilised. Fig. 6.3.2 displays the true stress-true strain curves produced, with Table 6.2 displaying the values and density achieved.

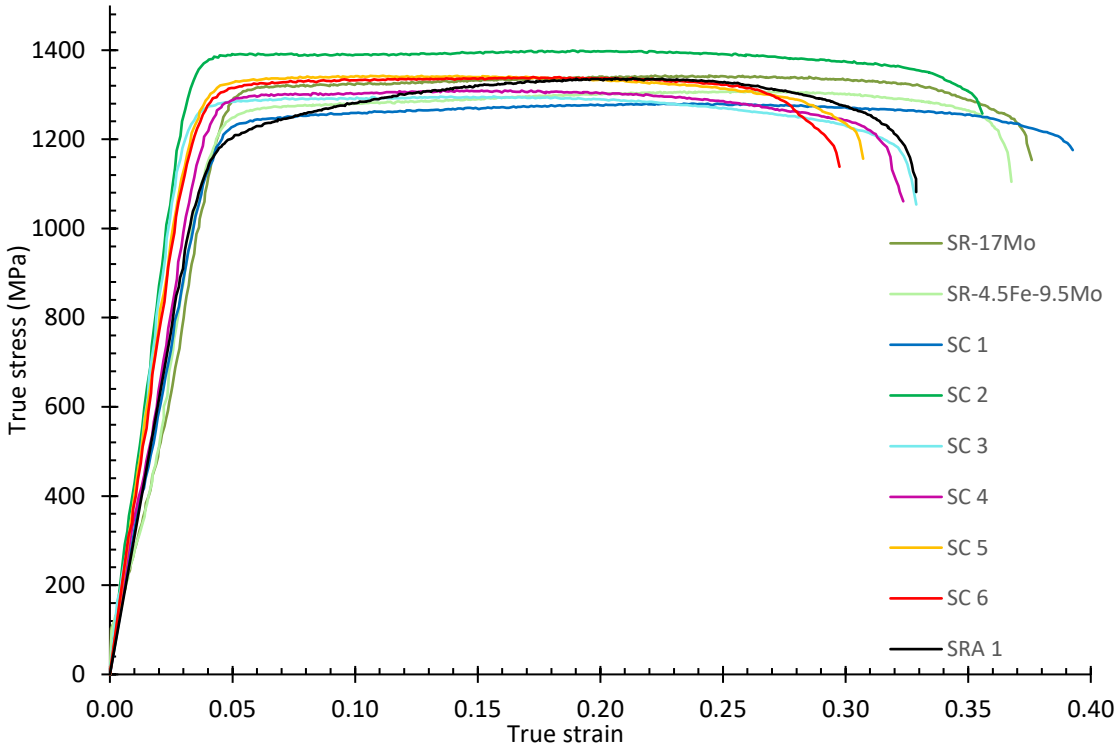

Fig. 6.3.2: True stress-true strain compressive yield strength at a strain rate of 0.1 s^{-1} and room temperature of various spring alloy candidate alloys and synthetic rutile derived titanium alloy baseline (SRA 1).

All of the spring alloy candidates produced possessed good ductility, either similar or superior to that of the baseline SR alloy. Further, all the spring alloy candidates also produced an enhanced 0.2% compressive yield strength value over that of the baseline SR.

Table 6.2: 0.2% compressive yield strength, true strain to failure and density of candidate SR spring alloys

Alloy	0.2% Compressive yield strength Mpa	True strain to failure	Density (%)
SRA 1	1090 (av. of 3)	0.339 (av. of 3)	97.5
SR-4.5Fe-9.5Mo	1222	0.368	98.7
SR-17Mo	1285	0.376	98.0
SC 1	1137	0.388	98.4
SC 2	1292	0.354	98.3
SC 3	1208	0.326	98.8
SC 4	1211	0.321	
SC 5	1175	0.306	98.5
SC 6	1171	0.282	98.8

6.3.2 Spring Alloy Candidate Comparison

Alloy SC2 gave the highest strength, while exhibiting a higher ductility than the baseline SR derived titanium alloy. However, this alloy contained significant quantities of Mo at 12.7 wt%. Alloy SC2 also possessed the highest oxygen content, which would have contributed to its high strength – however, the ductility obtained is superior than the majority of the other spring alloy candidates, suggesting the slightly increased oxygen value has not been excessively detrimental to the ductility of the alloy. The carbon concentration within this alloy was also the highest of all the spring alloy candidates. Hence, the high strength may be due to the combination of high Al, Mo and O and C values.

Alloy SC1 is also of interest, which is both the most ductile SR spring alloy candidate, as well as the most ductile of any SR derived titanium alloy produced throughout the entirety of this work. Although the strength has decreased by 12% from SR-17Mo, the Mo content has been reduced by 7 wt%. SC1 has a composition similar to that of SR-4.5Fe-9.5Mo, but with a slight increase in Mo and the addition of 1.5 wt% aluminium. The addition of aluminium was expected to increase the strength of the alloy, however a decrease in strength is observed. The reason for the decrease in strength is unclear, especially as the alloy has a higher oxygen and carbon content than alloy SR-4.5Fe-9.5Mo.

Despite the reduction in strength, the addition of aluminium should aid the precipitation of the alpha phase during post consolidation ageing heat treatment, allowing the production of a higher strength final alloy. If the alpha phase is dispersed uniformly, an increase in strength with minimal to no loss in ductility would be expected.

6.3.3 Overview of Spring Alloy Candidates

Without further control over the interstitial elements in the FFC process, further refinement of the alloy composition is challenging, as the individual effects of specific elements cannot be conducted at this stage, only general trends can be observed.

Hence, in terms of general trends, all spring alloy candidate alloys are significantly more ductile in comparison to the pseudo binary and pseudo ternary SR alloys of Chapter 5, as shown in Fig. 6.3.3 (with the exception of alloys abiding by the Al:Fe relationship, discussion Section 5.4.3). It is clear there is an underlying principle in producing more ductile alloys. The most significant difference between the spring candidate alloys and the pseudo ternary alloys (Section 5.8) is the high Mo equivalency. All of the spring alloy candidates possessed enough beta stabilisers to achieve a Mo equivalency of 16.0 or higher. High Mo equivalency allows the retention of the ductile beta phase at room temperature.

An exception to this is of pseudo binary alloy SR-8Mo (Sections 5.5.1 and 5.5.2). Despite a Mo equivalency of almost 16 (15.9), the alloy does not exhibit the enhanced ductility shown by the spring candidate alloys. In comparison to the spring candidate alloys, (with the exception of SR-17Mo) it is observed that SR-8Mo possesses less iron content. Hence, further investigations are required to determine the exact conditions required for high strength, ductile alloys, which should include a thorough investigation, specifically to study the effects of both Mo equivalency and iron concentration have upon the ductility of SR derived titanium alloys.

Interestingly, alloys displaying the most intensely segregated two-phase microstructures (SR-17Mo and SC2) also possessed the highest compressive strengths. Both of these alloys had high Mo contents, hence it is possible that these higher strengths were a result of the high Mo concentrations (>10 wt%). However, it would appear more likely that the increase in strength is due to the dual-phase microstructure. Previous research by Liu. et al has shown the dual-phase microstructure has produced high strengths in Ti-Ta alloys [13]. Further, work from Chapter 6 investigating the addition of Mo content to SR derived titanium alloys did not show a direct correlation between the increase in Mo and an increase in strength. More research is required

to fully understand the nature and implications of the dual-phase microstructure in SR-Mo alloys.

Finally, the spring alloys appeared to form two district groups, those alloys exhibiting superior ductility to SRA 1 and alloys exhibiting a strain to failure equal to, or less than SRA 1. Alloys displaying enhanced ductility also had the highest Mo equivalency values, with a minimum value of 20.2.

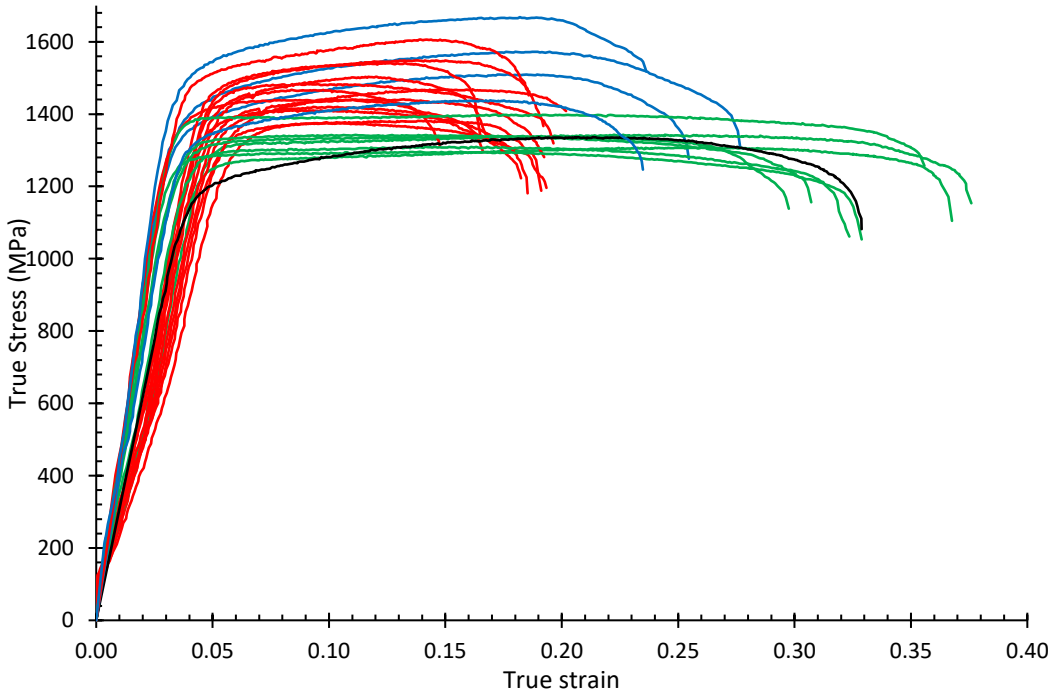

Fig. 6.3.3: True stress-true strain curve of all alloys tested within this thesis, using a strain rate of 0.1 s^{-1} and at room temperature. Blue = Al:Fe ratio between 0.9 and 1.3, green = spring candidate alloys, Mo equivalency above 16.0, red = all other alloys where Al:Fe not between 0.9 and 1.3 and the Mo equivalency is less than 16. Black line represents the baseline SR derived alloy, SRA 1.

Although more experimentation is required, producing SR alloys with increased ductility for spring applications appears to be closely linked to the Mo equivalency, regardless of specific alloy composition. As such, the addition of iron, which is cheap, easily added and a fast diffuser to produce both high Mo equivalency and low modulus for automotive spring applications is a clear area for further investigation in the future.

6.3.4 Conclusion of Spring Candidate Alloys

Of all the spring alloy candidates produced, alloy SC1 has the closest Mo equivalency compared with the initial SR-17Mo and SR-4.5Fe-9.5Mo alloys. It produced the best ductility with a good compressive yield strength of 1137 MPa. As such, alloy SC1 is deemed as an ideal starting point for future alloy development. Further, high Mo equivalency has been identified as a key criteria in developing ductile low modulus alloys, which is in keeping with classical titanium alloys.

6.4 Large Scale Production of Spring Alloy Composition Feedstocks

As a long-term goal, one possibility is the production of the SR spring alloy feedstock directly via the Becher process. Note, this would only be economical if near full retention of additional alloying elements added is achieved within the feedstock or an improved homogeneity and distribution of alloying elements was achieved.

As such, using data from the spring alloy candidates, Iluka Resources produced and supplied 3.2 kg of a modified SR feedstock with additional Mo (5.44 wt%), Fe (10.7 wt%) and Al (1.31 wt%).

The feedstock provided had a high iron content with a medium Mo addition and low aluminium contents. It is predicted that not all of the iron will be retained during reduction.

XRD spectra of the Iluka Resources produced feedstock is shown in Fig. 6.4.1. Similarly to the baseline synthetic rutile (Fig.4.1.1), the XRD spectrum produced is complex, due to the presence of the reduced rutiles. Note, a significant quantity of the pseudobrookite phase ($FeTi_2O_5$-Ti_3O_5) is present, possibly due to stabilisation of the phase from the additional presence of Fe. Note Mo and Al are also likely to be within the M_3O_5 structure.

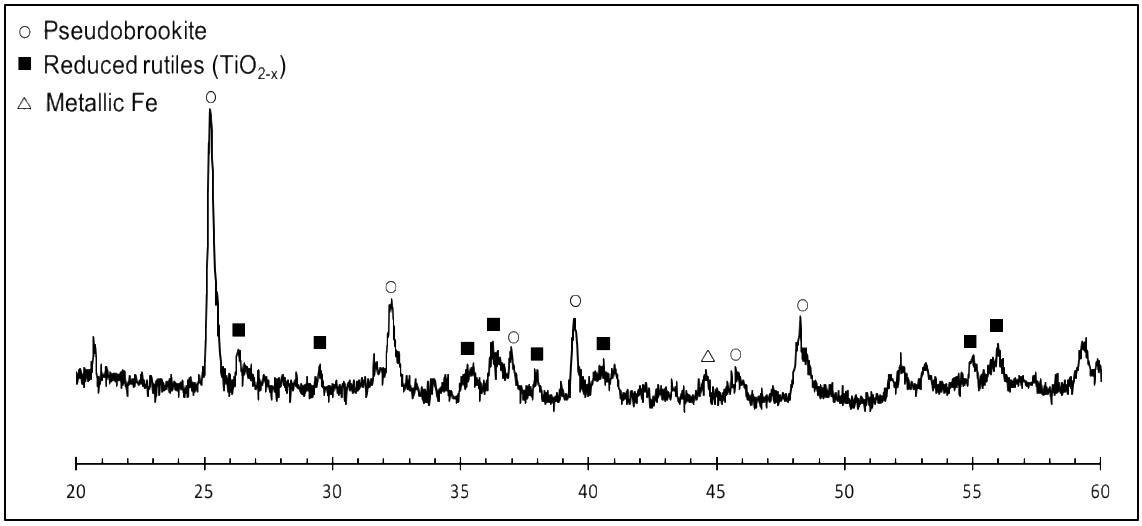

Fig. 6.4.1. XRD spectrum of as received enhanced SR feedstock of composition 10.7 wt% Fe, 5.4 wt% Mo and 1.31 wt% Al.

Following a heat treatment of 4 h at 1000°C, the feedstock was subjected to a further XRD analysis, shown in Fig. 6.4.2. Following calcination heat treatment, most of the feedstock is oxidised to the rutile, TiO_2 phase, however, the pseudobrookite phase is still present in noticeable quantities, however, the phase may now consist of mainly Fe_2TiO_5 following heat treatment [14].

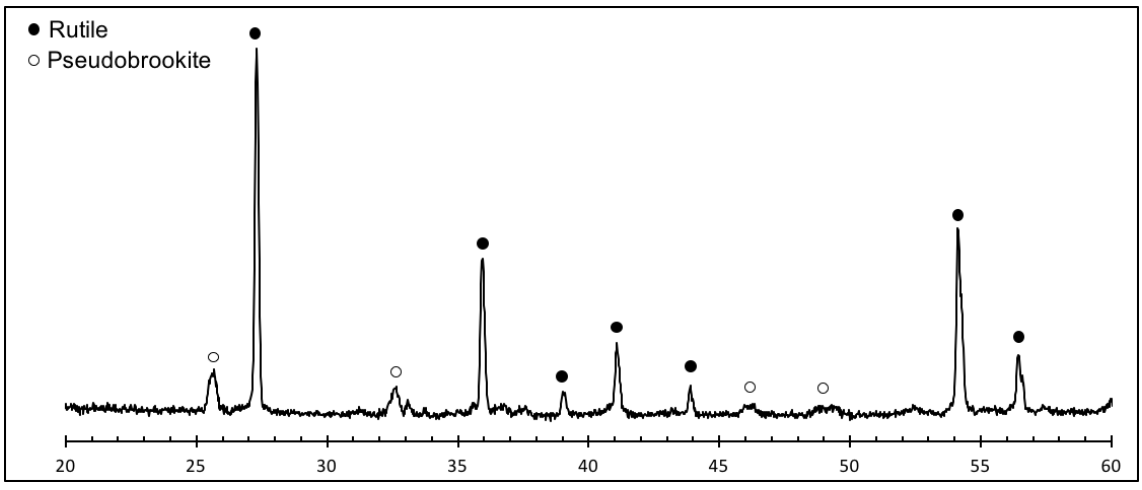

Fig. 6.4.2: XRD spectrum of enhanced SR feedstock of composition 10.7 wt% Fe, 5.4 wt% Mo and 1.3 wt% Al.

Distribution of additional alloying elements within the SR feedstock were analysed via SEM. The morphology and microstructure of the feedstock is shown in Figs 6.4.3, 6.4.4 and 6.4.5. Note, the production of modified feedstock is also in the development stages for Iluka resources, hence, the feedstock is not fully refined at this stage.

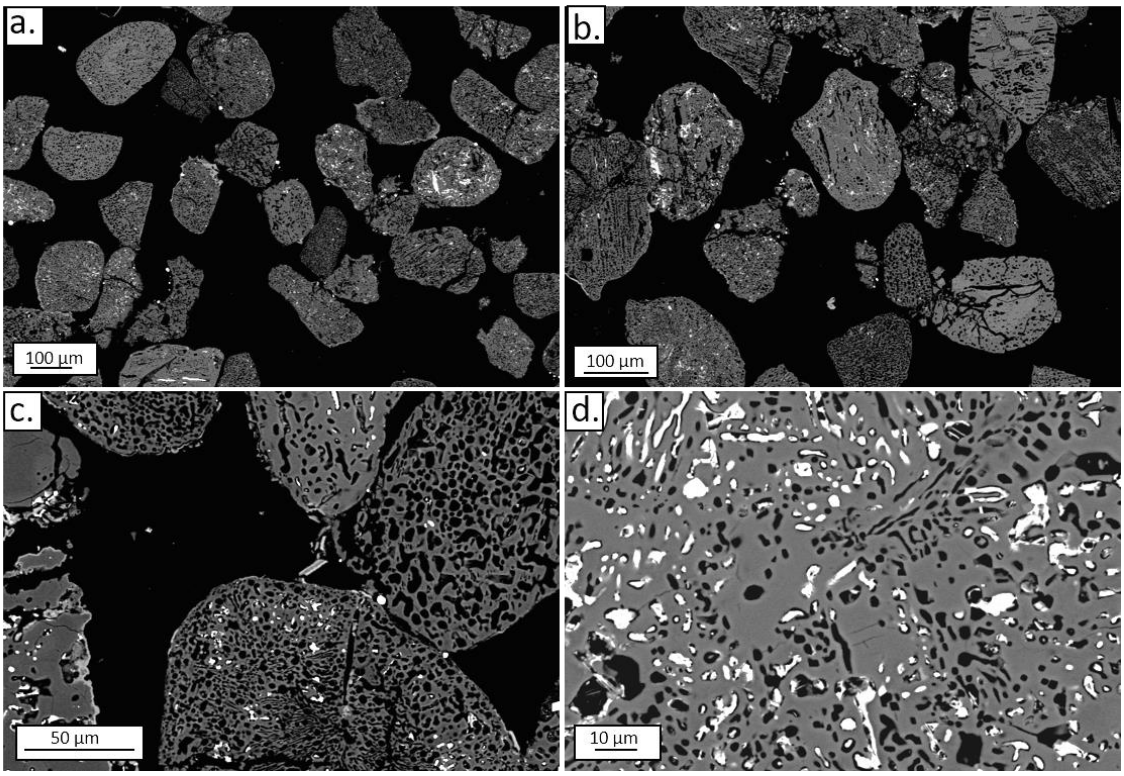

Fig. 6.4.3: Backscatter electron images of modified SR feedstock containing 10.7 wt% Fe, 5.4 wt% Mo and 1.3 wt % Al *Measured via XRF at Iluka resources. Bright spots are areas of Fe, Mo or a combination of the two.

The samples had a large iron concentration of approximately 10.7 wt%. Note, due to the inhomogeneous distribution of the Fe, Mo and Al, it is difficult to assess the true concentrations of these elements, despite riffling and careful analytical techniques. Fig 6.4.3a, b and c all show varying amounts of bright heavy phases within each of the particles, demonstrating the variation of heavy elements Mo and Fe within the feedstock.

X-ray mapsshown in Figure 6.4.4 also displays an inhomogeneous distribution of the additional elements. Both Fe and Al appear to coat the SR particles, in varying degrees of thickness, while Fe and Mo appear within the pores of the particles. Mo also appears as separate bright spots adjacent to particles.

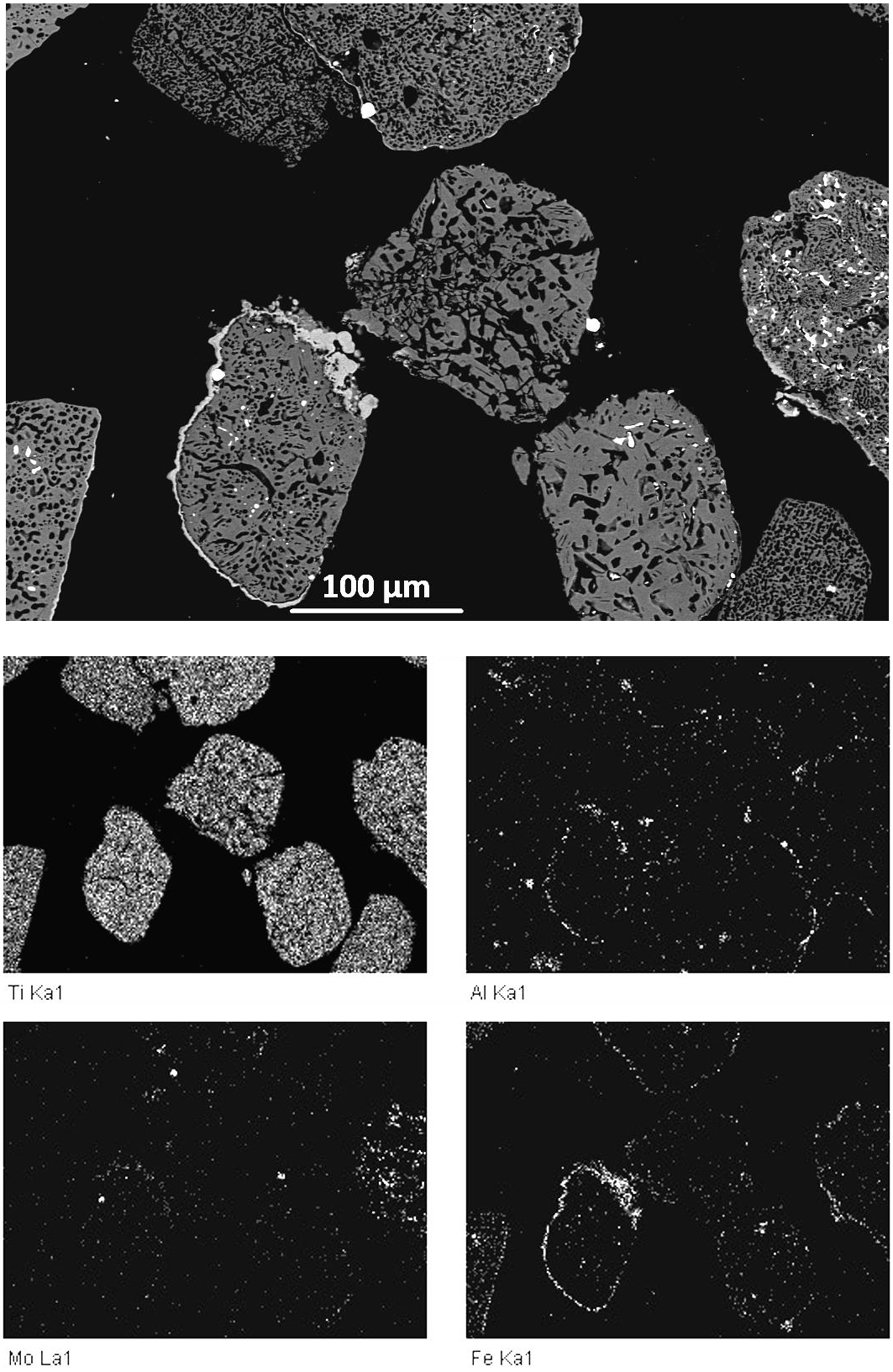

Fig. 6.4.4: Backscatter electron images of modified SR feedstock containing 10.7 wt% Fe, 5.4 wt% Mo and 1.3 wt% Al and corresponding X-EDS maps.

Figure 6.4.5 shows an X-EDS spectrum also highlighting the inhomogeneous distribution of the additional Fe, Mo and Al present within the feedstock. Note there are significant limitations associated with the X-EDS technique in terms of accuracy due to the interaction volumes involved. Hence, the data shown in Fig. 6.4.5 is indicative only. Aluminium is present within standard SR, hence the variation shown within particles consisting mainly of TiO_2 may be the natural variation in Al. However as shown in Fig. 6.4.4, some particles are coated in an alumina layer.

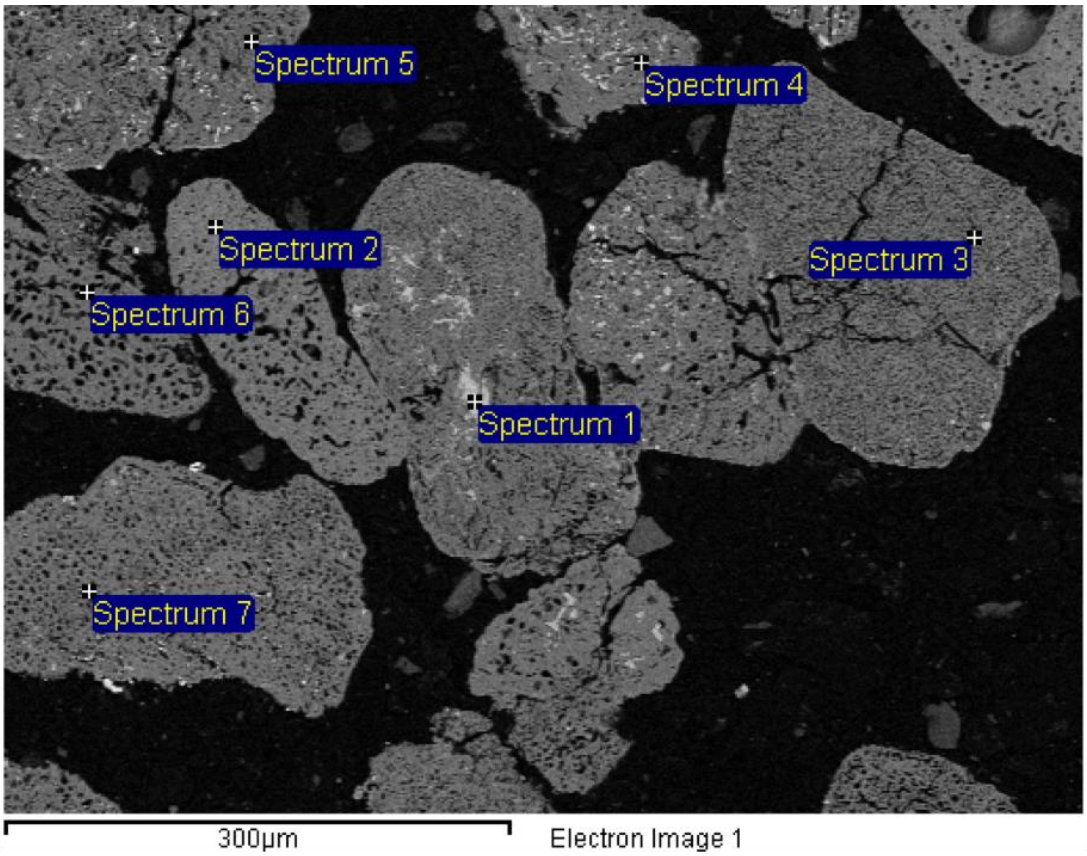

Spectrum	O (wt%)	Al (wt%)	Ti (wt%)	Mn (wt%)	Fe (wt%)	Mo (wt%)
Spectrum 1	2.07	0.01	1.79	0.03	93.87	2.22
Spectrum 2	35.34	0.17	31.74	3.4	29.35	-
Spectrum 3	50.84	0.41	46.44	1.33	0.89	0.09
Spectrum 4	43.54	0.93	49.34	1.79	4.39	0.01
Spectrum 5	44.86	0.35	53.66	0.5	0.29	0.34
Spectrum 6	41.62	1.39	53.99	2.02	0.98	-
Spectrum 7	39.05	0.27	46.7	3.18	10.53	0.27

Fig. 6.4.5: Backscatter electron image of modified SR feedstock containing 10.7 wt% Fe, 5.4 wt% Mo and 1.3 wt% Al and corresponding X-EDS data.

As shown in Fig. 6.4.3d, and the X-EDS data in Fig 6.4.5, some of the iron was found within the pores, sometimes alloyed with Mo. Usually during the production of SR, iron within the ilmenite is reduced to its metallic state before being leached out during an aeration process. However, in this modified feedstock, it appears some reduced metallic iron has not been oxidised during the aeration process. Details of the production of the feedstock are of a sensitive commercial nature, however it is thought that an increase aeration time may remove the additional iron. However, SR alloys with high iron contents are of significant interest following the outcomes of this thesis and the investigation of high iron SR feedstocks is an area of future work.

Although this feedstock will not be reduced and mechanically assessed as part of this work, this work has begun the initial characterisation of SR enhanced feedstock which will be developed further in future work.

6.5 Multiple Regression

At this stage in the development of SR derived titanium alloys, small differences in interstitial concentrations and materials of construction were unavoidable. As such, this makes an in-depth analysis and understanding of the individual contribution each additional alloying elements (Al, Mo) challenging. While the additions of alloying elements may allow a crude understanding of how to create alloys of a specific type (strong, ductile, low Young's modulus etc.), without a more refined resolution in alloy chemistry predictions, i.e., better control of both interstitial content and iron concentrations, in-depth analysis would be invalid. As such, to aid future alloy design, the data gathered from this work was used to generate an empirical model using a multiple regression technique.

Multiple regression is a powerful technique that allows the interplay of alloying elements to be assessed on a large scale, which is able to predict a variety of outcomes based on the input data. Hence, using the statistical software, Minitab V17 [4] a multiple regression technique was employed to assess how multiple independent variables (alloying elements) affected a dependant variable (compressive yield strength).

Using the multiple regression technique to determine the interplay between alloying elements and compressive yield strength allowed the production of an empirical model. Note, any model made must be used in conjunction with a basic understanding of how SR alloys behave. For example, while the model may predict certain strengths or strain to failure behaviour, it does not consider if effects are a product of the simultaneous synergistic effect of two or more alloying elements working in tandem. For example, it may not predict the higher strengths and strains afforded by the SR alloys if the Al and Fe values are in favourable ratios. A more detailed model would be required to take into account specific effects which is beyond the scope of this work.

Further, the model was been created using just 23 data sets, significantly more data would be required to accurately predict the strength of the relationship between variables and yield strength, typically over 55 are suggested [4].

Finally, it is imperative to note, this model was designed to be a starting point/guideline for future alloy development of SR derived titanium alloys, an orientative tool, rather than quantitative analysis.

6.5.1 Multiple Regression Model

Many of the remnant elements remain fairly constant throughout all of the SR alloys, such as V, Si, Cl and Nb (see Appendix 1). Therefore, concentrations of these alloying elements were taken to be 'constant' and not used in the analysis. Although this introduced approximations into the model, the small variations observed in these alloying additions were not deemed worthy of the additional complexity they would add to the system at this stage of refinement.

In the model developed, only the major sources of chemical variation Al, Fe, Mo, C and O were inputted. The values inputted were as independent variables and as such the total did not need to add up to 100%. All the modified SR derived alloys discussed throughout this work were used in the creation of the model (Appendix 1). However, an alloy was chosen at random to be removed from each of the three main data sets (a spring alloy candidate, a pseudo binary alloy of Al:Fe=0.9-1.3 and a pseudo tertiary alloy) which were not included in data used to create the model. These alloys were instead used to test the validity of the model created. Alloys chosen to be validation checks: Al2, T4 and SC5. Note alloy Al7 was also removed from the data set as this is a clear anomaly (section 5.4.1).

Using the multiple regression assistant within the Minitab software, a predictive model was determined as shown in Equation 6.1, where all values are in wt%.

Equation 6.1:

$$\begin{aligned}\text{Yield} = 1060 &- (14.4 \times \text{Al}) - (0.068 \times \text{O}) + (0.1272 \times \text{C}) + (61.2 \times \text{Fe}) + (39.6 \times \text{Mo}) \\ &+ (0.0414 \times \text{Al} \times \text{O}) - (0.0448 \times \text{Al} \times \text{C}) - (4.44 \times \text{Al} \times \text{Mo}) \\ &- (13.36 \times \text{Fe} \times \text{Mo})\end{aligned}$$

The relationship between the compressive yield strength and variables (Al, Fe, Mo, C and O) was determined to be statistically significant, with ρ value of 0.006 (where <0.10 is significant). The R^2, which determines the 'goodness' of the fit of data gave a value of 76.43%. Table 6.3 lists the alloys included in the production of the predictive model. 0.2% compressive yield strength of each of the alloys is listed alongside the yield value predicted by the model, and the difference between the two values in %. Chemical composition of each alloy within the model are listed within Appendix 1.

Table 6.3: Alloy, chemical composition alongside experimental 0.2% yield strength, corresponding predicted model yield strength and subsequent variation between experimental and modelled data)

Type	Alloy	0.2% Yield (Measured)	0.2% Yield (Model)	% variation
SR baseline	SRA 1	1090	1117	2.52
SR-Al (Al:Fe)	Al1	1257	1284	2.12
SR-Al	Al3	1402	1381	1.53
SR-Al (Al:Fe)	Al4	1348	1374	1.89
SR-Al (Al:Fe)	Al5	1416	1430	1.01
SR-Al	Al6	1397	1362	2.53
SR-Mo	SR-4Mo	1341	1362	1.57
SR-Mo	SR-6Mo	1365	1344	1.54
SR-Mo	SR-8Mo	1333	1292	3.11
SR-Mo (Mo)	SR-17Mo	1285	1300	1.14
SR-Mo (Mo)	SR-4.5Fe-9.5Mo	1222	1206	1.32
SR-Al-Mo	T1	1383	1390	0.53
SR-Al-Mo	T2	1334	1268	4.95
SR-Al-Mo	T3	1299	1275	1.87
SR-Al-Mo	T5	1258	1337	6.27
SR-Al-Mo	T6	1249	1258	0.70
SR-Al-Mo	T7	1355	1282	5.37
SR-Al-Mo	T8	1290	1225	5.04
SR-Al-Mo (Spring)	SC1	1137	1154	1.51
SR-Al-Mo (Spring)	SC2	1292	1262	2.32
SR-Al-Mo (Spring)	SC3	1208	1242	2.84
SR-Al-Mo (Spring)	SC4	1211	1244	2.75
SR-Al-Mo (Spring)	SC6	1171	1260	7.63

Using the predictive modelled equation, all yields were predicted to be within 8% of the experimentally determined values. 82% of predictive yields were within 5% of the experimental yield strength. Alloys with variation between 5 and 8% were alloys T7, T5, T8 and SC 6.

Figure 6.5.1 displays each of the 0.2% compressive yield strengths produced by the alloys plotted against values predicted by the model. A reasonably good fit was found, with an R^2 value of 0.76. While this value is acceptable for an orientative guide, improvements to the model could be made, which are discussed in more detail later.

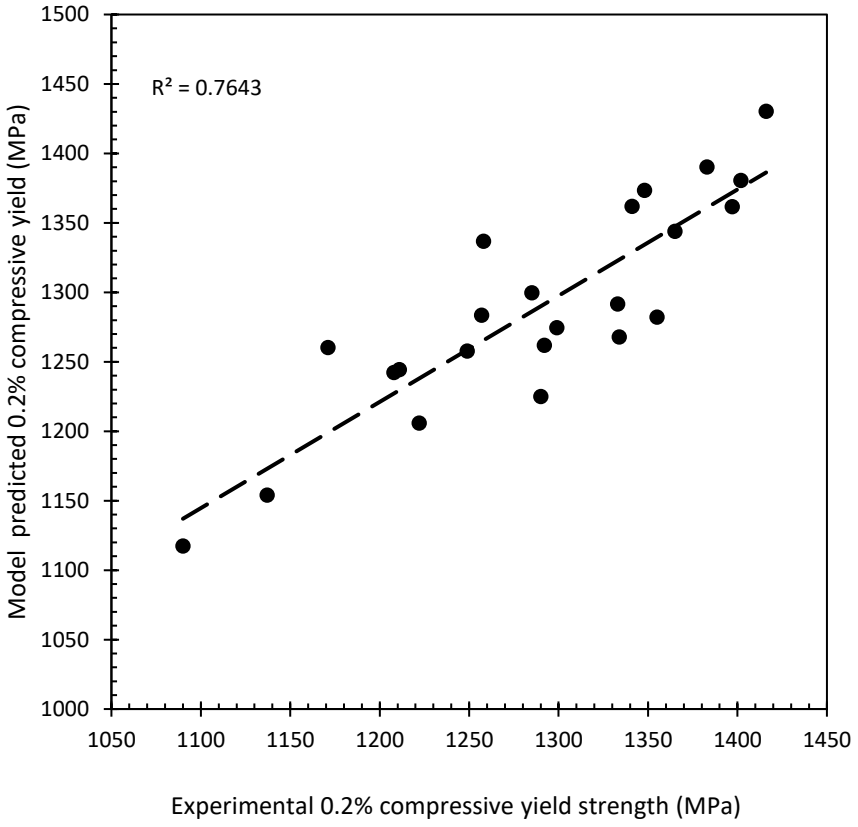

Fig. 6.5.1: Experimentally determined 0.2% compressive yield strength vs corresponding modelled value.

Validation of the model was achieved using the three test alloys which were not used to produce the model – alloys SC5 (spring candidate), Al 2 (Al:Fe) and T4 (other). Measured yield values along with predicted yield valued determined by the model are listed in Table 6.4. Chemical composition of the alloys can be found in Appendix 1.

Table 6.4: Chemical composition, as well as experimental and modelled 0.2% compressive yield strength of alloys used to validate yield prediction model

Category	Alloy	Yield measured	Yield Model	% variation
SR-Al (Al:Fe)	Al2	1282	1286	0.33
SR-Al-Mo	T4	1257	1260	0.21
SR-Al-Mo (Spring)	SC5	1175	1223	4.07
Additional 1	AD1	1231	1310	6.44
Additional 2	AD2	1256	1329	5.82
Additional 3	AD3	1248	1362	9.18

For all three of the validation test alloys, the variation between the model and experimental values were less than 5%. In the case of alloys T4 and Al2, the model produced a variation of less than 0.5%. Figure 6.5.2 replots the experimental Vs modelled data, including the validation test alloys shown in green and labelled as validation tests 1.

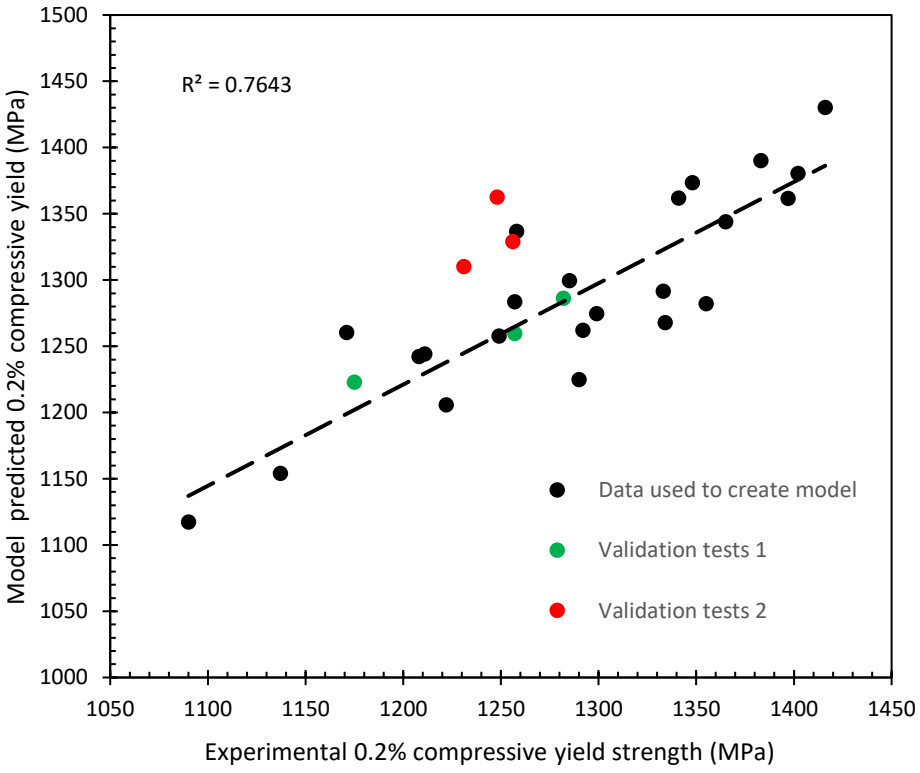

Fig. 6.5.2: Experimentally determined 0.2% compressive yield strength vs corresponding modelled value including validation tests.

A second validation test was applied of which three more alloys were tested in the model. These alloys were created throughout the duration of this work, but were not central to the study. When the model predicted the yield strength of these alloys, the variation was much higher – between 5.8 and 9.2%. These alloys are also shown in Fig. 6.5.2 in red as 'Validation test 2' and listed as additional alloys in Table 6.4.

However, for a fairly fundamental, basic empirical model to predict yield strengths within 9.5% of the measured values is a good starting point on which to build upon. Currently this model has shown it can predict yield strength values of SR derived alloys if the compositions are similar to that which have previously been assessed. The accuracy of the model in predicting the yield strengths of alloys with compositions containing higher concentrations than previously tested will likely be unreliable, as the model is built from empirical data. Hence, the model is not suitable for determining the yield strength of alloys with vastly different chemical compositions than those assessed throughout this work.

6.5.2 Improvements and Examples of the Multiple Regression Model

Improvements could be made to this crude model by including the Cr value, which can differ from run to run. For example, high iron alloys SC1 and SC6 had increased Cr values of 1.8 and 1.7 respectively from the baseline SRA 1 composition. As Cr is not accounted for within the model, the effects of increased Cr may be associated with high iron, as Cr typically increases with higher concentrations of iron due to contamination from materials of construction.

It is important to note that while the model was built using data gathered from experiments, it is a simple numerical build which does not take into account microstructure or other effects that may be observed.

For example, in the case of low and high aluminium SR derived alloys, assuming an iron content of 4 wt%, where low Al is considered 2 wt% and high Al is considered above 5 wt%, it is predicted that the microstructure would differ significantly between these two scenarios.

Assuming each of the alloys remained constant in terms of remnant elements (Cr =0.7wt%, Mn=0.3 wt%, Nb=0.3 wt%, Ta= 0.05 wt%) and interstitial elements (O= 2000 ppm and C = 1000 ppm) as well as the same processing technique (consolidated via FAST, no heat treatment), the differences between the alloys should result solely from the Al changes.

In the case of no additional Al (Al = 0.1 wt.%), due to the high quantity of potent beta stabiliser Fe and low contents of alpha stabilising interstitials, it is predicted that a microstructure consisting of metastable beta would prevail. In this scenario, a Mo equivalency of 11.6 is attained, which is consistent with a predominantly metastable beta microstructure, considering the Al equivalency is low. Small areas of secondary and grain boundary alpha would also be present. Hence, in this scenario, it is predicted that the compressive strength would be lower than that of standard SRA 1 due to the dominant presence of the softer beta phase.

As the aluminium content is increased from 0.1 wt% to 2 wt%, the Mo equivalency required to retain predominantly metastable beta is lost, leading to the precipitation of the alpha phase, resulting in a microstructure predicted to consist mainly of fine scale α+β lamellar. As this microstructure contains the harder alpha phase, it is typically stronger than that of a solely metastable beta microstructure.

Once the Al concentrations have increased to above 4 or 5 wt%, the alloy now contains a significant proportion of alpha stabilising alloying additions and the predicted microstructure contains a much higher proportion of the alpha phase, with smaller amounts of the beta phase.

Table 6.5 lists the predicted compressive yield strengths of these fictional alloys. The model has predicted a linear increase in compressive yield strength as the aluminium content increases. As previously discussed, due to the decrease in the retention of the softer metastable beta phase, and increase in solid solution strengthening, an increase in aluminium should result in an increase in compressive yield strength.

Table 6.5: Predicted compressive yield strength and chemical composition of theoretical Al enhanced SR derived alloys.

Alloy	Al (wt.%)	Fe (wt.%)	Mo (wt.%)	O (ppm)	C (ppm)	Predicted yield strength (MPa)
0	0.1	4	0	2000	1000	1298
1	1	4	0	2000	1000	1320
2	2	4	0	2000	1000	1343
3	3	4	0	2000	1000	1367
4	4	4	0	2000	1000	1390
5	5	4	0	2000	1000	1414

Further, typically, an increase in strength is usually associated with a decrease in ductility. However, in some cases, such as when the Al and Fe contents are present in equal concentrations significant ductility is retained, despite the high strengths attained. Hence, the model must only be used as an initial starting point, in combination with an in depth understanding of the SR baseline system. A further example of this is the formation of titanium aluminides, which will form upon the addition of Al concentrations above 8 wt%. Formation of aluminium titanates will result in enhanced strengthening, not predicted by the model. Aluminium titanates are known to be extremely embrittling and will result in a large loss in ductility.

As this is the first study into the production of alloys produced from SR, it is likely there are many other observations yet to be made that will have an influence over both the microstructure and resulting compressive yield strength/mechanical properties.

It is clear that a model built on mechanistic data would produce more accurate predictions of yield strengths, however, at this point of research a mechanistic model is not viable but is something that will be considered in future work.

6.6 Conclusions

Work within this chapter has built upon initial baseline investigations of the SR baseline alloy within Chapter 4 and preliminary alloy development work using Al and Mo as alloying additions within Chapter 5. Hence, utilising the data gathered in Chapters 4 and 5, several spring candidate alloys were created based around compositions determined to give good spring properties such as strength, ductility and a low Young's modulus.

Of the spring candidate alloys assessed, it was clear that a high molybdenum equivalency resulted in a higher strain to failure value which is beneficial for spring applications. A high Mo equivalent allows retention of the ductile metastable beta phase at room temperature, resulting in enhanced ductility. This work has shown that inexpensive Fe additions can be utilised to replace Mo to give similar compressive yield strengths and strain to failure values without the formation of intermetallic particles. Due to iron's high potency as a beta stabiliser, less alloying addition is required enabling the resulting alloy to maintain its low weight status.

Although further in-depth analysis of the spring alloys is required, alloy SC1 was identified as a potential starting alloy for future alloy development, due to its combination of high ductility and strength as well as a low Young's modulus.

Following the analysis of the spring alloy candidate alloys Iluka resources supplied 3.2 kg of modified SR feedstock as it is envisaged that in large scale operations alloying elements would be incorporated into the feedstock during the production of SR.

Finally, using all of the data within this work, an empirical based model was developed using a multiple regression technique. This model is capable of predicting the compressive yield strength of SR derived alloys within an accuracy ± 9.5%.

Hence, work within this Chapter has provided the preliminary baseline investigations necessary for further alloy development using SR derived titanium alloys as a starting point.

References

[1] J. D. Cotton, R. D. Briggs, R. R. Boyer, S. Tamirisakandala, P. Russo, N. Shchetnikov and J. C. Fanning, "State of the art in beta titanium alloys for airframe applications," *JOM,* vol. 67, no. 6, pp. 1281-1303, 2015.

[2] R. R. Boyer, "An overview on the use of titanium in the aerospace industry," *Materials Science and Engineering A213,* pp. 103-114, 1996.

[3] R. R. Boyer and R. D. Briggs, "The Use of beta Titanium Alloys in the Aerospace Industry," *Journal of Materials Engineering and Performance,* vol. 14, no. 6, pp. 681-685, 2005.

[4] Minitab, "Minitab V17," All such material remains the exclusive property and copyright of Minitab Inc. All rights reserved.

[5] A. M. Sherman, C. J. Sommer and F. H. Froes, "The use of titanium in production automobiles: potential and challenges," *JOM,* pp. 38-41, 1997.

[6] R. R. Boyer and R. D. Briggs, "The Use of beta Titanium Alloys in the Aerospace Industry," *Journal of Materials Engineering and Performance,* vol. 14, p. 681, 2005.

[7] R. R. Boyer, "An overview on the use of titanium in the aerospace industry," *Materials Science and Engineering ,* vol. A213, pp. 103-114, 1996.

[8] C. Leyens and M. Peters, Titanium and titanium alloys, Wiley-VCH, 2003.

[9] M. Jackson, "Automotive Applications for Titanium," in *Encyclopedia of Automotive Engineering*, 2014, pp. 1-15.

[10] T. Nishimura, "Forming technology of titanium (in Japanese)," in *Kobe Steel Data Book: Titanium*, NikkanKogyou Shinbun, 1992, p. 3.

[11] B. Thomas, "Continuous extrusion of commercially pure titanium powder," *Thesis University of Sheffield,* 2016.

[12] P. G. Esteban, L. Bolzoni, E. M. Ruiz-Navas and E. Gorgo, "PM processing and characterisation of Ti-7Fe low cost titanium alloys," *Powder Metallurgy,* vol. 54, no. 3, pp. 242-251, 2011.

[13] Y. Liu, S. Xu, X. Wang, K. Li, B. Liu, H. Wu and H. Tang, "Ultra-High Strength and Ductile Lamellar-Structured Powder Metallurgy Binary Ti-Ta Alloys," *JOM,* vol. 68, no. 3, pp. 899-907, JOM, Vol. 68, No. 3, 2016.

[14] J.Bultitude-Paull Iluka Resources Capel Western Australia, Private communication (unpublished) 2017.

[15] R. R. Boyer, J. C. Fanning and S. L. Nyakana, "Quick reference guide for beta titanium alloys in the 00s," *Journal of materials engineering and performance,* vol. 14, no. 6, pp. 799-811, 2005.

[16] B. Y. Chen, K. S. Kwang and K. L. Ng, "Effect of cooling process on the alpha phase formation and mechanical properties of sintered Ti–Fe alloys," *Materials Science and Engineering A,* vol. 528, pp. 4556-4563, 2011.

Chapter 7:

Conclusion and Impact Statement

7.0 Conclusion & Impact Statement

7.1 Conclusion

This work has fully characterised the chemical and physical properties of the synthetic rutile (SR) feedstock as well as assessing chemical, physical and mechanical properties of the corresponding SR derived titanium alloy. Alongside the characterisation of the SR feedstock and corresponding derived titanium alloy, the mechanism of reduction has also been determined.

Using partial in-situ experiments, the reduction mechanism was determined to be similar to that of previously reported work, detailing the reduction mechanism of a pure TiO_2 precursor [1] [2]. However, due to the presence of remnant iron, new features of the reduction process are observed, including the formation of $TiFe_2$ and TiFe. However, their subsequent breakdown is also observed as the iron dispersed throughout the entirety of each particle to form a homogeneous microstructure within each individual particle.

As the SR feedstock is derived from an ore, a slight difference in concentration of iron was found on a local scale. As such, the resulting SR derived titanium alloy powder also exhibited a slight difference in iron concentration from particle to particle. However, following consolidation, due to the fast diffusion coefficient of Fe within Ti, the resulting microstructure was homogeneous, with no intermetallic formation observed.

Subsequent mechanical property testing of the consolidated SR derived titanium alloy unprecedentedly revealed that the compressive 0.2% yield strength, strain to failure value and response to deformation were all similar to that of the widely used Ti-6Al-4V alloy. In comparison to the Ti-6Al-4V alloy, a titanium alloy derived directly from synthetic rutile and consolidation via a low cost downstream consolidation technique (such as the field assisted sintering technique or continuous rotary extraction) would require significantly less capital to produce. Hence, with further investment and investigation, the SR derived titanium alloy, in combination with low cost downstream processing techniques, has the potential to be a game-changer within the titanium industry.

Note, although promising at this stage, the SR derived titanium alloy is still in the developmental stages, with many more rigorous and large scale tests to be conducted, as discussed in chapter 8: future work.

However, at a laboratory scale, to further explore the potential of SR derived titanium alloys, pseudo-binary SR derived alloys were produced and tested.

To test the mechanical properties of SR derived titanium alloys produced on an R&D scale, a small-scale mechanical property testing technique was developed and validated using commercial titanium alloys. This small-scale testing technique consisted of consolidation via FAST using specifically designed moulds to produce a small consolidated sample from small volumes of material (4.2 g). Following consolidation, the puck is machined into a small compression sample of 6 mm x 9 mm which was subjected to a compression test at room temperature.

Once the small-scale mechanical testing technique was validated, pseudo-binary SR derived titanium alloys, doped with Mo or Al were tested to understand the individual effects of Al and Mo on the SR derived titanium alloy. These alloys were produced by mixing SR feedstock with the relevant oxide, prior to the reduction process. A major limitation of the experimental design was the variation from run to run in terms of interstitial values (O, C) and materials of construction (Fe, Cr). In particular, the presence of carbon led to the formation of TiC as discussed in section 4.8. As the concentration of carbon was different in each alloy, the scum carbon particles, coarse carbon precipitates and the finer lath shaped carbon precipitates were different between each run, further, the addition of alloying elements also affected the solubility of carbon within titanium which also made direct comparison difficult. Further, each alloy produced a slightly different porosity value. Although the differences in porosity were small, the differences must be noted.

However, although individual alloy compositions could not be directly assessed due to differences in interstitial values and porosity, overall trends between alloys could be identified.

In the case of the pseudo binary SR-Al derived titanium alloys, direct comparison was particularly difficult due to differences in the Fe content. However, the alloys could be individually assessed and the data generated was utilised in the production of a multiple regression model, used to predict the mechanical properties in future alloy development projects. A major outcome of this section of work was the discovery of enhanced strain to failure values if the ratio of Al:Fe in wt% remained between 0.9-1.1. Although interesting, the mechanism behind this favourable ratio is currently poorly understood and further experimentation, including transmission electron microscopy studies are required to both confirm this phenomenon and to determine the causation of the favourable properties.

Of the pseudo-binary SR-Mo alloys, all possessed Fe values of around 2 wt% and hence, could be directly compared against each other. A linear relationship with respect to yield strength or

strain to failure values with increasing Mo concentration was not observed, which may be due to the formation of the omega phase. However, this also cannot be confirmed without further investigation. All of the SR-Mo alloys assessed produced a two-phase microstructure consisting of Mo rich and Mo lean areas, due to the slow diffusion of Mo within Ti and inhomogeneity within the pseudo-binary SR-Mo titanium powder. Improved homogenisation may be achieved via several techniques discussed in the future work section. Previous research into Ti-Ta alloys, have also exhibited this two-phase structure, which was reported to be of high strength [3] [4].

SR-17Mo produced the most ductile alloy, achieving a ductility surpassing that of the SRA 1 baseline alloy. Improved ductility is thought to be due to the increase in the ductile beta phase and possibly due to the two-phase microstructure.

As an attempt to lower the cost of the ductile SR-17Mo alloy, a novel alloy was tested, replacing 7.5 wt% Mo with 2.25 wt% Fe. As iron is three times more potent at stabilising the beta phase, the Mo equivalency of the SR-17Mo alloy and SR-4.5Fe-9.5Mo alloy was retained at 26.0 and 26.1 respectively. Following compression testing, SR-4.5Fe-9.5Mo exhibited a similar true stress-true strain curve to that of the original SR-17Mo. Hence, it was postulated that low cost iron could replace the costly Mo in the production of ductile alloys, specifically springs.

Hence, the final strand of work within this thesis was the production of SR derived titanium alloys, based around the SR-4.5Fe-9.5Mo composition with the aim of producing an alloy for use as a spring within the automotive industry. Of the alloys tested, alloy SC1 (SR-1.5Al-4.5Fe-9.9Mo) produced the most ductile alloy with a good strength. As such, SC1 was the alloy of choice for further alloy development for spring applications. By coincidence, this alloy has a similar composition to Timetal LCB (Ti-1.5Al-4.5Fe-6.8Mo), a low cost metastable beta alloy specifically designed for springs within the automotive industry. Unfortunately, the cost of the ferro-molybdenum used to make this alloy low cost significantly increased at the turn of the century, rendering the alloy redundant as it was no longer low cost. However, it is a testament of the alloy design approach used within this thesis, that the most ductile alloy produced had a close composition to an alloy separately developed for spring applications via the melt-wrought processing route.

Future work will consist of the scaling up and production of ~5 kg of a candidate spring alloy, as such, initial feedstock for this task was analysed and is also reported.

Finally, multiple regression software, MiniTab [5], was utilised in the production of a predictive model to be used in future alloy development projects. Although this model is based on

empirical data, rather than mechanistic understanding, it is a useful tool in determining rough values in combination with the users own knowledge and understanding of SR derived titanium alloys.

7.1.2 Final Remarks

It is the opinion of the author that the FFC process technology stands in a unique position to exploit ore like material for titanium alloys, in particular, ore like material with high iron content. Although iron is can form titanium intermetallic compounds, its formation is known to be sluggish [6]. As a strong beta stabilising element and fast diffuser within titanium it is an excellent candidate as an alloying addition when producing titanium alloys through a solid-state production route.

Traditionally, alloys have been designed for use with classical ingot metallurgy routes, in which beta fleck formation was a common issue for iron containing alloys during the melting procedure (due to differences in density of Ti and Fe). As the extraction route, consolidation method, and final processing occur in the solid state, beta fleck formation can be avoided. Further, in designing alloys for downstream consolidation routes, an entirely new set of properties are deemed to produce homogeneous alloys, namely, the ability to quickly diffuse within the alloy, a property determined by the diffusion coefficient. As both a potent beta stabiliser (requiring less alloying addition to stabilise the beta phase) and a fast diffuser within titanium, iron is uniquely positioned as an excellent alloying addition for alloys produced within the solid state. Although, large scale tests are required to confirm there is no beta fleck formation on larger components.

Although this work utilised Mo to create alloys, it is perhaps possible to entirely replace the Mo content with the addition of iron. Iron is a much faster diffuser than Mo within titanium which can aid both densification using powder metallurgy consolidation routes and homogenisation.

The creation of Ti alloys with higher iron content is also economically viable as less processing, specifically, less aeration of the reduced ilmenite is required. High iron titanium alloys reduced from an ore like material via a low-cost extraction route and produced via low cost downstream consolidation techniques offer an entirely novel stream of titanium alloys, previously unexplored with the potential of opening new markets.

7.2 Impact Statement

Prior to this work, only initial proof of concept experimentation had been conducted on the reduction of this synthetic rutile. This work has presented for the first time a full characterisation of the synthetic rutile feedstock, the mechanism by which the SR reduces, including an understanding of the behaviour of iron throughout the reduction process and the baseline mechanical properties SR derived alloys produce. This work has aided the understanding of SR derived alloys and will significantly aid the future development of both baseline SR derived alloys as well as SR derived alloys modified and tailored toward specific applications.

Following this work, Metalysis have now up scaled their production of SR derived titanium alloy to developmental scale (generation 2) and their generation 3 reactors which produce around 5-6 kg per run.. Results from this work are regularly included in presentations by technology company Metalysis, highlighting the progression of their research. Further, this work has aided the procurement of investment of both large automotive and aerospace companies in increasing the technology readiness level (TRL) level of the SR baseline alloy. One such project, sponsored by Innovate UK and led by aerospace company Safran Landing Systems, known as 'FAST-*forge*' and is currently undertaking the scaling up of the SR baseline alloy and subsequent large scale forging and mechanical testing. The baseline work on SR has also been useful to the Mining company, Iluka Resources Limited, who produce large scale quantities of the SR feedstock for the titanium pigment industry.

Experimentation on modified SR derived alloys had not been attempted prior to this work. This work has provided an initial understanding of the effects of Mo, Al and Fe on the baseline SR derived titanium alloy, aiding any future alloy development projects. Future projects will benefit from the baseline knowledge outlined within this thesis as well as the multiple regression model which can aid future alloy design. Relationships previously unobserved such as the Al:Fe effect are novel and may provide the starting point for future alloy development.

A major outcome of this work was the replacement of Mo with Fe, which was shown to be a viable method to reduce costs without sacrificing ductility. Hence, further investigation of high iron SR based alloys should have a significant impact on the cost of spring alloys. Large scale spring alloys are currently under investigation by Metalysis with future projects with large automotive companies currently under negotiation.

Significant industry and academic value has been gained from this work and some aspects of it will be continued further. A further PhD student has been assigned to follow this work and to further refine alloys derived directly from synthetic rutile for specific applications.

Chapter 8:

Future Work

8.0 Future Work

This work is the first academic assessment of synthetic rutile derived titanium alloys and its derivatives. As such, the nature of this seminal work has led to many more potential lines of investigation. SR derived alloys are a complex system and to fully take advantage of this alloy system, a substantial amount of further work is required. This thesis has provided preliminary scientific investigations, providing a baseline for many areas of further work, which are highlighted below.

8.1 Further Experiments on the Reduction Process

Further investigation into the pathway of SR throughout reduction

Partial experiments conducted within this work have been useful in identifying the main reduction mechanism of synthetic rutile. However, a loose powder was used, the 'cake' produced after 0.5, 1, 2 and 4 h of reduction was fragile and quickly disintegrated into a powder. As such, it was not possible to determine if 'direct reduction' (Section 4.2) occurred throughout the reduction of SR. Hence, future work may consist of partial reductions of pressed and sintered pellets of SR to determine if the direct reduction pathway is active.

Investigation into the reduction pathway of additional elements through the reduction of SR

In a similar vein, the behaviour and role of aluminium, as a whole, throughout the electrodeoxidation process appears to still be poorly understood. Partial reductions of Ti alloys containing high concentrations of aluminium will help to understand its behaviour and optimise the process for alloys containing high concentrations of this elusive alloying element. Likewise, this also applies to other additional alloying elements such as Mo.

Further cost reduction of alloys by optimisation of electrolytic procedures

Optimisation of the reduction profile of synthetic rutile will lead to a reduction in time and energy consumed, making the resulting alloy powder product cheaper. By calculating the quantity of phases present at each stage of the reduction process, the process may then be optimised (altering current efficiency, time) to produce low oxygen alloys within the shortest time frame. Further, kinetic studies on the reduction rate of synthetic rutile versus that of a pure TiO_2 precursor, would be beneficial in future work, involving the optimisation of the reduction profile for other SR derived titanium alloys. Due to the presence of beta stabilisers within the SR feedstock, it is thought that the SR reduces at a faster rate than that of a pure TiO_2, due to

local alloy chemistry facilitating entering the beta phase at an earlier stage in the reduction process, compared to pure TiO_2. The slowest stage of the reduction process is known to be the removal of oxygen from the solid solution of oxygen in titanium. Hence, presence of beta stabilising iron should expand the α+β phase field allowing a faster reduction. However, this has not been experimentally validated.

Consistency in reductions

Similarly with the optimisation experiments, and likely to result an outcome of optimisation of the reduction profile, is the ability to consistently produce SR alloys within narrow limits of both interstitial elements (O, C) and materials of construction (Fe, Cr). At an R&D scale, throughout this project, there has been a degree of variation between runs of interstitial elements, as well as Fe and Cr content. Hence, optimisation experiments would also include the ability to consistently produce alloys with a very narrow range of chemical composition variation.

For any further alloy development to occur, the degrees of freedom within the experiments need to be reduced to correctly understand the individual effects each alloy element is having upon the baseline SR derived alloy.

8.2 Further Alloy Development

Investigation of tolerance limits of remnant and interstitial elements

This work has begun to explore the viability of the usage of synthetic rutile derived alloys within the titanium industry. As a new alloy, the tolerance level of the interstitials O and C upon the mechanical properties has not yet been determined. Further, the boundaries and tolerances of remnant elements present need to also be fully assessed.

Alternative ilmenite sources and altered Becher process to produce high iron SR derived titanium alloys

Based on the original source of the ilmenite, as well as the method chosen to convert the ilmenite to SR, different chemical compositions of SR can be produced. Hence, a particularly interesting study would be to investigate the effect of using alternative sources of ilmenite upon the resulting titanium alloy produced. Further, as shown in Chapter 5, high iron contents may be utilised to replace Mo, providing beta stabilisation and solid solution strengthening to provide satisfactory mechanical properties. It is possible to alter the reduction process to produce a

lower conversion of iron oxide to metallic iron, hence baseline SR feedstocks can be produced to contain higher iron concentrations.

As an extreme example, the investigation of the reduction of the intermediate product of the Becher process, reduced ilmenite, would be particularly interesting. Reduced ilmenite (RI) is the name given to ilmenite which has undergone the initial reduction of iron, leaving behind a porous structure interlaced with specs of metallic iron [1]. As such, this product has a high iron content. The success of a titanium alloy derived directly from reduced ilmenite, would depend upon the ability of iron within the alloy to uniformly distribute throughout the titanium, rather than forming TiFe intermetallics. Although the high diffusion rate of iron has enabled the avoidance of iron intermetallics within this work, (and other work up to 7 wt% Fe [30]) higher concentrations of iron may lead to the formation of TiFe during the reduction or sintering process. Recent work has shown the reduction of ilmenite leads to the production of ferrotitanium [2]. Hence, further work is required to assess a) the boundaries and tolerance of SR derived titanium alloys of iron concentration and b) feasibility of such alloys. Further, calcination of an RI feedstock to remove carbon impurity is not possible, as the RI would convert back to ilmenite.

Effects of other alloying elements on the reduction process and mechanical properties of SR derived titanium alloys

While this work has determined the effect of Al/Mo/Fe on the reduction process and resulting mechanical properties, there are many more alloying additions to be explored. In particular, alloying elements which were previously unreliable as additions in titanium alloys, due to segregation effects from large differences in density and or melting point may be revisited to provide a commercial advantage.

However, within this work, and work completed by other researchers [3], alloying elements with fast diffusion rates with titanium alloys appear to produce the most homogenous alloys. Hence, with the aims of producing homogeneous alloys, the investigation of alloying additions with high diffusion rates (or at least equal to that of the self-diffusion of titanium) within titanium may be most fruitful.

Further investigation into the dual-phase microstructure of SR-Mo alloys

SR alloys doped with significant quantities of Mo resulted in the production of a dual-phase microstructure in the post FAST consolidation billet. The formation of this microstructure was

due to both inhomogeneous chemical distribution of Mo within the Mo enhanced SR derived titanium alloy powder and the slow diffusion of Mo within Ti. Although homogeneity of these alloys may be achieved by improved mixing techniques, optimised FAST consolidation conditions, or consolidation via techniques employing severe plastic deformation (such as continuous extrusion), it would be interesting to fully investigate the properties of the dual-phase microstructure. Work by Liu et. al studying the two-phase microstructure formed by the sintering of Ti and Ta, reported the excellent mechanical properties observed were due to the unique lamellar microstructure, refined lamellar and the high toughness of the Ta enriched areas [4]. Hence, further work would include a comparison of mechanical properties of the two-phase microstructure of SR-Mo alloys compared with homogenised microstructures as well as investigations into the specific properties of the Mo rich/lean areas.

Homogenisation of SR-Mo microstructures

As previously mentioned, the SR-Mo alloys resulted in an inhomogeneous microstructure, due to the insufficient diffusion of Mo within Ti alloys. Further work may investigate pathways to improve the homogenisation of the alloys via consolidation methods that induce severe plastic deformation, such as continuous extrusion or through various heat treatments. Production of homogeneous metal particles following the FFC reduction process, should result in a homogeneous microstructure following consolidation, hence improved mixing techniques or smaller size fraction of powder could be utilised. Another stream of investigation would be the initial heat treatment of the SR and Mo oxides that could form a solid solution which may aid homogenisation during the reduction process.

Omega phase studies in Mo alloys

Titanium alloys containing Mo are known to form the embrittling omega phase. However, it was not determined if the omega phase formed within the alloys produced in this thesis. Presence of the omega phase is known to significantly increase the Young's modulus of titanium alloys, an undesirable characteristic within spring beta alloys. However, the omega phase has also been used to precipitate finely dispersed alpha, which could be beneficial due to the increase in strength values acquired. Hence, further investigation including transmission electron microscopy studies are required to both determine the presence of the omega phase, and if further heat treatments can lead to the uniform finely dispersed precipitation of the alpha phase.

Kirkendall studies

Section 5.5.3 postulated the formation of Kirkendall porosity within the SR-Mo alloys. However, at this stage, further evidence would be required to fully prove this mechanism is active within the stated alloys. Such experimentation could include annealing the alloys, if the porosity increases, it is likely the Kirkendall effect is active due to uneven diffusion.

Understanding the effect of remnant elements on the SR derived titanium alloy

Although the presence of the remnant elements, (known colloquially as 'the soup') present within SR derived alloys are known to add to the solid solution strengthening of the alloy, the exact amount of strength added has not been quantitatively defined.

As such, an interesting experiment would be to determine the effect the remnant elements or 'soup' has upon the strength of titanium alloys. To quantitatively determine this, a range of alloys consisting of a TiO_2 precursors base + alloying addition and a SR feedstock base + alloying addition could be produced and their mechanical properties compared. Additionally, a pure Ti alloy produced with ~2.6 wt% Fe could be produced and compared to the baseline SR derived titanium alloy (SRA 1) to determine the effects of the remnant elements excluding iron may also yield valuable information.

Further refinements and improvements made to the multiple regression model

While the model produced within this work is a good starting point to begin future alloy development, there is significant area for improvement. A larger set of data would allow a more accurate empirical model to be produced. Further, at present the model cannot account for specific trends, such as that of the enhanced properties found in alloys with an Al:Fe ratio of ~0.9-1.1. Hence, future work may consist of further refining this model or developing a new model to incorporate observed trends also.

Investigation of Metal Matrix Composites produced by the FFC process

During this work, TiC based metal matrix composites have been produced and their microstructures analysed in Section 4.9. Metal matrix composites are known to produce exceptionally stiff titanium alloys. Further, the FFC process may be able to provide a low-cost method of producing uniformly dispersed TiC particulate metal matrix composites. Future investigation of these alloys would consist of a full investigation of the dispersion of the TiC particulate phase, mechanical property testing and a review of potential applications.

8.3 Downstream Processing

Optimisation of FAST conditions

Throughout this work, a 'black box' technique using the field assisted sintering technique (FAST) has been utilised to consolidate the SR derived titanium alloy powders. However, it is thought that by optimising the FAST processing conditions, a full consolidation may be achieved (98.6% density at present for SR, consolidated at 1200°C and 97.5% using the small-scale technique, 1090°C). Further, optimisation of the consolidation technique and cooling profile could also lead to different microstructures (e.g volume fraction of primary alpha, size of alpha lamellar), which may also provide further enhancement to the mechanical properties.

Alternative consolidation techniques

Only the FAST was utilised throughout this work to consolidate the SR derived titanium alloys. It would be of significant interest to observe the consolidation behaviour (and homogenisation of slow diffusing elements such as Mo) using consolidation techniques that employ severe plastic deformation such as continuous extrusion. Application of spheroidised SR derived titanium alloys may also be of interest in additive layer manufacturing (ALM) processes, although the alloys within this thesis have not been specifically designed for ALM consolidation techniques. Hence, further alloy development may be required to tailor the chemistry of the SR derived titanium alloy towards ALM consolidation methods.

8.4 Upscaling

Further mechanical testing of alloys made & scaling up

This work has provided an initial mechanical property assessment of the baseline SR derived titanium alloy as well as its derivatives. To fully assess the feasibility of these alloys, the alloys must be produced at a large scale and a full assessment of their mechanical properties completed, including tensile testing, fatigue testing and corrosion resistance tests.

Investment into the process by external automotive and aerospace companies has led to the upscaling and large scale testing of the baseline SR derived titanium alloy. The SR derived titanium alloy has been consolidated into 100 mm diameter pucks as part of an external project known as 'FAST-*forge'*, which will undertake large scale mechanical property testing of the SR derived titanium alloy, such as tensile and fatigue tests.

Initial proof of concept mechanical testing on the spring alloys developed within this work has begun. Iluka resources provided 3.2 kg of spring alloy SR feedstock which has been analysed within Chapter 6. However, the reduction of this material and its subsequent analysis/mechanical testing is out of the scope of this work and will be completed in future work by Metalysis and the University of Sheffield.

8.5 Future Work Conclusions

Alongside the production of a small-scale testing technique, full characterisation of SR feedstock and its subsequent titanium alloys, this work has also led to the identification of two main subgroups of potential modified SR titanium alloys.

The first of which are alloys intended to have a lower modulus and improved ductility over that of standard SR with a basic formulation of high Mo (over 6 wt%) and high iron (over 4 wt%). These alloys received the largest portion of investigation throughout this work, but require much more in-depth studies, including further optimisation of composition, optimisation of reduction process, as well as further mechanical testing, physical and corrosion testing, and upscaling.

The second branch of SR derived alloys identified are those in which the aluminium value is close to the iron value. These alloys have demonstrated a combination of high strength and ductility and are worth investigating further. Their associated high stiffness values in combination with their all-round good properties make them potential candidates for a variety of applications, such as connecting rods within the automotive industry. However, the relationship between iron and aluminium within the alloys is poorly understood and requires significantly more research. Alongside further investigation of the baseline SR derived titanium alloy, these two routes of enhanced SR alloys have shown promise and will likely lead to further investigative studies.

This work has been successful in its aims of investigating the use of SR derived titanium alloys and their mechanical properties, as well as exploring the production of novel alloys branching from this new unexplored area of titanium alloys. As the baseline SR derived titanium alloy has shown to have mechanical properties similar to that of Ti-6Al-4V at this early stage in the investigation, with no real optimisation, SR derived alloys show real promise and may facilitate the introduction of low-cost titanium alloys into automotive or novel applications.

Due to the fruitful nature of low-cost SR derived titanium alloys produced via the FFC process, particularly when coupled with low cost downstream consolidation techniques, significant interest has been developed throughout the duration of this work, and research projects are

currently planned to continue further investigation, particularly in areas of high iron alloys, Al:Fe alloys, optimisation of both extraction and downstream consolidation and further consolidation. A new PhD project has been commissioned which will directly follow on from this work and large research projects involving external companies may also carry forward some of the future work outlined in this section.

References

[1] J. B. Farrow , I. M. Ritchie and P. Mangano, "The reaction between reduced ilmenite and oxygen in ammonium chloride solutions.," *HydrometaUurgy,,* vol. 18, pp. 21-38., 1987.

[2] Z. Zhou, Y. Hua, C. Xu, J. Li, Y. Li, Q. Zhang, L. Xiong and Y. Zhang, "Phase transitions observations during the direct electrolysis of ilmenite to ferrotitanium in CaCl-NaCl Melt," *International journal of the Electrochemical society,* vol. 11, pp. 5448-5458, 2016.

[3] P. G. Esteban, L. Bolzoni, E. M. Ruiz-Navas and E. Gorgo, "PM processing and characterisation of Ti-7Fe low cost titanium alloys," *Powder Metallurgy,* vol. 54, no. 3, pp. 242-251, 2011.

[4] Y. Liu, L. F. Chen, H. P. Tang, C. T. Liu, B. Liu and B. Y. Huang, "Design of powder metallurgy titanium alloys and composites," *Materials Science and Engineering: A,* vol. 418, no. 1-2, pp. 25-35, 2006.

Appendix 1: Full chemical composition of SR derived titanium alloys listed within this thesis. All elements over 0.6 wt% measured via XRF spectroscopy and under 0.6 wt% by ICP-MS, with the exception of Cl, measured by XRF and O/C measurements measured by an Eltra ON-900 and CS-800 respectively. Strain to failure values are true strain and 0.2% yield strength values are in MPa.

Table A1: SR baseline alloy SRA 1 (Chapter 4)

	Al	Ca	Cr	Fe	Mn	Mo	Nb	V	Si	Cl	Ta	Zr	O	C	Mo eq:	Density %	Strain to failure	0.2% yield strength
SRA 1	0.09	0.09	0.1	2.57	0.54	0	0.51	0.16	0.33	0.23	0.05	0.08	3528	1041	8.702	97.5	0.339 (av. of 3)	1090 (av of 3

Table A2: Pseudo-Binary SR-Al alloys (Chapter 5)

Alloy	Al	Ca	Cr	Fe	Mn	Mo	Nb	V	Si	Cl	Ta	Zr	O	C	Mo eq:	Density %	Strain to failure	0.2% yield strength
Al 1	2.76	0.02	0.66	2.21	0.31	0	0.48	0.24	0.3	0.17	0.47	0.07	2572	2562	5.6	98.2	0.239	1257
Al2	2.41	0.09	0.92	2.17	0.29	0	0.34	0.22	0.4	0.19	0.06	0.07	3779	416	6.1	98.5	0.248	1282
Al3	5.3	0.02	0.39	3.38	0.42	0	0.32	0.19	0.48	0.22	0.17	0.06	2030	1065	6.1	98.6	0.184	1402
Al4	3.35	0.06	0.45	3.02	0.42	0	0.38	0.21	0.37	0.19	0.13	0.08	2828	1004	7.1	98.4	0.264	1348
Al5	3.61	0.11	0.95	3.87	0.56	0	0.35	0.2	0.44	0.19	0.11	0.07	3235	2261	10.3	98	0.234	1416
Al6	2.73	0.189	1.37	3.91	0.35	0	0.48	0.24	0.31	0.18	0.44	0.08	2030	2111	11.8	98.6	0.165	1397
Al7	2.39	0.14	0.42	3.44	0.34	0	0.33	0.2	0.4	0.17	0.12	0.07	1532	2467	9.1	98.3	0.127	1612

Table A3: Pseudo-Binary SR-Mo alloys (Chapter 5)

Alloy	Al	Ca	Cr	Fe	Mn	Mo	Nb	V	Si	Cl	Ta	Zr	O	C	Mo eq:	Density %	Strain to failure	0.2% yield strength
SR-4Mo	0.22	0.14	0.71	2.17	0.32	4.26	0.4	0.22	0.37	0.32	0.71	0.07	2195	2221	12.4	98.8	0.183	1341
SR-6Mo	0.1	0.15	0.91	2.01	0.29	5.63	0.43	0.25	0.36	0.27	0.09	0.05	2723	2176	13.6	98.2	0.148	1365
SR-8Mo	0.5	0.14	1	2	0.26	8.34	0.35	0.2	0.52	0.17	0.12	0.06	2380	1336	15.9	97.9	0.185	1333
SR-17Mo	0.23	0.14	1.07	2.25	0.29	17.2	0.355	0.21	0.44	-	0.07	0.02	2833	1062	26	98	0.376	1285
SR-4.5Fe-9.5Mo	0.39	0.16	1.9	4.58	0.29	9.41	0.36	0.2	0.5	-	0.15	0.07	1740	1648	26.1	98.7	0.368	1222

Table A4: Pseudo-ternary SR-Al-Mo alloys (Chapter 5)

Alloy	Al	Ca	Cr	Fe	Mn	Mo	Nb	V	Si	Cl	Ta	Zr	O	C	Mo eq:	Density %	Strain to failure	0.2% yield strength
T1	3.47	0.05	0.59	1.53	0.2	1.54	0.35	0.21	0.53	0.18	0.05	0.06	4143	1155	4	94.4	0.192	1383
T2	3.11	0.05	0.32	2.18	0.22	1.7	0.33	0.19	0.58	0.28	0.05	0.06	2804	1846	6	98.8	0.17	1334
T3	2.8	0.06	0.65	1.47	0.22	5.91	0.35	0.2	0.56	0.25	0.17	0.06	2477	1037	9.1	98.8	0.205	1299
T4	1.76	0.06	0.57	2.4	0.15	2.71	0.23	0.14	0.22	0.23	0.07	0.03	1922	1438	9.3	98.7	0.218	1257
T5	1.93	0.07	0.57	1.4	0.22	7.31	0.32	0.2	0.46	0.228	0.03	0.06	3409	2167	11	98.9	0.204	1258
T6	3.27	0.2	0.89	2.18	0.35	7.22	0.34	0.21	0.52	0.34	0.23	0.05	2750	2317	12.6	98.3	0.191	1249
T7	2.83	0.07	0.2	2.76	0.29	7.94	0.33	0.19	0.49	-	0.04	0.06	3481	2502	14.2	98.9	0.196	1355
T8	0.93	0.13	0.9	2.44	0.31	6.99	0.35	0.2	0.37	-	0.07	0.05	3879	1443	15.4	98.4	0.162	1290

Table A5: Spring candidate alloys (Chapter 6)

Alloy	Al	Ca	Cr	Fe	Mn	Mo	Nb	V	Si	Cl	Ta	Zr	O	C	Mo eq:	Density %	Strain to failure	0.2% yield strength
SC 1	1.48	0.13	1.82	4.53	0.3	9.87	0.35	0.22	0.35	-	0.09	0.03	2980	2126	25.2	98.4	0.388	1137
SC 2	3.57	0.04	1.39	2.77	0.35	12.7	0.32	0.2	0.35	-	0.13	0.06	4071	2233	20.2	98.3	0.354	1292
SC 3	1.92	0.14	1.81	2.61	0.3	8.83	0.33	0.2	0.46	-	0.06	0.07	2473	1342	18.1	98.8	0.326	1208
SC 4	1.86	0.23	0.90	3	0.33	8.06	0.39	0.23	0.47	-	0.07	0.06	3039	1608	17.2		0.321	1211
SC 5	2.90	0.17	0.71	3.90	0.33	6.16	0.28	0.22	0.49	-	0.03	0.06	2454	2053	16.5	98.5	0.306	1175
SC 6	2.77	0.13	1.74	3.16	0.23	6.19	0.25	0.21	0.44	-	0.03	0.06	2855	1920	16	98.8	0.282	1171

Table A6: Additional alloys used in multiple regression (Chapter 6)

Alloy	Al	Ca	Cr	Fe	Mn	Mo	Nb	V	Si	Cl	Ta	Zr	O	C	Mo eq:	Density %	Strain to failure	0.2% yield strength
Ad 1	0.19	0.12	0.76	2.14	0.22	7.79	0.4	0.23	0.4	0.34	0.13	0.08	1174	956	15.7	98.3	0.246	1231
Ad 2	0.25	0.21	0.89	2.79	0.25	0.773	0.41	0.23	0.41	0.23	0.08	0.08	3025	2374	10.8	98.3	0.208	1256
Ad 3	1.1	0.12	0.56	1.60	0.2	12.46	0.43	0.24	0.35	-	0.09	0.01	2781	1503	17.5	98.7	0.269	1248

Appendix 2: Enlarged images of SR-Al feedstock

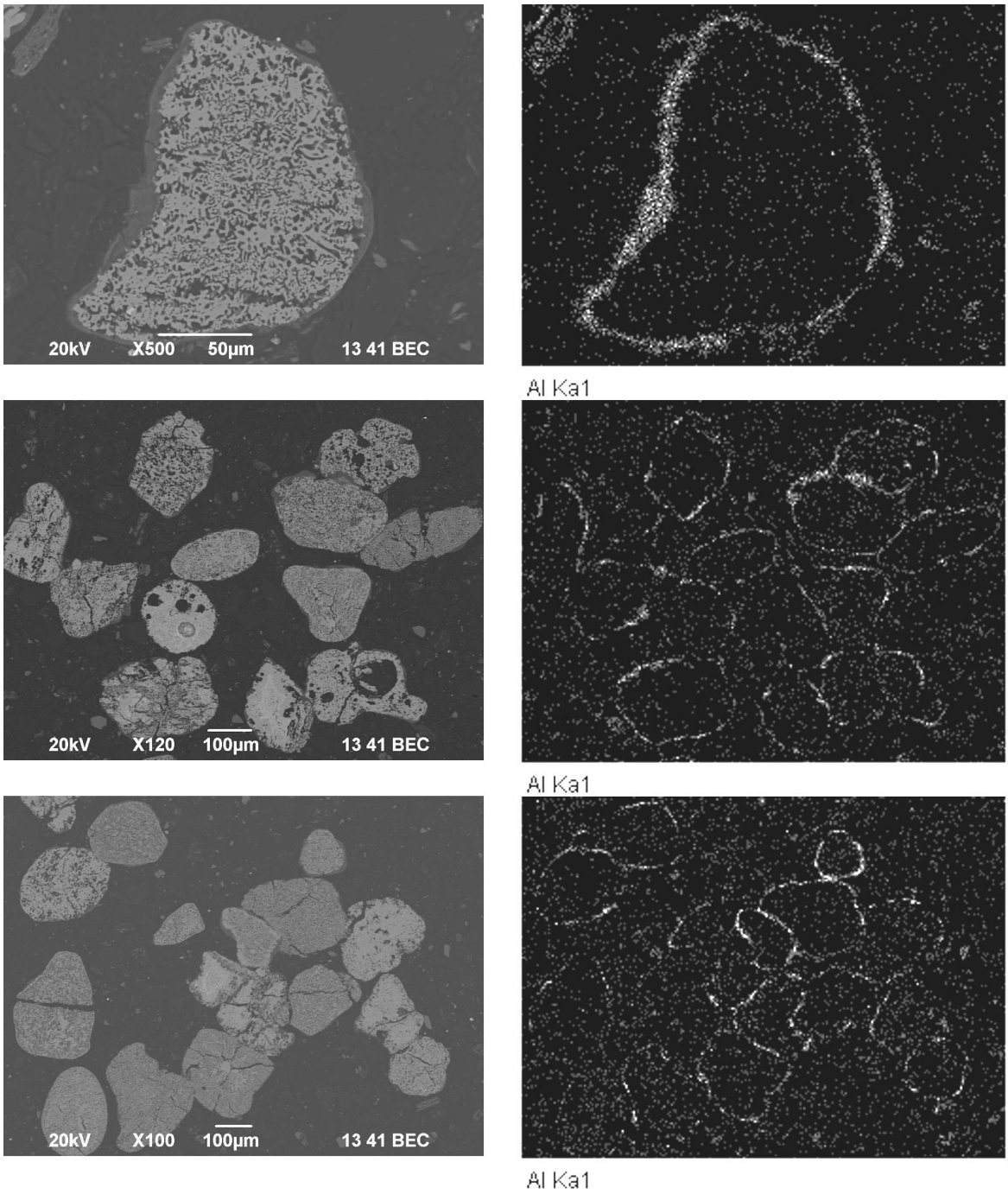

Fig. a1: 6 wt% Al2O3 enhanced SR feedstock, heat treated at 1100°C for 4 h.

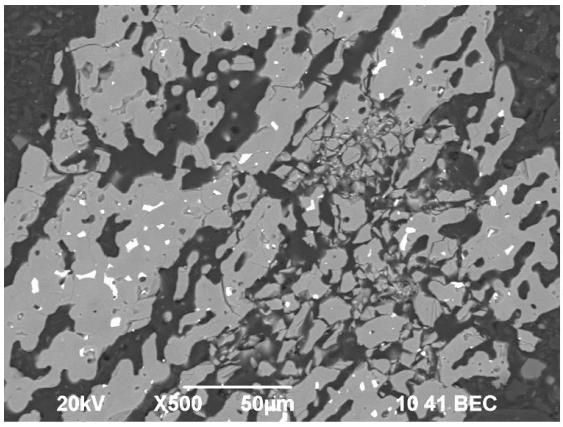

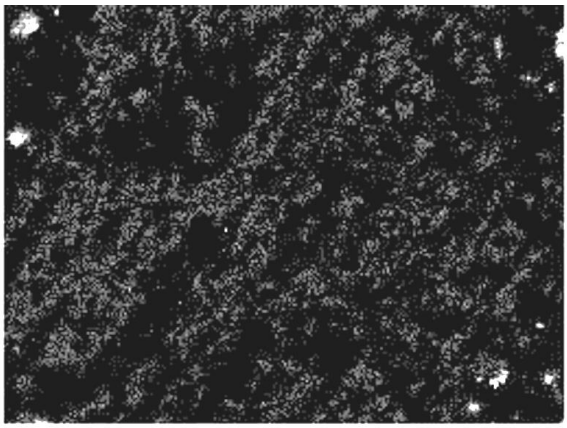

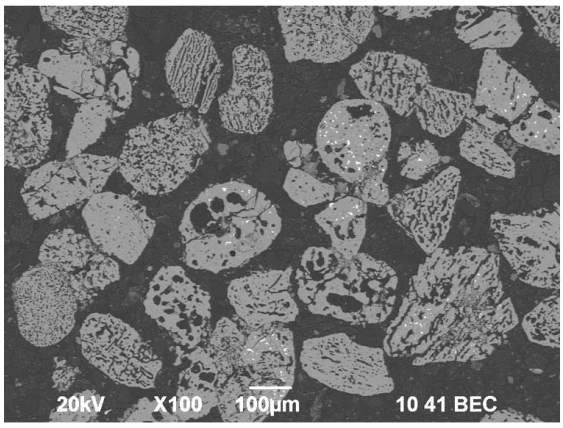

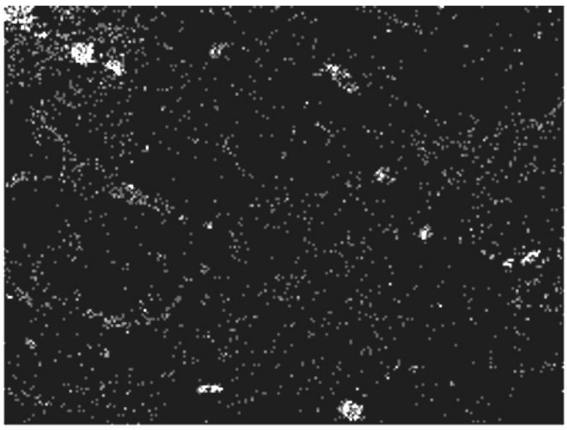

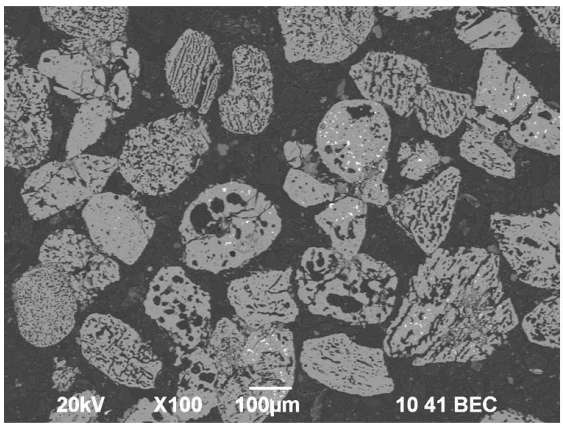

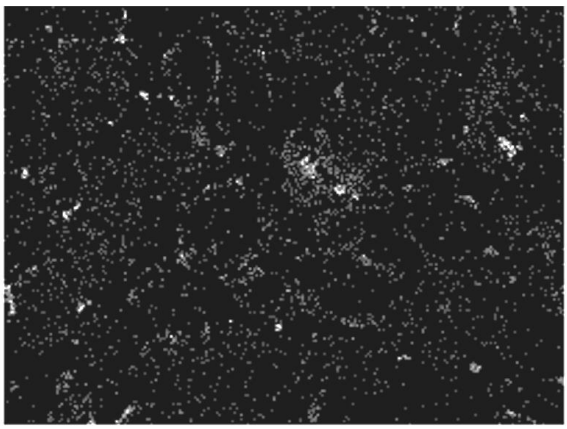

Fig. a2: 6 wt% Al enhanced SR feedstock, heat treated at 1350°C for 4 h.

Appendix 3: Notes

Ferric pseudobrookite and reduced rutile crystallographic data files used by Iluka to refine XRD spectra of SR (Chapter 1) came from CSIRO who derived the crystallographic data from:

Grey I.E., Li C., Ness T. (1998), Nonstoichiometric Li-Pseudobrookite (SS) in the Li2O-Fe2O3-TiO2 System Journal of Solid State Chemistry, 141, 221-228

The aluminium content of the fully reduced SR sample (Chapter 4) produced via R&D differs from that of the scaled up alloy produced at developmental scale used for subsequent consolidation and mechanical testing. The increase in aluminium is likely due to contamination from the alumina insulator. Other runs of SR exhibited increased Al content when the insulator was corroded after each run.

Contamination of insulator into the titanium alloy product was determined early during the work of this thesis and the insulator set up altered to increase the distance of the insulator and the cathode tray. As such, subsequent experiments were monitored for insulator corrosion and none of the alloys consolidated and testing in Chapter 4 have aluminium introduced from contamination of the insulator.

Carbon precipitates found analysed via X-EDS are shown below in Fig. a3 and a4 and a5 below, representing carbides in consolidated SR derived titanium alloys.

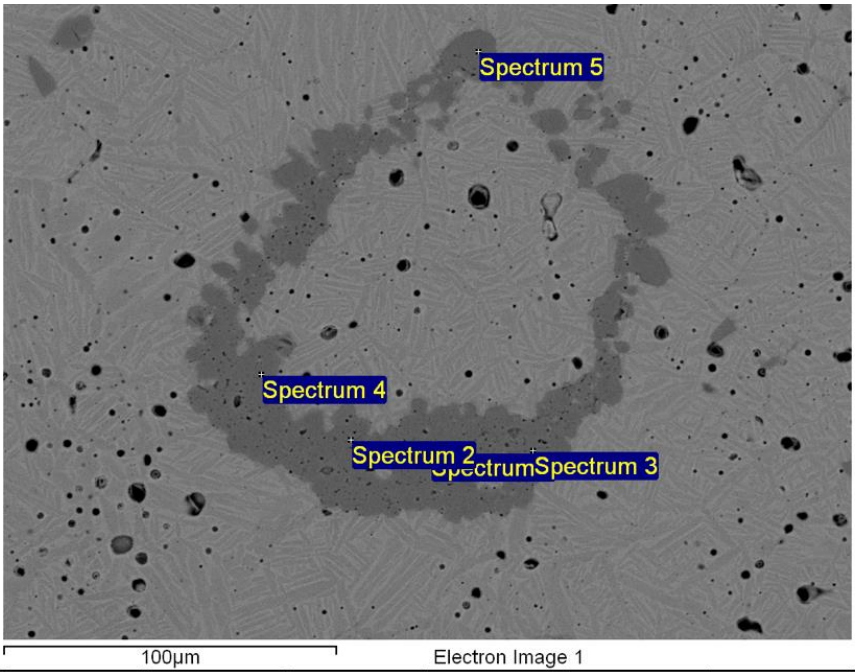

Spectrum	C	Al	Si	Cl	Ca	Ti	Total
Spectrum 1	17.95	-	-	-	-	82.05	100
Spectrum 2	4.47	-	-	0.52	0.45	94.56	100
Spectrum 3	5.22	-	-	0.42	0.33	94.03	100
Spectrum 4	5.19	0.25	0.31	0.27	0.21	93.77	100
Spectrum 5	18.11	-	-	-	-	81.89	100

Fig. a3: X-EDS analysis of a ‘scum’ particle in a SR derived titanium alloy containing 2.8 wt% Al following consolidation via FAST for 30 minutes at 1090°C.

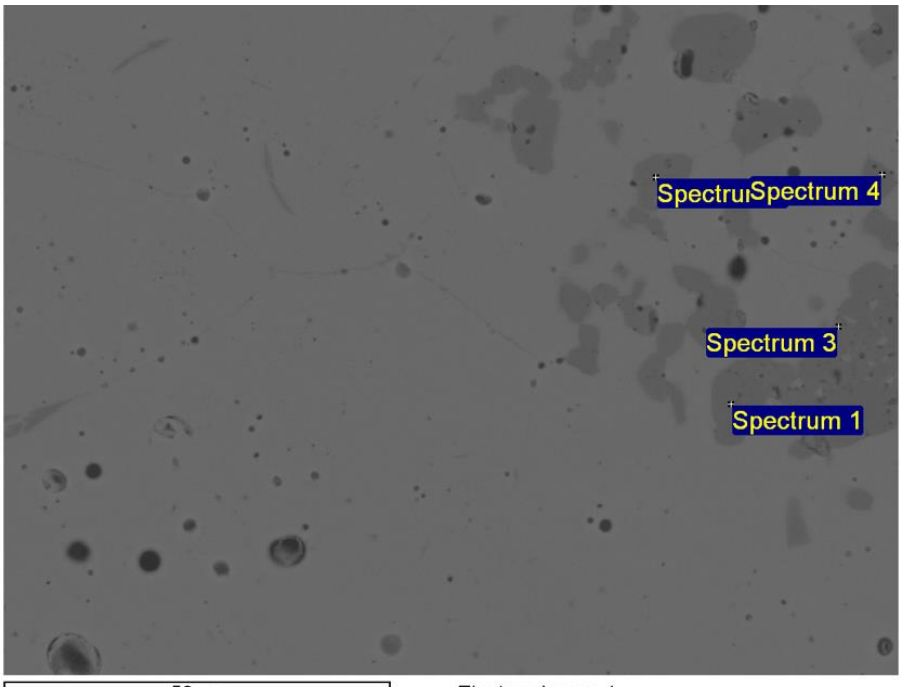

Spectrum	C	Cl	Ca	Ti	Total
Spectrum 1	6.15	0.41	0.24	93.2	100
Spectrum 2	5.6	0.22	-	94.18	100
Spectrum 3	15.51	-	0.17	84.32	100
Spectrum 4	6.27	0.44	0.26	93.04	100

Fig. a4: X-EDS analysis of coarse precipitate particles in a SR derived titanium alloy containing 9.5 wt% Mo following consolidation via FAST for 30 minutes at 1090°C.

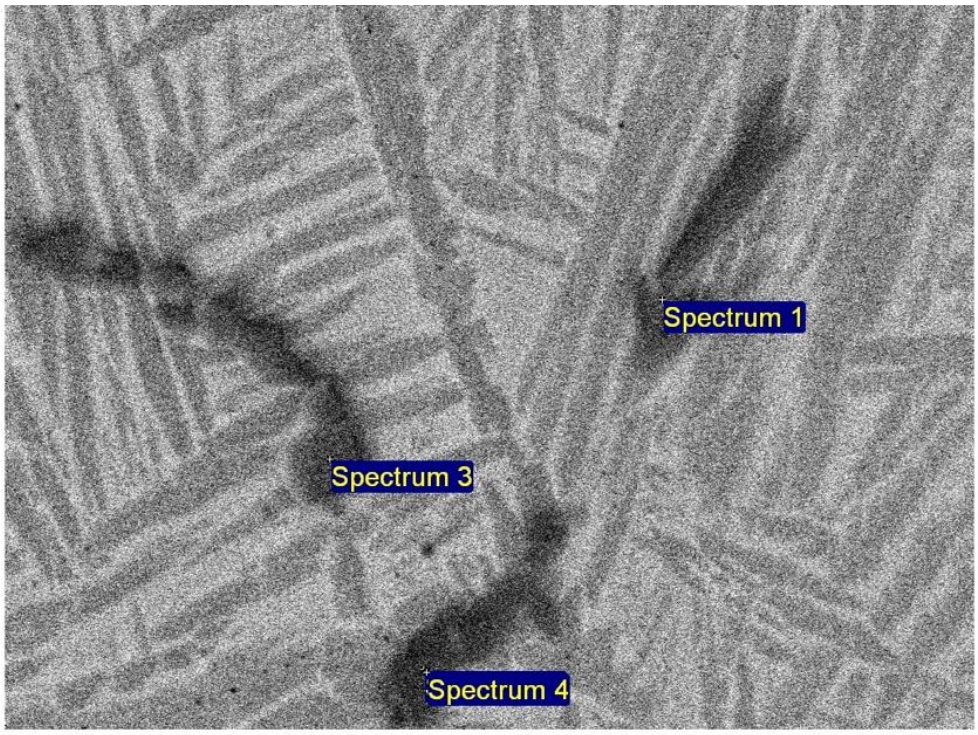

Spectrum	C	Al	Ti	Fe	Total
Spectrum 1	18.91	0.33	79.34	1.42	100
Spectrum 2	16.88	-	82.5	0.62	100
Spectrum 3	11.09	-	86.94	1.97	100
Spectrum 4	12.85	0.36	83.76	3.03	100

Fig. a5: X-EDS analysis of a lath like particle in a baseline SR derived titanium alloy following consolidation via FAST for 30 minutes at 1090°C.

Typically, the carbon values were between 16-20 wt% or around 5-7 wt%. Further investigation is required to determine the stoichiometry of the titanium carbide phases forming, although previous work has determined that the TiC_{1-x} phase forms during FFC reductions on the cathode surface [1].

Appendix 4: Oxygen Error Analysis

Error analysis for oxygen values was determined by measuring the oxygen content of a SR derived titanium alloy containing 2912 ppm oxygen a total of twenty times. The values were then used to determine a standard deviation value of ± 118 ppm. Therefore 2 standard deviations are equal to ± 236. The values measured are listed below.

Test	Oxygen (ppm)
1	2945
2	2750
3	2912
4	2985
5	2977
6	2624
7	2828
8	2821
9	3024
10	2871
11	3073
12	2991
13	2955
14	2944
15	3123
16	2816
17	2762
18	3001
19	2921
20	2910
Average:	2912

Appendix 5: Enlarged image of Fig. 4.2.7b.

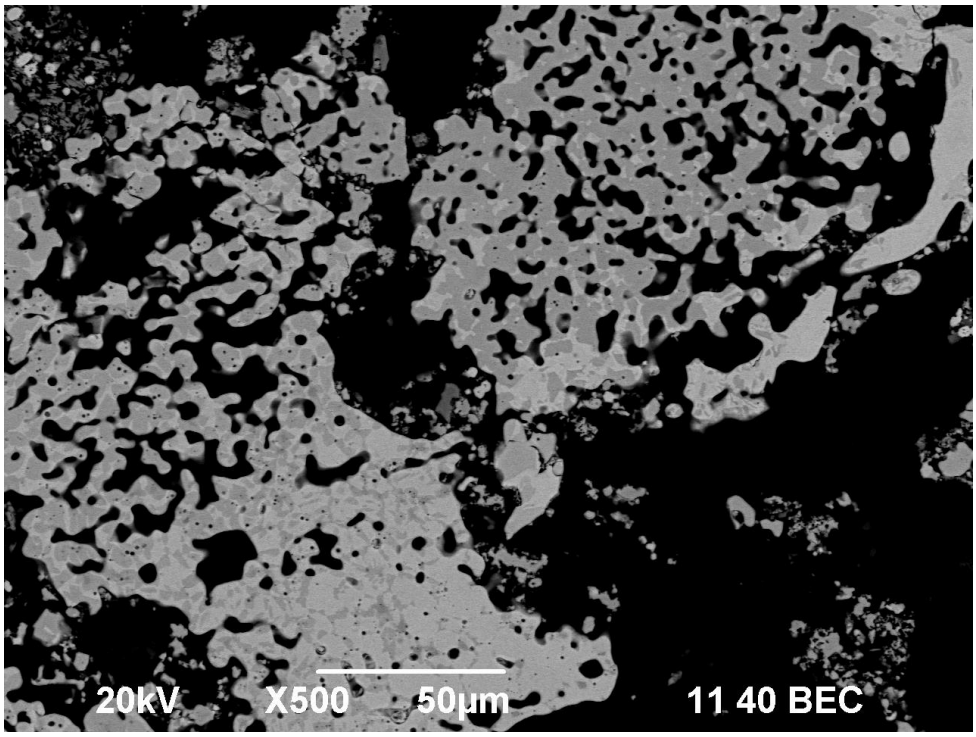

Fig. a6: Enlarged backscattered electron image of Fig. 4.2.7b showing the difference in contrast of the alpha (dark) and beta (light) phases.

Appendix 6: Porosity vs other phases

Using backscattered electron detection using the SEM, it can be difficult to discern between porosity and light phases, typically carbon based phases. However, by detecting secondary electrons, the difference between porosity and light phases can be asserted. Fig. a7 displays images of SR-17Mo which have been taken in both secondary electron and backscattered electron modes. The smaller spherical shapes are typically pores whereas the larger angular shapes are usually carbides.

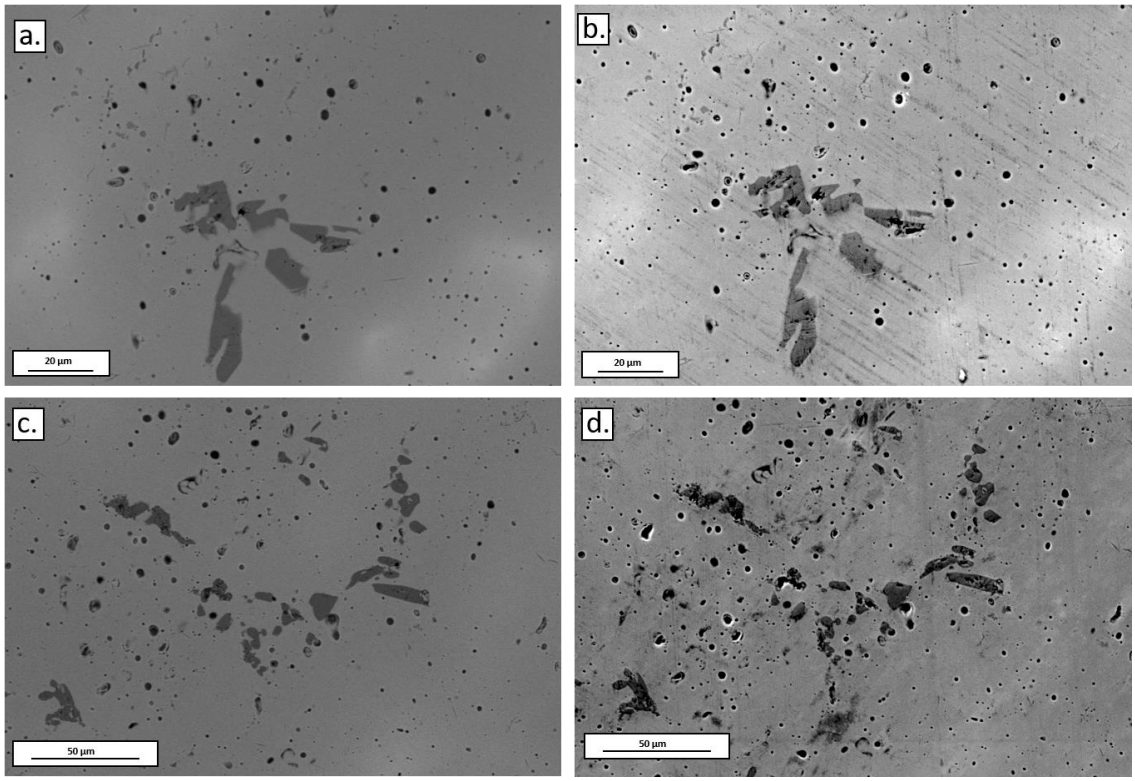

Fig. a7: Backscattered and secondary electron images of SR-17Mo displaying porosity and a second phase a) and c) backscattered electron images b) and d) secondary electron images.

References

[1] C. Osarinmwain, E. P. L. Roberts and I. Mellor, "Solid state electrochemical synthesis of titanium carbide," *Chemical Physics Letters,* vol. 621, pp. 184-187, 2015.